Reduced-Order-Models for Strongly Nonlinear Multi-Degree of Freedom Systems: a Quantitative and Qualitative Assessment

Cristiano Martinelli

Faculty of Engineering

Doctor of Philosophy in Engineering

This thesis is submitted for the degree of *Doctor in Philosophy*

Supervisors

Prof. Maurizio Collu

Dr. Andrea Coraddu

Dr. Andrea Cammarano

This thesis is the result of the author's original research. It has been composed by the author and has not been previously submitted for examination which has led to the award of a degree.

Abstract

The increasing demand for eco-sustainable structures and low-carbon emission systems is driving the research in many engineering fields, pushing the boundaries of scientific knowledge. High-performance structures, i.e. more efficient and lighter structures, are required to comply with the continuously more stringent regulations, nowadays imposed by many countries. This undermines the linear approximation used for modelling the behaviour of mechanical systems and structures, exposing their ultimately nonlinear nature. In this context, the need for a better understanding of the nonlinear dynamics behaviour of mechanical structures is becoming of primary importance, serving as a motivation for this work. In the literature, many authors have investigated the nonlinear behaviour of mechanical systems, mostly focusing on simplified mathematical representation with a single degree of freedom, especially in the analysis that involves the study of the global dynamic behaviour of the systems. This is particularly evident for systems which show strong nonlinear behaviour, e.g. systems with contact and impact, whose dynamics are extremely complicated and rich. In addition, it is not well known how accurate the identified mathematical models are, especially under which conditions they fail to capture the system dynamics from a qualitative and quantitative point of view.

This thesis focuses on the dynamics of multi-degree freedom systems that exhibit strong nonlinear behaviours and aims to improve the tools/methods for their analysis and identification. In particular, mechanical systems with two degrees of freedom and piecewise (non-smooth) stiffness characteristics are considered. The dynamics of the systems are studied from a numerical and experimental point of view, tackling practical problems that currently represent an issue for their analysis and identification. Firstly, the rich dynamics of the system are investigated using numerical procedures. The presence of multiple period-doubling isolas and a bifurcation of the backbone curve is numerically proven using path-following techniques and numerical integration schemes. This represents an improvement in the fundamental understanding of the dynamics and bifurcation mechanisms of two-degree-of-freedom piecewise systems. Then, the effect of smoothing functions in approximating piecewise stiffness characteristics is assessed via a comparison of the dynamics of the approximate and non-approximate systems. It is demonstrated that the usage of the smoothing function permits obtaining a high level of accuracy, especially when chaos or quasi-periodic behaviours are avoided, significantly reducing the computational effort of the numerical calculations and simplifying the overall procedure. To prove the existence of bifurcation of the backbone curves and the presence of period doubling isolas encountered during the numerical analyses, an experimental test rigs are designed and tested exciting the main structure in two different ways, i.e. using an asymmetric (test-rig #1) and symmetric excitation (test-rig #2) condition. The obtained results confirm the existence of the investigated nonlinear phenomena and provide an accurate base of experimental data that can be used for testing nonlinear models and/or methods for parameters identification. Building on existing techniques, a novel method for the identification of nonlinear systems is proposed. The method, named the Nonlinear Restoring Force (NRF) Method, is capable of interfacing with linear identification methods and can be easily implemented in current industrial identification procedures, improving the accuracy of the identified models. The proposed method is used to identify the parameters of reduced-order models associated with the experimental test rigs. The identified reduced-order models are then validated against experimental results, using levels of excitation that are different from the one used for the identification process. This demonstrates the efficacy of the proposed identification method and proves that the identified reduced-order models are capable to capture the dynamics of strongly nonlinear systems from a qualitative and quantitative point of view.

Contents

List of Figures

List of Tables

Acknowledgements

I would like to thank my PhD supervisors for their dedication, support, and infinite patience during the development of this research project. In particular, I would like to express my sincere gratitude to Dr Andrea Cammarano for his support, advice and commitment in helping me during this project. Without him, I would have not been able to complete this dissertation and achieve this great milestone. I would like also to thank Dr Andrea Coraddu for his continuous support, despite the distance that separates the two institutions. I am also very grateful to Prof. Maurizio Collu who helped me and supported me on different occasions during the development of this research project.

A special thank is reserved for my wife who supported me during positive and negative moments that are part of this incredible journey. I am also very grateful to all my colleagues from the University of Glasgow and the University of Strathclyde who helped and stimulated my research with interesting questions and advises. I would like also to thank Katrick Technologies and its employees who made possible this project.

Also, I would like to thank all my previous supervisors, Dr Elvio Bonisoli, Dr Sebastiano Fichera, and Prof. John Mottershead who inspired me and introduced me to the field of structural dynamics and vibrations.

Last but not least, I would like to thank my family and friends for their unconditional support.

Chapter 1

Introduction

1.1 The Importance of Nonlinear Dynamics of Mechanical Structures

Mechanical systems and structures have been studied for many years by engineers as they are fundamental to developing new technologies and improving current engineering solutions. In the scientific literature, they are studied in terms of static response, e.g. when static loads are applied, or in terms of dynamic behaviour, i.e. when time-varying excitation is applied and the inertial effect of the structure is considered to be relevant. The focus of this thesis is the study of the dynamic response of mechanical systems and structures when sinusoidal-like excitation is applied. Linear mathematical models capable of representing the dynamics of mechanical systems and structures have been developed and are currently used in industry and academia. The capability of such models to be effective and simple in their implementation has been proved in practical and experimental [7] engineering applications. Nonetheless, these models are based on the assumption of linear behaviour which represents an idealisation of the real world as mechanical systems and structures are ultimately nonlinear in their dynamic behaviour. When an underlying linear system exists, mechanical structures show a linear dynamic behaviour at low amplitudes of excitation. On the contrary, nonlinear phenomena and nonlinear dynamics effects appear frequently in mechanical structures when large amplitudes of excitation are applied or/and when boundary conditions facilitate the generation of nonlinear characteristics in the structure, e.g. the presence of joints may introduce friction or contacts. Following this perspective, linear models correctly describe the dynamic behaviour of mechanical systems and structures only in certain operational ranges: this represents a problem for their design and simulation as, most of the time, it is not known a priori if the operational conditions can trigger nonlinear dynamic behaviour in the mechanical structures. The consequences of this

Figure 1.1: Tacoma bridge (1940) vertical and twisting limit cycle oscillations due to the fluid-structure interaction.

could be catastrophic, e.g. unstable dynamic response, unexpected amplitude of vibration, and, in the worst cases, collapse of structures. One of the most famous examples is the collapse of Tacoma Bridge (1940) which occurred due to the interaction between the slender structure of the bridge and the wind. The aerodynamic loading led the system to uncontrolled vibration which resulted in high-amplitude limit cycle oscillations (represented in Fig. 1.1 [1]) and ultimately in the collapse of the structures. Other examples come from aerospace engineering where ground test vibrations of spacecraft and aircraft revealed the presence of nonlinear dynamic behaviours in the Cassini spacecraft [8] and the Airbus A400M [9]. The presence of nonlinear dynamic phenomena

[1]Figure available from https://www.structuremag.org/?p=19995

complicated the ground test activities and required time and effort to understand the source of nonlinearity and its effect on the dynamics of the systems. The complexity of the phenomenon did not allow for finding a nonlinear dynamic model capable of representing the observed dynamics. Therefore, in both cases, linear models were modified so that a conservative envelope or modified linear model would incorporate the nonlinear effect in the Frequency Response Functions (FRFs). This approach is very conservative, but still needed to overcome the certification of the aircraft/spacecraft and obtain the clearance to fly. On the other hand, the necessity to improve the model representing the dynamics of mechanical structures considering nonlinear effects has been felt since the 80' [10], were first studies on nonlinear flutter were commissioned by international organisations like NATO. Nowadays, the scientific literature offers many examples of nonlinear behaviour in aerospace structures: Kerschen and collaborators [11, 12] showed the presence of complex dynamic behaviour in real aircraft and spacecraft investigating the nature of the nonlinearities and demonstrated that nonlinear models are able to characterise and represent the complex dynamic behaviour of the considered systems. Coetzee et al. [13–16] demonstrated that typical instabilities in ground manoeuvres of aircraft can be represented with nonlinear models and numerical continuation techniques. High-aspect ratio wings have also been extensively studied in aerospace engineering to optimise the drag/lift ratio and several studies [17–20] concluded that nonlinear aeroelastic models, which account for structural nonlinearities, are necessary to correctly capture the dynamics of the high aspect-ratio wings. Other applications of nonlinear dynamic models for the analysis of aerospace structures can be found in [21–23].

Nonlinear behaviour is typically found in mechanical systems and structures: Snoeys et al. [24] showed that typically used mechanical structures like car frames, measurement instruments, rubber and others, show nonlinear behaviours due to the presence of nonlinear properties in their damping or stiffness characteristics. In early experimental studies, De Langre et al. [25] showed the intricate dynamics scenarios behind a fairly simple Duffing oscillator that presents symmetric and asymetric contacts. The authors demonstrated the presence of co-existing stable solutions which cannot be described with any linear dynamic model. Claeys [26] demonstrated, numerically and experimentally, the importance of non-ideal boundary conditions to describe the highly nonlinear behaviour of a mechanical beam in clamped-clamped conditions which cannot be reduced to a simple linear system. More recently, Thomas and collaborators [27–29] studied the nonlinear dynamic response of a circular plate, a Chinese gong and a piezoelectric cantilever beam. The authors showed the presence of complex dynamics in the considered systems characterised by internal resonances and demonstrated that some acoustic features (e.g. pitch glide in a Chinese gong) are generated by the presence of nonlinearities in the structures. In aerospace, mechanical, marine and civil engineering, nonlinear dynamic phenomena found practical applications in the study of impacting capsule systems [30], impact drilling systems [31], cracked systems [32], geared system with backslash [33, 34], mechanical oscillators [35–39] and aeroelastic systems with free-play gaps [40, 41], description of aerodynamics forces [42], buildings subjected to earthquakes [43], impact oscillators with rigid walls [44–46], nonlinear energy sinks [47–53] for vibration suppression and mitigation, load in vessels [54], dynamic positioning control of floating marine structures [55], and vortex-induced vibration of marine risers [56].

In the field of energy harvesting, instead, nonlinearities are introduced to improve the performance of the system; in fact, linear Vibration Energy Harvesters (VEHs) suffer from a reduced frequency bandwidth in which a high amplitude of response is reached. This limits their energy output, and thus their potential applications. In this context, researchers have tried to improve the frequency bandwidth of harvesters by adding purposeful nonlinear characteristics: Cammarano et al. [6] designed, tested, and characterised a bistable Electromagnetic Vibration Energy Harvester (EVEH) which exploited the magnetic forces to generate a double-potential well. In certain conditions, the harvester is able to trigger inter-well oscillations, generating a substantial amount of energy. Under sinusoidal excitation, the author demonstrated the presence of a broadband high-amplitude response, highlighting its potential applicability as broadband VEH. Wang et al. [57] introduced a frequency-up converted Piezoelectric Vibration Energy Harvester (PVEH). The system exploits the presence of magnets to generate quintuple-well potential and stoppers to induce vibrations at frequencies of excitation lower than the natural frequency of the harvester. In general, nonlinearities in energy harvesters are associated with a wider frequency bandwidth and higher performance of the harvesters [58, 59] and their presence, intentional or unintentional, is well documented in the scientific literature [60–67].

All these examples show the presence of considerable nonlinear dynamic behaviours in mechanical, aerospace, civil, and marine systems which should not be neglected and, in some cases, could be exploited to enhance the system performance (e.g. in the case of vibration energy harvesters). Under this perspective, nonlinear dynamic models become important because:

1. they can describe the dynamics of systems that linear models are unable to capture, from a quantitative and qualitative point of view.

2. they represent a more general and accurate representation of the dynamics of the systems which include both the linear and nonlinear dynamic behaviours.

Although these statements may appear similar at first glance there is a subtle and important difference between them. The first statement suggests that nonlinear models are necessary only when linear models are proved to be inadequate, i.e. when the linear models are not able to capture the dynamics of the investigated system. This approach to the problem has pushed industries and engineers to develop nonlinear analyses only occasionally, often after the occurrence of catastrophic events, like incidents due to shimmy oscillations in landing gears [13]. In this context, nonlinear models are perceived as a last resource for the characterisation of a certain phenomenon of the investigated system, following the principle of 'functionality', i.e. understanding when the effect of nonlinearities is not negligible anymore, or in other words when and under which conditions the linear approximation fails to describe the dynamic behaviour of the investigated system.

The second statement, instead, considers nonlinear models as an upgraded version of linear models. This has more profound consequences, especially nowadays that the industry is trying to reduce its carbon footprint: in fact, the stringent green policies, imposed by many countries, are forcing industries to move towards more efficient and performing structures. For example, the automotive and aviation transport sectors [68,69] have shown a change of paradigm in recent years, moving from a design strategy based on the strength and durability of materials to a design strategy based on lightweight structures. To reduce the weight, less material and more slender sections are utilised in the structures. This inevitably generates large stresses and deformation, which leads to nonlinear dynamic behaviours, and thus requires the usage of nonlinear models for the analysis and design of these structures. A second example comes from the aerospace industry: the usage of high-aspect-ratio wing in commercial aircraft would allow to reduce fuel consumption and emissions in the aviation sector. Nonetheless, aircraft would have a very large wing span which would not allow them to access airports during operations like boarding/disembarking of passengers. To solve this problem, hinges in the wings have been proposed as a possible solution [22]. However, the presence of hinges may generate friction and contact between components, leading to a severe nonlinear response of the structure. Under this perspective, nonlinear models play a central role not only in the understanding of the dynamics of mechanical structures but also in the improvement of their performance and capabilities and, ultimately, in the reduction of associated CO2 emissions.

1.2 Overview on the Dynamics of Nonlinear Structures

This section focuses attention on nonlinear mechanical systems and structures and proposes an overview of the methods and the areas of engineering that might be involved in the study of their dynamics. From an engineering perspective, nonlinear vibrations can be divided into three main application areas: numerical and analytical analyses, system identification, and experimental analyses. The proposed classification is graphically illustrated in Fig. 1.2. The first area incorporates all the numerical and analytical methods that are used for solving nonlinear systems and obtaining a solution from a mathematical point of view; this ranges from numerical techniques like nonlinear Finite Element Analysis (FEA) and numerical continuation to approximate analytical solution like the Multiple-Scales (MS) or Harmonic Balance Method (HBM). Chapter 2 will provide an extensive overview of this area with practical examples. The second group

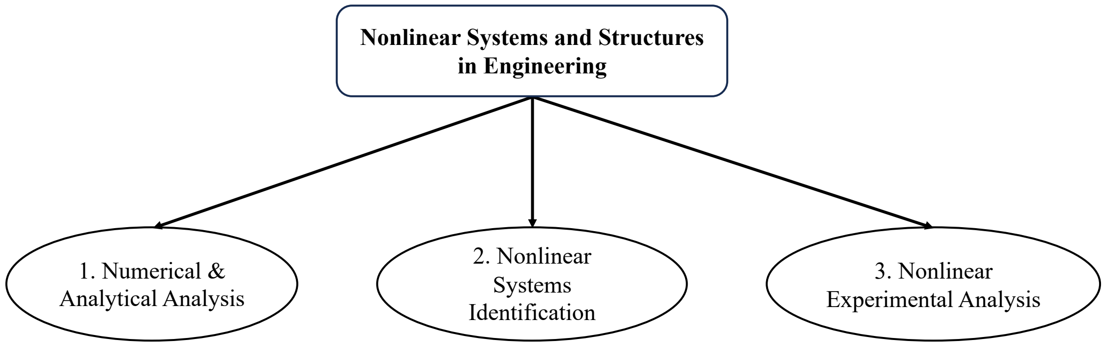

Figure 1.2: Application areas of nonlinear systems and structures in engineering.

considers all the techniques and methods that are used to identify equivalent nonlinear mechanical models and their parameters from experimental data. These techniques require different sets of data and therefore are generally distinguished into time-domain, frequency-domain, and time-frequency domain (see [70, 71] for a complete overview about the different classes of methods in nonlinear systems identification). Finally, the last group considers the experimental techniques that are used to investigate the behaviour of nonlinear structures. The development of mathematical theory behind nonlinear vibrations, instead, has not been considered in the above classification as it is equally shared between mathematicians and engineers, and it will not be considered in this work. In the field of nonlinear vibrations, the above-mentioned areas share the same problem: the increase in complexity of nonlinear analyses when the number of Degrees of Freedom (DOFs) of the system increases. This problem is sometimes referred as the *curse of dimensionality* [72], and can make unpractical or, in certain cases, impossible the analysis/identification of nonlinear systems. The concept is graphically explained in Fig. 1.3 where the dynamic models typically used in engineering applications are reported in terms of the number of degrees of freedom and degree of nonlinearity. When Multiple-Degrees-of-Freedom (MDOFs) structures are considered in the analysis/identification process, the degree of nonlinearities of the model is generally very small or absent. This means that models are linear or that nonlinearities are localised and affect only one or few DOFs. On the contrary, when the degree of nonlinearities of the structure is large, simple Single-Degree-of-Freedom (SDOF) models are generally

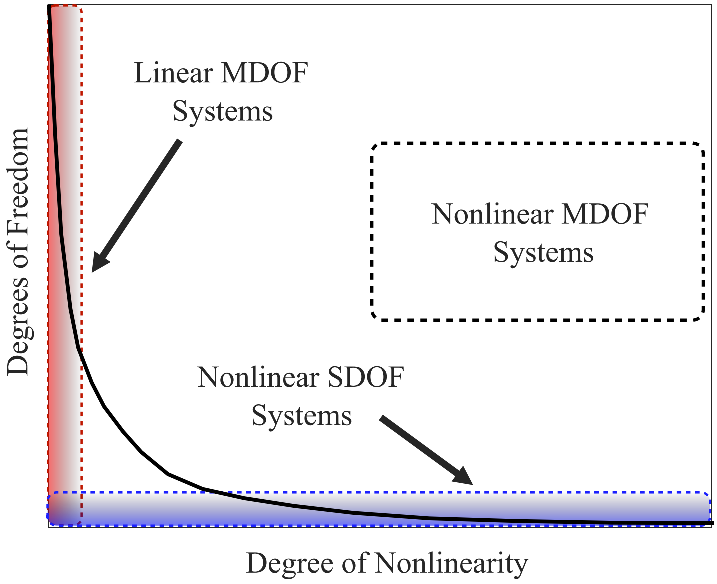

Figure 1.3: Mathematical models adopted for describing and analysing dynamic phenomena in terms of the degree of nonlinearities of the system and number of degrees of freedom.

used to study the dynamics. In the literature, only a few studies have addressed the problem of the dynamics of strongly nonlinear MDOF systems. This thesis focuses on the investigation of the dynamics of these systems, specifically considering those which feature an *underlying linear behaviour* [73,74]. The dynamic behaviour of these systems is graphically described in Fig. 1.4 in terms of the degree of nonlinearity and amplitude of excitation. The light-grey area indicates the presence of a linear dynamic behaviour, hence the system obeys the linear dynamic theory for these levels of nonlinearities and forcing amplitude. This area is associated with low amplitudes of excitation and a large degree of nonlinearity or, conversely, large amplitudes of excitation and a low degree of nonlinearity. When higher forcing is applied to a system with a discrete degree of nonlinearity, the system starts to show a weak nonlinear behaviour. This condition is characterised by the presence of forces associated with linear terms (e.g. inertial and linear stiffness for a Duffing oscillator) that are orders of magnitude higher than the forces associated with nonlinear terms (e.g. the cubic stiffness for a Duffing oscillator). Typical examples are the presence of bent peaks in the FRF due to the presence of

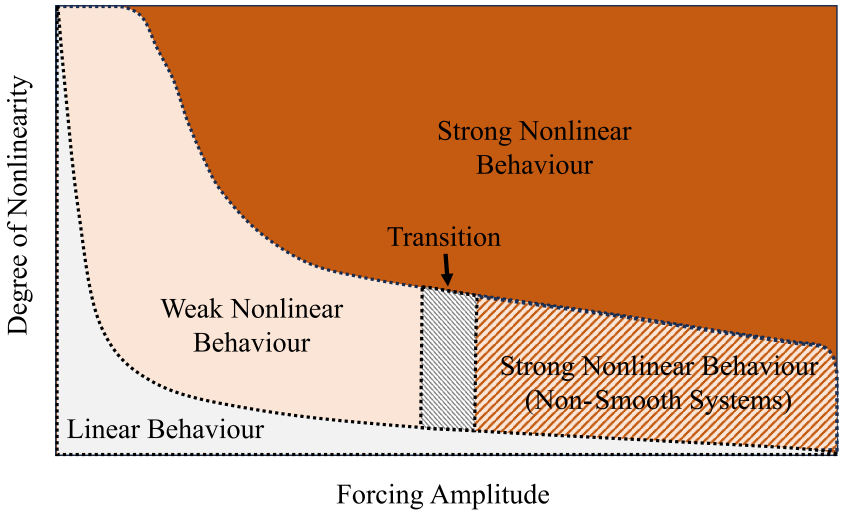

Figure 1.4: Dynamic behaviour of mechanical systems in terms of the degree of nonlinearities and forcing amplitude.

hardening/softening characteristics [73]. If the level of forcing increases, the system starts to develop a strong nonlinear behaviour with the appearance of complicated dynamics phenomena [75] which include chaos and quasi-periodic responses. Fig. 1.5 shows the four types of possible dynamic behaviour [76] that may arise from nonlinear systems when a sinusoidal excitation is applied: between them, there are aperiodic and multi-harmonic responses which are typically found in strongly nonlinear systems. Finally, the dashed area of Fig 1.4 indicates a region where strong nonlinear behaviour may occur at a lower amplitude of excitation. This typically occurs on systems that present non-smooth characteristics such as backlash or contacts. Non-smooth terms generate higher forces and therefore trigger strong nonlinear behaviour even when the amplitude of excitation is not particularly large.

1.3 Research Motivation

The thesis project finds motivation from the following research questions:

- What is the dynamic behaviour of strongly nonlinear mechanical systems with multiple degrees of freedom?

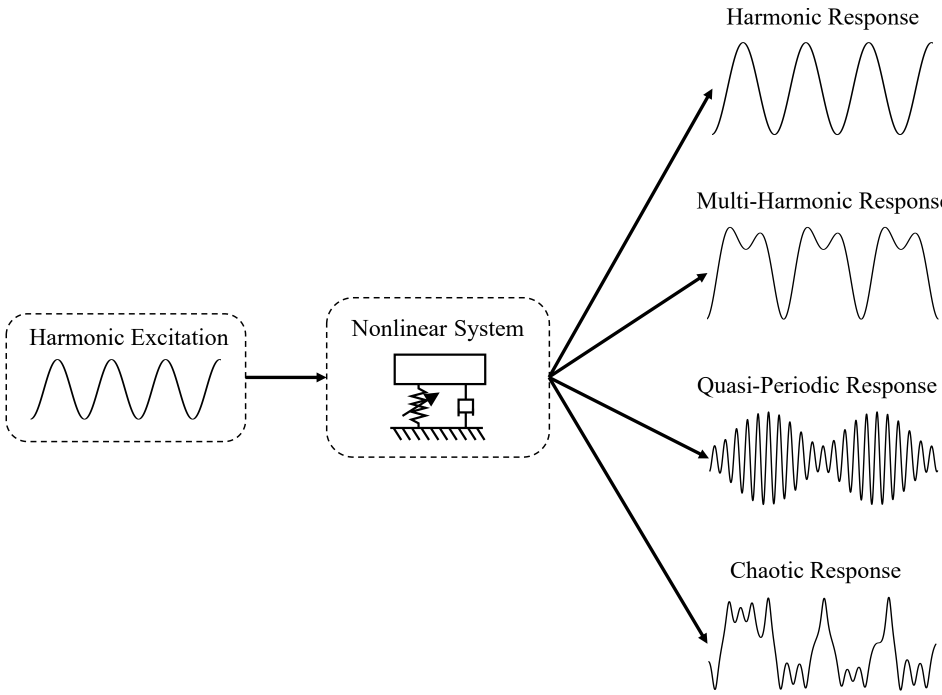

Figure 1.5: Dynamic behaviours of nonlinear mechanical systems.

- To what extent mathematical are models capable of reproducing the complex dynamics behaviour of nonlinear structures and when linear models fail to accurately predict the dynamics of the investigated system?

To answer these questions, the thesis has the following specific objectives:

- to further investigate the dynamics behaviour of mechanical multi-degree of freedom systems with a strong nonlinear behaviour, especially in the presence of contact. This includes studying particular dynamics phenomena such as backbone curve bifurcations and modal interactions in nonlinear systems.

- develop system identification procedures based on well-established identification methods and numerical tools for nonlinear mechanical systems with the intent to ease their implementation in industrial practices.

- validate the identified models against experimental results and evaluate their prediction capabilities at different excitation conditions.

1.4 Thesis Outline

The rest of the thesis is outlined as follows:

- Chapter 2 provides an overview of the scientific literature on the numerical and analytical techniques for analysing nonlinear systems. This chapter aims to introduce the reader to the mathematical approaches commonly used to compute the dynamic response of mechanical nonlinear systems. Particular attention is devoted to highlighting the limitations, problems, and validity of the solution obtained with the different methodologies.

- Chapter 3 introduces a strongly nonlinear MDOF system featuring piecewise stiffness (contacts). The nonlinear system is analysed with numerical integration and continuation schemes. The most interesting dynamic features, like the bifurcations of the backbone curves, isolas, and aperiodic dynamic responses are analysed utilising the numerical tools introduced in Chapter 2. Finally, it is demonstrated that, under certain conditions, approximated definitions of piecewise stiffness characteristics do not affect the dynamics of the system, resulting in simplified numerical analyses.

- Chapter 4 discusses the design of the test rigs representing the previously analysed system. This test rig serves as the ground truth to validate the complex nonlinear phenomena encountered in the numerical analyses of the previous chapter. Firstly, the product design specifications of the experimental test rig are introduced and then a numerical design is carried out. To this end, FEA and CAD are used to obtain a Reduced Order Model (ROM) of the experimental system and to perform the linear design of the test rig. The ROM is then used to conduct the design of the nonlinear behaviour of the system, paying particular attention to the associated bifurcation scenario.

- Chapter 5 describes the experimental results obtained using two versions of the designed test rig, named Test Rig #1 and Test Rig #2. The dynamics of the systems are analysed in terms of time histories, steady-state orbits, frequency response, and Poincaré sections, investigating the route to chaos and demonstrating the presence of quasi-periodic oscillations. In order to generate a consistent database, the dynamics of test rigs are investigated with and without the presence of the piecewise stiffness characteristic, simulated by two motion limiting constraints.

- Chapter 6 discusses the identification of ROMs representing the two test rigs. Following the experimental activities, the smooth and non-smooth characteristics are identified separately, using meta-heuristic optimisation methods and a novel methodology, named the Nonlinear Restoring Force (NLRF) method. The method is based on the separation of the linear and nonlinear restoring force of the system and aims to simplify the identification procedure of the nonlinear system, thanks to the possibility of being interfaced with linear identification methods. The method is introduced through a numerical example and it is used to identify the nonlinear characteristics associated with the two experimental test rigs.

- In Chapter 7, the identified ROMs are used to perform additional numerical simulations, carrying out comparisons with experimental data and Finite Element (FE) models. The scope of the chapter is two-fold: firstly it aims to validate the identified nonlinear models and then it wants to show their extrapolation capabilities. To this end, the numerical models are tested at different excitation amplitudes, comparing the numerical simulations with a set of experimental data that were not used during the identification procedure. At the end of the chapter, the identified and validated model is used to obtain a complete characterisation of the experimental system, proving the presence of complex dynamic phenomena such as the bifurcation of the backbone curves and the detached isolas in the investigated frequency domain.

- Chapter 8 proposes the analysis and investigation of mechanical engineering systems for which the implementation of nonlinear characteristics may have beneficial effects on their dynamics and performance. To this end, mechanical systems that require high performance, such as vibration energy harvesters, are considered. Specifically, two case studies are analysed: the first case study investigates the dynamics of an electromagnetic bistable nonlinear energy harvester while the second one shows the optimisation of a 3D planar-shaped piezoelectric energy harvester that behaves linearly. The chapter concludes by discussing the performance of two vibration energy harvesters, highlighting the advantages and disadvantages of the different mechanical structures from an engineering point of view.

- Finally, Chapter 9 discusses the conclusion of the project and highlights the direction of further works.

1.5 Publications

The following publications, journal and conference papers, have been produced as a result of this project:

- Martinelli, C., Coraddu, A., & Cammarano, A. (2023). Performance-aware design for piezoelectric energy harvesting optimisation via finite element analysis. International Journal of Mechanics and Materials in Design, 19(1), 121-136..

- Martinelli, C., Coraddu, A., & Cammarano, A. (2023). Approximating piecewise nonlinearities in dynamic systems with sigmoid functions: advantages and limitations. Nonlinear Dynamics, 111(9), 8545-8569.

- Martinelli, C., Coraddu, A., & Cammarano, A. (2024). Strongly nonlinear multi-degree of freedom systems: Experimental analysis and model identification. Mechanical Systems and Signal Processing, 218, 111532.

- Martinelli, C., Avadhani, R., & Cammarano, A. (2023). Identification of Nonlinear Characteristics of an Additive Manufactured Vibration Absorber. In Society for Experimental Mechanics Annual Conference and Exposition (pp. 229-235). Cham: Springer Nature Switzerland.

- Martinelli, C., Coraddu, A., & Cammarano, A. (2023). Experimental Parameter Identification of Nonlinear Mechanical Systems via Meta-heuristic Optimisation

Methods. In Society for Experimental Mechanics Annual Conference and Exposition (pp. 215-223). Cham: Springer Nature Switzerland.

- Martinelli, C., Coraddu, A., & Cammarano, A. (2023). Experimental Analysis of a Nonlinear Piecewise Multi-degrees-of-Freedom System. In International Conference on Nonlinear Dynamics and Applications (pp. 665-675). Cham: Springer Nature Switzerland.

Chapter 2

Numerical and Analytical Techniques for the Analysis of Nonlinear Systems

2.1 Introduction

This chapter provides an introduction to the analytical and numerical techniques that are used in the following chapters for analysing the nonlinear dynamics behaviour of mechanical systems. A comprehensive and complete overview of all the analytical and numerical techniques is out of the scope of this thesis and the proposed overview should be considered as an introduction to the most common methods/techniques for the analysis of nonlinear mechanical systems. In the considered cases, the systems are representable as a set of Ordinary Differential Equations (ODEs) and practical numerical examples are also presented, discussing the potential advantages/limitations of the different methods. In detail, the chapters treat the following aspects:

- Section 2.2 introduces the numerical integration techniques and provides guidelines for their usage in the analysis of nonlinear mechanical systems. The concept of bifurcation diagrams, Poincaré section, and basin of attraction are described in detail, providing numerical examples and linking the numerical results with practical physical aspects. To this end, simple nonlinear systems, i.e. the Duffing oscillator (in its mono- and bistable configurations) and the Van der Pol oscillator, are utilised as reference examples.

- Section 2.3 introduces the analytical methods that are mostly used in the scientific literature to compute the steady-state behaviour of mechanical systems. Particular attention is dedicated to the harmonic balance method, highlighting its advantages and limitations.

- Section 2.4 provides an introduction to numerical continuation techniques: firstly collocation methods are introduced and then the concept of pseudo-arc-length continuation is explained by solving nonlinear algebraic equations.

2.2 Numerical Integration Based Techniques - Bridging Mathematics and Engineering Perspective

Direct numerical integration of ODEs represents one of the most important tools for the analysis of nonlinear systems. These methods are generally referred to as *numerical integration* in the scientific literature and consist of directly integrating the equation of motion associated with the system under investigation. By performing the integration, it is possible to obtain approximate dynamic response of the system in the time domain. Formally, numerical integration techniques are applied to an Initial Value Problem (IVP), representing a general nonlinear system, in the following form

$$\begin{aligned} \dot{\mathbf{y}}(t) &= \mathbf{f}(t, \mathbf{y}(t)) \\ \mathbf{y}(t=0) &= \mathbf{y_0} \end{aligned} \tag{2.1}$$

where $\mathbf{y}$ represents state vector and $\mathbf{y_0}$ is the set of initial conditions. Differently from some approximate methods, numerical integration provides a solution for the nonlinear system only in the time domain, introducing numerical errors [77] with respect to the exact solution. In the literature, such methods are considered a valuable tool for understanding the dynamics of nonlinear mechanical systems, nonetheless a formal treatment of numerical integration procedures, e.g. Runge-Kutta or linear multi-step methods, is not presented and it is considered outside the scope of this thesis. The interested reader should refer to references [77, 78] to have more insights about this aspect. Instead, this Section aims to show how numerical integration schemes are used to obtain valuable information and graphical representations of the dynamic behaviour of nonlinear systems, particularly using the following tools: (1) phase portrait, (2) bifurcation diagrams, (3) Poincaré stroboscopic maps and sections, and (4) basins of attractions. These graphical representations of systems dynamics are constantly used in the scientific literature (see for example [6, 33, 37, 38, 40, 41, 46, 79–83] and references therein), therefore they are considered essential tools for the analysis of nonlinear systems.

2.2.1 Orbits, Phase portrait, and Poincaré Maps

The time response is fundamental to understanding the dynamic behaviour of a nonlinear system. In mathematics, the time-history of a nonlinear system (dynamical system) is generally called a *trajectory* or *orbit* [75, 84]. One powerful tool for visualising the dynamics of a nonlinear system is the *phase portrait*; from a mathematical point of view, the phase portrait is formally defined as *the partitioning of the state space into orbits* [84] [1], i.e. it is a projection of the system trajectory into a limited number of states (generally two or three for graphical reasons). In engineering applications, the phase portrait is intended as the representation of the system trajectory in terms of displacement and velocity, see for example the references [33, 37, 41]. Although the phase portrait could be qualitatively obtained with analytical techniques, an analytical solution of the nonlinear system is generally not achievable, thus numerical integration is used for quantitative representation. In order to practically visualise a phase portrait of a nonlinear system, a Van der Pol oscillator is considered. The Van der Pol oscillator is a non-conservative system with nonlinear damping, generally used in engineering to represent self-excited vibrations. The system is characterised by a single degree of freedom and the associated phase portrait of the steady-state dynamic orbit is shown in Fig. 2.1. The equation of motion of the Van der Pol oscillator is represented by the

[1] formally, the state space is the space of all the families of trajectory associated with a nonlinear system.

following expression:

$$\ddot{x} + \Gamma(x^2 - 1)\dot{x} + x = 0 \tag{2.2}$$

where Γ is the nonlinear damping parameter, x is the displacement, $\dot{x}$ is the velocity, $\ddot{x}$ is the acceleration. Fig. 2.1(a-b) show the trajectories of the oscillator, in two different conditions and starting from the same initial condition (1,0). When the parameter Γ is equal to -1 the system shows the presence of a stable *fixed point* [75], i.e. an equilibrium point where the trajectory ends, while instead when $\Gamma = 1$ the system exhibits a stable *limit cycle*, i.e. a cycle in a neighbourhood of which there are no other cycles [84], which attracts the trajectory of the oscillator and results in a steady-state orbit. It

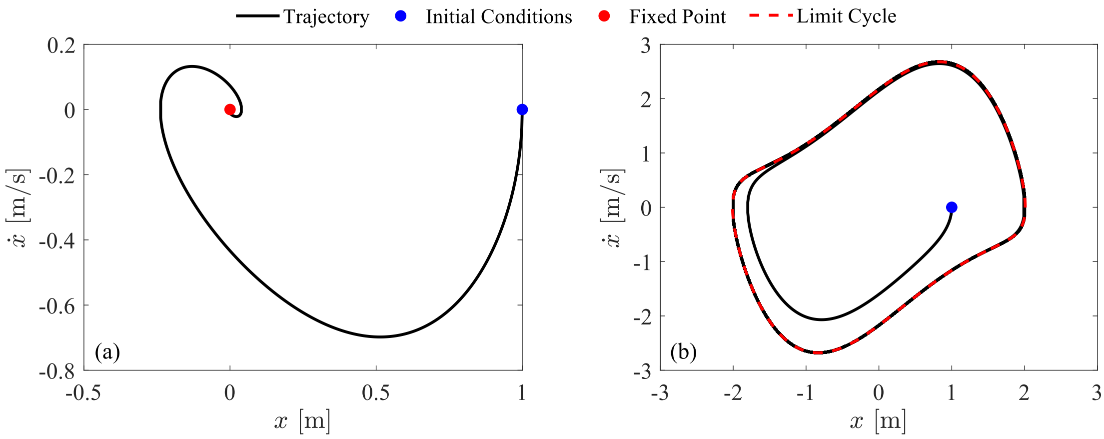

Figure 2.1: Phase portrait representation of the dynamics of the van der Pol oscillator for a fixed point when $\Gamma = -1$ (a) and a limit cycle when $\Gamma = 1$ (b).

is worth noticing, that, under this definition, periodic orbits of undamped unforced mechanical systems are not considered limit cycles. The change of behaviour in the system is due to a Hopf bifurcation which transforms the fixed point (equilibrium) into a limit cycle when the parameter Γ is modified. Fig. 2.1 shows the two *attractors* [75], i.e. a set of states towards which the systems tends. Attractors are stable by definition, thus the opposite is referred to as *repellers* [75], i.e. a set of states from which the systems escape. From an engineering point of view, these conditions correspond to two typical states encountered in the dynamics of the system: fixed or equilibrium points are steady-state static conditions, e.g. a mass-damper oscillator at the resting position; limit cycles, instead, correspond to the periodic response of mechanical systems, e.g. the steady-state periodic response of a mechanical oscillator. Nonetheless, nonlinear systems also offer other types of attractors: named torus attractors and strange attractors. The first one is characterised, in certain conditions, by the presence of quasi-periodic oscillations, a form of aperiodic response which only occurs on state spaces with *torus* shape [75]. These oscillations are characterised by the presence of at least two incommensurable harmonic components in the response [85], i.e. harmonic components whose ratio is irrational. This causes the presence of a long-term oscillation which goes around the torus never closing itself. From a mechanical perspective, this phenomenon occurs in MDOF nonlinear or self-excited systems driven by an external harmonic excitation. In these cases, the system can show the presence of both periodic oscillations (lock-in condition) and quasi-periodic oscillations (lock-off condition). In both conditions, the trajectory of the system is moving along the torus but in the first case, the trajectory repeats itself after a certain number of periods. Strange attractors, instead, are associated with chaotic behaviours. *Chaos* is a deterministic aperiodic dynamic behaviour that nonlinear systems exhibit in certain conditions and it is characterised by a strong sensitive dependence on initial conditions [75]. From a practical point of view, this means that neighbouring trajectories, i.e. trajectories that are slightly perturbed one from the other, can separate very fast from each other leading to completely different dynamic states after a certain amount of time. The four

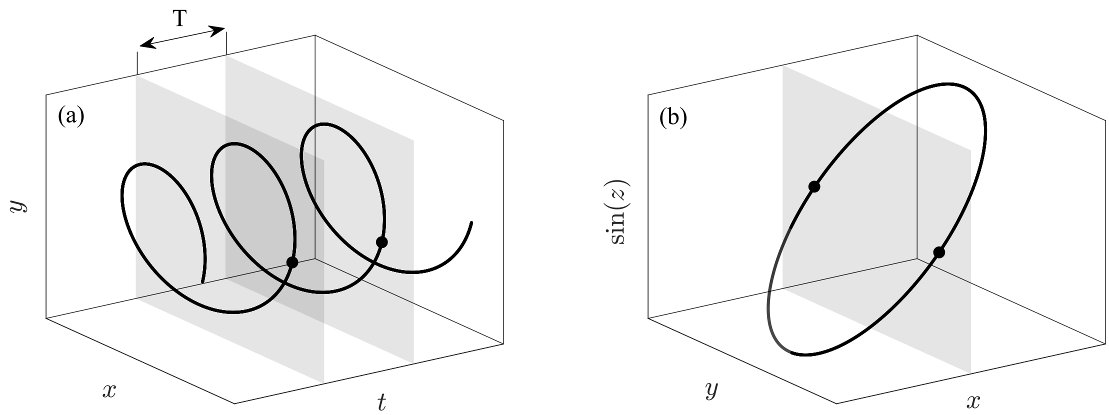

Figure 2.2: Poincaré maps: stroboscopic map (a) and section maps (b) for forced periodic oscillations (limit cycle). In the panels, x represents the displacement, y denotes the velocity, t indicates the time, and z is defined as the product Ωt.

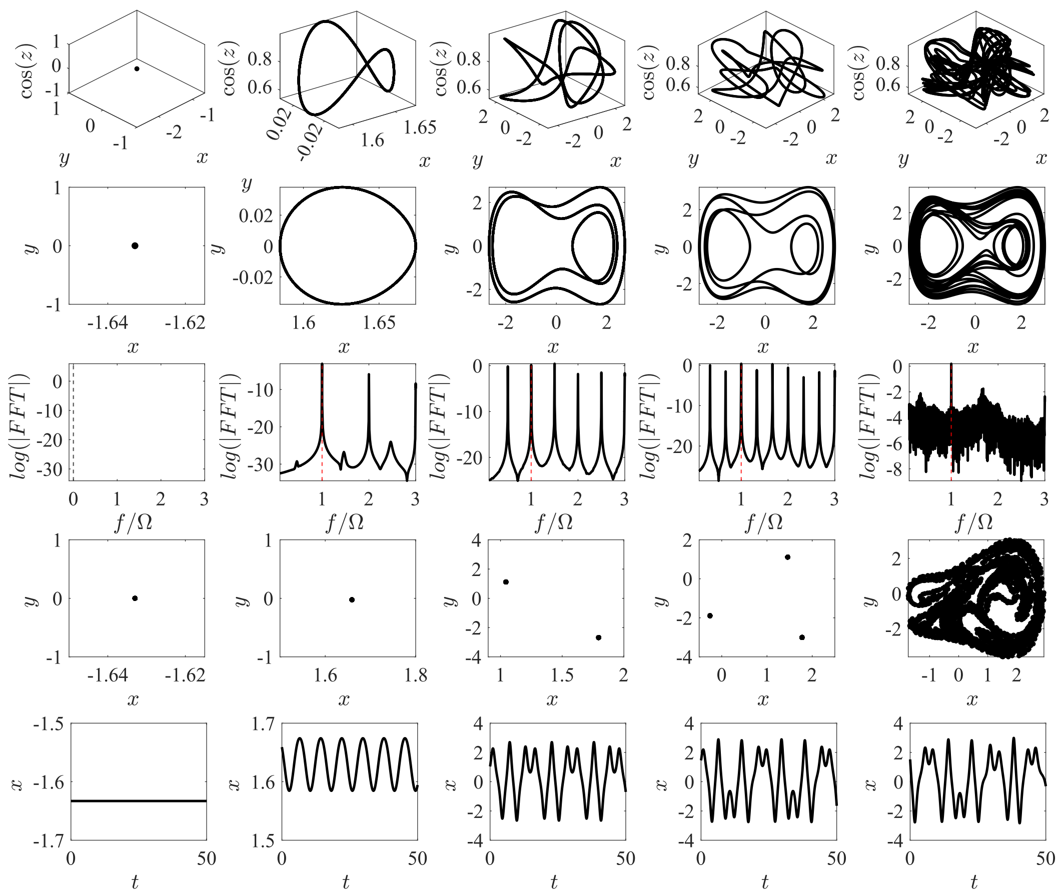

Figure 2.3: Attractors of a bistable oscillator ($m = 1$ kg, $c = 0.04$ Ns/m, $k = -2$ N/m, $\mu = 0.75$ N/m^3, and $\Omega = 0.81$ rad/s) analysed in terms of 3D phase portrait, 2D phase portrait, FFT, Poincaré stroboscopic map, and time-history. In the panels, x represents the displacement, y denotes the velocity, t indicates the time, and z is defined as Ωt.

attractors previously mentioned, i.e. fixed point, limit cycle, torus, and strange attractors, show different dynamic behaviours and, although not being an exhaustive list of all the possible attractors/repellers, they are sufficient to describe most of the dynamic phenomena associated with the mechanical systems, especially the ones considered in this thesis.

Graphical representations can facilitate the visualisation of the dynamic behaviour of nonlinear mechanical systems, showing what type of attractor is driving its dynamics. Together with the phase portrait, *Poincaré maps* are one of the graphical tools for the analysis of nonlinear systems. Formally, the Poincaré map is a mapping of the trajectory

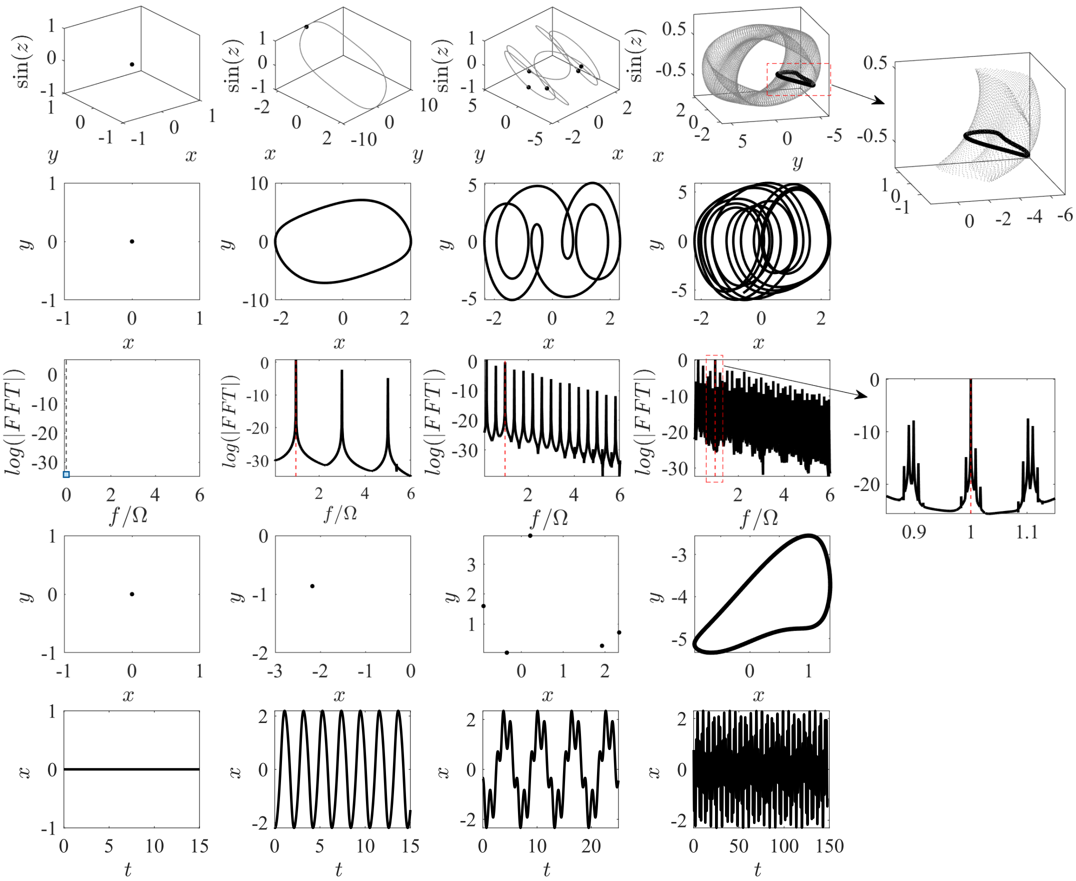

Figure 2.4: Attractors of a forced Van der Pol ($F = 18$ N and $\Gamma = 1$) oscillator analysed in terms of 3D phase portrait, 2D phase portrait, FFT, Poincaré stroboscopic map, and time-history.In the panels, x represents the displacement, y denotes the velocity, t indicates the time, and z is defined as Ωt.

of a system from section P of the state-space to itself [75]. The intersection between the trajectory and the section P defines the Poincaré map. From a mathematical point of view, the section can represent any state of the system, including the time. This happens because, in *non-autonomous* systems, i.e. systems with direct expression of the time t in the equation of motion, the time represents one state of the system. Non-autonomous systems can be reduced to an *autonomous version* by adding additional states to the set of equations that describe the dynamics of the system. Let's consider a simple linear mechanical forced oscillator as a reference example. The associated equation of motion can be written as:

$$m\ddot{x} + c\dot{x} + kx = F\cos(\Omega t) \tag{2.3}$$

where m, k, c, and F are the mass, damping, stiffness, and forcing amplitude. The term $\cos(\Omega t)$ contains the frequency of excitation Ω and the time t. Reducing the system to its first-order form, an additional equation is added to the system along with a second variable $y = \dot{x}$. Similarly, it is possible to eliminate the direct dependence from the time t by adding an equation and another state; in this case, the variable $z = \Omega t$ is added. The system of Eq. 2.3 is transformed into the following first-order system:

$$\begin{cases} \dot{x} = y \\ \dot{y} = -\frac{c}{m}y - \frac{k}{m}x + \frac{F}{m}\cos(z) \\ \dot{z} = \Omega \end{cases} \tag{2.4}$$

From an engineering perspective, time is generally considered a special state. This results in a slight distinction between Poincaré stroboscopic maps and Poincaré section maps: the first one represents a map which samples the trajectory every period T (or combinations of it) while the second one indicates a Poincaré map which samples the trajectory of every time that it passes to physical phase space section, e.g. $x = 0$. The two concepts are graphically reported in Fig. 2.2 for a steady state limit cycle, Fig. 2.2(a) describes a Poincaré stroboscopic map and Fig. 2.2(b) describes a Poincaré section for $x = 0$ forced oscillator. It should be noted that in both cases a periodic oscillation (limit cycle) is represented but in the stroboscopic map the additional state is the time and the mapping occurs every n period T (in the figure $n = 1$) while in the Poincaré section consider the additional state $z = \Omega t$

In order to visualise the different types of attractors, two simple SDOF nonlinear models are considered: a bistable and a forced van der Pol oscillator. These systems possess the four attractors previously introduced and therefore are chosen as reference examples. Firstly a bistable oscillator is considered to visualise: fixed points, limit cycles, and chaotic attractors. The bistable oscillator presents the following equation of motion in the autonomous form:

$$\begin{cases} \dot{x} = y \\ \dot{y} = -\frac{c}{m}y + \frac{k}{m}x - \frac{\mu}{m}x^3 + \frac{F}{m}\cos(z) \\ \dot{z} = \Omega \end{cases} \tag{2.5}$$

where μ represents the cubic stiffness coefficient. The forced Van Der Pol oscillator has the following equation of motion instead:

$$\begin{cases} \dot{x} = y \\ \dot{y} = -\Gamma(x^2 - 1)y - x + F\sin(z) \\ \dot{z} = \Omega \end{cases} \tag{2.6}$$

The attractors of the two oscillators are obtained by varying the force F and the excitation frequency Ω. The attractors associated with the first system are reported in Fig. 2.3 where the panels in the first row represent 3D attractors, the second row represents the phase portrait, the third row the FFT of the state x, the fourth row indicates the Poincaré stroboscopic maps, and the last row shows the associated time histories. Each column is associated with a different force level in the following order from left to right: 0, 0.15, 0.5, 0.99, and 1.05 N. At $F = 0$ N, the bistable oscillator shows one of its stable equilibrium points (in the potential well at negative displacement) [2], at $F = 1.05$ N the oscillator shows the presence of a chaotic attractor, and at $F = 0.15$, 0.5, and 0.99 N the oscillator is characterised by periodic responses with different periods, respectively, single period (1:1), period-doubling (2:1), and period-tripling (3:1) [3]. Moving from left to right it is possible to see that the steady-state orbits increase in complexity, requiring more periods of excitation to complete a cycle. When the force is large enough, the system ends in chaos, as shown by the last column of Fig. 2.3. It is possible to note that the increment of the periods in the response is associated with an increment in the frequency content of the FFT of the associated

[2]For graphical reasons, the 3D attractor is represented with a point.

[3]Period doubling responses are defined as $M : N$, where M represents the number of periods of the excitation frequency and N is the number period necessary to complete a multi-periodic response.

time history. The Poincaré maps provide useful information about the dynamics of the system: when a fixed point or single period limit-cycle is found, the map shows just a point. This occurs because the map is sampling the trajectory every period of excitation; in the case of the fixed point the system does not move so the sampling occurs in the same point of the phase space, leading to a single point in the Poincaré map. In the case of a single-period response, instead, the system returns to the same point of the phase space at every period. Since the sampling occurs every period, the Poincaré map appears, once again, as a single point. When the response of the system passes through a period-doubling bifurcation, more points appear in the Poincaré maps. This occurs because period-doubling dynamic responses require more periods of excitation to complete a cycle. This leads to finding the system at different locations of the phase space if the map samples the trajectory at every period of excitation. Specifically, if sampled every period, the number of points in the map indicates the number of periods that are required to complete a periodic response. For example, the Poincaré map of Fig. 2.3 associated with F = 0.5 N (third column) shows two points which evidence the presence of a 2:1 period doubling dynamic response. Moving towards a higher amplitude of excitation, the bistable oscillator passes through the typical period-doubling cascade that ends with the generation of chaos. The chaotic response is represented by the last column of the figure: in this condition, the dynamics of the system is aperiodic and the system continuously oscillates around the two equilibrium points. Given the presence of chaos, the associated Poincaré map results in a strange attractor. The last row of Fig. 2.3 shows the time histories associated with the investigated attractors. Differently, from the FFT and Poincaré maps, the time histories do not provide particularly useful information about the dynamics of the system. It is quite difficult to see the difference between the multi-periodic and chaotic attractors. On the contrary, phase portrait and Poincaré maps offer more insights into the dynamics of the system.

A sinusoidally excited bistable oscillator does not show quasi-periodic behaviour; to visualise the attractor associated with this dynamic condition, a forced Van der Pol oscillator (Eq. 2.6) is taken as a reference example. Similarly to the bistable oscillator, the attractors of the system are studied in terms of 3D phase portraits, 2D phase portraits, FFT of the time-histories, Poincaré maps, and time-histories. Fig. 2.4 shows the results when the frequency and force are varied. The figure follows the same description of Fig. 2.3 with the different columns, from left to right, representing the following conditions: $F = 0$ N and $\Omega = 0$ rad/s, $F = 18$ N and $\Omega = 3$ rad/s, $F = 18$ N and $\Omega = 5$ rad/s, and $F = 18$ N and $\Omega = 4$ rad/s. The system shows the presence of a fixed point (first column), a single limit cycle (second column), a 5:1 period-doubling limit cycle (third column), and a limit torus (last column). Again, the FTT shows the increment in the frequency content of the response which results in a more complicated phase portrait. In the case of a limit torus, the frequency response is composed of incommensurable frequencies, as shown in the detail of the FFT. This is a clear indication of the presence of quasi-periodic oscillations in the system response. More interestingly, the quasi-periodic oscillations result in an *invariant circle* in the Poincaré map, i.e. a continuous closed line. The detail of the limit torus attractor demonstrates that the 3D representation of the invariant circle coincides with a section of the torus, as expected from the definition of quasi-periodic oscillations.

Fig. 2.3 and Fig. 2.4 presented the attractors associated with a bistable oscillator and a forced Van der Pol oscillator. The figures demonstrate the usefulness of graphical representations such as Poincaré maps and phase portraits, showing how they allow gathering additional insights into the system dynamics.

2.2.2 Bifurcations and Bifurcation Diagrams

Poincaré sections, time histories, and phase portraits are useful tools to understand the dynamics of nonlinear systems and their attractors. Nonetheless, as shown by the analysis of the van der Pol and bistable oscillator, attractors may change when a parameter of the system is modified. In the scientific literature, the topological change in the phase-portrait is known as a *bifurcation* [84]. Formally, the bifurcation is defined as a topological change of the attractor and indicates a change in the dynamic behaviour of the system. A complete classification of bifurcations is out of the scope of this section, and the interested reader is invited to refer to the references [75, 84] for more information about the classification of bifurcations. Nonetheless, to introduce the reader to the concepts discussed in the next chapters, a short list of the bifurcations, typically encountered in the dynamics of mechanical nonlinear systems, is presented:

- **Saddle-Node bifurcation of a cycle**: indicates the coalesce and annihilate of two limit cycles. An example of this bifurcation is the change of stability in the periodic response of a Duffing oscillator.

- **Period doubling bifurcation**: it occurs when the topology of limit cycles changes and a different number of periods is required to complete the cycle. In the previous examples, both the forced Van der Pol oscillator and the bistable oscillator showed the presence of period-doubling bifurcations when the frequency and/or amplitude of the forcing function changes.

- **Hopf bifurcation**: it is the transformation of a fixed point into a limit cycle. This bifurcation is typically encountered in self-excited systems, e.g. aeroelastic systems that overcome the flutter speed. In the previous examples, a Hopf bifurcation is found in the unforced Van der Pol oscillator when the parameter Γ changes from -1 to 1.

- **Neimark-Sacker bifurcation**: this bifurcation occurs when the periodic response of the system changes and becomes aperiodic. It is also called secondary Hopf bifurcation as it is equivalent to a Hopf bifurcation in the Poincaré maps, i.e. a point becomes an invariant closed curve.

- **Branch bifurcation**: this bifurcation occurs when a cycle or a fixed point bifurcates into two possible solutions, e.g. pitchfork bifurcation.

Engineers and mathematicians rely on the bifurcation analysis to understand and visualise how one or more system parameters influence the dynamic of the system and its bifurcation scenario. In the field of nonlinear vibrations, the bifurcation parameter, generally called λ, is typically represented by the forcing amplitude F or by the frequency of excitation Ω, although times to times other parameters might be used. The *bifurcation diagrams* describe the evolution of the system dynamics for a certain bifurcation parameter λ; they can be obtained by exploiting numerical integration schemes:

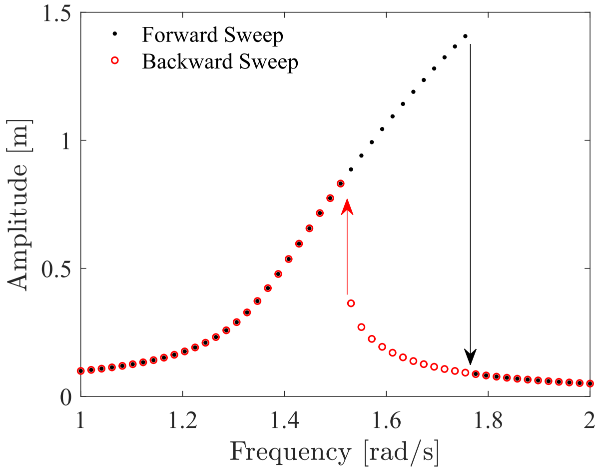

Figure 2.5: Bifurcation diagram of the Duffing oscillator ($m = 1$ kg, $c = 0.04$ Ns/m, $k = 2$ N/m, $\mu = 0.75$ N/m^3, and $Q = 0.1$ N) in terms of displacement amplitude.

firstly the steady-state dynamic response must be achieved for a certain set of system parameters. This can be obtained by letting the transient dynamics die throughout a long enough numerical integration procedure. At this point, the obtained steady-state condition is post-processed and plotted for a single value of the bifurcation parameter in the bifurcation diagram. The procedure is then repeated changing the bifurcation parameter to obtain more points in the bifurcation diagram. Authors often use either amplitude, maximum/minimum value, or value of the Poincaré section of the selected signal, achieving a different representation of the bifurcation diagram. The subsequent steady-state conditions can be obtained by 'continuing' the previous solution. The 'continuation' of the solution can be performed without resetting the initial condition [73], i.e. passing the final condition of the system as initial conditions for the next integration procedure, or by continuously resetting the initial condition to achieve multiple co-existing steady-state solutions.

Taking a forced Duffing oscillator as a reference example, Fig. 2.5 shows the bifurcation diagram in terms of the amplitude of response at different excitation frequencies Ω. In this case, the bifurcation parameter λ is set equal to Ω. The equation of motion for a forced Duffing oscillator is represented by the following expression:

$$m\ddot{x} + c\dot{x} + kx + \mu x^3 = F \cos \Omega t \tag{2.7}$$

where μ represents the cubic stiffness parameter. The diagram is obtained without resetting the initial conditions and by performing forward/backward frequency sweeps. This allows obtaining a clear understanding of the region where co-existing steady solutions exist. The arrows indicate the typical *jump* phenomenon: this occurs when the system loses stability and, moving to the adjacent frequency, it is forced to 'jump' to another stable steady-state response.

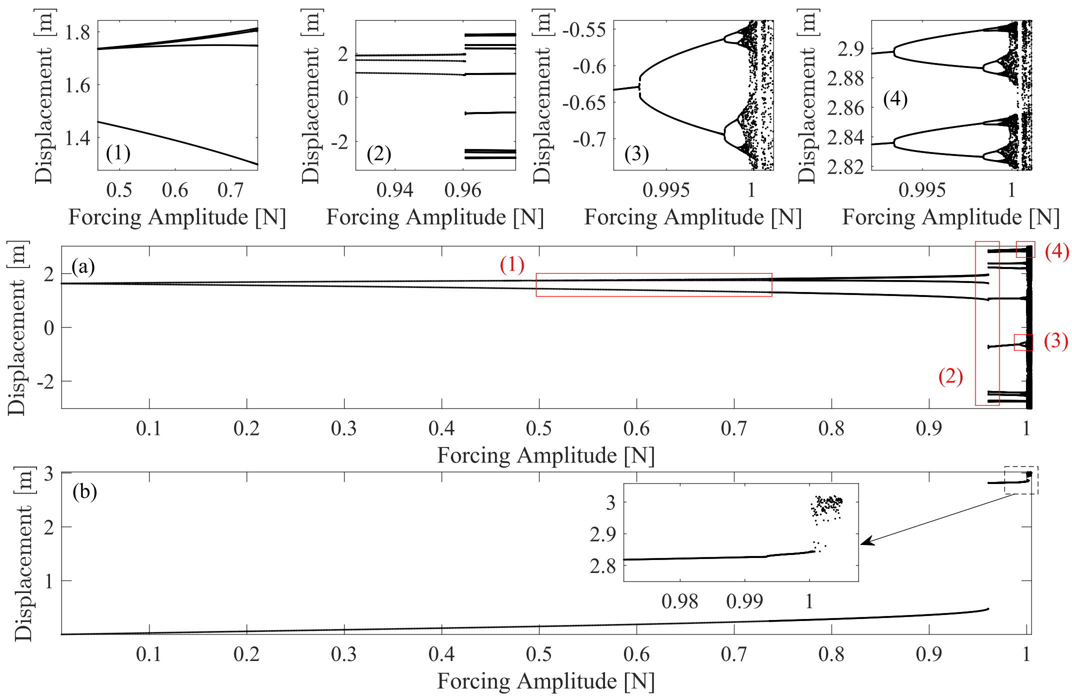

Figure 2.6: Bifurcation diagram of the bistable oscillator ($m = 1$ kg, $c = 0.04$ Ns/m, $k = -2$ N/m, $\mu = 0.75$ N/m^3, and $Q = 1.5$ N) in terms of value of the Poincaré sections (a) and displacement amplitude (b).

It should be noted that the bifurcation diagram obtained with the numerical integration has the disadvantage of considering only stable solutions. On the contrary *numerical continuation* techniques are capable of continuing both stable and unstable solutions; these methods utilise path-following continuation, e.g. pseudo-arc length continuation, to track the changes of limit-cycles or fixed points when one or more bifurcation parameters are modified. These methods are quite powerful and allow obtaining the bifurcation diagrams of nonlinear systems. Numerical continuation methods are discussed in detail in Section 2.4, nonetheless, it is worth pointing out that these methods have also limitations. Indeed, aperiodic solutions, such as chaotic and quasi-periodic responses, are difficult to track with numerical continuation and, thus the associated bifurcation diagrams often cannot be obtained. Differently from numerical continuation, bifurcation diagrams obtained with numerical integration procedures can track the evolution of the system dynamics through chaotic behaviours. This results in an extremely valuable tool for understanding the route to chaos of a system. To demonstrate this concept, the bistable oscillator described by Eq. 2.5 is now used as a reference example to compute the bifurcation diagram. By increasing the forcing amplitude F, the bistable oscillator passes through period-doubling cascades [73, 75] and reaches chaos. Two different output quantities, i.e. value of the Poincaré sections and displacement amplitude, are used to create the bifurcation diagram of the bistable oscillator and monitor the evolution of the response towards chaos. The results are reported in Fig. 2.6: when the value of the Poincaré section is considered as output quantity (Fig. 2.6(a)), it is possible to appreciate the period doubling evolution, especially near chaos (indicated by a dense band full of Poincaré points), as shown by the zooms Fig. 2.6(1-4). On the contrary, when the amplitude of the response is considered as output quantity (Fig. 2.6 (b)), the period-doubling cascade cannot be appreciated and chaos is barely detected by the proposed zoom. This happens because the amplitude of the response does not detect effectively the presence of period-doubling responses and their evolution in terms of the number of periods to complete a cycle, especially when these do not change abruptly in amplitude. Nonetheless, the amplitude of response can be a good output quantity for the bifurcation diagram. This depends on the nonlinear phenomenon under investigation. As a reference example, the bifurcation diagram of Fig. 2.5 can be considered again; the diagram uses the amplitude of the Duffing oscillator as the output quantity for the bifurcation diagram and aims to show the jump phenomenon. In this case, the use of the amplitude of the response is appropriate and permits understanding and appreciating in full the nonlinear phenomenon, showing the presence of jumps in the frequency response.

These examples show the necessity and the importance of selecting the appropriate output quantity, e.g. Poincaré section, amplitude, or max value, in the bifurcation diagrams to illustrate and investigate different nonlinear phenomena.

2.2.3 Basins of Attractions

The bifurcation diagrams provide useful information about the system bifurcations and the presence of co-existing steady-state dynamic responses. Nonetheless, these

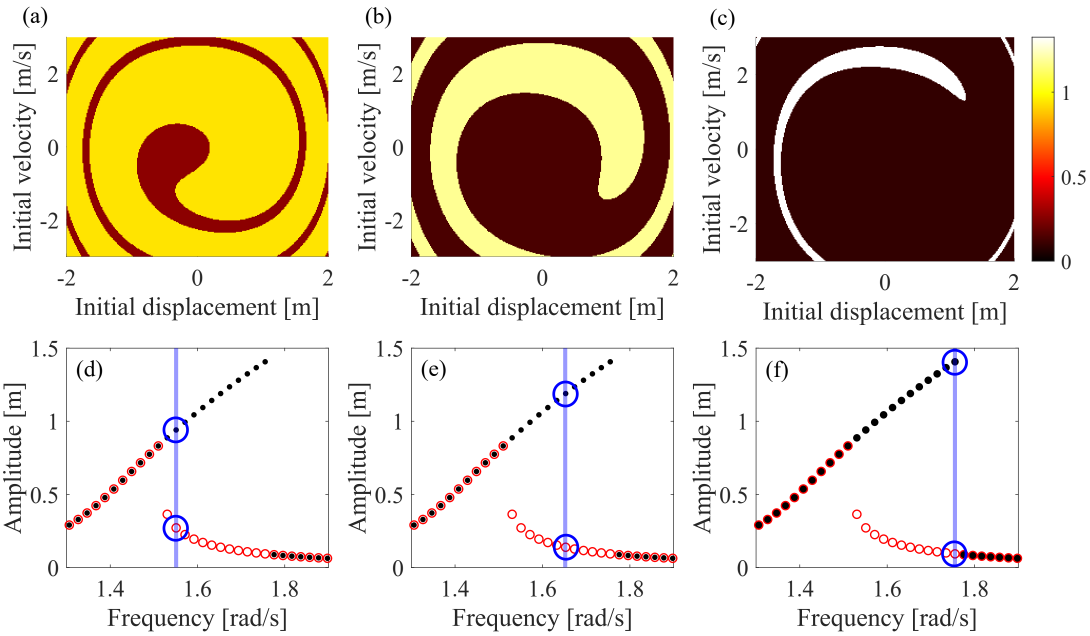

Figure 2.7: Basin of attraction for a Duffing oscillator ($m = 1$ kg, $c = 0.04$ Ns/m, $k = 2$ N/m, $\mu = 0.75$ N/m^3, and $Q = 0.1$ N) at different excitation frequency Ω equal to 1.55 (a), 1.65 (b), and 1.75 (c) rad/s. Panels (d-f) graphically show the two considered coexisting solutions for each basin of attraction. The intensity scale indicates the amplitude of the solutions in the different regions of the basin.

diagrams provide little information about the effect of the initial conditions on system dynamics, often not sufficient for in-depth analysis of the system. To this end, *Basins of Attractions* (BoA) are often used to study in detail the effect of initial conditions on the dynamics of the system. The BoA represent the steady-state response of the system that is achieved when certain initial conditions are used, graphically showing a direct link between these two quantities. Generally, the amplitude, the maximum, or the minimum of the response of the system is used to create the BoA, however, different quantities can be used to illustrate different nonlinear phenomena. BoA are a powerful illustration of the dynamics of the system when co-existing solutions exist: they illustrate the set of initial conditions that allow reaching a certain stable steady-state solution, identifying boundaries in the investigated domain of initial conditions. In the case of a system with a single steady-state stable solution in the initial conditions domain and for the set of parameters selected (e.g. for a linear system) the BoA becomes trivial, showing a constant plain diagram. One problem of the BoA is the resolution: the domain of initial conditions of the BoA is discretised and each set of initial conditions is used to identify the final steady-state dynamics once the transient dynamics have vanished. To increase the resolution of the BoA and visualise the boundaries of different steady-state solutions, a fine discretisation is required. When an approximate analytical solution is not available, numerical integration schemes are often used to compute the final steady-state response. The presence of fine discretisation of the initial conditions domain can lead to millions of sets of initial conditions, which require an equivalent number of simulations. This can lead to computationally expensive simulations, often possible only in clusters via parallel computation.

Taking as a reference example, the Duffing oscillator of Eq. 2.7, the associated BoA for different values of the frequency of excitation Ω are reported in Fig. 2.7. In the top panels, the figure shows the three basins of attraction for excitation frequencies equal to 1.55, 1.65, and 1.75 rad/s. The three excitation conditions are chosen in the portion of the frequency domain where two co-existing solutions exist for the Duffing oscillator. This is demonstrated by the bottom panels Fig. 2.7 that show the bifurcation diagram of the Duffing oscillator and highlight the considered frequency of excitation with a vertical blue line. The blue circles indicate the considered amplitude of response of the Duffing oscillator that is plotted with a scale of colour in the above BoA. The basins of attraction provide very valuable information about the dynamics of the system and the sets of initial condition that leads to a certain dynamic response: when $\Omega = 1.65$

rad/s (Fig. 2.7(b)) we are in the middle of the frequency region where two co-existing solutions are present, as shown by (Fig. 2.7(e); this results in the possibility of ending in both the lower and upper branch of Fig. 2.7 with approximately the same probability, as the basin of attraction show around one half of the considered initial condition domain covered by high-amplitude responses (light yellow) and then other half covered by low-amplitude responses (dark red). When we move towards lower frequencies of excitation, the lower branch destabilises leading the upper branch of the steady-state solution to be 'more attractive': this results in basins of attraction that have more combinations of initial conditions (as shown in Fig. 2.7(a)) which lead to high-amplitude of responses (yellow), thus making more probable to end in those dynamic state. Contrarily, when the frequency of excitation moves towards higher frequencies, the upper branch of the solution tends to destabilise, making it more likely to end in dynamic states that show a low-amplitude response (dark red). This is demonstrated by Fig. 2.7(c) which shows that the dark region associated with low amplitude is much larger than the high amplitude counterpart.

In conclusion, the BoA are a powerful tool to monitor and visualise how initial conditions influence the dynamics of nonlinear systems. Although often computationally expensive to achieve, they represent a fundamental tool for the investigation of nonlinear systems, integrating the information obtained from bifurcation diagrams and phase portraits.

2.3 Approximate Methods for Nonlinear Systems

This section provides an overview of the approximate methods that are mostly used in engineering applications to solve nonlinear systems. These methods have been widely used in the literature for analysing nonlinear mechanical systems. Some examples can be found in the following references [29, 34, 48, 50, 86, 87] which demonstrate the usefulness of approximate methods in understanding the dynamic behaviour of nonlinear structures. Approximate methods, conversely to direct numerical solutions, utilise approximations to obtain a simplified solution representing the dynamic behaviour of the system. To distinguish the linear behaviour in the frequency domain from the nonlinear one, the terms *Frequency Response Curve* (FRC) is adopted to refer to the FRF of a nonlinear system. This clarification is justified by the fact that, in nonlinear systems, co-existing solutions may exist at the same frequency of excitation, making it impossible to represent the frequency response with a function.

2.3.1 Harmonic Balance

One of the most adopted methods for obtaining the approximated solution of a nonlinear system is the Harmonic Balance Method (HBM) [73, 85]. The HBM is a technique that allows for the calculation of the approximate steady-state system response by approximating the solution with a truncated Fourier series. Essentially, the response of the system is assumed to be of the following form (typically called *ansatz*) :

$$x(t) = a_0 + \sum_{k=1}^{H} (a_k)\cos(k\lambda t) + (b_k)\sin(k\lambda t) \tag{2.8}$$

where a_k and b_k are the coefficients of each harmonic and H is the higher harmonic order considered in the ansatz. Ideally, an infinite number of harmonics would be required to represent a general response of a nonlinear system. Nonetheless, to make the process feasible, the order of the harmonics is limited, introducing an approximation into the sought solution. Substituting the ansatz and its derivatives into the governing equations of motion and balancing the coefficients of each harmonic term lead to a set of nonlinear Algebraic Equations (AE). This process of moving from a set of ODEs to a set of algebraic equations is known in the literature as *Weighted Residual Methods* [88]. In the case of nonlinear systems, the response is composed of many harmonics therefore increasing H leads to a better approximation of the solution. In some cases, it is possible to achieve a closed-form solution of the nonlinear AEs, e.g. for a Duffing oscillator at the first-order approximation. This closed-form solution becomes exact in the case of a linear system. Nonetheless, closed-form solutions are generally achievable when the system is characterised by few DOFs, polynomial nonlinearities, and few harmonics are considered. More generally, the associated set of AEs can be solved numerically or in combination with path-following methods, e.g. pseudo-arc-length continuation. In these cases, the HBM can be applied to more complicated systems, even characterised by many degrees of freedom, especially when the nonlinearities are confined only to few DOFs of the considered structure. The HBM can be applied to solve both self-excited and forced systems with different types of nonlinear behaviour, as long as the sought solution is representable as a periodic function. Therefore, the HBM cannot be used to find transient, random, or aperiodic responses.

For example, the HBM can be used to find the steady-state dynamic response of the Duffing oscillator. In this case, the mechanical oscillator is characterised by hardening/softening nonlinear stiffness that can be represented with a polynomial function. Let's start recalling the ODE that represents the harmonically forced version of the Duffing oscillator:

$$m\ddot{x} + c\dot{x} + kx + \mu x^3 = f\cos(\Omega t) \tag{2.9}$$

where k is the linear stiffness coefficient, c is linear damping coefficient, m is the mass, μ is the nonlinear stiffness coefficient, x is the displacement of the oscillator, f is the forcing amplitude, and Ω forcing frequency. Truncating the ansatz to the first-order harmonic (H = 1), the following approximate solution is obtained:

$$x(t) \approx X_1\cos(\Omega t) - X_2\sin(\Omega t) \approx |x|\cos(\Omega t + \phi) \tag{2.10}$$

where $X_1 = |x|\cos(\phi)$, $X_2 = |x|\sin(\phi)$, ϕ is the phase, and $|x|$ represents the amplitude of response of the Duffing oscillator. Substituting Eq. 2.10 and its derivatives into Eq. 2.9 leads to the following equation:

$$\begin{aligned}
&- m\Omega^2 X_1\cos(\Omega t) + m\Omega^2 X_2\sin(\Omega t) - cX_1\Omega\sin(\Omega t) - cX_2\Omega\cos(\Omega t) + kX_1\cos(\Omega t) + \\
&- kX_2\sin(\Omega t) + \mu(X_1^3\cos^3(\Omega t) - X_2^3\sin^3(\Omega t) + 3X_1X_2^2\cos(\Omega t)\sin^2(\Omega t) + \\
&- 3X_1^2X_2\cos^2(\Omega t)\sin(\Omega t)) = F\cos(\Omega t)) + h.o.t.
\end{aligned} \tag{2.11}$$

where higher order terms (h.o.t.) are terms generated by higher harmonics of the solution. Considering the previous operation of truncation of Eq. 2.10, these terms are neglected and not considered in the following harmonic balance. Eq. 2.11 can be simplified using the following trigonometric relationships:

$$\cos(\Omega t)^3 = 3/4\cos(\Omega t) + 1/4\cos(3\Omega t) \tag{2.12a}$$

$$\sin(\Omega t)^3 = 3/4\sin(\Omega t) - 1/4\sin(3\Omega t) \tag{2.12b}$$

$$\cos(\Omega t)^2\sin(\Omega t) = 1/4\sin(\Omega t) + 1/4\sin(3\Omega t) \tag{2.12c}$$

$$\sin(\Omega t)^2\cos(\Omega t) = 1/4\cos(\Omega t) - 1/4\cos(3\Omega t) \tag{2.12d}$$

Once again, higher order terms (i.e. $\cos(3\Omega t)$ and $\sin(3\Omega t)$), generated by the substitution of Eq. 2.12 are neglected. At this stage, it is possible to balance the remaining harmonics, obtaining the following system of nonlinear algebraic equations:

$$-m\Omega^2 X_1 - c\Omega X_2 + kX_1 + 3/4\mu X_1^3 + 3/4\mu X_1 X_2^2 = F \tag{2.13a}$$

$$m\Omega^2 X_2 - c\Omega X_1 - kX_2 - 3/4\mu X_2^3 - 3/4\mu X_1^2 X_2 = 0 \tag{2.13b}$$

Eq 2.13 can be solved and a closed-form solution can be obtained in terms of X_1 and X_2. To this end, the MATLAB function *solve* is used and a symbolic closed-form solution is obtained. The solution is then combined to obtain the amplitude and phase of response of the Duffing oscillator by using the following relationships:

$$|x| = \sqrt{X_1^2 + X_2^2} \tag{2.14a}$$

$$\phi = \mathrm{acos}(X_1/|x|) = \mathrm{asin}(X_2/|x|) \tag{2.14b}$$

In this example, the unstable solutions are retrieved by searching for the regions of the frequency domain where there are three co-existing solutions. Then the solutions with the largest and the lowest amplitude of response are known to be stable while the remaining solution is assumed to be unstable. Using Eq. 2.13 and Eq. 2.14 it is possible to compute the FRC of the Duffing oscillator; Fig. 2.8 compared the FRC of a Duffing oscillator with hardening/softening behaviour with the linear counter-part when the following properties are considered: $m = 1$ kg, $c = 0.04$ Ns/m, $k = 2$ N/m, $\mu = \pm 0.15$

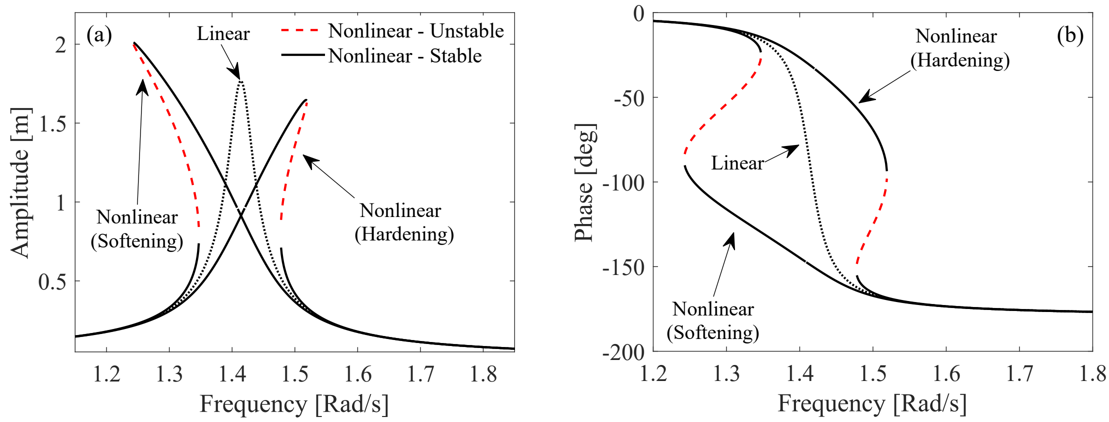

Figure 2.8: FRCs of the Duffing oscillator obtained with HBM (H = 1) in three different conditions: nonlinear (hardening), nonlinear (softening), linear. Amplitude (a) and phase (b) of the response are shown.

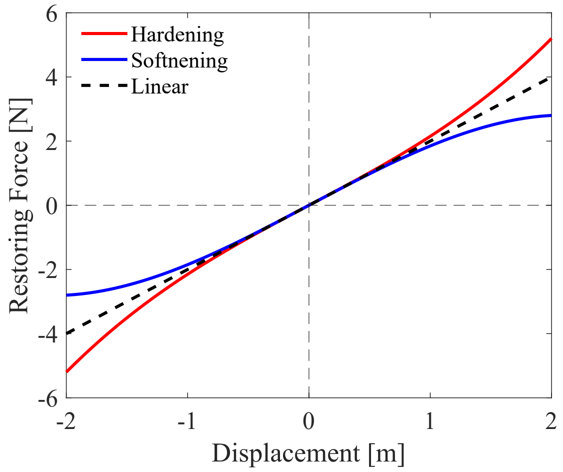

Figure 2.9: Restoring forces associated with the stiffness characteristics: linear (dashed black line), nonlinear hardening (red continuous line), nonlinear softening (blue continuous line).

N/m^3, and $F = 0.1$ N. The figure shows that the resonance peak is bent toward higher frequencies when the hardening stiffness characteristic is applied to the oscillator, and toward lower frequencies when a softening stiffness characteristic is considered. This nonlinear effect is responsible for the classic jumps in the frequency sweep of the nonlinear oscillator. Fig. 2.9 shows the restoring forces generated by softening/hardening stiffness characteristics: the softening stiffness shows a reduction of the restoring force for large displacements while the hardening characteristic leads to an increment of the

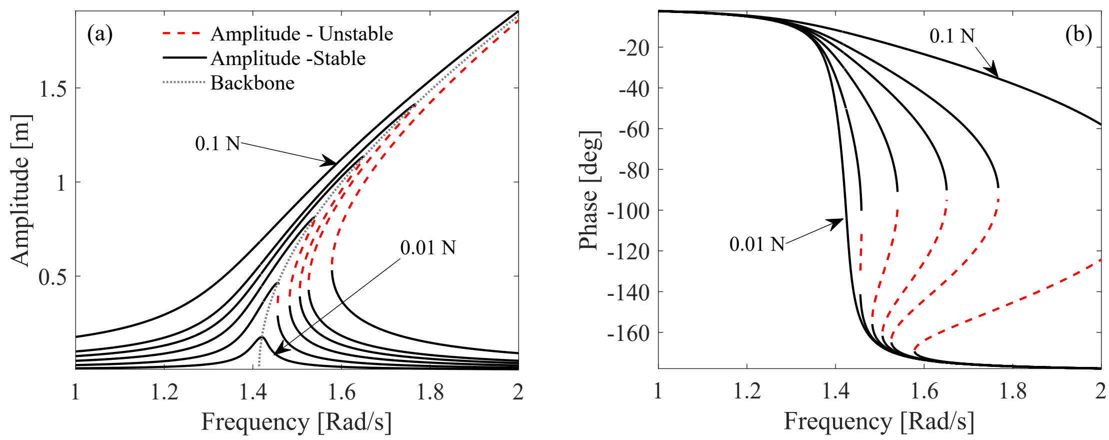

Figure 2.10: Frequency response of the Duffing oscillator (H = 1) with $m = 1\ kg$, $c = 0.04\ Ns/m$, $k = 2\ N/m$, and $\mu = 0.75$ at different excitation amplitudes: 0.01, 0.18, 0.027, 0.05, 0.075, and 0.1 N. Amplitude (a) and phase (b) of the dynamic response are shown.

restoring force. This behaviour is in agreement with the results of the harmonic balance which shows the bending of the resonance peak towards higher/lower frequencies when hardening/softening stiffness characteristics are applied to the oscillator. Focusing the attention on the hardening behaviour, the FRC of the Duffing oscillator is computed for different excitation amplitudes (Fig. 2.10): when low forcing amplitudes are applied, the system tends to behave linearly and its FRC does not show any unstable regions. Instead, when the system is forced with a medium level of excitation amplitudes, the FRC starts to become skewed and unstable regions appear in the steady-state solution. Finally, when large excitation amplitude is used, the system shows a strong nonlinear behaviour with large regions of frequency domain characterised by the presence of co-existing steady-state solutions at high- and low-amplitude. This behaviour is typically found in nonlinear systems characterised by the presence of an underlying linear system. The FRCs and the steady-state dynamics of these nonlinear systems are described by the behaviour represented in Fig. 1.4, i.e. there is a tendency towards a linear behaviour when the forcing amplitude is very small. In addition to the steady-state response, Fig. 2.10(a) shows the backbone curve of the considered Duffing oscillator: this curve represents the unforced undamped response of the system and provides valuable information about the dynamic behaviour of the system. For example in the considered oscillator, the backbone is bent towards higher frequencies indicating that the natural frequency of the system increases with the amplitude of response, as expected in the case of hardening stiffness characteristics. The backbone curve is computed with the same approximation (H=1) used in the computation of the forced response. The only difference is that the forcing and damping terms are dropped and the resulting set of algebraic equations is simplified.

Thanks to its simplicity, the HBM has been widely used to find an approximate solution for nonlinear systems [85]. The method is theoretically applicable to strong nonlinear systems and it is based on the following assumption: the response of the system can be approximated with a combination of a few harmonics. When the system is linear, one harmonic is sufficient to find an exact solution, while when the system has smooth nonlinearities [4] the response is composed of many harmonics with the first ones being sufficient to cover most of the dynamic content. This is particularly true for weakly nonlinear systems. Nonetheless, the HBM is considered to be inconsistent [73] because higher frequency terms are not balanced, especially when H = 1. In addition, it is important to note that in the previous example, the system of algebraic equations (Eq. 2.13) is solved by looking for a closed-form solution. When this solution is available, it is possible to obtain all the solutions of the system, stable and unstable, for each frequency of excitation. In most of the engineering applicative cases, there is the necessity to deal with more complicated systems characterised by many DOFs and different nonlinear characteristics. In these cases, the ansatz needs to consider higher harmonics to better represent the dynamic response of the system and, thus, it is extremely complicated to achieve a closed-form solution. To solve this problem, numerical techniques are often used to obtain the dynamic response of the investigated systems. This includes the usage of numerical solvers, e.g. Netwon-Rapson method, and continuation techniques, e.g. pseudo-arc-length continuation. Differently from the proposed simplified example, more sophisticated techniques for the computation of the stability of the system (e.g. the Floquet Theory) and for handling the switch between bifurcating branches of solution are often used in literature [85, 86, 88–91].

[4]Smooth nonlinearities are characteristics that can be approximated with continuous function with continuous derivative.

2.3.2 Other Approximation Techniques

The HBM is not the only available method to obtain approximate solutions of nonlinear systems. A full description of the different approximate methods for solving nonlinear systems is out of the scope of the thesis and the reader is invited to consult the references [73, 92] for more information. For completeness, two widely used methods in engineering applications are briefly described. These methods, differently from the harmonic balance, are applicable only to weakly nonlinear systems, i.e. nonlinear systems whose nonlinear terms are relatively small compared to the linear ones, and have the form:

$$\ddot{x} + \omega_n^2 x = \epsilon N(x, \dot{x}) \tag{2.15}$$

where ω_n is the natural frequency, $N(x, \dot{x})$ is the nonlinear terms, and ϵ is a small parameters. It should be also noted that the methods work on systems that are slightly damped and forced as $N(x, \dot{x})$ contains the damping and forcing terms. Finally, different from the harmonic balance, these methods can be used to obtain the both transient and steady-state response of the systems. Among these methods, there are:

- **Averaging method**: this method can be used to find an approximate solution to weakly nonlinear systems. The sought solution has the form: $x = x_c(t)\cos(\omega_n t) + x_s(t)\sin(\omega_n t)$, where $x_c(t)$ and $x_s(t)$ are unknown time dependent functions. A first-order representation of their derivative is obtained and averaged over one cycle of oscillations via analytical integration. The result is the underlying amplitude envelope which represents the approximate response of the system purified by higher frequency content. The approximation is made so that the terms $x_c(t)$ and $x_s(t)$, associated with the weakly nonlinear function $\epsilon N(x, \dot{x})$, are considered to be constant over a cycle. This method can be used to find transient and steady-state approximate solutions, with the steady-state solution requiring frequency detuning and time scaling parameters [73].

- **Perturbation method**: this method applies to weakly nonlinear systems and it is based on the idea that the system response can be approximated with the following power series: $x(t) = x_0 + \epsilon x_1 + \epsilon^2 x_2 + ... + \epsilon^n x_n$. Often, the first term in the series (x_0) represents the linear response while the additional terms are perturbations of the linear response. Two approaches can be adopted: (1) *Regular Perturbation Theory:* substitute the response above in the equation of motion and balance the terms of different exponent ϵ. This could result in erroneous results since secular terms, unbounded with time, may arise; (2) *Multiple Scale Approach*: This technique is based on the observation that the response of mechanical systems consists of terms that change rapidly and terms that change slowly (e.g. the decay rate is much slower than the frequency oscillation in most of the mechanical systems). In this case, before applying the series expansion, the following solution is sought $x = X_c(\epsilon t)\cos(\omega t) + X_s(\epsilon t)\sin(\omega t)$, where $T = \epsilon t$ and $\tau = \omega t$ represents the two time scale variables. The solution, steady-state or transient, is achieved by considering the derivatives of the sought solution, by balancing/solving the equation associated with each scale of the power series, and, by solving the secular equations, i.e. the equations that allow to remove the secular terms.

2.4 Numerical Continuation

The previous sections demonstrated that nonlinear structures excited with harmonic forcing functions may have complex dynamic responses which include bifurcations and unstable dynamic periodic responses. In this context, numerical integration schemes and approximate methods may struggle to provide a complete understanding of the dynamics of the system. *Numerical continuation* is a powerful technique for the analysis of nonlinear systems: this method is particularly useful in understanding the behaviour of solutions under varying parameters and identifying branching points. Applications range from studying equilibrium solutions in algebraic systems to analysing the stability of periodic orbits in dynamic systems. This permits obtaining a clear understanding of the dynamics of the system in terms of stable/unstable solutions and bifurcating branches that are not achievable with other numerical tools. Numerical continuation has been successfully used to study the dynamic behaviour of a variety of mechanical systems, ranging from piecewise-linear systems [30, 31], nonlinear energy sinks [48], piezoelectric energy harvesters [86], reduced-order models of geometrically nonlinear structures [93], full-scale aircraft [11] and circular plates [29]. This section introduces the mathematical background behind numerical continuation, highlighting how the technique can be used to continue solution branches of periodic oscillations in nonlinear systems.

2.4.1 An Introduction to Numerical Continuation

Numerical continuation is a method for computing solutions of parameterised nonlinear systems in the form:

$$\mathbf{G}(\mathbf{u}, \lambda) = \mathbf{0} \tag{2.16}$$

where $\lambda \in \mathbb{R}$ represents the general continuation parameter, $\mathbf{u} \in \mathbb{R}^n$ is the variable vector, and $\mathbf{G}(\mathbf{u}) \in \mathbb{R}^n$ is a nonlinear set of equations. The basic idea behind numerical continuation is to continue the *solution branch* (or *solution family*) $\mathbf{u}(\lambda)$ varying the parameter λ. To this end, the continuation process is initialised from a known solution $\mathbf{u_0}$. The continuation procedure is based on the persistence of the solution $\mathbf{u}_0$ in its neighbourhood [5] while the parameter λ is varied. Two basic theorems are used:

1. **Contraction Theorem**: given a function $F : \mathbb{R} \to \mathbb{R}$, it guarantees the existence and the uniqueness of a solution x^* in the neighbour x_0 for the problem $x = F(x)$

2. **Implicit Function Theorem** (IFT): given a function $G : \mathbb{R}^m \times \mathbb{R} \to \mathbb{R}$ that satisfy:

    (a) $\mathbf{G}(\mathbf{u}_0, \lambda_0) = \mathbf{0}$

    (b) $\mathbf{G}_u(\mathbf{u}_0, \lambda_0)$ (the Jacobian) is nonsingular (full rank) with bounded inverse, i.e. $\mathbf{u}_0$ is an isolated solution

    (c) $\mathbf{G}_u$ and $\mathbf{G}$ are smooth [6] (or at least Lipschitz continuous)

    then there exists a unique smooth (or Lipschitz continuous) solution family $\mathbf{u}(\lambda)$ such that $\mathbf{u}(\lambda_0) = \mathbf{u}_0$ and $\mathbf{G}(\mathbf{u}(\lambda)), \lambda) = \mathbf{0}$ for all λ near λ_0.

[5] For a formal definition of neighbourhood, the reader should refer to [94]

[6] A smooth function is continuous differentiable function with continuous derivative

Therefore, under the assumption of smoothness (or Lipschitz continuity) and isolated solution, the IFT guarantees the existence of a locally unique solution branch $\mathbf{u} = \mathbf{u}(\lambda)$ with $\mathbf{u}(\lambda_{\mathbf{0}}) = \mathbf{u}_0$. In the case of a set of nonlinear equations (e.g. equilibrium point of nonlinear system), for which $\mathbf{u}_0$, λ_0, and $\mathbf{u}'_0$ [7] are known the next solution $\mathbf{u}_1$, λ_1 can be found using a nonlinear root-finding method, like the Newton-Raphson method:

$$\begin{cases} \mathbf{G}_u(\mathbf{u}_1^{(\nu)}, \lambda_i)\Delta\mathbf{u}_i^{(\nu)} = -\mathbf{G}_\lambda(\mathbf{u}_1^{(\nu)}, \lambda_i) \\ \Delta\mathbf{u}_i^{(\nu+1)} = \mathbf{u}_i^{\nu} + \Delta\mathbf{u}_i^{(\nu)} \end{cases} \tag{2.17}$$

where ν is the iteration number and i identifies the solution along the branch. Thanks to the implicit function theorem, the solution branch $\mathbf{u}(\lambda)$ is known to exist and be unique, therefore parametric-continuation can be enforced with $\lambda_1 = \lambda_0 + \Delta\lambda$ and $\mathbf{u}_1^{(0)} = \mathbf{u}_0 + \Delta\lambda\mathbf{u}'_0$. After the convergence, $\mathbf{u}_1$ is used to obtain an estimation of the new direction vector $\mathbf{u}'_1$:

$$\mathbf{G}_u(\mathbf{u}_1, \lambda_1)\mathbf{u}'_1 = -\mathbf{G}_\lambda(\mathbf{u}_1, \lambda_1) \tag{2.18}$$

This technique is repeated for different values of λ and fails when there is a fold of the solution. In order to avoid this problem *pseudo-arc-length continuation* is introduced: it consists in increasing the dimension of the problem by adding an arc-length equation. This additional equation 'locks' the selection of the parameter λ which will follow the solutions branch. The problem can be rewritten as follows:

$$\begin{cases} \mathbf{G}(\mathbf{u}_1, \lambda_1) = \mathbf{0} \\ (\mathbf{u}_1 - \mathbf{u}_0)^T\mathbf{u}'_0 + (\lambda_1 - \lambda_0)\lambda'_0 - \Delta s = \mathbf{0} \end{cases} \tag{2.19}$$

where Δs represents the continuation step and ($\mathbf{u}'_0$ and λ'_0) are the new direction vector. If we incorporate Newton's Method, we obtain:

$$\begin{bmatrix} (\mathbf{G}_u^1)^{(\nu)} & (\mathbf{G}_\lambda^1)^{(\nu)} \\ \mathbf{u}_0'^T & \lambda'_0 \end{bmatrix} \begin{Bmatrix} \Delta\mathbf{u}_1^{(\nu)} \\ \Delta\lambda_1^{(\nu)} \end{Bmatrix} = - \begin{Bmatrix} \mathbf{G}(\mathbf{u}_1^{(\nu)}, \lambda_1^{(\nu)}) \\ (\mathbf{u}_1^{(\nu)} - \mathbf{u}_0)^T\mathbf{u}'_0 + (\lambda_1^{(\nu)} - \lambda_0)\lambda'_0 - \Delta s \end{Bmatrix} \tag{2.20}$$

[7] $\mathbf{u}'_0 = \frac{\partial \mathbf{u}_0}{\partial \lambda}$ is the tangent vector

with the new direction being:

$$\begin{bmatrix} (\mathbf{G}_u^1) & (\mathbf{G}_\lambda^1) \\ \mathbf{u}_0'^T & \lambda_0' \end{bmatrix} \begin{Bmatrix} \mathbf{u}_1' \\ \lambda_1' \end{Bmatrix} = \begin{Bmatrix} \mathbf{0} \\ 1 \end{Bmatrix} \tag{2.21}$$

It is important to note that the orientation of the branch is preserved if Δs is sufficiently small and the direction vector is scaled so that $||\mathbf{u}_1'||^2 + {\lambda'}_1^2 = 1$. It is possible to demonstrate that the Jacobian of the pseudo-arclength system is nonsingular at a *regular point* [8]. The implicit function theorem fails at branching points where the solution branches bifurcate in more than one branch [94, 95]. There the $\mathbf{x}_0$ is not a regular solution and the Jacobian $\mathbf{G}_x(\mathbf{x}_0)$ is singular. To handle a branching point three steps are necessary: (1) detection, (2) localisation, and (3) switching of the branch. Different techniques exist for solving these problems like the usage of the bifurcation test functions or specific perturbation methods [85, 95].

Eq. 2.20 and 2.21 can be used to continue an equilibrium point of nonlinear systems; in the case of periodic solutions, a Boundary Value Problem (BVP) problem must be formulated. In general, the BVP can be formulated as follows:

$$\dot{\mathbf{u}}(t) = \mathbf{f}(\mathbf{u}(t), \lambda), \quad with \quad \mathbf{u}(t) = \mathbf{u}(t+T) \tag{2.22}$$

where T is the period. Now, in the context of numerical continuation, we can say:

$$\dot{\mathbf{u}}(t) = T\mathbf{f}(\mathbf{u}(t), \lambda), \quad with \quad \mathbf{u}(0) = \mathbf{u}(1) \tag{2.23}$$

In this way, the periodic solution can be confined in the range [0,1] and the period T becomes one of the unknown. In order to fix the periodic solution in time, a *phase condition* (see [94] for more information) is also added. At this stage, it is possible to discretise the BVP with techniques like finite difference and reconstruct an equivalent set of nonlinear equations. Often, *orthogonal collocation* is used to discretise a periodic solution and solve the BVP. Specifically, piecewise polynomials are used to approxi-

[8] A regular solution is defined such that $\mathbf{G}_x^0 = \mathbf{G}_x(\mathbf{x}_0)$ is full rank where $\mathbf{G}(\mathbf{x}) = \mathbf{0} \quad with \quad \mathbf{x} = \{\mathbf{u}, \lambda\} \quad \mathbf{G} : \mathbb{R}^{n+1} \to \mathbb{R}$, see [94] for more information

mate the periodic solution of nonlinear systems [94]. Another possibility consists of directly reducing the set of ODEs to a set of nonlinear algebraic equations by imposing the periodicity of the solution. This process is typically utilised in the application of the HBM and the resulting nonlinear algebraic equations can be cast in a numerical continuation procedure [85]. Finally, the stability analysis of the continued solution is important to address the behaviour of the system. Different methodologies exist: for equilibrium points (fixed points) linearisation is often used to analyze stability. This involves linearising the system around the equilibrium point and examining the eigenvalues of the resulting linear system matrix. For periodic solutions, instead, the *Floquet Theory* is often used. This requires computing the *Monodromy Matrix* and the associated Floquet multipliers which provide information about the stability and the type of bifurcation [85]. A practical discussion on different methods for computing the monodromy matrix using numerically can be found at [88].

Today many toolbox implements numerical continuation and collocation methods such as MatCont [96], COCO [97] and AUTO-07 [98]. This software allows for solving nonlinear systems and continuing their solution, therefore in this work, they are used to perform the continuation analyses.

2.4.2 Solving Nonlinear Systems with Pseudo-Arclength Continuation

In its most simple form, numerical continuation can be applied to solve algebraic nonlinear equations. If we consider the parametrised equation of a circle, the associated set of nonlinear equations with pseudo-arclength continuation is:

$$\begin{cases} u_1^2 + \lambda_1^2 - 1 = 0 \\ (u_1 - u_0)^T u_0' + (\lambda_1 - \lambda_0)^T \lambda_0' - \Delta s = 0 \end{cases} \tag{2.24}$$

Eq. 2.24 is then solved with the numerical continuation procedure previously outlined. To this end, the MATLAB function *Fsolve* is used to solve the nonlinear system of equations with iterative methods, similar to the Newton-Raphson method. Then, the direction (u_0', λ_0') is updated and the procedure is repeated for the next point. A nu-

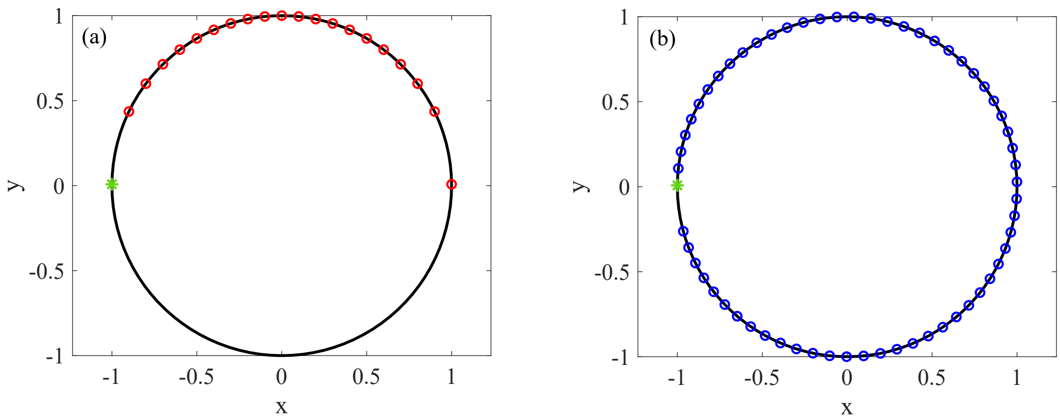

Figure 2.11: Solving numerically the parametrised equation of a circle: (a) iterative method and (b) numerical continuation. The continuous black line represents the analytical solution while the circles denotes numerical solutions.

merical example is reported in Fig 2.11 where a circle with centre (0,0) and radius equal to 1 is solved with (Fig 2.11(b)) and without (Fig 2.11(a)) pseudo-arclength continuation. When the pseudo-arclength continuation is not used, the previous solution is used as the initial guess for obtaining the next solution and the continuation parameter is increased as follows: $\lambda_1 = \lambda_0 + \Delta\lambda$. As shown in the figure, the two numerical solutions start from the same point identified by $*$, nonetheless, only the numerical continuation is able to pass the folding point. A detailed representation of the predictor-corrector procedure is reported in Fig 2.12: the dotted line indicates the tangent direction of the branch in the initial point (u_0, λ_0); this is exploited to find predictor point (u_0^*, λ_0^*), from which, enforcing the perpendicular direction to the tangent (dashed line), it is possible to obtain the corrected point (u_1, λ_1).

The path-following techniques can be also used to continue a solution branch of the set of nonlinear equations obtained from a weighted residual method (e.g. from the HBM). Fig. 2.13 shows the use of numerical continuation for computing the amplitude of response of a Duffing oscillator. Specifically, Fig. 2.13 (a) illustrate the continued solution of the oscillator when continuation methods are used together with the HBM: in this case, the resulting nonlinear equations (Eq. 2.13) are continued with the pseudo-arclength continuation. This technique can be also combined with the methods for computing the monodromy matrix, thus obtaining the stability of the system, as shown

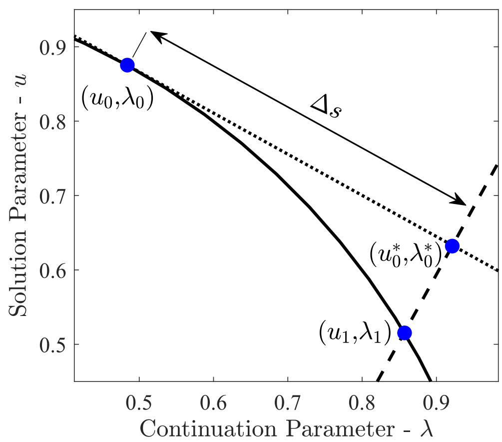

Figure 2.12: Predictor-correct procedure: (u_0, λ_0) is the initial point, (u_0^*, λ_0^*) is predicted point, and (u_1, λ_1) is the corrected point.

in many works in the literature [85, 86, 88]. Fig. 2.13 (b), instead, shows the numerical continuation performed with collocation methods directly applied to systems of ODEs. Bifurcation points are identified by the symbol • along with the description of the type of bifurcation (SN = Saddle Node, and FP = Fold Point). In this case, the toolbox COCO [97] is used to perform the continuation: this toolbox is able to continue periodic responses or equilibrium of nonlinear systems, compute their stability, and detect, locate, and switch between branching solutions.

Numerical continuation with collocation methods is often used as a reference solution when approximate solutions with harmonic balance or other methods are developed [87, 99]. This is because this technique is very accurate and easy to implement for solving general BVP associated with periodic solutions. Nonetheless, the technique has also limits. This includes numerical instabilities, difficulties in dealing with aperiodic solutions (in the presented form), high computational burden in high-dimensional systems, lack of parallelisation, and initial guess dependency. The latter is particularly important for the dynamics of systems that exhibit the presence of *isola*, i.e. detached closed solution branch in the bifurcation diagram, and it will be better discussed in the next chapters.

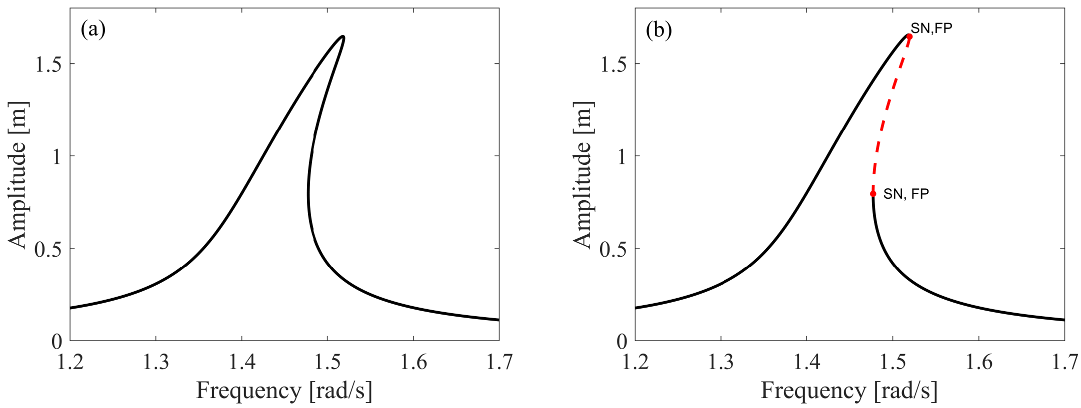

Figure 2.13: Duffing oscillator with $m = 1$ kg, $c = 0.04$ Ns/m, $k = 2$ N/m, $\mu = \pm 0.15$ N/m^3, and $F = 0.1$ N: the amplitude of the response is continued using the harmonic balance method (H = 1) (a) and collocation methods (b).

2.5 Summary

This section introduces the most common mathematical tools for the analysis of nonlinear systems that are representable with a set of ODEs. For each tool, a description of the mathematical background and a discussion about the advantages and limitations are proposed. Specifically, the section discusses how numerical integration schemes can be used to generate phase portraits, Poincaré sections/maps, basins of attraction, and bifurcation diagrams. In addition, approximate methods for nonlinear systems are discussed and numerical continuation techniques are introduced. These techniques will be used in the next chapters for the analysis/validation of various numerical models.

Chapter 3

Numerical Analysis of a Multi-Degree of Freedom System with Contacts

3.1 Introduction

This chapter analyses the dynamic behaviour of a strongly nonlinear system with soft contacts and multiple degrees of freedom. Most of the literature focuses attention on the analysis of the dynamics of non-smooth systems with a single DOF, missing phenomena like modal interactions that may occur when additional DOFs are considered. The chapter utilises the previously introduced tools, such as basins of attraction, bifurcation diagrams, and numerical continuation, to analyse the dynamics of a two-DOF mechanical system with soft contacts. To this end, piecewise-smooth continuous characteristics are used to simulate the presence of the contacts. The chapter, also, aims to understand how smoothing approximations of piecewise characteristics, like sigmoid functions, affect the dynamics of the system. Specifically, the following points are discussed:

- The admissibility of smoothing approximation for piecewise-smooth continuous characteristics representing contact in mechanical systems: in particular, an indicator called the *radius of influence* is introduced and proposed for the selection of the parameters that control the degree of smoothness of the approximating function (e.g. sigmoid functions).

- The steady-state dynamic behaviour of a piecewise-smooth continuous MDOF system with soft contacts: the identified smoothing function is utilised to perform numerical analyses and to investigate the system dynamic features, including chaotic and quasi-periodic behaviour, period-doubling bifurcations, and detached isolas.
- The undamped-unforced dynamic behaviour of a piecewise-smooth continuous MDOF system with a soft contact: the concept of bifurcation of the backbone curve and modal interaction is discussed and investigated via numerical continuation.
- The comparison between the dynamics of the approximate (i.e. the system with sigmoid approximation) and non-approximated (i.e. ideal non-smooth system) system: in particular, the dynamics of two versions of the system are compared using numerical integration and numerical continuation methods in terms of quality of the bifurcation diagram, robustness of the simulation, and computational effort.

3.2 Smoothing Approximations in Non-Smooth Systems

This section discusses the methodology employed for approximating non-smooth characteristics using smoothing functions in nonlinear mechanical systems. The advantages of the approximation are examined, and an indicator (the radius of influence) to evaluate the appropriateness of the approximation parameter that regulates the degree of smoothness is proposed.

3.2.1 Introduction to Non-smooth Systems

Mechanical systems incorporating free-play gaps and contacts have captured the attention of researchers in recent decades. These systems find practical engineering appli-

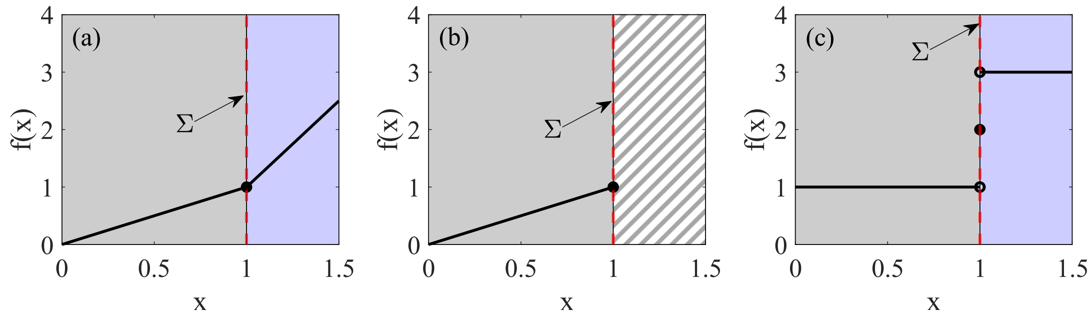

Figure 3.1: Example of piecewise-smooth continuous (a), reset-map (b), and discontinuous (c) characteristics. The discontinuity boundary is indicated by Σ and dashed regions indicate non-physical regions of the domain.

cations in the investigation of the dynamics of impacting capsule systems [30], impact drilling systems [31], cracked systems [32], mechanical oscillators [35–37,39], aeroelastic systems with free-play gaps [40, 41], buildings exposed to earthquakes [43], and impact oscillators with rigid walls [44–46]. These systems belong to the category of *non-smooth dynamical systems*, i.e. they are mechanical systems with non-smooth properties. From the mathematical perspective, they involve discrete events which guide the associated solution through regions of the domain where different properties are applied. They demonstrate unique dynamic features, named *discontinuity-induced bifurcations*, which are not present in smooth dynamical systems. These phenomena include border collisions, border-equilibrium, grazing, sliding-sticking, and corner angle bifurcations [100]. Non-smooth systems are distinguished [1] in *Filippov systems*, *hybrid dynamical systems*, and *piecewise-smooth continuous systems*, depending on the type of non-smooth characteristic. Filippov systems possess discontinuous characteristics that define different regions of the domain. Hybrid systems, instead, are mathematically defined by reset maps that impose specific initial conditions when the discontinuity boundary Σ of the domain is reached. Finally, piecewise-smooth continuous systems are characterised by the presence of continuous characteristics whose derivative might be discontinuous at the discontinuity boundary Σ.

An example of the three types of characteristics is reported in Fig. 3.1. The figure illustrates a piecewise-smooth continuous characteristic (a), a reset map (b), and dis-

[1]This work considers the classification introduced by di Bernardo et al. [100].

continuous characteristic (c). The piecewise-smooth continuous characteristic (Fig. 3.1 (a)) shows that there are two regions of domain x (grey and blue regions) where two different mathematical functions govern the behaviour of the nonlinear characteristic $f(x)$. The nonlinear property is valid on both regions of the domain and the governing functions have the same value on the discontinuity boundary Σ. This property characterises the piecewise-smooth continuous systems and it is often used to model impact oscillators that have deformable walls [37,38]. Hybrid systems are instead characterised by nonlinear properties with 'inaccessible' regions, i.e. regions of the domain where the solution of the system is non-physical. Fig. 3.1 (b) proposes an example of such characteristic and highlights the non-physical regions of domain x with dashed areas. When the system reaches the discontinuity boundary Σ it cannot proceed in the dashed regions but its energy must be conserved or dissipated imposing a certain law, e.g. elastic/inelastic impact. This can be done by using a reset map that re-initialises the initial conditions of the system after the interaction with the discontinuity boundary. Reset maps are typically used to model impact oscillators that interact with rigid walls [44–46] and this class of systems possess dynamic phenomena (e.g. *chattering sequences* [101] and sticking conditions [100]) that are not present in piecewise-smooth continuous systems. The last class of non-smooth systems is represented by the Filippov systems. Fig. 3.1 (c) shows a typical nonlinear characteristic associated with a Filippov system. As shown, the nonlinear characteristic possesses a discontinuity at the boundary Σ and requires functions such as $sign(x)$ for its mathematical representation. It is worth noticing that the mathematical functions representing the system characteristics of two adjacent regions of the domain do not converge to the same value at the discontinuity boundary. This may trigger dynamic phenomena that do not exist in piecewise-smooth continuous systems. For example, the system could remain 'stuck' in the discontinuity boundary Σ, giving birth to sliding bifurcations [72,100,102].

The proposed explanation and examples are a functional/practical description of non-smooth systems. For a more rigorous and exhaustive definition, the reader is encouraged to consult the book [100]. Nevertheless, this brief description serves to introduce various types of non-smooth systems and comprehend their characteristics along with the potential implications on the dynamic response of dynamical systems.

3.2.2 Grazing Bifurcations and Smoothing Functions

In engineering applications, nonlinear systems with free-play gaps and contacts are often modelled with piecewise-smooth continuous characteristics [37, 38, 41, 83]: these systems are characterised by the presence of discontinuity-induced bifurcations, named *grazing bifurcations* [45,103]. An example of grazing bifurcation is described in Fig. 3.2 where a piecewise stiffness characteristic (similar to one proposed in Fig. 3.1 (a)) is added to a Duffing oscillator. The figure shows the phase portraits before, during, and after the occurrence of the grazing bifurcation. The bifurcation occurs exactly when the steady-state orbit is 'grazing' the discontinuity boundary Σ. After the grazing condition, the orbit is forced to enter the second region of the phase space where the properties applied to the system are different, i.e. where the stiffness is larger. This induces a topological change in the phase-portrait, i.e. the generation of a bifurcation in the system dynamics. In practice, under harmonic loading, the bifurcation can be achieved by modifying the excitation conditions of the oscillator i.e. the amplitude Q, or the frequency Ω. Although nonlinear dynamic phenomena that typically occur in Filippov systems, e.g. sliding bifurcations [100] or *hidden dynamics* [2] [72,102,104,105], are not present in piecewise-smooth continuous systems, their dynamics may end in very complex behaviours [1, 39, 41, 45] that include all the dynamic phenomena discussed in Chapter 2, such as stability change, period-doubling, chaos, etc.

In the literature, authors have proposed analytical solutions [35, 106, 107] and mapping techniques [45, 103, 108–110] to study the dynamics of these systems, nonetheless, numerical methods are typically adopted in engineering applications as they are flexible and applicable to a wide range of systems. Direct numerical integration has found significant application in existing literature [36, 37, 40, 41, 43, 111]. It can handle non-smooth characteristics through two distinct approaches: either by identifying the precise discontinuity point, referred to as the boundary point Σ, and restarting the integration process, or by directly integrating the function across its discontinuity. If

[2] In Filippov systems, dynamic responses may occur during sliding motion at the discontinuity boundary. These phenomena are generally referred to as hidden dynamics [102].

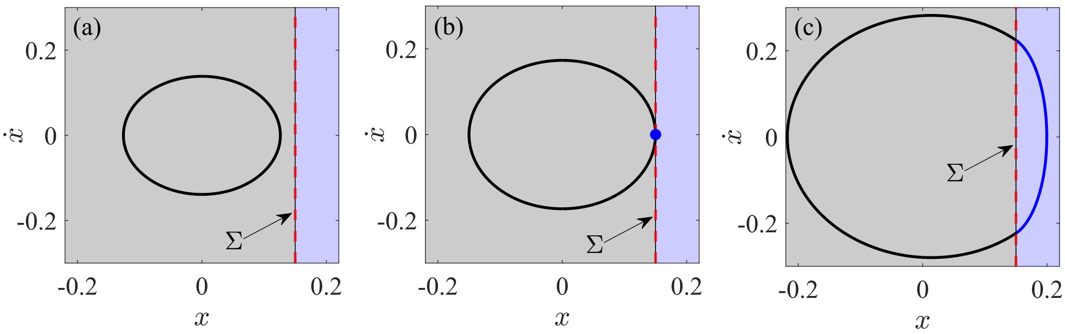

Figure 3.2: Phase portraits of a grazing bifurcation a Duffing oscillator with asymetric piecewise characteristic: (a) before, (b) at, and after (c) the bifurcation. Parameters considered: $m = 1$ kg, $c = 0.04$ Ns/m, $k = 2$ N/m, $\mu = 0.15$ N/m^3, and $Q = 0.1$ N with piecewise stiffness $k_p = 10$ N/m and gap $a = 0.15$ m.

the discontinuity point is not correctly identified, the dynamics of the piecewise-smooth systems might be affected: thus, methods such as the Henon's method [112] and the MATLAB built-in event function [113] have been utilised in recent studies [37, 40]. Although this approach offers higher accuracy in the numerical solution, the process demands significant computational resources, strict tolerances, and more complicated algorithms to handle the identification of the discontinuity point. Alternatively, path-following continuation methods have been used to study the dynamics of non-smooth systems [80, 81, 114–117]. Numerical continuation techniques are based on the implicit function theorem which guarantees the presence of a single family of solutions only when sufficiently smooth functions are adopted. This makes most of the numerical continuation toolboxes, like MatCont [96] and AUTO-07 [98], incapable of treating non-smooth systems without introducing proper smoothing approximations. Other toolboxes, instead, can deal with non-smooth dynamical systems, introducing the *multi-segments continuation* [97, 118] which consents to continue periodic solutions in portions of the domains where the system characteristics are sufficiently smooth. Examples of multi-segment continuation applied to mechanical systems can be found in the following references [30,31,118]. Nonetheless, the adoption of the multi-segment continuation method is time-consuming, complex, and long, especially when multiple re-segmentation procedures are required [97]. This affects the overall numerical analysis and prevents the adoption of such methodologies in common industrial practices.

To address this challenge, researchers have proposed the use of smoothing functions to convert non-smooth dynamical systems into their smoothed version [38,40,82,83,89]. In some works [91, 119, 120], authors employed smoothed functions to avoid numerical problems during the computation of the response of non-smooth dynamical systems with the Harmonic Balance methods. Among the most adopted approximation functions there are: arctangent, hyperbolic tangent, and generalised sigmoid approximation. Other approximations can be found at [38]. Taking as reference the following symmetric piecewise stiffness:

$$F_p = \begin{cases} k_p\,(x_1 - a) & \text{if } x_1 > a \\ 0 & \text{if } -a \leq x_1 \leq a \\ k_p\,(x_1 + a) & \text{if } x_1 < -a \end{cases} \tag{3.1}$$

the associated arctangent, hyperbolic tangent, and generalised sigmoid approximations are expressed by the following relationships:

$$F_{p,1} = \frac{k_p}{2}\left(\left(1 - \frac{2}{\pi}\text{atan}(\delta(x+a))\right)(x+a) + \left(1 + \frac{2}{\pi}\text{atan}(\delta(x-a_2))\right)(x-a_2)\right) \tag{3.2a}$$

$$F_{p,2} = \frac{k_p}{2}((1 - \tanh(\delta(x+a)))(x+a) + (1 + \tanh(\delta(x-a)))(x-a)) \tag{3.2b}$$

$$F_{p,3} = k_p\left(\frac{a+x}{(\exp(\delta(a+x))+1)^n} - \frac{a-x}{(\exp(\delta(a-x))+1)^n}\right) \tag{3.2c}$$

where k_p is the piecewise stiffness and a represents the upper and lower limit of the free gap. $F_{p,1}$, $F_{p,2}$, and $F_{p,3}$ are, respectively, the arctangent, hyperbolic tangent, and generalised sigmoid approximation. The parameter δ defines the degree of approximation: when $\delta \to \infty$ the smoothing approximation becomes equivalent to the piecewise characteristic. In such a scenario, the benefits of having a smooth function are compromised, and the previously mentioned issues persist. On the contrary, using a too-small δ the smooth function does not approximate very well the piecewise characteristic, leading to erroneous dynamic responses of the system. Fig. 3.3 shows the approximation functions for a bilinear stiffness characteristic when $k_p = 10$ N/m, $a = 0.15$ m, and $\delta = 50$. The

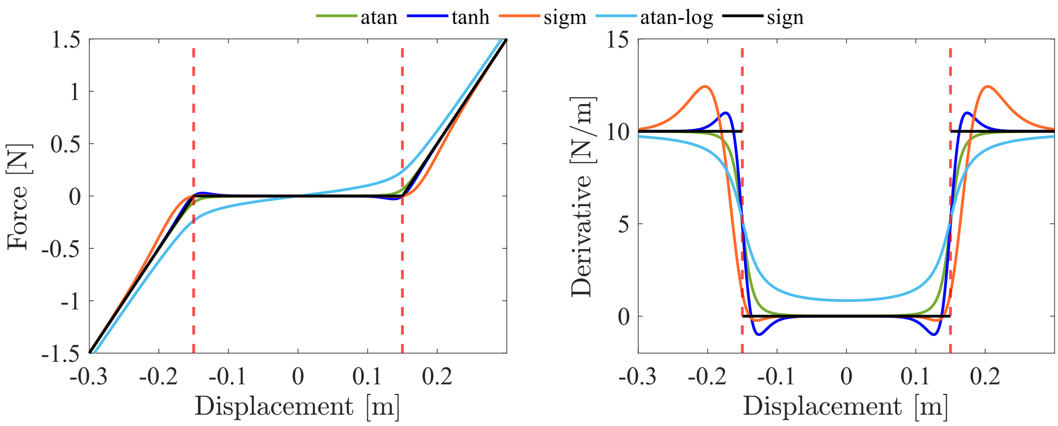

Figure 3.3: Bilinear stiffness characteristic and the associated smooth approximations. Panel (a) show the restoring force, while panel (b) illustrates the derivative.

figure highlights that the smoothing approximations are quite good in reproducing the restoring force, nonetheless, the discontinuity in the derivative introduces a substantial error in the approximation which may affect the dynamics of the approximate system. One of the main problems in selecting δ is represented by the lack of physical interpretation of the parameter. To address this problem, an indicator called *radius of influence* is introduced in the following subsection and the resulting approximate characteristic is used to perform the dynamic analysis of a two-mass non-smooth system characterised by a piecewise-smooth continuous characteristic.

3.2.3 Sigmoid Approximations in a Mechanical Non-smooth System

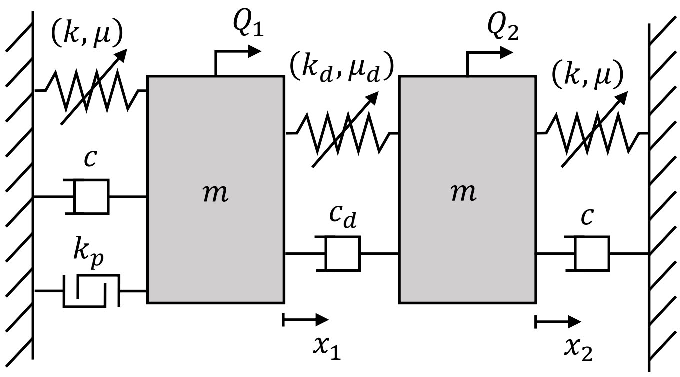

Figure 3.4: Schematic of the two-mass system with a free-play gap [1].

To study the effect of smoothing approximation on the dynamics of MDOF non-smooth systems, the mechanical system depicted in Fig. 3.4 is considered. The system is slightly damped and presents cubic and free-play nonlinearities. The latter is modelled using the bilinear piecewise stiffness characteristic represented by Eq. 3.1. The

Table 3.1: Non-dimensional parameters of the two-mass system.

Non-Dimensional Parameter	Dimensional Parameter
$\underline{x}_1$	x_1/l_r
$\underline{x}_2$	x_2/l_r
$\tilde{\Omega}$	Ω/Ω_r
$\tilde{t}$	$t\Omega_r$
$\tilde{m}$	m/m_r
$\tilde{Q}_1$	$Q_1/(m_r l_r \Omega_r^2)$
$\tilde{Q}_2$	$Q_2/(m_r l_r \Omega_r^2)$
$\tilde{k}$	$k/(m_r \Omega_r^2)$
$\tilde{k}_d$	$k_d/(m_r \Omega_r^2)$
$\tilde{c}$	$c/(m_r \Omega_r)$
$\tilde{c}_d$	$c_d/(m_r \Omega_r)$
$\tilde{\mu}$	$\mu l_r^2/(m_r \Omega_r^2)$
$\tilde{\mu}_d$	$\mu_d l_r^2/(m_r \Omega_r^2)$
$\tilde{a}$	a/l_r
$\tilde{k}_p$	$k_p/(m_r \Omega_r^2)$

second order non-dimensional equation of motion is reported in Eq. 3.3 and the non-dimensional parameters are defined in Tab. 3.1. The reference values Ω_r [rad/s], t_r [s], and l_r [m], are chosen to be 1. For simplicity, the following sections will refer to non-dimensional equations without employing the symbols $\tilde{\bullet}$ and $\underline{\bullet}$.

$$\tilde{m}\ddot{\underline{x}}_1 + \tilde{c}\dot{\underline{x}}_1 + \tilde{k}\underline{x}_1 + \tilde{\mu}\underline{x}_1^3 - \tilde{k}_d(\underline{x}_2 - \underline{x}_1) - \tilde{\mu}_d(\underline{x}_2 - \underline{x}_1)^3 - \tilde{c}_d(\dot{\underline{x}}_2 - \dot{\underline{x}}_1) + \tilde{F}_p = \tilde{Q}_1\cos(\tilde{\Omega}\tilde{t}) \tag{3.3a}$$

$$\tilde{m}\ddot{\underline{x}}_2 + \tilde{c}\dot{\underline{x}}_2 + \tilde{k}\underline{x}_2 + \tilde{\mu}\underline{x}_2^3 + \tilde{k}_d(\underline{x}_2 - \underline{x}_1) + \tilde{\mu}_d(\underline{x}_2 - \underline{x}_1)^3 + \tilde{c}_d(\dot{\underline{x}}_2 - \dot{\underline{x}}_1) = \tilde{Q}_2\cos(\tilde{\Omega}\tilde{t}) \tag{3.3b}$$

Following the procedure outlined in Chapter 2, Eq. 3.3 can be easily converted in its *autonomous* first order version, reported for completeness in the Appendix A.1. The obtained set of equations of motion formally represents a piecewise-smooth continuous dynamical system. This system is characterised by a C^0 class function on the right-hand side, i.e. a Lipschitz continuous function. This definition is fundamental in demonstrating that the considered piecewise function can be mathematically approximated using a smoothing approximation [3]. Table 3.2 presents the parameters utilised

[3] The mathematical admissibility of smoothing regularisation in approximating piecewise-smooth is demonstrated in [1], using the theorems developed by Danca [121–123]

for analyzing the two-mass system. These dimensional parameters are derived from data employed in previous analyses of slightly damped nonlinear systems [99].

Table 3.2: Numerical parameters of the two-DOF system.

Parameter	Value	Units
m	1	kg
k	1	N/m
c	0.009	Ns/m
μ	0.5	N/m^3
k_d	0.5	N/m
c_d	5e-05	Ns/m
μ_d	0.1	N/m^3
Q_1	0	N
Q_2	0.015	N
k_p	10	N/m
a	0.05	m

To evaluate the effect of smoothing functions on the mechanical response of the two-mass system, the piecewise bilinear restoring force of Eq. 3.1 is approximated with the sigmoid function $F_{p,3}$ $(n = 1)$ outlined in Eq. 3.2c. The error introduced by the approximation function $F_{p,3}$ with respect to the ideal piecewise function F_p is illustrated in Fig. 3.5 for a value $\delta = 1500$. An appropriate value for δ can be determined by comparing the dynamic responses of the ideal and approximate smooth dynamical systems using the values specified in Table 3.2

For this purpose, the vector fields of both versions of the system, piecewise and approximate, are calculated analytically and compared around the discontinuity boundary Σ with $\delta = 1500$. To simplify the computation and prevent intersecting lines, the vector fields are computed for the undamped unforced version of the two-mass system, considering the second mass blocked, i.e. imposing $x_2 = 0$ and $\dot{x}_2 = 0$. The piecewise function can be expressed with a linear combination of $sign(x)$ functions, as follows:

$$F_p = k_p \frac{(x_1 + a)}{2}(sign(-x_1 - a) + 1) + k_p \frac{(x_1 - a)}{2}(sign(x_1 - a) + 1) \tag{3.4}$$

The comparison is reported in Fig. 3.6. Blue and black arrows represent the system vector fields for the approximate and non-approximate conditions and appear to be completely overlapped. The pseudo-colour images, instead, represent the percentage error between the vector fields obtained with sigmoid and the ideal piecewise functions in terms of magnitude (Fig. 3.6(a)) and direction (Fig. 3.6(b)). Three orbits associated with the first mass are computed numerically and are displayed in the figure: the smallest (PO_A) illustrates the non-contact condition, the largest (PO_C) denotes a fully-developed contact condition, and the middle orbit (PO_B) represents the grazing condition. Both vector fields appear to completely overlap throughout the entire domain, including near the discontinuity boundary Σ. This indicates that the chosen degree of approximation δ does not introduce significant distortion in the vector field of the two-mass system. The percentage error maps reveal that the distorted

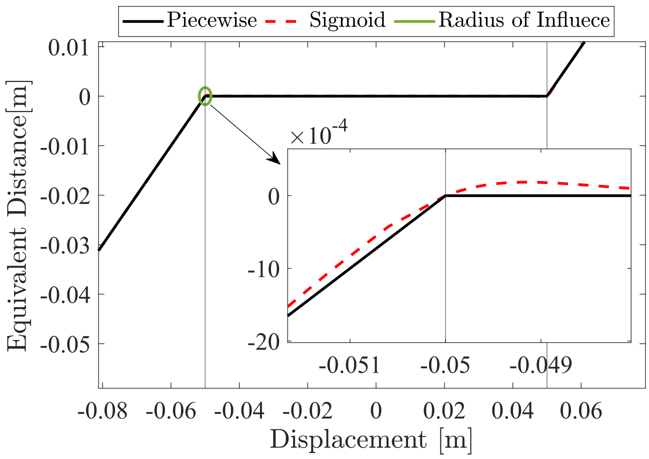

Figure 3.5: Graphical representation of the radius of influence and comparison between approximated and ideal piecewise functions. The approximation is obtained using $\delta = 1500$ and the relevant data from Tab. 3.2 [1].

field is restricted to regions of the domains very close to the discontinuity boundary Σ. The identified maximum errors in magnitude and direction of the approximate field are respectively equal to 2.4% and 1.8%. This proves that the chosen approximation parameter $\delta = 1500$ is accurate enough to describe the dynamics of the considered piecewise-smooth continuous system. To further demonstrate the accuracy of the chosen approximation, numerical experiments are performed. Specifically, two numerical attractors of the two-mass systems are considered and the associated orbits are computed using the smoothing approximation with $\delta = 1500$ (Eq. 3.2c) and adopting a piecewise function (Eq. 3.4). The numerical simulations are performed in MATLAB,

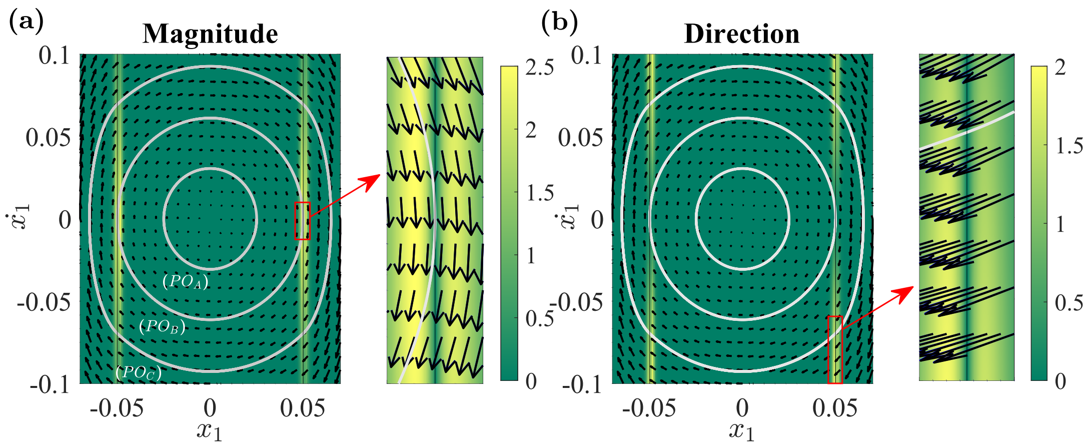

Figure 3.6: Vector fields of the undamped unforced piecewise system, represented by Eq. 3.3, when the second mass is blocked ($x_2 = 0$ and $\dot{x}_2 = 0$). Numerical periodic orbits at different amplitudes of response (PO_A, PO_B, and PO_C) are also reported. The intensity scale indicates the numerical difference between the vector fields of the approximate and non-approximate systems, in terms of magnitude (a) and direction (b). The parameters of Tab 3.2 and $\delta = 1500$ are used for the analysis [1].

using the function *ode45* with a maximum time step $\Delta t = 0.4s$. Two forcing frequencies, namely $\Omega = 1.2$ and $\Omega = 1.3$ are utilised to identify the two attractors in both versions of the system. Fig. 3.7 shows the comparison between the numerical orbits: the attractors are very similar and practically overlapped therefore, the chosen parameter $\delta = 1500$ is considered to be sufficiently accurate to describe system dynamics, also from a numerical point of view.

To improve the comprehension of the relationship between the approximating parameter δ and the distortion introduced by the approximated function, the *radius of influence* R_i is introduced. This mathematical tool serves to identify a suitable smoothing parameter δ, bypassing the need for the analytical and numerical analyses previously described. This in turn enhances and simplifies the parameter selection process. As the approximation error typically concentrates around the discontinuity point, the radius R_i tries to delineate the extent of the error from that point, considering both an approximate and non-approximate definition of the characteristic. The radius is computed by considering the sum of two areas, indicated by area 1 and area 2 in Fig. 3.8. These areas define the error between the chosen approximation and a piecewise func-

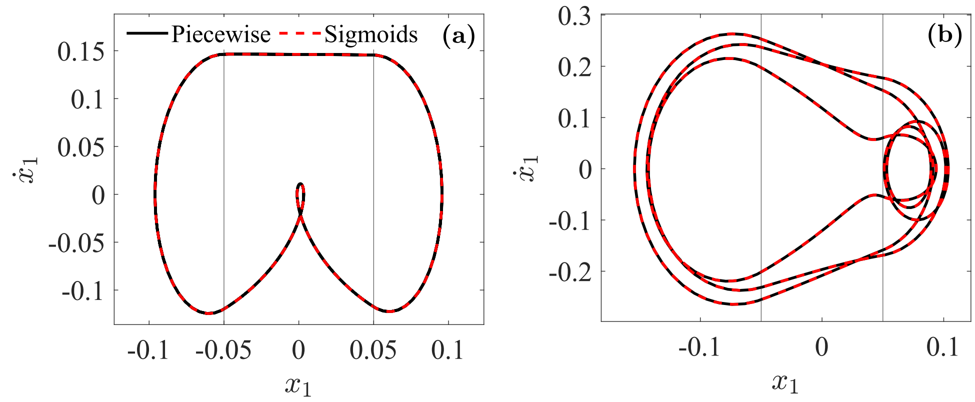

Figure 3.7: Comparison between approximate and non-approximate attractors. The attractors are obtained using a forcing function equal to $\Omega = 1.2$ (a) and $\Omega = 1.3$ (b) and using an approximation parameter equal to: $\delta = 1500$. The parameters of Tab 3.2 are utilised to perform the numerical analysis [1].

tion. Starting from the discontinuity point, it is possible to calculate the error area of a sufficiently large portion of the domain such that we reach an asymptotic numerical value of the error. This is guaranteed by the smoothing functions such as sigmoids, arc-tangent, and hyperbolic tangent functions which globally approximate piecewise-smooth continuous characteristics. The total error is reached for an infinite distance from the discontinuity; to make the procedure feasible it is possible to consider a finite distance from the discontinuity point, specifically the one that constitutes the 68.0% of the total asymptotic error, i.e., the σ_1 error. Considering the discontinuity point at negative displacement, the error can be numerically evaluated as follows:

$$E_a = \int_{-a}^{-a+r} \frac{F_{p,s}(x)}{k_p} + \Big| \int_{-a-r}^{-a+r} \frac{F_p(x)}{k_p} - \int_{-a-r}^{-a} \frac{F_{p,s}(x)}{k_p} \Big| \tag{3.5}$$

where r indicates the radius extension around the discontinuity point. Similarly, it is straightforward to derive the expression of the error at the discontinuity point with positive displacement. The radius is computed within a domain where the horizontal axis represents the physical displacement, and the vertical axis indicates the equivalent displacement of the piecewise restoring function, i.e., F_p/k_p. This ensures that δ is the only parameter influencing the radius R_i. Taking into account the soft symmetric piecewise constraint employed in this study ($k_p = 10$ and $a = 0.05$) along with the

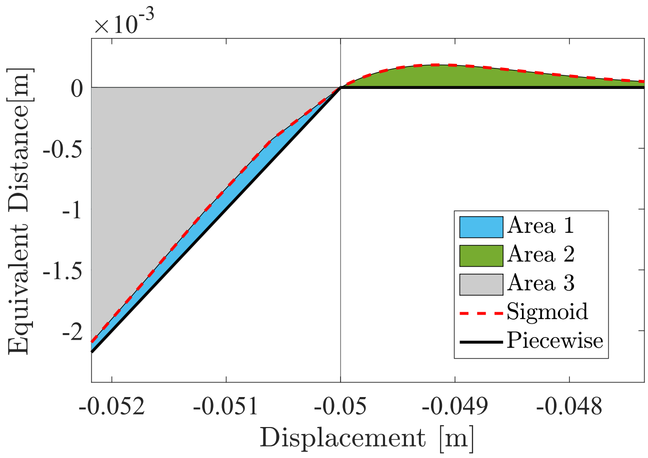

Figure 3.8: Areas considered in the computation of the radius of influence R_i. The approximate function considers an approximation parameter equal to $\delta = 1500$ [1].

sigmoid approximation using $\delta = 1500$, the radius results in the following value: $R_i = 0.0017$. This indicates that the region of the domain around the discontinuity point and within the radius contains 68% of the distortion error due to the introduction of a smoothing function. This result is acceptable as it accounts for only 3.4% of the non-contact gap and indicates that the region affected by approximation error is quite limited, and so confirms that the chosen parameter δ is sufficiently accurate to describe the dynamics of the piecewise system.

3.3 Steady-State Behaviour of the Non-Smooth System

This section investigates the dynamic behaviour of the previously introduced MDOF non-smooth system. Initially, the system is studied using the sigmoid approximation $F_{p,3}$ (Eq. 3.2c), employing the identified approximation parameter $\delta = 1500$, $n = 1$, and the parameters of Tab. 3.2. Subsequently, to verify the accuracy of the approximation, the obtained dynamic response is compared against the dynamic behaviour of the ideal counterpart, computed with a piecewise function F_p (Eq. 3.1).

3.3.1 Approximate System Dynamics

Initially, the dynamics of the system are investigated by computing the bifurcation diagram. The diagram is obtained via numerical integration using the MATLAB function *ode45*, a Runge-Kutta scheme, sampling 100 Poincaré points from the steady-state response. The final diagram is illustrated in Fig. 3.9 and reveals the presence of co-existing attractors. The bifurcation diagram provides a clear overview of the system

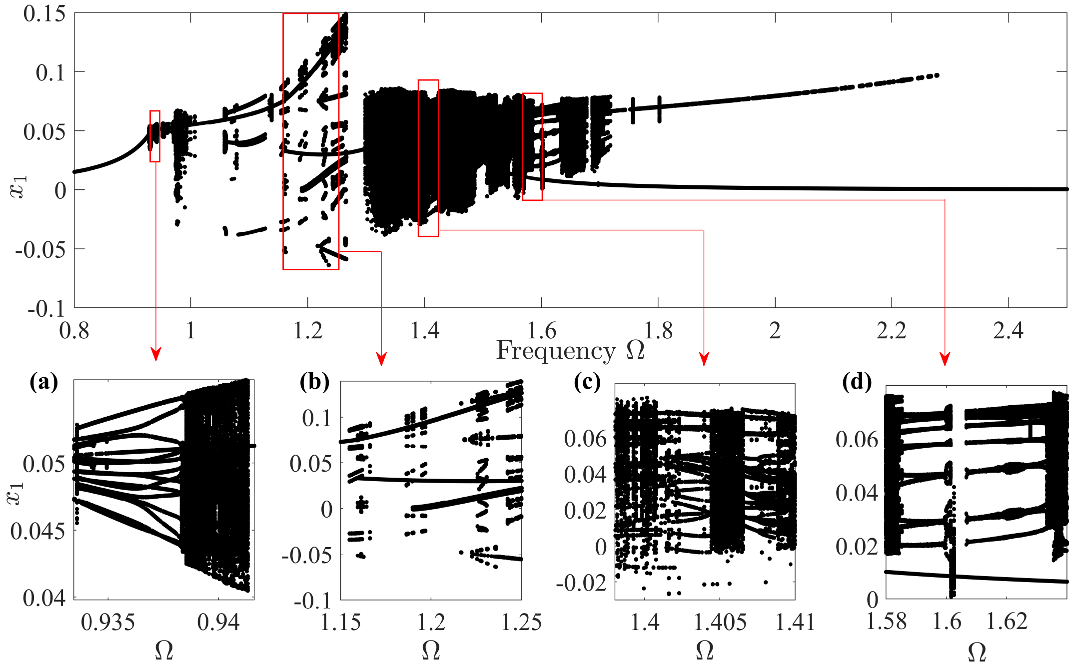

Figure 3.9: Bifurcation diagram of the approximate MDOF system. Numerical simulations are carried out using the parameters of Tab. 3.2 and different initial conditions ($x_0 = [x_1; \dot{x}_1; x_2; \dot{x}_2]$), i.e. $x_0 = [\pm 0.2; 0; \pm 0.2; 0]$, $x_0 = [0; 0; 0.1; 0]$, and $x_0 = [0; 0; 0; 0]$. The Poincaré section $\dot{x_1} = 0$ are utilised to create the diagram [1].

dynamics, highlighting the presence of chaotic and multi-periodic regions. However, solutions with small basins of attraction, are difficult to obtain and result in scattered non-continuous branches, as shown in Fig. 3.9(b). As generally happens for impact oscillators [81, 103], chaos originates after the grazing bifurcations. This behaviour is evident in two regions: $\Omega \approx 0.93 - 0.98$ and $\Omega \approx 1.3 - 1.75$. Interestingly, chaos does not occur via the typical period-doubling cascade [124] but, instead, it seems to be generated by sudden bifurcations, which abruptly transform regular attractors into chaotic ones [81, 82]. These sudden shifts transform periodic responses into chaotic ones. This phenomenon is illustrated in Fig. 3.9(a) and 3.9(c-d) which highlights a mixture of multi-periodic and chaotic responses.

The bifurcation diagram provides important information about the system dynamics, locating frequency ranges where stable period-doubling orbits exist and where chaotic or quasi-periodic behaviour is prevalent. One important by-product of the bifurcation diagram is the associated steady-state dynamic responses: they are particularly valuable to initialise path-following procedures. This enables the continuation of both stable and unstable branches, solving the challenges highlighted by Fig. 3.9(b), and facilitates the exploration of solution branches that cannot be easily continued from other solution branches, i.e. isolas. To this end, the module *po* of the continuation toolbox COCO [97] is utilised to perform numerical continuation analyses: the results of the analyses are shown in Fig. 3.10 and Fig. 3.11, where PD denotes a period-doubling bifurcation point, BP indicated a branch bifurcation point, and TR indicates a Neimark-Sacker (torus) bifurcation point. PO indicates the periodic orbit amplitude used to initialise the branch and, to help the graphical interpretation, fold (FP) and saddle-node (SN) bifurcations are not reported in the obtained bifurcation diagrams. Finally, continuous and dashed lines indicate stable and unstable solutions.

Fig. 3.10(a) shows the numerical continuation of single-period orbits. The chosen projection, i.e. amplitude of the first DOF (x_1) versus excitation frequency (Ω), is used to obtain the frequency response of the system, i.e. the Frequency Response Curve (FRC). Branch B_1 shows the continued solution of single period orbits originated from the steady-state solution PO_1. This orbit is associated with the 'main' response of the system and persists in both the contact and non-contact regions, transitioning through a grazing bifurcation. After the contact, B_1 show the presence of branch (BP) and torus (TR) bifurcation points, as highlighted in Fig. 3.10(b-c): the first bifurcation point generates a second stable branch of solutions, named B_2, whose associated periodic orbits are described by PO_{2A} and PO_{2B} at two different level of amplitude of response. These periodic orbits show a symmetric behaviour which generates two peaks in the plane $max(x_1)$ vs Ω, as shown in Fig. 3.10(a). The second bifurcation, instead, produces

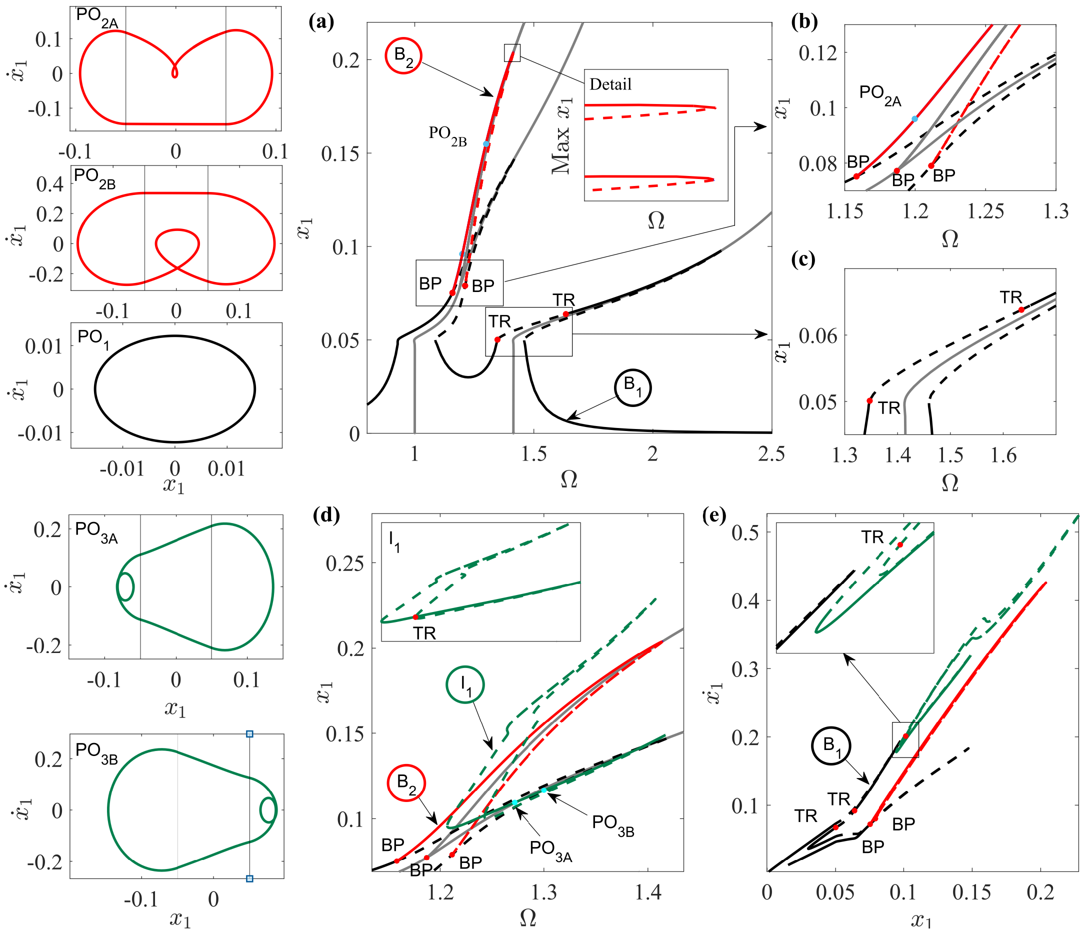

Figure 3.10: Numerical continuation of single period branches/isolas and associated periodic orbits [1]. Parameters of Tab. 3.2 and $\delta = 1500$ are utilised to carry out the simulations. The panels on the left column show the steady-state orbits of the system, panels (a,d,e) illustrate the FRCs of the system in terms of amplitude x_1 and frequency of excitation Ω, and panels(b,c) highlight zooms and details of the FRCs.

a region of frequencies where the system exhibits chaotic and quasi-periodic behaviour.

Fig. 3.10(d) shows the continuation of the single periodic orbits PO_{3A}, and PO_{3B}. These periodic orbits exhibit a symmetric behaviour similar to those of PO_{2A} and PO_{2B}. In both cases, the vertical axis serves as the plane of symmetry and initial conditions that are opposite in sign allow to achieve the two symmetric orbits. The continuation of this solution branch results in a closed isola, named I_1 which appears to be overlapped to B_2 in the projection plane that considers the amplitude of the first DOF (x_1) versus excitation frequency (Ω). To demonstrate that I_1 is not connected to other branches, the branches B_1, B_2, are I_1 are projected to another plane which considers the amplitude of the first DOF in terms of displacement (x_1) and velocity ($\dot{x}_1$). Fig. 3.10(e) shows the new projection, demonstrating that the solution is closed

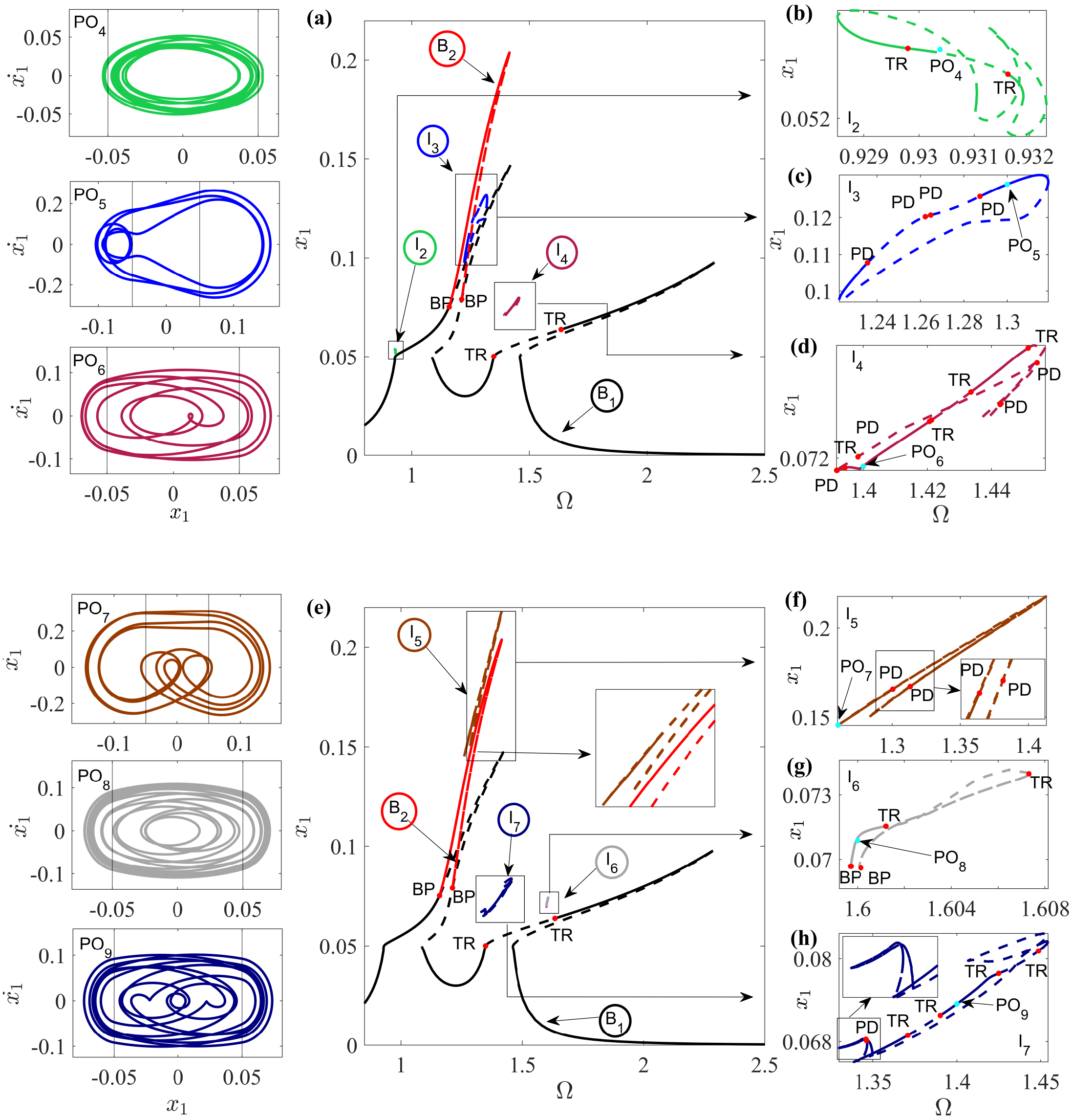

Figure 3.11: Numerical continuation of period-doubling isolas and associated initial periodic orbits [1]. Parameters of Tab. 3.2 and $\delta = 1500$ are utilised to carry out the simulations. The panels on the left column show the steady-state orbits of the system, the panels in the central column illustrate the FRC in terms of amplitude x_1 and frequency of excitation Ω, and the panels in the right column show zooms and details of each isola.

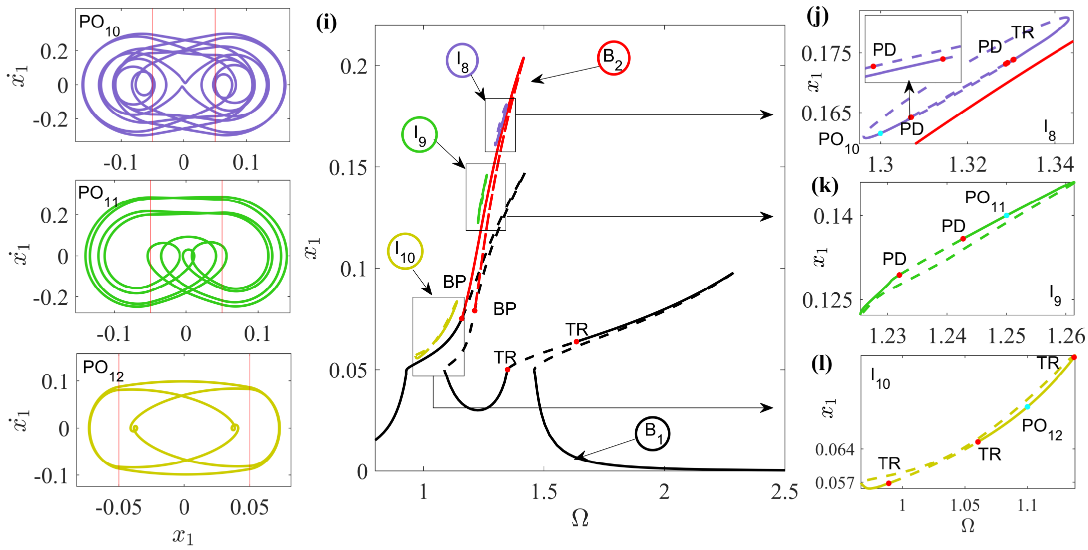

Figure 3.11: Numerical continuation of period-doubling isolas and associated initial periodic orbits [1]. Parameters of Tab. 3.2 and $\delta = 1500$ are utilised to carry out the simulations. The panels on the left column show the steady-state orbits of the system, the panels in the central column illustrate the FRC in terms of amplitude x_1 and frequency of excitation Ω, and the panels in the right column show zooms and details of each isola. (cont.)

and detached, and thus represents an isola.

At this point, multi-periodic stable orbits are continued with path-following analyses. To this end, the steady-state multi-periodic responses previously identified in the bifurcation diagram are used as the initial solution of the numerical continuation. The idea is to obtain the intricate network of branches that originate from the multi-periodic orbits, by exploiting the numerical continuation. Nonetheless, given the multitude of co-existing solutions, it is expected that some orbits will not be identified and thus continued, especially the ones close to chaos. Once again, the initial steady-state responses are reported in the left column of Fig. 3.11. Fig. 3.11(a,e,i) illustrates the location of the isolas in the frequency domain and their position with respect to the main branches B_1 and B_2. Most of the isolas appear to be completely detached from the main branches in the considered projection, i.e. frequency Ω versus the amplitude of the first DOF x_1. As shown earlier for I_1, the ones that appear to be overlapped, e.g. I_3, are demonstrated to be completely detached from other branches by project-ing the continued solution in a different space. Panels (b,c,d), (f,g,h), and (j,k,l) of Fig. 3.11 show the detailed views of each isola: the isolas demonstrate the presence of many period-doubling (PD) and torus (TR) bifurcation points. Certain isolas, such as I_2 and I_6, are notably small and predominantly unstable. However, larger isolas like I_{10} exhibit a broad range of frequencies where solutions are stable. This poses a potential concern for mechanical systems featuring contacts. If the presence of isolas is not carefully assessed, the system dynamics could become trapped in one of these isolas, where the amplitude response exceeds the one predicted by the main branch B_1. This may ultimately lead to unwanted vibration states and amplitude of responses that might exceed the design envelopes of the mechanical system. Finally, it is important to note that isolas I_4, I_6, and I_7 are partially located within chaotic regions, posing challenges for their identification without the use of path-following continuation procedures. Overall, the obtained frequency response diagrams show the presence of branches of the solution, chaotic regions, and period-doubling isolas, highlighting the highly rich and complex dynamics of the investigated two-mass systems.

The dynamics of the unforced undamped version of the system are also studied via numerical continuation: to perform this analysis the modal version of the equation of motion is obtained by applying a linear modal transformation to Eq. 3.3. The resulting system of equations is obtained:

$$\ddot{q}_1 + 2\zeta_1\omega_{n,1}\dot{q}_1 + \omega_{n,1}^2 q_1 + \frac{\mu}{2m}(q_1+q_2)^3 + \frac{\mu}{2m}(q_1-q_2)^3 + \frac{F_p}{2m} = 0 \tag{3.6a}$$

$$\ddot{q}_2 + 2\zeta_2\omega_{n,2}\dot{q}_2 + \omega_{n,2}^2 q_2 + \frac{\mu}{2m}(q_1+q_2)^3 + \frac{8\mu_2}{m}q_2^3 - \frac{\mu}{2m}(q_1-q_2)^3 + \frac{F_p}{2m} = 0 \tag{3.6b}$$

where q_1 and q_2 indicate the modal coordinates. Backbone curves are then computed by tracking the limit cycle oscillations generated by the Hopf bifurcation (HB) which is identified by moving the stable equilibrium point $x_1 = 0$, $\dot{x}_1 = 0$, $x_2 = 0$, and $\dot{x}_2 = 0$ from positive to negative modal damping parameter. Finally, the identified periodic responses are continued keeping the modal parameters equal to zero [125]. The presence of two modal damping consents to easily control and continue the periodic oscillations arising from the two modes of the system. Fig. 3.12 displays the outcomes of the

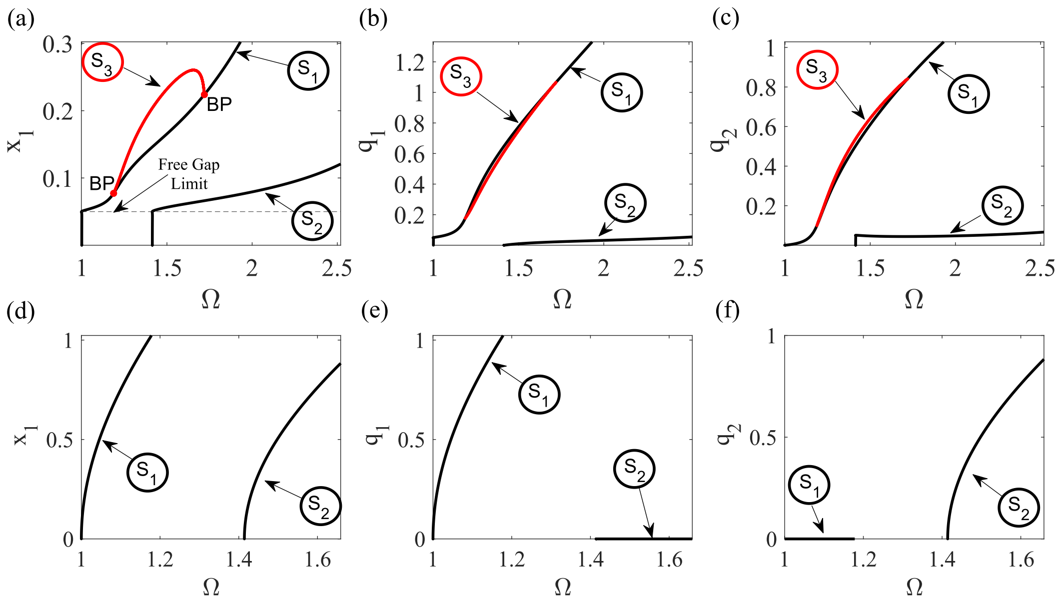

Figure 3.12: Backbone curves of the nonlinear system in real (x_1) and modal coordinates (q_1 and q_2). The panels in the first row show the backbone curves of the system when the piecewise characteristic (approximated by a sigmoid function) is considered while the panels in the second row illustrate the backbone curves of the system when the piecewise characteristic is not present. Several backbones are represented: S_1 and S_2 denote the main curves, i.e. the backbone curves that originate the linear mode shape, while S_3 indicates the backbone curve that branches from the bifurcation point. The parameters of Tab 3.2 and $\delta = 1500$ are utilised to perform the analysis

analysis, presenting the backbone curves plotted under various conditions and different coordinates. Panels (a),(b) and (c) describe the backbones of the approximate non-smooth system while panels (d), (e), and (f) show the backbones of the system when the piecewise stiffness is completely removed. The backbone curves are reported in terms of real (x_1) and modal (q_1, q_2) amplitude: specifically, Fig. 3.12 (a,d) show the backbones in terms of real coordinates, while Fig. 3.12 (b,c,e,f) show the same curves in terms of modal amplitudes. In the free-play region, below $x_1 = 0.05$, there is no significant coupling between the modes, i.e., the first backbone S_1 has a low contribution from the second modal DOF and vice versa. This is valid in both the considered version of the two-mass system and it is proven by the analysis of the backbone in the absence of contact. In addition, panels (e,f) show that the effect of q_2 on the first backbone, and conversely, the effect of q_1 on the second backbone, is small and negligible even at high

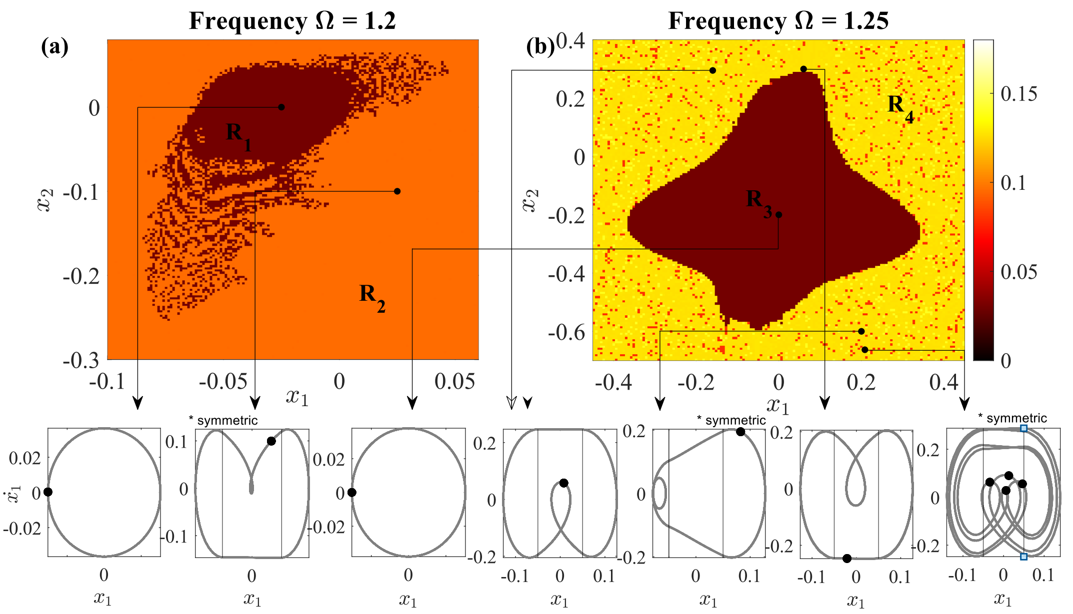

Figure 3.13: Basins of attraction at Ω equal to 1.2 (a) and 1.25 (b). The colour map indicates the maximum amplitude of the first mass. For each region of the basin of attraction, the associated periodic orbits are shown. The black dots represent the points obtained from the Poincaré sections. The parameters of Tab 3.2 and $\delta = 1500$ are utilised to perform the numerical analyses [1].

amplitudes of response when the piecewise characteristic is not applied. Above the free-play gap limit, instead, the backbones, S_1 and S_2 have strong modal coupling when the piecewise stiffness is present. This results in the presence of non-negligible components of q_1 and q_2 in both backbones, as shown by Fig 3.12 (b,c). At a certain amplitude, the modal interaction results in a bifurcation of the backbone curve and generates the branch S_3. This phenomenon is probably triggered by the incremental frequency of the first mode which may trigger a 1:1 internal resonance and further investigation is needed to identify the root causes. It is worth noticing that the bifurcation of the backbone curve results in a bifurcation of the stable single-period branch B_1 which initiates the branch B_2 as shown by Fig. 3.10(b).

The dynamic behaviour of the approximate system is further examined by analysing its Basins of Attraction (BoA). The BoA are computed using direct numerical integration and considering various excitation frequencies Ω, namely equal to 1.2, 1.25, 1.30 and 1.35. These values are chosen because the system shows multiple co-existing at-

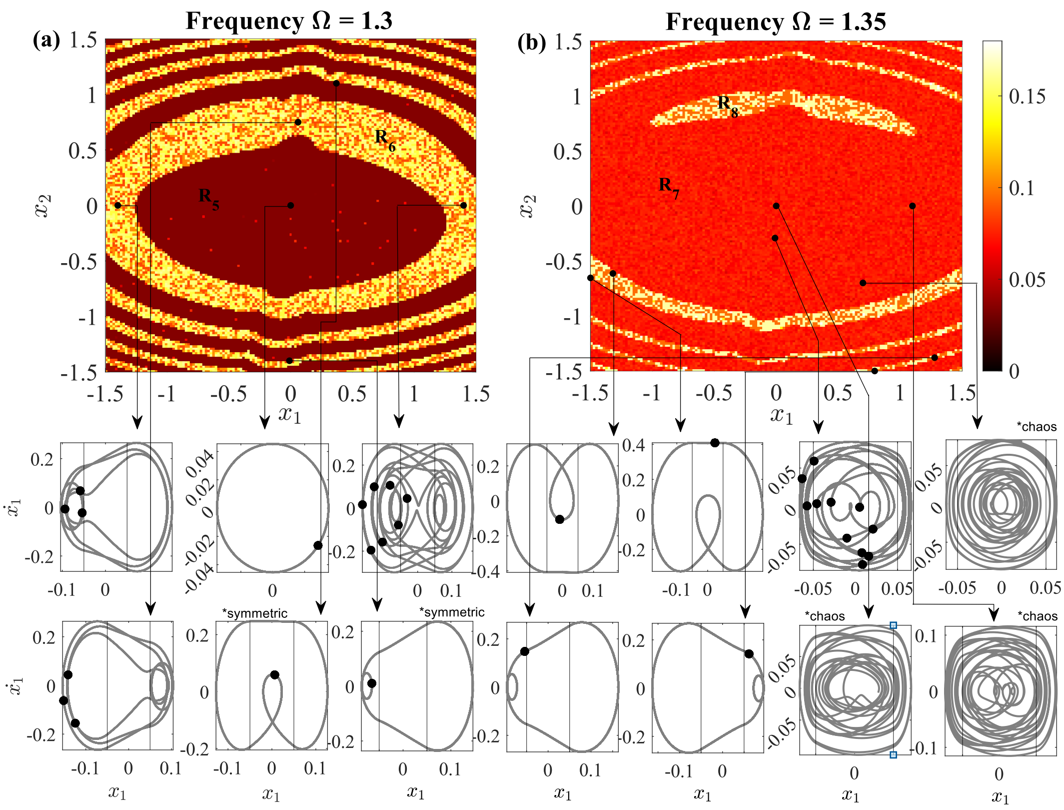

Figure 3.14: Basins of attraction at Ω equal to 1.3 (a) and 1.35 (b). The colour map indicates the maximum amplitude of the first mass. For each region of the basin of attraction, the associated periodic orbit is shown. The black dots represent the points obtained from the Poincaré sections. The parameters of Tab 3.2 and δ = 1500 are utilised to perform the numerical analyses [1].

tractors and transitions to chaos in the interval $\Omega = [1.20 - 1.35]$. To facilitate the graphical representation and interpretation of the results, the maximum amplitude of the first mass is considered as the output quantity to represent the BoA and its value is indicated by the colour map. The BoA are computed by keeping the initial velocities $\dot{x}_1$ and $\dot{x}_2$ equal to zero and by imposing different initial displacements x_1 and x_2. The ranges of the initial displacements are adjusted so that diverse steady-state conditions are achieved for all the considered excitation frequencies while the resolution of the BoA, i.e. the total number of simulations to achieve the steady-state dynamics, is kept constant (150 × 150). The resulting BoA are shown in Fig. 3.13: when Ω is equal to 1.20 (Fig. 3.13(a)) two distinct regions, denoted as R_1 and R_2, are identified: the first one delineate the initial conditions that lead to the single-period orbits PO_1 of branch B_1, whereas the second one shows the initial conditions that allow reaching the higher amplitude orbits PO_2 associated with branch B_2. Moving towards higher frequencies of excitation, the BoA becomes more complicated: co-existing steady-state solutions increase in number and the different regions become more complicated in terms of shape. Fig. 3.13(b) shows the BoA of the approximate two-mass system when $\Omega = 1.25$. In this case, the BoA is dominated by quite a large region of low amplitude solutions, named R_3. This region is associated with the single-period orbit PO_1 and represents the evolution of region R_1. The BoA shows also the presence of a second region, named R_4, where single-period and multi-period orbits coexist. Specifically, the following periodic orbits are found: PO_2, PO_3, and PO_{11}; the first two steady-state solutions are single-period solutions, while the last one has period 4. R_4 lacks a well-defined shape, and the coexistence of such varied solutions within the same area of the BoA indicates the proximity to chaotic behaviour. The chaos in this system appears to be generated from the continuous transition between different periodic orbits within the same region of the basin of attraction.

A similar analysis applies to the BoA of the system obtained at the frequency of excitation $\Omega = 1.30$, reported in Fig. 3.14 (a). In this case, the regions R_5 and R_6 show the alternation of low amplitude single-period solution and bands of co-existing attractors. Differently, from the previous BoA, the low amplitude region repeats itself even when significantly large initial conditions are applied to the system. In addition, the BoA shows the presence of a consistently larger number of steady-state solutions, namely the orbits PO_1, PO_2, PO_3, PO_5, and PO_{10}. Complete chaotic solutions begin to emerge at $\Omega = 1.35$ as demonstrated by Fig. 3.14 (b). Once again, two regions are visible: the first one, R_7, is associated with a low amplitude of response, and the second one, R_8, shows a significantly larger amplitude of response. Chaos appears in the regions with lower amplitude response, and it is mixed with regular multi-periodic orbits, while the high amplitude region R_8 shows again the co-existence of multiple periodic solutions, but not chaos.

3.3.2 Comparison between Approximate and Non-approximate Systems

The previous analyses showed the dynamics of the two-mass system when the piecewise characteristic is approximated using a sigmoid function. To understand the effect of this approximation, the obtained dynamics are compared against the dynamics of the non-approximate version of the system, i.e. a version of the system that utilises a piecewise-smooth continuous characteristic for describing the presence of the contact. To this end, numerical integration and numerical continuation analyses are utilised and, to account for the presence of a non-smooth characteristic, ad-hoc procedures are adopted. Specifically, numerical continuation is performed using the COCO toolbox named *hspo*. This toolbox allows to continue limit-cycles associated with non-smooth dynamical systems, enabling the so-called multi-segment numerical continuation. This technique exploits the fact that different portions of the orbit, referred to as segments, are defined on different but smooth domains and thus they can be continued without invalidating the implicit function theorem. A detailed explanation of the multi-segment continuation procedures is out of the scope of this thesis and the interested reader should refer to reference [97]. The practical application of the procedure employed in this study is similar to the approach utilised by Liu et al. [117], wherein each segment of the orbit is represented by a smooth equation corresponding to a specific condition of the piecewise characteristic. Since more than one segment is present, a set of smooth equations called *vector field equations*, must be defined to perform the numerical continuation of the system. An event function delineates the boundary between adjacent segments, capturing the behaviour at the discontinuity point. Subsequently, a restart function is employed to establish the initial conditions for the next segment of the orbit. The vector field equations, the event function, and the restart function for the considered system are reported in Appendix A.1.

Although this procedure does not require any approximation of the piecewise characteristic, its practical application is often difficult, computationally expensive and time-consuming: this is especially true for systems that show many grazing bifurcation points in the same branch. Indeed, grazing bifurcation generates or eliminates segments

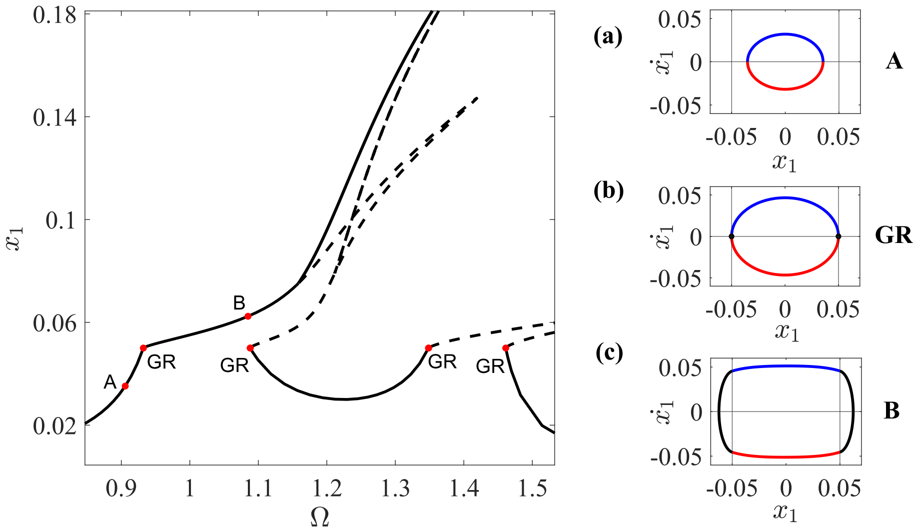

Figure 3.15: Re-segmentation procedure after grazing bifurcations (GR). Orbits obtained before (A), at (GR), and after (B) the grazing bifurcation are reported on the left. The parameters of Tab 3.2 are utilised to perform the numerical analyses [1].

during the path-following continuation process: this demands a re-segmentation of the orbits to avoid ending in non-physical dynamic responses [97]. The re-segmentation procedure is graphically shown in Fig. 3.15: when the orbit is small enough and contact does not occur, two segments fully describe the steady-state dynamics of the system, as depicted in Fig. 3.15(a). The two segments belong to the non-contact condition and they are used only for practical reasons as they allow for monitoring the maximum and minimum amplitude of the orbit, identifying when the grazing bifurcation occurs. As the frequency increases, the orbit approaches the grazing condition (GR): here, the maximum and minimum displacements of the first mass correspond to the free-play gap a and a grazing contact occurs at both the extremities of the orbits when the velocity is zero, i.e. at $y_1 = 0$. From a numerical continuation point of view, two degenerate segments represent the occurrence of the grazing condition. Fig. 3.15(b) represents the degenerate segments as two additional points at $x_1 = \pm a$. By further increasing the excitation frequency, the system overcomes the grazing condition and the two degenerate segments increase their length as shown in Fig. 3.15(c). This process, termed re-segmentation, is necessary at every grazing bifurcation point to prevent the formation of non-physical dynamics.

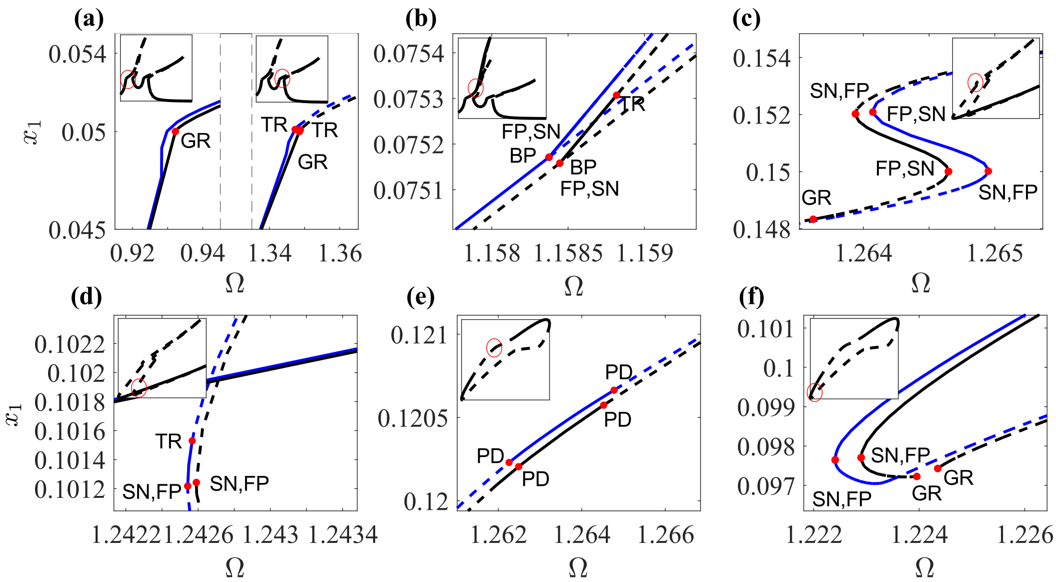

Figure 3.16: Comparison between continued branches associated with the approximate version (blue) and the non-approximate version (black) of the non-smooth system. The parameters of Tab 3.2 and $\delta = 1500$ (only for the approximate version) are utilised to perform the numerical analyses [1].

Considering the challenges associated with the re-segmentation procedure, only a subset of solutions obtained using the sigmoid approximation are now reproduced for the comparative analysis. Fig. 3.16 presents the comparison between the dynamics of the system when the sigmoid approximation is used (blue lines) and when the piecewise characteristic (black lines) is adopted. To visualise the difference between the different branches, each panel represents a zoom. The location of the zoom is indicated in each panel, using a red circle. Fig. 3.16 (a) shows the two grazing bifurcation points associated with the main branch B_1 (i.e. the continuation of single-periodic orbits): given its smooth nature, the sigmoid approximation can not detect the grazing condition, however, it correctly identifies torus bifurcations nearby grazing bifurcation points and the change of stability of the response. Fig. 3.16(b) shows the continuation of the two versions of the system across the bifurcation point between branches B_1 and B_2. In this case, the sigmoid function correctly locates branch, flip, and saddle-node bifurcation points. However, it fails to detect the instability of the first branch before the point BP and the occurrence of a torus bifurcation. It is worth mentioning that employing smaller steps in the continuation procedure could help to improve the quality of the continued solution, reducing the difference between the two systems. Moreover, the inaccuracies are confined to a small region surrounding the BP point, suggesting that also in this case the dynamic response of the systems is very similar. Fig. 3.16(c,d) compare the single period isolas I_1 obtained with the approximate and non-approximate systems. Once more, stability and amplitude are generally accurately identified; however, discrepancies arise near the grazing bifurcation points. This is evident in Fig. 3.16(c), where the S-shaped solution is shifted towards higher frequencies when the approximation is adopted, and in Fig. 3.16(d), where a torus bifurcation is identified in the approximated solution but it is not observed when the multi-segment procedure is adopted. Finally, Fig. 3.16(e,f) compare the period-tripling isolas I_3 obtained with the two versions of the system. In Fig. 3.16(e), the sigmoid function correctly locates the period-doubling bifurcation points and the changes in the stability of the continued solution. Fig. 3.16(f), instead, shows a point where multiple grazing bifurcations occur: differences between the approximate and non-approximate solution are visible in terms of the amplitude of response only near the grazing conditions. Nevertheless, such discrepancies remain minimal even in this complex scenario, characterised by the presence of multi-periodic attractors. Overall, the usage of the sigmoid function allows for obtaining dynamic responses that are close to the dynamics of the non-approximate counterpart in terms of amplitude and stability of the solution. Differences emerge only near the grazing bifurcation points where the smoothed function fails to precisely replicate the piecewise characteristic. It is important to note that such differences are limited and do not significantly impact the overall solution, both when single-period and multi-period dynamics are considered.

As a final demonstration of the good approximation capabilities of the identified sigmoid function, the BoA of the approximate and non-approximate versions of the system are compared. To perform the comparison, the BoA of the non-approximate version of the system are computed using numerical integration procedures. The MATLAB function *ode45* and the built-in event function are used to handle the discontinuity point of the piecewise characteristic, using a procedure similar to the one adopted

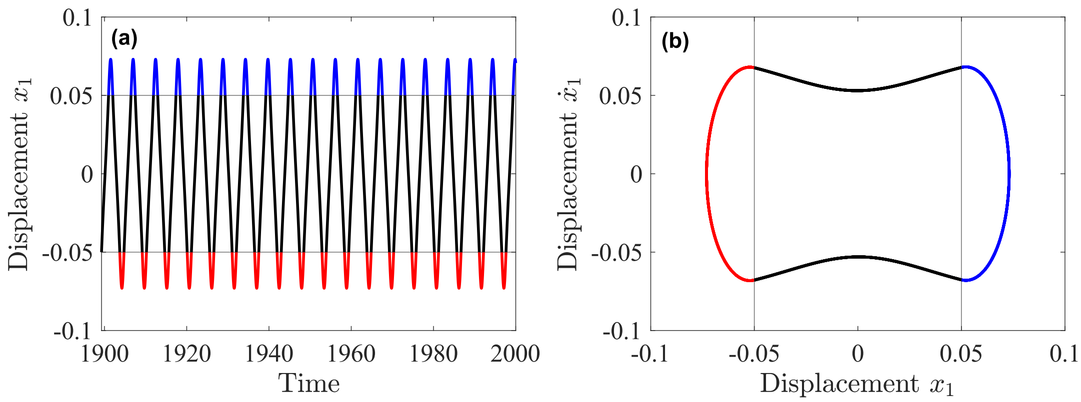

Figure 3.17: Time history (a) and associated steady-state orbit (b) at $\Omega = 1.15$ computed with MATLAB event function. The parameters of Tab 3.2 are utilised to perform the numerical analyses

in [37, 111, 126]. For each event occurrence, i.e. when the contact occurs or ends, the integration procedure is stopped, the time at which the event occurred is identified, and the associated final conditions are saved. These final conditions are then used as initial conditions for the next integration step, which accounts for a different set of equations of motion that correctly describe the new situation, e.g. the presence of a larger stiffness if the contact has occurred. To correctly represent the dynamics of the contact, Eq. 3.1 is used to define the event function, and the governing equations of motion are changed accordingly to the piecewise characteristic. An example of time history and steady-state orbit is described by Fig 3.17. The black line indicates solutions computed in the non-contact region, i.e. when the additional piecewise stiffness is not considered. The red and blue lines, instead, define solutions obtained in the presence of contact.

The comparison of the BoA is carried out using the relative and absolute tolerances, the maximum time step, and the time span, described in Tab. 3.3. Fig. 3.18 shows the BoA of the two versions of the system when the excitation frequency Ω is equal to 1.20, 1.25, 1.30, and 1.35. The BoA in the top row of Fig. 3.18 are obtained using the exact event location while the BoA in the bottom row are generated using the approximate smoothing function. Fig. 3.18 shows that the sigmoid approximation correctly represents the BoA of the considered two-DOF system with high accuracy, without introducing significant errors or distortions in the dynamics of the system and

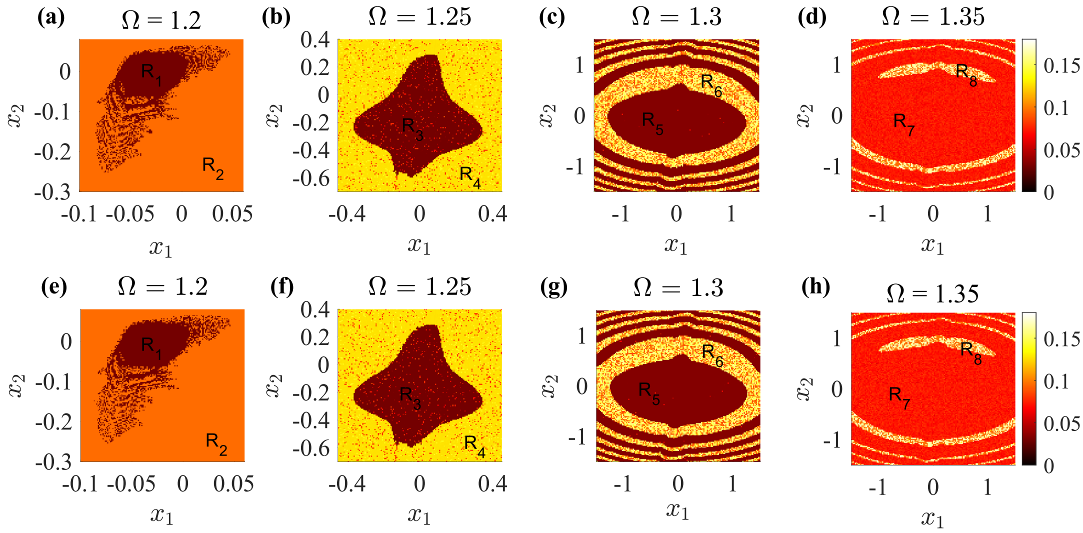

Figure 3.18: Basins of attraction of the system at Ω equal to 1.2, 1.25, 1.3 and 1.35. The colour map indicates the maximum amplitude of the first mass. The panels in the top row (a-d) show the BoA of the non-smooth version of the system while the panels in the bottom row illustrate the BoA of the smoothed version of the system. The parameters of Tab 3.2 and $\delta = 1500$ (only for the approximate version) are utilised to perform the numerical analyses [1].

Table 3.3: MATLAB options for the computation of the BoA with event function and sigmoid approximation [1].

Ω	Rel. & Abs. Tol.	Max Step	Time Span
1.20	1e-09	0.08 s	3500 s
1.25	1e-09	0.08 s	7500 s
1.30	1e-09	0.08 s	28500 s
1.35	1e-09	0.08 s	28500 s

its BoA. Across all examined excitation frequencies, the introduction of the approximation does not significantly alter the shape, boundaries, or maximum amplitude of the basins. Tab. 3.4 shows the elapsed time of a single simulation of the BoA when the sigmoid function and event location are utilised. The results show that the simulation time is significantly reduced when the smoothing approximation is utilised, with an elapsed time up to ten times shorter than the simulations with event location.

Table 3.4: Elapsed time in the numerical simulations of the first point of the BoA. For each frequency, the options prescribed in Tab. 3.3 are used [1].

Approx.	$\Omega = 1.2$	$\Omega = 1.25$	$\Omega = 1.3$	$\Omega = 1.35$
Sigmoids	0.800 s	1.652 s	6.183 s	6.364 s
Event Loc.	6.590 s	15.448 s	61.905 s	39.149 s

3.4 Summary

This chapter analysed the dynamic behaviour of a strongly nonlinear system characterised by multiple degrees of freedom and soft piecewise constraints. The system is studied using numerical continuation and numerical integration procedures, with a specific focus on investigating how smoothing approximations of piecewise characteristics affect the system dynamics. To this end, bifurcation diagrams, frequency response curves, and basins of attraction are computed for the smoothed and ideal version of the system, comparing the obtained dynamics.

Firstly, the mathematical admissibility of the proposed smoothing approximation is verified, using analytical and numerical tests. To facilitate the selection of the smoothing approximation parameter δ, a tool, named the radius of influence, is proposed. This tool aims to link the mathematical parameter δ with the distortion induced by the smoothing approximation. Then, the dynamics of the obtained nonlinear MDOF smoothed system are investigated. The numerical simulations demonstrate that the presence of a soft contact generates strong nonlinear phenomena and a rich dynamic behaviour, characterised by the presence of bifurcation of the backbone curves and period-doubling isolas. It is demonstrated that these isolas are associated with higher amplitudes of response. In addition, the bifurcation of the backbone curve generates a second branch of high-amplitude stable steady-state response. These phenomena are potentially dangerous for mechanical structures as they may lead the system to unwanted vibrations and stress levels, higher than the ones predicted by the main branch (B_1). Linear models are unable to predict similar nonlinear phenomena, and missing these dynamics might lead to a mismatch between experimental data and numerical results, especially in common industrial practice. Finally, the effect of the smoothing approximation on the dynamics response of the system is analysed: a comparison between the dynamics of the non-approximate (piecewise) and the approximate (smoothed) version of the system is carried out; by using numerical continuation techniques, the main branches B_1 and B_2, and some isolas, namely I_1 and I_3, are compared in terms of the bifurcation scenario and amplitude of the response; in addition, exploiting numerical integration schemes, the BoA of the two versions of the system are compared in terms of shape of the basins and computational effort. The results show that the smoothed version of the system is able to capture the dynamics of the non-smooth system, especially when periodic responses are considered. The main discrepancies between the non-approximate and the approximate systems are found near grazing bifurcation points, where the smoothing approximation is less accurate. No distorted or non-physical solutions are identified during the analysis, however, a systematic increase in the amplitude response of the approximate solution is encountered: this is due to the approximation error introduced by the sigmoids function and remarks the necessity of tools, like the proposed radius of influence, to control the degree of approximation introduced in such systems.

In general, the robustness, lower computational burden, and efficacy of smoothing approximations make the proposed approach very attractive, especially in industrial-related contexts where simple and robust solutions are necessary.

Chapter 4

Design of an Experimental Multi-Degree-of-Freedom Non-Smooth System

4.1 Introduction

This chapter discusses the design of the experimental test rig utilised in the project. The model consists of an MDOF mechanical system with piecewise stiffness characteristics and has two main purposes: firstly it serves as ground truth to validate the complex dynamics phenomena encountered in the numerical simulations of previous chapters and, secondly, it is used to develop novel methods/approaches to identify MDOF nonlinear systems from experimental data. In particular, the experimental activity seeks to find evidence about the presence of bifurcation of backbone curves and isolated solutions that have been encountered during the numerical investigations of Chapter 3. Specifically, the following points are discussed:

- Section 4.2, borrowing from design techniques, introduces the Product Design Specifications (PDS) document of the experimental model, highlighting the constraints and the functional requirements of the test rig. This comprises the required dynamic features as well as practical constraints such as the budget and time allocated for the design of the model and its experimentation.

- Section 4.3 discusses the design of the proposed mechanical structure, using numerical tools. Different versions of the test rig are proposed and investigated highlighting practical problems and design constraints. Along with classical tools, i.e. linear MDOF models and FEA, the usage of numerical continuation techniques is proposed to design the mechanical structure. In particular, a ROM is derived from a full FE model and it is used to design the nonlinear behaviour of the experimental system. Then, the unknown nonlinear characteristics are investigated via parametric study demonstrating that the bifurcation of backbone curves persists in many different model versions.

- Section 4.4 discusses the initial experimental tests that are carried out to check that the model behaves as expected. To this end, the model is built, assembled, and tested. Particular care is paid to the excitation conditions, which are modified to guarantee the respect of all the product design specifications. The section concludes by showing that, using the proposed adjustments, the experimental test rig guarantees the occurrence of nonlinear dynamic behaviours, fundamental to the proposed investigation.

4.2 Product Design Specifications

This section shows the product design specifications that are considered in the design of the experimental test rig. The specifications affect the model and its complexity, specifying the resources (time and budget) available for the experimental activities. In particular, the following specifications are taken into account:

1. **Research Objectives**: the experimental activities aim to investigate the dynamic behaviour of nonlinear MDOF systems with strong nonlinearities. Its primary objective is the investigation of the nonlinear phenomena identified in the previous numerical analysis. Particular attention is dedicated to obtaining evidence about the presence of isolated solutions and bifurcation of the backbone curves. The experimental data serve also to validate the numerical results previously obtained and contribute to increasing the limited experimental data on

MDOF nonlinear systems in the existing literature.

2. **Functional Requirements**: the model must respect the following functional requirements: the experimental model must have (1) multiple degrees of freedom, (2) a high degree of smooth nonlinearity, (3) the presence of non-smooth characteristics, and (4) the presence of two modes in a close range of frequencies.

3. **Nonlinear Dynamic Features**: the model has to show the presence of isolas, bifurcation of backbone curves, and modal interactions between two modes. These phenomena are not easy to identify prior to the experimental tests, therefore the model must be made adjustable so that characteristics like the piecewise stiffness and the non-contact gap can be controlled and modulated in a simple manner.

4. **Data**: the model and the experimental set-up need to be able to generate experimental data in the time and frequency domain. The experimental setup must be made so that the system can be excited in the frequency range of interest and that the post-processing of the data in the frequency domain is feasible.

5. **Practical Constraints**: The model should be compatible with the current laboratory instrumentation and tools, such as unidirectional accelerometers, electromagnetic contact shakers with specified maximum displacement and force, table dimensions, available sensors, and control units.

6. **Resources Constraints**: the experimental activities must not exceed the available resources in terms of budget and time. In particular, the time required for the design and testing (up to 6 months) is limited due to the availability of the laboratory and mechanical workshop as well as the budget for building the experimental model ($\approx$ £500).

4.3 Test Rig Design: Numerical Simulations

In this section, the design of the experimental model is introduced and discussed. To satisfy the nonlinear and functional requirements, a parallel beam configuration with mechanical motion limiting constraints (also called stoppers) is chosen. This configuration has been successfully implemented in previous experimental analyses of nonlinear impacting systems with a single degree of freedom [25, 119]. Contrarily to those studies, the proposed model considers two masses (see Fig. 4.1 and Fig. 4.5 for graphical representation of the initial versions of the system) to simulate the presence of multiple degrees of freedom in the mechanical structure and it offers the following features: (1) it allows the addition of non-smooth characteristics to the system, by adding motion limiting constraints, (2) it introduces a hardening stiffness behaviour to the system (due to the parallel beam configuration), (3) it incorporates multiple masses, generating an MDOF structure, and (4) it enables tuning two modes in a close frequency range. These properties allow the experimental model to effectively meet the functional requirements of the experimental activity as described in the PDS. The required nonlinear dynamic features like backbone curves and isolas, instead, cannot be guaranteed a priori but numerical analyses and experimental tests are necessary to identify them and prove their existence.

At the initial design stage, most of the properties are unknown and can only be estimated; this is particularly true for nonlinear properties like hardening and contact stiffness. To address this challenge, FEA and numerical continuation techniques are utilised: firstly a linear FE model of the structure is created and a ROM is obtained by comparing the dynamic response of the two models. Then, numerical continuation is used to perform parametric analyses of the system, investigating the effect of parameters on the nonlinear dynamic behaviour of the system. This process is repeated for different versions of the system until the final configuration is achieved.

4.3.1 Initial Design: Model Version 1 & 2

A finite element model is created in Ansys APDL as depicted in Fig. 4.1: the system is composed of two parallel beams, modelled with shell elements (SHELL281) and two main masses, modelled with solid elements (SOLID186). The extremities of the model are fully constrained to simulate the presence of external rigid supports. The figure shows the different components: external beams (light blue), internal beams (purple), external locking components (red), and mass blocks (blue). In order to transfer the

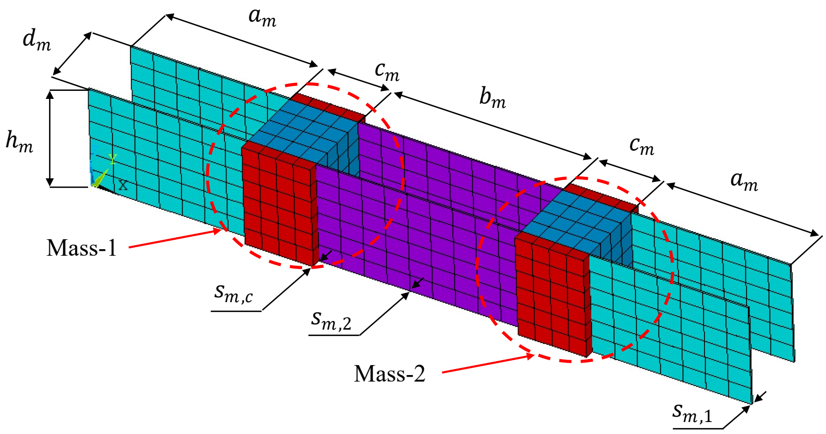

Figure 4.1: Finite element model of the two-mass system (Version 1) and main dimensions.

Table 4.1: Dimensions and material properties of the two initial versions of the FE model.

Parameter	Version 1	Version 2
Y_{steel}	210 GPa	210 GPa
ρ_{steel}	7800 kg/m^3	7800 kg/m^3
ζ	1 %	2 %
a_m	70 mm	160 mm
b_m	90 mm	250 mm
c_m	30 mm	80 mm
d_m	30 mm	80 mm
h_m	45 mm	60 mm
$s_{m,1}$	0.8 mm	1 mm
$s_{m,2}$	0.8 mm	1 mm
$s_{m,c}$	5 mm	15 mm

rotational stiffness of the beams to the solid blocks, the external locking components are modelled with shell elements and are attached to the solid element of the masses.

Linear Analysis and Reduced Order Model Identification

The system is studied in two different versions: the first one is smaller and presents a small damping ratio while the second one is larger with a larger damping ratio. In both versions, the model is entirely designed with metallic components whose dimensions and properties are reported in Tab. 4.1. The two versions of the model are obtained after initial practical considerations and three analyses are performed to evaluate its dynamic

Table 4.2: Modal and static analysis of the FE models representing the experimental test-rig (version 1 and 2).

Analysis	Version 1	Version 2
mode 1 (global)	40.8 Hz	6.2 Hz
mode 2 (global)	57.6 Hz	7.7 Hz
mode 3 (local)	543.4 Hz	87.3 Hz
next global mode	998.4 Hz	168.3 Hz
max static deflection	0.3 μm	13.3 μm

and static behaviour: static analysis, modal analysis, and harmonic analysis. The first simulation allows us to understand the static deflection of the model. The second one instead provides the natural frequencies and the modes shapes, and the third analysis consents to obtain the linear harmonic response of the system. These analyses are important to identify the correct dynamic behaviour of the experimental model: the static deflection must not be excessive while the first two natural frequencies must exist in a close range of frequencies to show strong modal interaction. In addition, modes higher than the required number of DOFs must be found at very high frequencies so that a simplified ROM can be used to capture most of the system dynamics. The results of the modal analysis are reported in Fig. 4.2 and 4.3: the first figure shows the first two modes of the two versions of the system while the second one shows the third mode and the next first global mode, i.e. the first mode after the second one that involves the motion of the entire structure. Tab 4.2 summarises the results of the modal and static analyses. Additional details about the static/dynamic analyses can be found in Appendix B.1. The static deflections of the two versions of the system are small enough to avoid significant deformation of the test rigs under gravitational loads. The first two modes affect the whole structures and are found in a close frequency range in both model versions. The third mode of the structure is represented by a local mode whose frequency is one order of magnitude larger than the second mode. This guarantees to maximise the possibility of interaction between the first two modes, i.e. the modes of interest, minimising the interferences from the higher modes. In addition, the next global mode is found at even higher frequencies for the proposed configurations. These results satisfy some of the functional and dynamic constraints of the experimental analysis and allow us to proceed to identify a reduced-order model

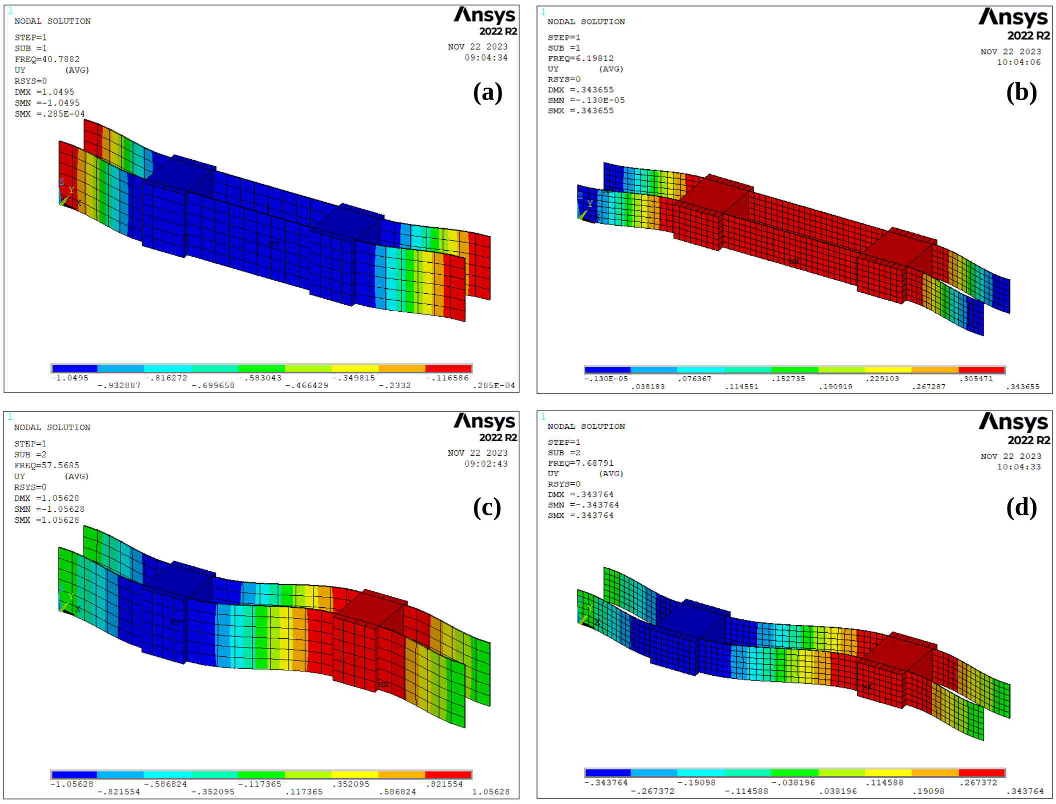

Figure 4.2: First two modes of the first (a,c) and second (b,d) version of the experimental test rig. The material properties and the dimensions of the FE models are reported in Tab. 4.1. The following natural frequencies are identified: 40.8 Hz (a), 6.2 Hz (b), 57.6 Hz (c), 7.7 Hz (d).

of the structure. A ROM is obtained by comparing the harmonic response of the FE model with the dynamics of a lumped parameter model whose equation of motion is represented by:

$$m\ddot{x}_1 + c\dot{x}_1 + kx_1 - k_d(x_2 - x_1) - c_d(\dot{x}_2 - \dot{x}_1) = Q_1 \cos(\Omega t) \tag{4.1a}$$

$$m\ddot{x}_2 + c\dot{x}_2 + kx_2 + k_d(x_2 - x_1) + c_d(\dot{x}_2 - \dot{x}_1) = Q_2 \cos(\Omega t) \tag{4.1b}$$

In matrix form, the ROM is represented by the following equation:

$$\begin{bmatrix} m & 0 \\ 0 & m \end{bmatrix} \begin{Bmatrix} \ddot{x}_1 \\ \ddot{x}_2 \end{Bmatrix} + \begin{bmatrix} c + c_d & -c_d \\ -c_d & c + c_d \end{bmatrix} \begin{Bmatrix} \dot{x}_1 \\ \dot{x}_2 \end{Bmatrix} + \begin{bmatrix} k + k_d & -k_d \\ -k_d & k + k_d \end{bmatrix} \begin{Bmatrix} x_1 \\ x_2 \end{Bmatrix} = \begin{Bmatrix} Q_1 \\ Q_2 \end{Bmatrix} \tag{4.2}$$

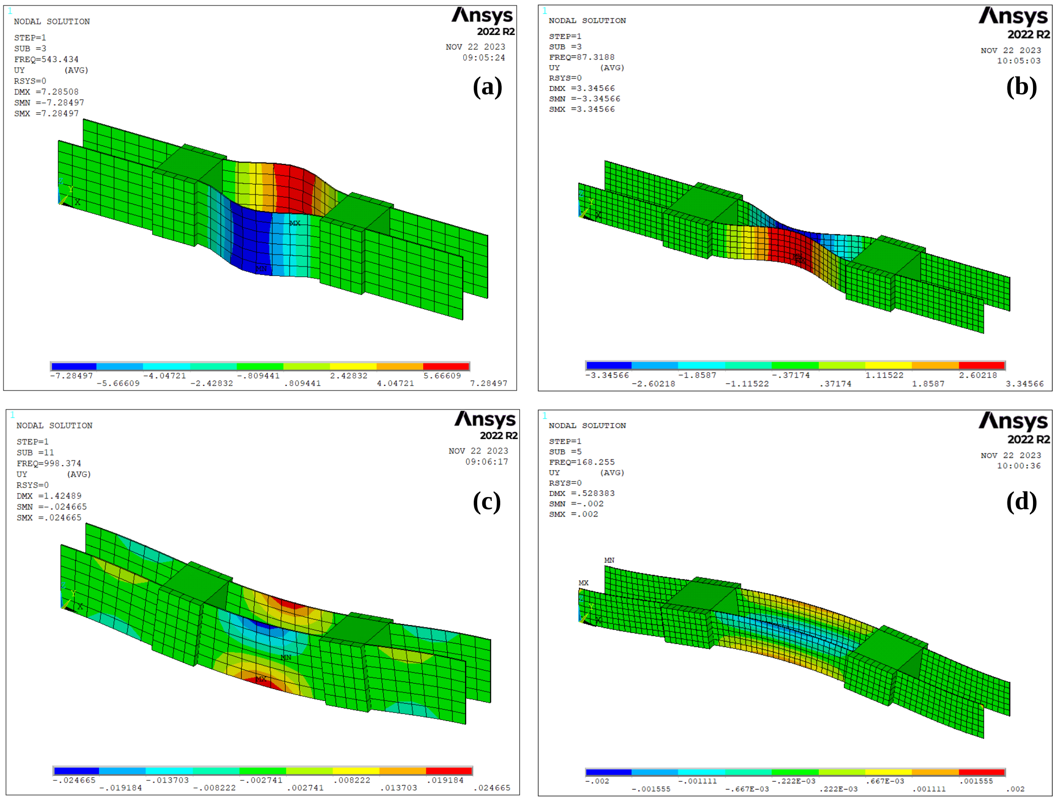

Figure 4.3: Third (local) modes of the first (a) and second (b) version of the experimental test rig, and first next global mode of the first (c) and second (d) version of the experimental test rig. The material properties and the dimensions of the FE models are reported in Tab. 4.1. The following natural frequencies are identified: 543.4 Hz (a), 87.3 Hz (b), 998.4 Hz (c), 168.3 Hz (d).

By performing the modal analysis and by applying the modal transformation to Eq. 4.2, it is possible to obtain the following relationships (see Appendix B.1 for their derivation):

$$k = \omega_{n,1}^2 m \tag{4.3a}$$

$$k_d = \frac{\omega_{n,2}^2 m - k}{2} \tag{4.3b}$$

$$c = 2\zeta_1 m \omega_{n,1} \tag{4.3c}$$

$$c_d = \frac{2\zeta_2 m \omega_{n,2} - c}{2} \tag{4.3d}$$

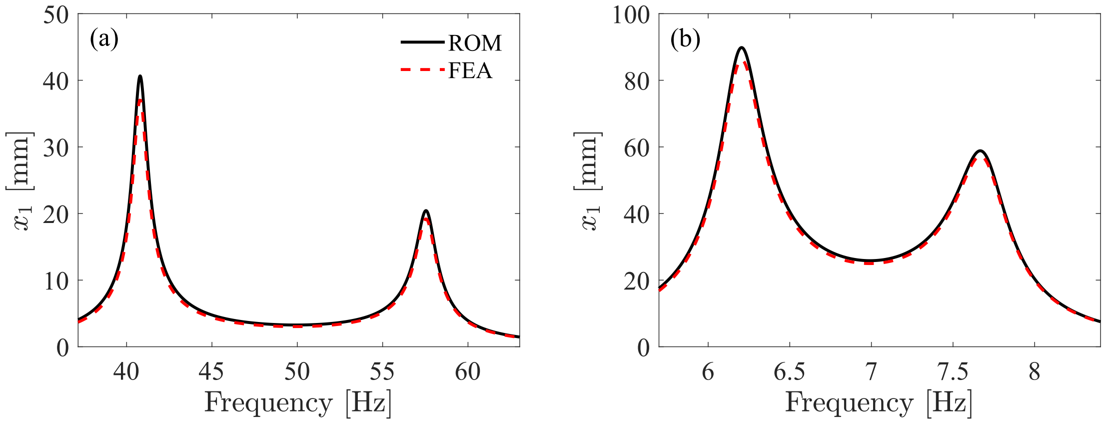

Figure 4.4: FRF computed using the ROM and the FE model for the first (a) and second (b) versions of the model. The FRFs are computed using the linear parameters reported in Tab. 4.3 for the ROM and the material properties and dimensions reported in Tab. 4.1 for the FE models. Forcing amplitudes Q_1 and Q_2 are set equal, respectively, to 0 N and 45 N for all the models.

Table 4.3: Parameters of the ROMs representing the FE models. The parameters are obtained using information about the geometry, the material of the structure, and Eq. 4.3 (see Appendix B.1 for more details).

Parameter	Version 1	Version 2
m	0.4212 Kg	4.1184 Kg
k	2.7664×10^4 N/m	6.2461×10^3 N/m
c	2.1589 Ns/m	6.4154 Ns/m
k_d	1.3722×10^4 N/m	1.6817×10^3 N/m
c_d	0.4441 Ns/m	0.7710 Ns/m

where ω_n is the natural frequency and ζ is the damping ratio. These relationships are exploited to compute the numerical value of the equivalent parameters of the reduced-order models. In particular, the equivalent mass m of the two blocks can be calculated by using the volume of the masses and the density of the material utilised (see Appendix B.1) while the stiffness and damping parameters are computed with Eq. 4.3 using the natural frequencies and the damping ratio of the FE model. The final parameters of the ROMs are reported in Tab. 4.3 and they are used to compute the dynamic response of the ROM under harmonic excitation. The obtained FRFs are then compared against the response of the FE models: the results for the two versions of the system are reported in Fig. 4.4 in terms of the amplitude of the first mass. The ROMs are shown to be in good agreement with the full FE model, confirming the capability

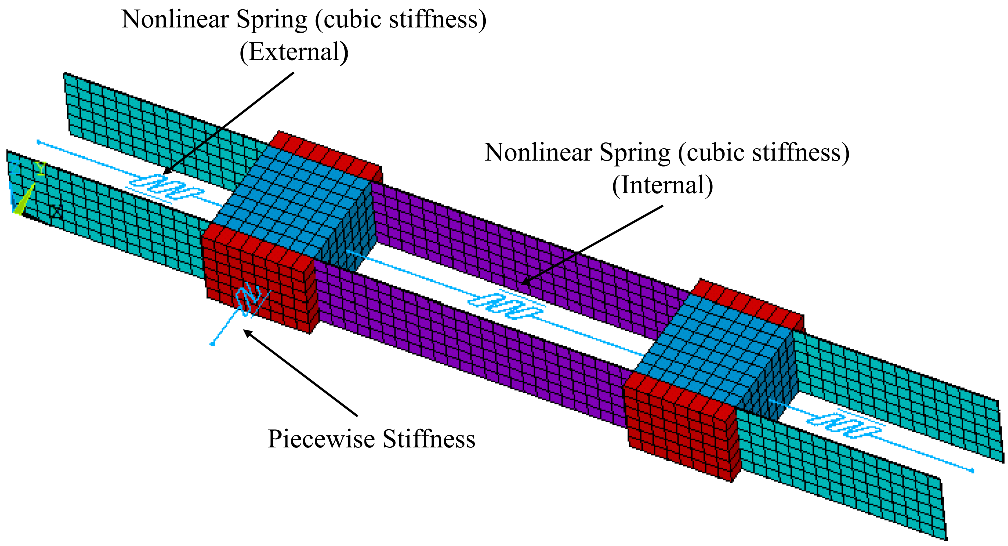

Figure 4.5: Experimental model (Version 2) with nonlinear elements.

of a reduced model to correctly predict the linear dynamic behaviour of the considered system.

Nonlinear Reduced Order Models and Parametric Analysis

The previous analyses confirmed the capability of the equivalent ROM to predict the linear dynamics of the FE model. Nonetheless, the ability of the ROM to capture the nonlinear dynamic behaviour of the full FE model remains unconfirmed at this stage. To this end, nonlinear analyses are performed and the dynamics of the ROM and the FE models are compared. For the sake of simplicity, the second version of the system is chosen to perform nonlinear analyses. Firstly the FE model is slightly modified to account for the presence of nonlinear characteristics which are simulated by adding nonlinear elements as shown in Fig. 4.5. Specifically, COMBIN39 elements are added: they consent to add lumped spring/damper nonlinear elements between two nodes of the model. In this case, cubic stiffness elements acting in the Y direction are placed between the masses and the ground, which represent the supports. Then a piecewise stiffness is applied between the centre of the first mass and the ground to simulate the presence of a contact. Consistently, the ROM is updated by adding cubic stiffness and piecewise stiffness terms in the equation of motion which results in the following

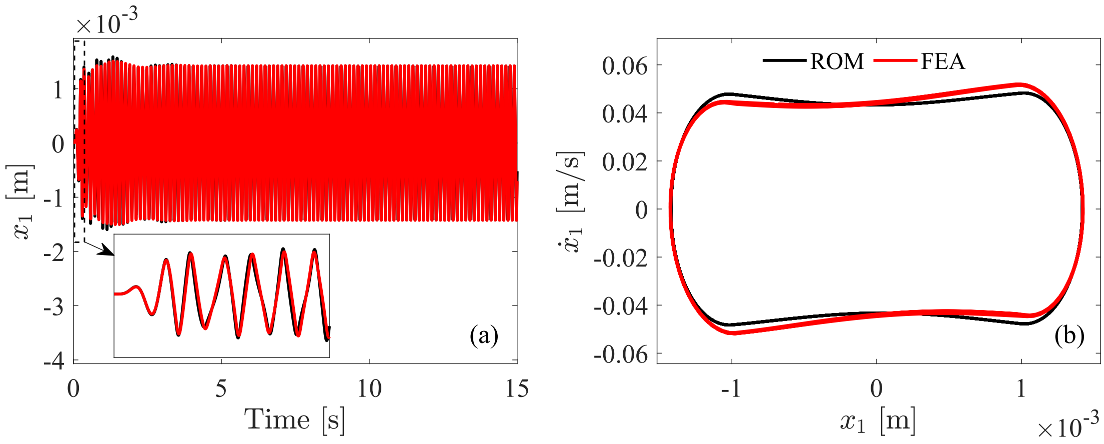

Figure 4.6: Nonlinear response of the model (Version 2) under harmonic loading using a full finite element (FEA) and a reduced order model (ROM). Time histories (a) and steady-state orbits (b) of the first mass are shown. The dynamic responses are computed using the FE model of Fig. 4.5 and the ROM of Eq. 4.4 with the following parameters: $Q_1 = 0$ N, $Q_2 = 4$ N, $\mu = 3e7$ N/m^3 (internal cubic stiffness), $\mu_d = 1e7$ N/m^3 (external cubic stiffness), $k_p = 56400$ N/m (piecewise stiffness), $a = 1$ mm (non-contact gap), and $\Omega = 7$ Hz (frequency of excitation). The remaining linear parameters utilised in the analysis are reported in Tab. 4.3 (model Version 2) for the ROM and in Tab. 4.1 (model Version 2) for the FE model.

expression:

$$m\ddot{x}_1 + c\dot{x}_1 + kx_1 + \mu x_1^3 - k_d(x_2 - x_1) - c_d(\dot{x}_2 - \dot{x}_1) - \mu_d(x_2 - x_1)^3 + F_p = Q_1\cos(\Omega t) \tag{4.4a}$$

$$m\ddot{x}_2 + c\dot{x}_2 + kx_2 + \mu x_2^3 + k_d(x_2 - x_1) + c_d(\dot{x}_2 - \dot{x}_1) + \mu_d(x_2 - x_1)^3 = Q_2\cos(\Omega t) \tag{4.4b}$$

Eq. 4.4 represents the equation of motion of the two-mass system discussed in Chapter 3, specifically represented by Eq. 3.3, where F_p denotes the restoring force of a piecewise stiffness element. Direct numerical integration is used to compute the dynamic response of the FE model and the ROM. To this end, the piecewise restoring force is approximated using Eq. 3.4 and the following parameters are considered: $Q_2 = 4$ N, $\mu = 3e7$ N/m^3, $\mu_d = 1e7$ N/m^3, $k_p = 56400$ N/m, and $a = 1$ mm or $a = 0.4$ mm. The results are reported in Fig. 4.6 and 4.7: the first figure shows the transient and steady-state dynamic behaviour of the system when contact occurs. The simulations are started from the resting position, i.e. with initial conditions equal to $x_1 = x_2 = \dot{x}_1 = \dot{x}_2 = 0$, using an excitation frequency $\Omega = 7$ Hz and a free-play gap $a = 1$ mm. The obtained dynamic behaviour corresponds to a period-1 response (PO_1

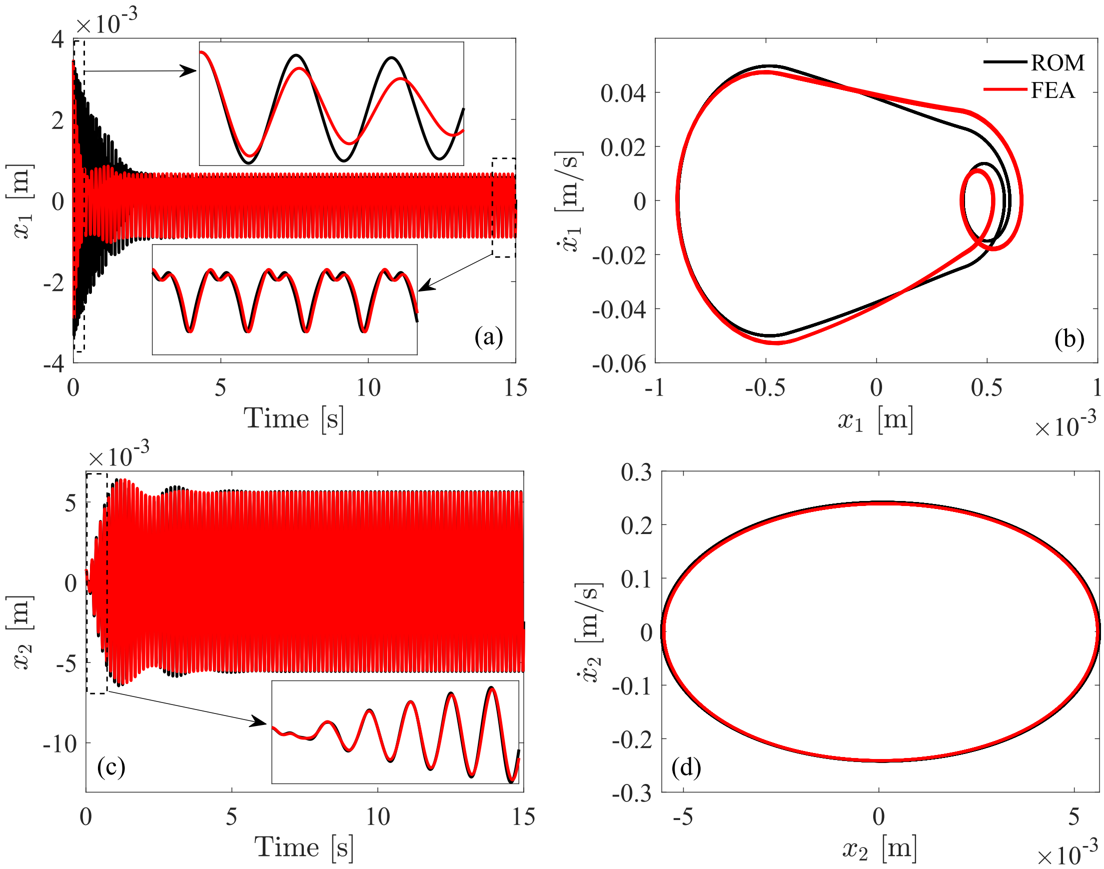

Figure 4.7: Nonlinear responses of the model (version 2) with full (FEA) and reduced (ROM) model. Time histories (a,c) and steady-state orbits (b,d) of the masses are shown. The dynamic responses are computed using the FE model of Fig. 4.5 and the ROM of Eq. 4.4 with the following parameters: $Q_1 = 0$ N, $Q_2 = 4$ N, $\mu = 3e7$ N/m^3 , $\mu_d = 1e7$ N/m^3, $k_p = 56400$ N/m, $a = 0.4$ mm, and $\Omega = 7$ Hz. The remaining linear parameters are reported in Tab. 4.3 and Tab. 4.1 (model version 2).

of Fig. 3.10) that is generated after the first grazing bifurcation, as demonstrated in the analysis of Chapter 3. The second figure instead, shows the transient and steady-state behaviour when contact occurs and when $\Omega = 7$ Hz, $a = 0.4$ mm, and initial conditions equal to $x_1 = 3.44$ mm, $x_2 = 0.73$ mm and $\dot{x}_1 = \dot{x}_2 = 0$ are imposed. The resulting steady-state dynamics (Fig 4.7(b)) is very similar to the orbit (PO_3 of Fig. 3.10) which belongs to a period-1 isola. The figures demonstrate that the dynamic response of the ROM is in good agreement with the dynamics of the full FE model both in the transient and in the steady state condition. It is also demonstrated that the ROM can find the same attractors of the FE model when initial conditions are imposed, confirming that

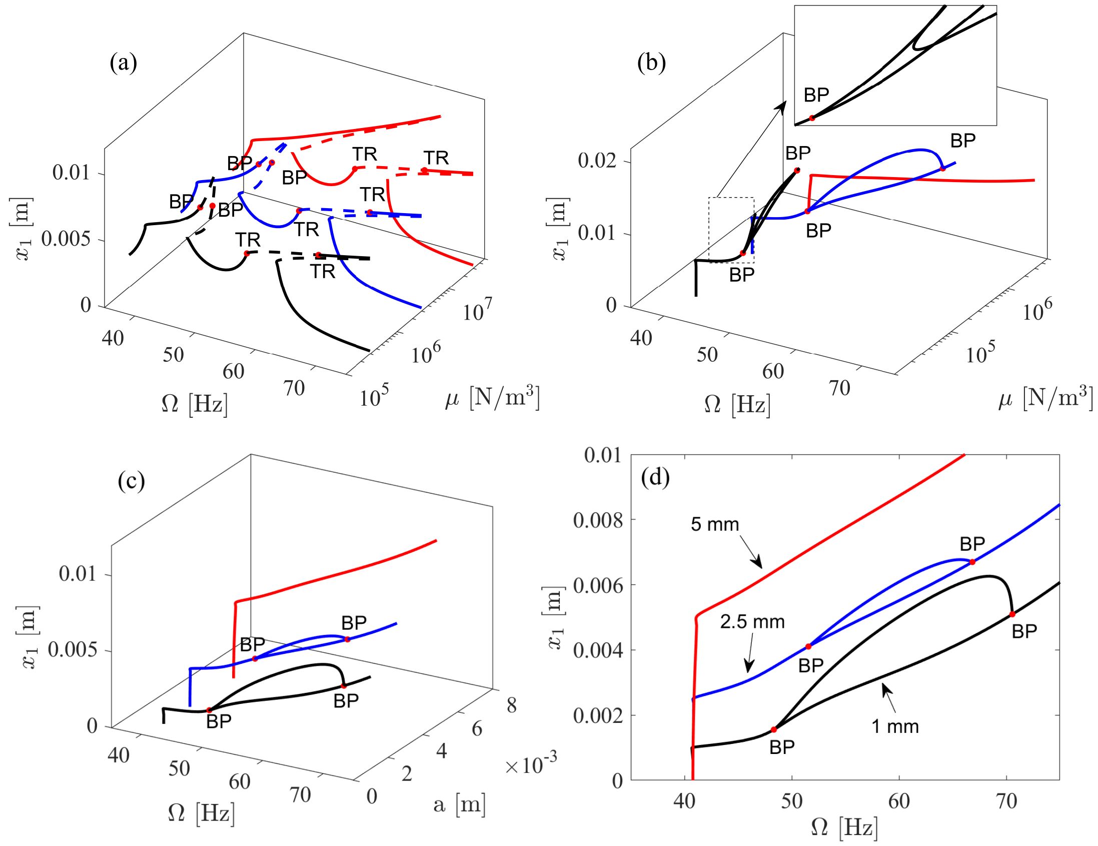

Figure 4.8: Numerical continuation of the ROM (Version 1) considering different cubic nonlinear stiffness μ and μ_d (a,b) and different non-contact gaps a (c,d). Linear parameters are reported in Tab. 4.3 while the following nonlinear parameters and amplitudes of excitation (where applicable) are considered: $a = \{0.005, 0.0025, 0.001\}$ m, $k_p = 270000$ N/m, $\mu = \{3e5, 3e6, 3e7\}$ N/m^3, $\mu_d = \{1e5, 1e6, 1e7\}$ N/m^3, $Q_1 = 0$ N, and $Q_2 = 45$ N. The parameter δ is selected as follows: $\delta = 15000$ for $a = 5$ mm, $\delta = 30000$ for $a = 2.5$ mm, and $\delta = 75000$ for $a = 1$ mm.

the considered ROM is capable of correctly predicting the nonlinear dynamics of the two-mass system.

The nonlinear ROM of Eq. 4.4 is now utilised to perform the numerical continuation of stable solutions. For the sake of simplicity, only the main branch (B_1) is continued. In addition, the backbone curves of the system are computed to provide additional details to the analysis. To facilitate the analysis, the numerical continuation of the non-smooth system is performed with the sigmoid regularisation (Eq. 3.3): to this end, the radius of influence is used to keep constant (or smaller) the distortion error to 3.5

%. Firstly the ROM associated with the first version of the model is analysed: since it is not known in which conditions the bifurcation of the backbone curve occurs, a parametric study is performed. Different values of the cubic stiffness (μ and μ_d) are utilised along with different non-contact gaps (a). The stiffness of the impact springs (i.e. the piecewise stiffness k_p) is obtained from commercial websites. The results are reported in Fig. 4.8: panels (a) and (b) describe the variation of main branch under harmonic loading and the associated backbone curves of the first mode for three cubic stiffness pairs, namely: $\mu = 3 \times 10^5$ and $\mu_d = 1 \times 10^5$ (black line), $\mu = 3 \times 10^6$ and $\mu_d = 1 \times 10^6$ (blue line), $\mu = 3 \times 10^7$ and $\mu_d = 1 \times 10^7$ (red line). The following nonlinear characteristics and amplitude of excitation are also considered: $a = 0.005$ m, $k_p = 270000$ N/m, $Q_1 = 0$ N, and $Q_2 = 45$ N (where applicable). To guarantee a distortion error of 3.5 %, the following parameter is utilised: $\delta = 15000$. The remaining properties of the ROM are obtained from Tab. 4.3 (Version 1). The the first two panels show that the nonlinear cubic characteristic influences the dynamic behaviour of the system: in particular, it is proven that when μ and μ_d are small enough, a modal interaction in the system occurs, inducing the generation of a bifurcation in the first backbone curve, as demonstrated by Fig. 4.8(b). For $\mu = 3 \times 10^6$ and $\mu_d = 1 \times 10^6$ the backbone curve associated with the first mode shows the same bifurcation previously encountered in the numerical analyses of Chapter 3. When the nonlinear parameters are set equal to $\mu = 3 \times 10^5$ and $\mu_d = 1 \times 10^5$ the backbone shows an even more complicated behaviour, as demonstrated by the detail of Fig. 4.8(b). Finally, when the cubic stiffness is large enough, i.e. when $\mu = 3 \times 10^7$ and $\mu_d = 1 \times 10^7$, no bifurcation of the backbone curve is found. It is worth noting that the generation of bifurcation on the backbone induced a change in the stability in the first peak of the main branch, as shown by Fig. 4.8(a). This is in agreement with the results obtained in the previous numerical analyses of Chapter 3 and provides a simple way to understand when this phenomenon occurs.

Since the cubic stiffness is not easily controllable in an experimental setup, the properties of the non-smooth nonlinearities are varied to understand if it is possible to obtain the bifurcation of the backbone for the worst-case scenario, i.e when $\mu = 3 \times 10^7$

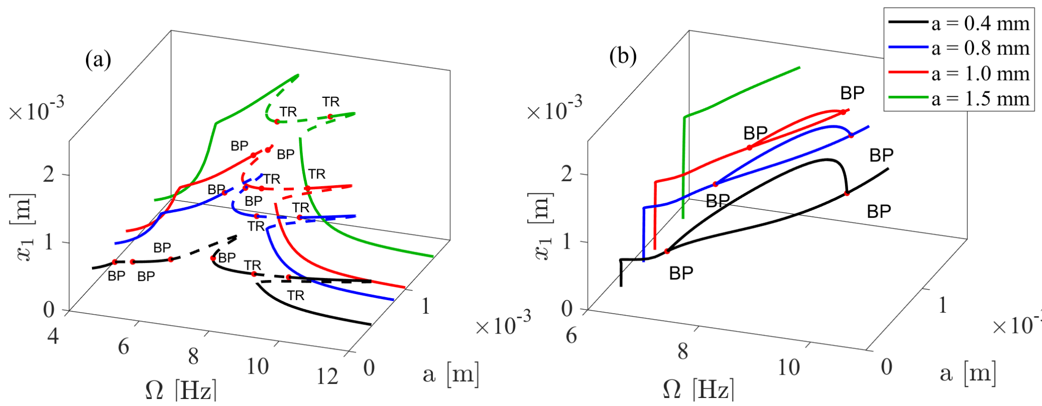

Figure 4.9: Numerical continuation of the ROM (Version 2) considering different non-contact gaps a. Forced responses (a) and backbone curves (b) are shown. Linear parameters are reported in Tab. 4.3 while the following nonlinear parameters and amplitudes of excitation (where applicable) are considered: $k_p = 56400$ N/m, $\mu = 3e7$ N/m^3, $\mu_d = 1e7$ N/m^3, $\delta = 190000$, $a = \{0.0004, 0.0008, 0.001, 0.0015\}$ m, $Q_1 = 0$ N, and $Q_2 = 4$ N.

and $\mu_d = 1 \times 10^7$. To this end, the following non-contact gaps are used: $a = 0.005$ m (red line), $a = 0.0025$ m (blue line), and $a = 0.001$ m (black line). Also in this case, to guarantee a distortion error of 3.5 %, the following approximation parameters are utilised: $\delta = 15000$ for $a = 5$ mm, $\delta = 30000$ for $a = 2.5$ mm, and $\delta = 75000$ for $a = 1$ mm. The results of the numerical continuation are shown in Fig. 4.8 (c,d): the panels show the continuation of the backbone curves of the first mode from two perspectives (3D and 2D representations). The analysis shows that by reducing the non-contact gap, the influence of the non-smooth characteristic on the dynamic response of the system becomes prevalent and leads to a bifurcating branch in the first backbone. More importantly, the analysis demonstrates that is possible to control the bifurcation of the backbone by appropriately changing the non-smooth characteristic. This is particularly important for obtaining the desired nonlinear dynamics behaviour (i.e. the bifurcation of the backbone curve) in the experimental test rig, where only certain parameters, such as the non-contact gaps, can be easily modified.

A similar parametric analysis is performed for the second version of the model. The parameters of Tab. 4.3 are used to perform the analysis along with: $k_p = 56400$ N/m, $Q_1 = 0$ N, $Q_2 = 4$ N, $\mu = 3 \times 10^7$, $\mu_d = 1 \times 10^7$, $\delta = 190000$. Different non-contact gaps

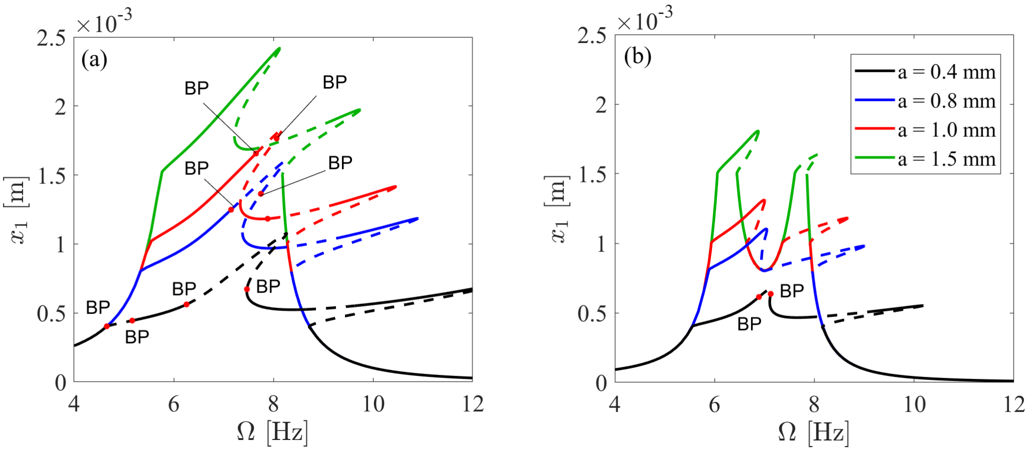

Figure 4.10: Numerical continuation of the ROM (Version 2) considering different non-contact gaps $a = \{0.0004, 0.0008, 0.001, 0.0015\}$ m and two levels of excitation amplitude: $Q_2 = 4$ N (a) and $Q_2 = 1.4$ N (b). Linear parameters are reported in Tab. 4.3 while the following nonlinear parameters and amplitudes of excitation are considered: $k_p = 56400$ N/m, $\mu = 3e7$ N/m^3, $\mu_d = 1e7$ N/m^3, $\delta = 190000$, and $Q_1 = 0$ N.

are used, namely $a = 0.4$ mm, $a = 0.8$ mm, $a = 1.0$ mm, and $a = 1.5$ mm. The results are reported in Fig. 4.9: again, reducing the non-contact gap induces the backbone of the first mode to generate a bifurcation and this results in the destabilisation of the first peak of the forced response. To investigate the effect of the bifurcation on the forced response, the system is excited with another level of excitation ($Q_2 = 1.4$ N) keeping unchanged the other parameters. The results are shown in Fig. 4.10. The figure shows that for $Q_2 = 4$N (Fig. 4.10(a)) bifurcation points are present on the first peak of the forced response only when the bifurcation of the backbone exists. Nonetheless, if the excitation amplitude is reduced to $Q_2 = 1.4$ N (Fig. 4.10(b)), the bifurcation points disappear. Only when $a = 0.4$ mm, BP points persist on the forced response of the system. This numerical analysis demonstrates that two conditions must be met to obtain the bifurcation of the main branch in the forced response: firstly the system must show a bifurcation of backbone at a certain amplitude of response, and second, the excitation must be large enough to reach the amplitude threshold. Finally, it is worth noticing that Neimark-Sacker bifurcation appears on the second peak in all the considered cases when contact occurs (not reported in Fig. 4.10).

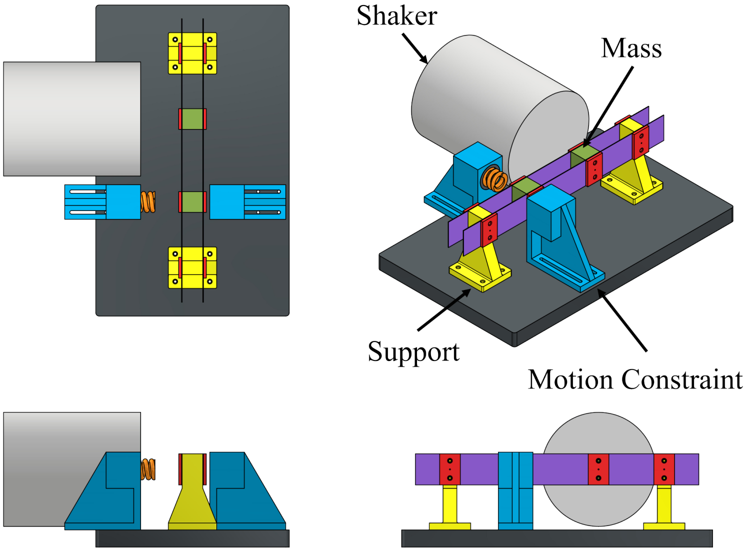

Figure 4.11: CAD assembly representing the designed model (Version 1).

Final Design and CAD Assembly

The numerical analyses of the two versions of the system provided satisfying results: the FEA and linear analysis of the ROMs proved that the functional requirements of the experimental model are satisfied in the proposed configurations. In addition, the nonlinear analyses demonstrated that the required nonlinear dynamics features can be obtained under certain parameter conditions. Specifically, it was shown that by reducing the non-contact gap, the bifurcation of the backbone curve occurs even for high values of cubic stiffness. At this point, a detailed CAD of the model is used to understand if practical requirements, like space, are satisfied and if the assembling of the system is feasible. Specifically, the dimensions of the supports, shaker, table, and motion limiting constraints are considered and their compatibility with the selected designed version is analysed. The CAD models for the two versions of the system are reported in Fig. 4.11 and 4.12. The motion limiting constraints are modelled with supports and impact springs and they are adjustable in terms of housed spring and distance from the mass. This allows for control of the non-contact gap and the stiffness of the piecewise characteristic. The masses are instead placed at a predefined distance,

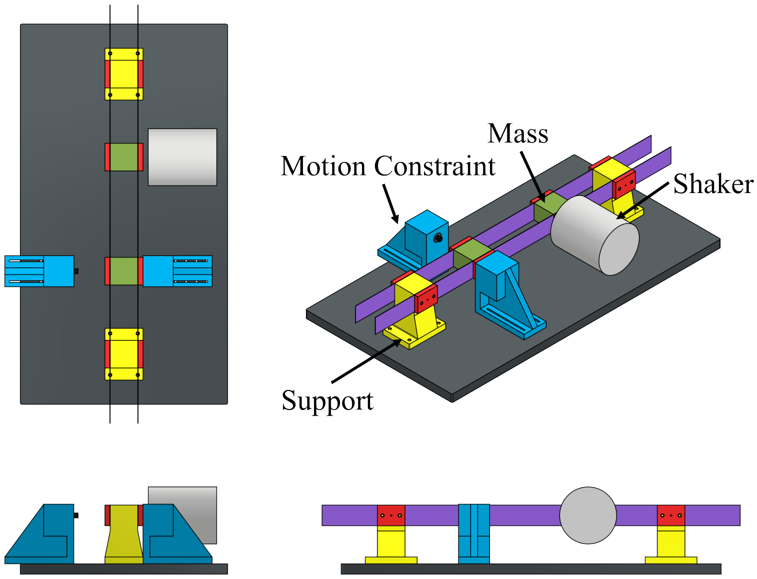

Figure 4.12: CAD assembly representing the designed model (Version 2).

which can be set with different holes in the parallel beams. The CAD demonstrates that practical requirements in terms of space and occupancy of the model are satisfied, thus confirming that the model is suitable for the experimental analysis.

4.3.2 Initial Design: Model Version 3

Although the proposed designs (Version 1 and Version 2 of the model) satisfy the product specification in terms of research objective, data format, functional requirements, nonlinear dynamics features, and practical constraints they are not compatible with the available budget and time constraints. Therefore, to reduce the time and the cost of manufacturing, the presence of metallic components is reduced as much as possible and, where possible, 3D-printed components are used. Two metallic stainless steel rulers are used as parallel support beams. They provide (1) low damping, (2) the desired stiffness and hardening effect in the parallel configurations, and (3) they are particularly helpful in accurately measuring the distance between the masses and the supports. After a preliminary design, a new configuration (version 3) is achieved, whose dimensions are reported in Tab. 4.4. The dimensions of the model are similar to the ones of the

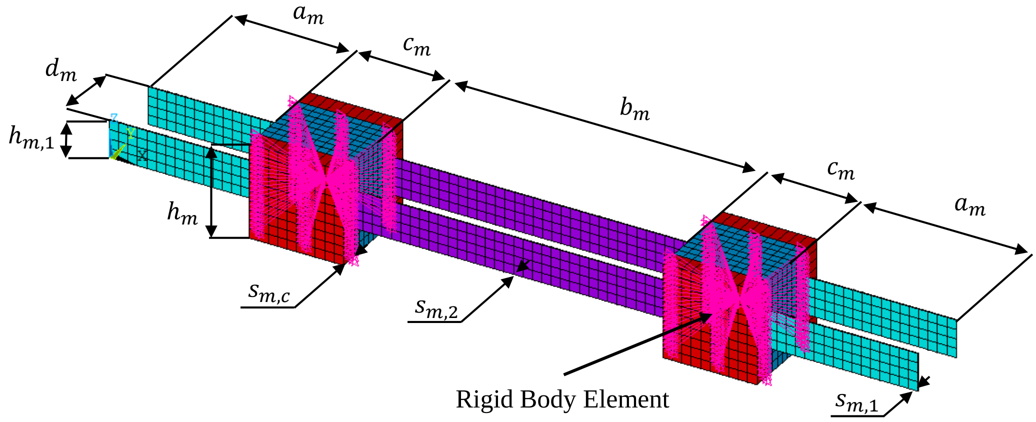

Figure 4.13: FE model representing the version 3 of the designed system.

Table 4.4: Dimensions and material properties for third version of the experimental model.

Parameter	Version 3
Y_{steel}	210.0 GPa
Y_{PLA}	3.3 GPa
ρ_{steel}	7800 kg/m^3
ρ_{PLA}	1240 kg/m^3
ζ	1 %
a_m	80 mm
b_m	170 mm
c_m	50 mm
d_m	35 mm
h_m	20 mm
$h_{m,1}$	50 mm
$s_{m,1}$	0.5 mm
$s_{m,2}$	0.5 mm
$s_{m,c}$	10 mm

previous designs but now two different materials, i.e. PLA (Polylactic acid) and steel, are used to build the structure. Using the scheme previously outlined, numerical simulations and comparisons between FE and reduced order models are performed once again. To this end, an FE model representing the third version of the model is created, as shown by Fig. 4.13. In the new configuration, all the components of the system, except the beams, are made in PLA, leading to a substantial mass reduction in the

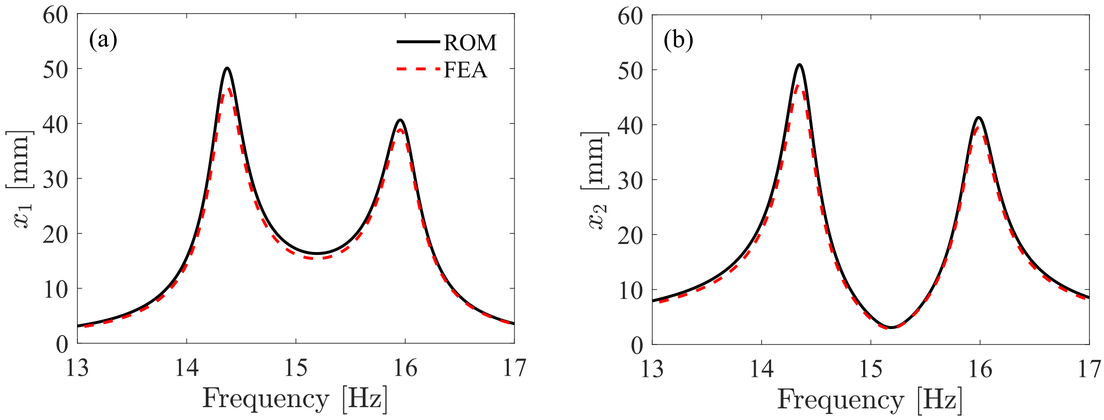

Figure 4.14: Frequency response of the model (Version 3) under harmonic excitation. The linear FRFs are reported in terms amplitude of the first (a) and second (b) mass. The FRFs are computed using the linear parameters and the forcing amplitudes reported in Tab. 4.5 for the ROM and the material properties and dimensions reported in Tab. 4.4 for the FE model.

Table 4.5: Parameters of the ROM for linear and nonlinear analyses (Version 3)

Parameter	Version 3
m	0.244 87 Kg
k	1.9934×10^3 N/m
c	0.4419 Ns/m
k_d	2.3651×10^2 N/m
c_d	0.0248 Ns/m
Q_1	0.0 N
Q_2	4.0 N

two blocks that represent the two masses of the system. This, in combination with the presence of metallic support beams, increases the first two natural frequencies of the system by orders of magnitude, leading to frequency ranges completely different from the previous analyses which might be difficult to manage experimentally. To avoid this problem, the model implements metallic components inside the two blocks, i.e. inside the first and second mass of the system, for a total mass of 159.6 g each. To model the presence of metallic components inside the two blocks, point masses are added to the FE model using the element MASS21: rigid body elements (CERIG) are then used to connect the nodes of the solid elements (representing the PLA components) with the point mass. The PLA components are printed using a 50% infill to reduce the amount of material consumed and to speed up the printing process. To account for the 50%

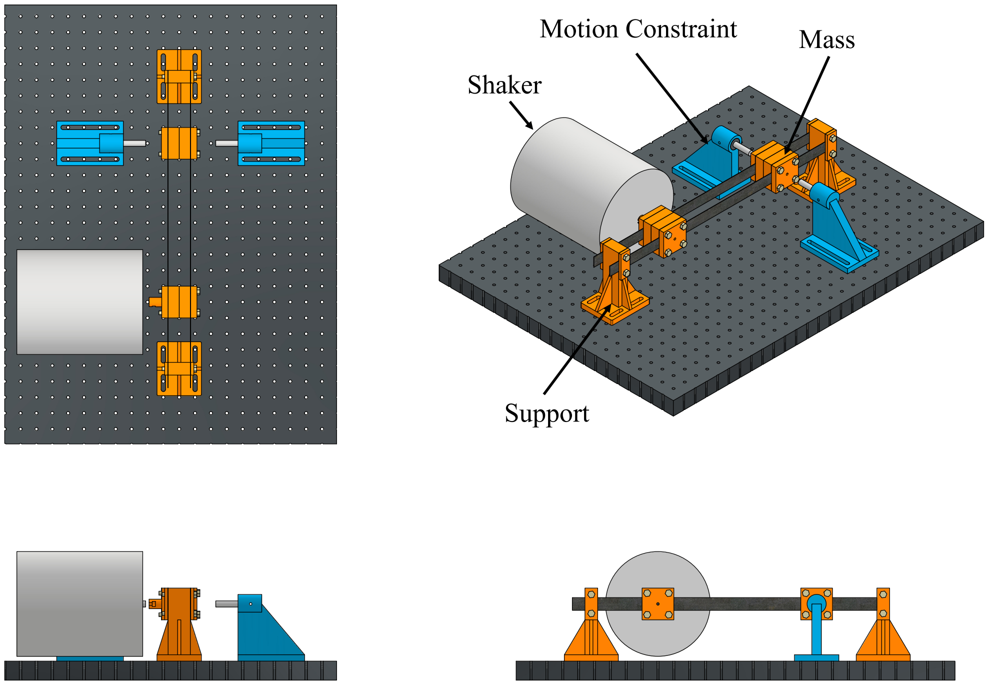

Figure 4.15: CAD assembly representing the designed model (Version 3).

infill, the density of the PLA is reduced by a factor of 2 in the FE model.

Linear Analysis and Reduced Order Model Identification

FE simulations under the linear approximation are performed. Static and modal analyses are carried out to check that the functional requirements of the experimental test rig are satisfied: the results show that the deflection under the weight is limited and the first two natural frequencies are found in a close range of frequencies, precisely at 14.4 Hz and 16.0 Hz (see Appendix B.1). The modal analysis demonstrates that the higher modes are located at frequencies about one order of magnitude higher than the second natural frequency, satisfying the requirement of minimal interaction between the first two modes and the higher modes. The same procedure used before to obtain a ROM is now implemented: the first two natural frequencies of the system, the imposed damping ratio, and the mass of the two blocks are used to identify a linear ROM and its parameters (reported in Tab. 4.5). Once again, the FRFs obtained with FEA and the associated ROM are remarkably similar, as shown in Fig. 4.14. This demonstrates

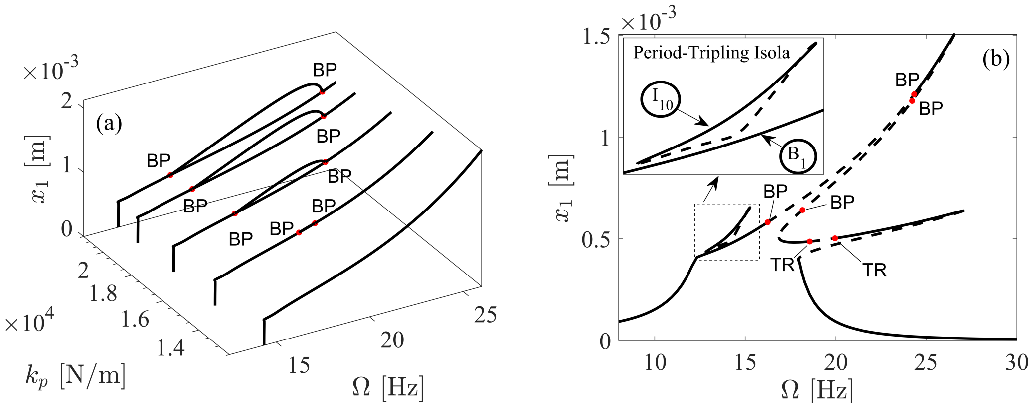

Figure 4.16: Numerical continuation of the ROM, representing model Version 3: backbone curves with different piecewise stiffness k_p (a) and forced response for $k_p = 2e4$ N/m (b). Linear parameters are reported in Tab. 4.5 while the following nonlinear parameters and amplitudes of excitation (where applicable) are considered: $a = 0.4$ mm, $k_p = \{1.25e4, 1.50e4, 1.75e4, 2.00e4, 2.15e4\}$ N/m, $\mu = 3e7$ N/m^3, $\mu_d = 1e7$ N/m^3, $\delta = 190000$, $Q_1 = 0$ N, and $Q_2 = 0.4$ N.

the suitability of the identified ROM in representing the dynamics of the system under the hypothesis of linear behaviour.

Nonlinear Linear Analysis and Final CAD Assembly

The CAD assembly of the third version of the test rig is shown in Fig. 4.15: as demonstrated the model satisfies the practical constraints, allowing the presence of the shaker and the adjustable motion limiting constraints. It is worth noticing that the components representing the masses are re-designed: now their position can be adjusted along the parallel beams by simply shifting and clamping the squared blocks, allowing for the creation of different configurations of the system.

Finally, nonlinear analyses are performed via numerical continuation to understand if the proposed configuration possesses the required nonlinear features, i.e. the bifurcation of the backbone curves and the presence of isolas in the forced response. The numerical continuation analyses are performed using the identified parameters of Tab. 4.5 and the following ones: $Q_1 = 0$ N, $Q_2 = 0.4$ N, $\mu = 3e7$ N/m^3, $\mu_d = 1e7$ N/m^3, $k_p = 2e4$ N/m, and $a = 0.4$ mm. Once again the non-smooth characteristic is approximated with a sigmoid function, and the distortion error is limited to 3.5 % of the non-contact gap. This results into a parameter $\delta = 190000$. The backbone curves are now computed by varying the stiffness of the piecewise characteristic rather than the non-contact gap. In particular, the backbones curves of the first mode are computed using k_p equal to 1.25e4, 1.50e4, 1.75e4, 2.00e4, and 2.15e4 N/m. Fig. 4.16(a) shows the results of the parametric study: the figure demonstrates that the backbone curve generates a bifurcation branch when the piecewise stiffness k_p is large enough. In the specific case, $k_p = 1.50e4$ N/m is sufficient to generate the bifurcation of the backbone curve. These results, along with the previous nonlinear analyses of Fig. 4.8 and Fig. 4.9, demonstrate that the bifurcation of the backbone curve can be induced by either increasing the piecewise stiffness or reducing the non-contact gap. The presence of period-doubling isolas in the frequency response of the system, instead, is demonstrated by computing the forced response of the system. To this end k_p is set equal to 2e4 N/m and the FRC is computed. The results are reported in Fig. 4.16(b): the figure shows the presence of a period-tripling isola I_{10} completely detached from the main branch B_1. The isola is found after the first grazing bifurcation (around 13 Hz) and produces large amplitude steady-state responses that persist for about 2 Hz. In this case, the force is large enough to trigger the bifurcation of the main branch B_1 which becomes unstable.

From a preliminary design point of view, the proposed model (Version 3) has demonstrated to satisfy the product design specification in terms of research objective, functional requirements, nonlinear dynamic features, and data format. Practical constraints are also satisfied as the experimental model can be analysed using the available sensors and instruments, i.e. three unidirectional accelerometers, a single-point laser vibrometer, and a dynamic load cell. In addition, the 3D CAD has demonstrated that the proposed configuration respects the volume constraints imposed by the dimension of the table and the shaker. Finally, the usage of fast prototyping techniques like additive manufacturing and cost-effective materials like PLA, allows the proposed model to satisfy the resource constraints in terms of budget and time.

4.4 Test Rig Design: Experimental Adjustments

The model obtained from the preliminary design (model Version 3) is manufactured and assembled in the *Space and Exploration Technology Laboratory* of the University of Glasgow. Although the numerical model shows the required dynamic features, practical experimental tests and adjustments are necessary to prove their existence in an experimental setup. To this end, the dynamic behaviour of the test rig is investigated experimentally by performing frequency sweeps. One of the main problems encountered during these tests is associated with the excitation mode. During the numerical analyses, the system is excited by a perfect sinusoidal force that is applied to one mass of the system. This excitation mode is particularly difficult to replicate experimentally using the available shakers, as they necessitate direct connection with the structure. This connection, indeed, influences the dynamics of the test rig, limiting the maximum amplitude of response of the excited mass and reducing the nonlinear dynamic behaviour of the system. Therefore, different excitation conditions are experimentally tested to prove the presence of the required dynamic features, including a sufficiently large amplitude of response on both masses, capable of triggering nonlinear dynamic phenomena like jumps.

4.4.1 Directly Forced System

As an initial experimental trial, the model is manufactured and excited following the product design specifications. The components are manufactured and engineered so that these specifications are respected. Fig. 4.17 shows the assembled two-mass model in two configurations: fixed shaker and suspended shaker. The model shows the presence of the two masses, the motion limiting constraints , and the adjustable supports. The motion limiting constraints are designed so that they can be adjusted to reproduce different piecewise characteristics: the piecewise stiffness can be changed by using different contact springs and symmetrical and unsymmetrical gaps can be achieved by adjusting the position of the motion limiting constraints . The blocks, instead, can regulate their masses by housing internally metallic components (see Fig. B.3). In ad-

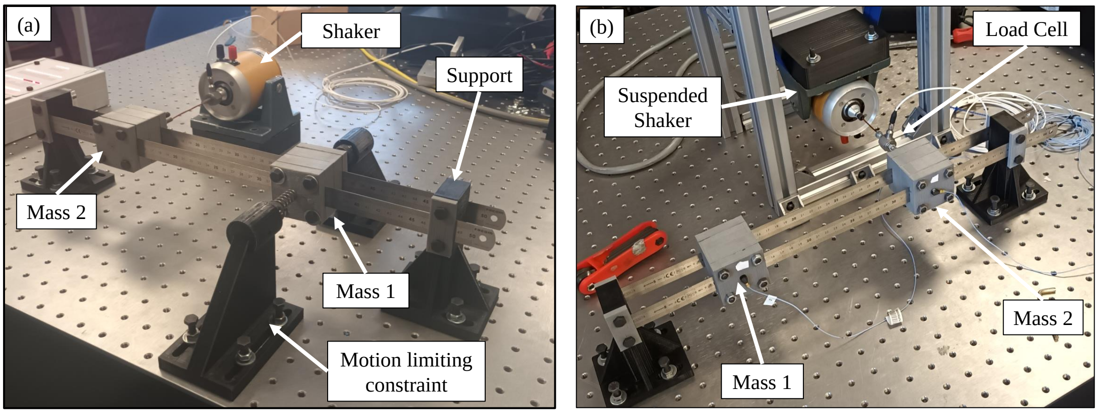

Figure 4.17: Experimental test-rig with fixed (a) and suspended (b) shaker.

dition, they allow the correct contact with the external springs and present attachments for the connection to the shaker. In both the shaker configurations, a stinger is used to minimise the misalignment forces produced by the shaker. The suspended configuration transmits less reaction forced to the excited mass therefore it is chosen to carry out the initial experimental test to verify the dynamic behaviour of the experimental test rig. The test consists of verifying that given a certain excitation condition, the system behaves as a two-DOF system and shows nonlinear dynamic behaviours. To facilitate the analysis, the experiments are conducted in the absence of motion limiting constraints and the nonlinear FRC is obtained by imposing large amplitude excitation so that nonlinear dynamic phenomena, like jumps between stable dynamics responses, are achieved. Before the measurement of the FRC, the underlying linear behaviour of the system is analysed by applying a low-amplitude random excitation. The transfer functions from load input to the output displacement are acquired with the unit *DataPhysics Abacus 901* (DP-901) and with the aid of the commercial software *SignalCalc 900 Series*. To this end, two unidirectional accelerometers (PCB Piezotronics, model: 352C22) are used to measure the output acceleration of the masses and a load cell is used to measure the excitation force, as shown in Fig. 4.17. The results are reported in Fig. 4.18 where the amplitude and the phase of the system at the position of the first and second mass are shown in terms of mobility (Transfer Function (TF) between velocity and excitation force). The figure shows the presence of two peaks

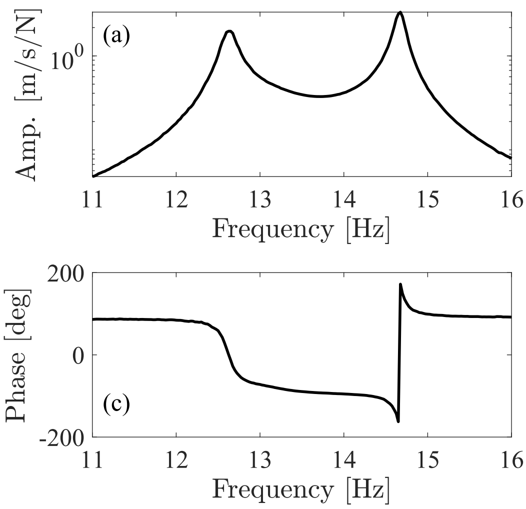

Figure 4.18: Bode diagram of the experimental TF. Panels (a,b) show the amplitude of the first and second mass while panels (c,d) show the associated phase.

in the frequency range of investigation, i.e. 11-16 Hz, with the natural frequencies of the experimental test rig (12.6 Hz and 14.7 Hz) close to the ones predicted by the numerical simulations of the preliminary design (14.3 Hz and 16.0 Hz). The FRC is obtained by performing forward/backward frequency sweeps using a sinusoidal excitation. During the experiments, the frequency sweeps are obtained by changing discretely the excitation frequency and, after every change, the excitation is kept constant for a certain amount of time to let the transient dynamics die. This allows the measurement of the steady-state response from which it is possible to compute the amplitude of the response. Then, the frequency is changed again and the process is repeated until the desired frequency range is not completely covered. To simplify the experimental procedure, the time history of the two masses is measured for the entire frequency sweep. Then, to obtain the FRC, the signal is divided into chunks. In each chunk the frequency of excitation is constant and the amplitude of the response is computed from the steady-state portion of the signal, averaging its amplitude. An example of the averaging procedure is provided by Fig. 4.19: the maxima and the minima over N_p periods of the steady-state signal are recorded. Then maximum and minimum values are averaged and they are used to compute a robust estimation of the system amplitude

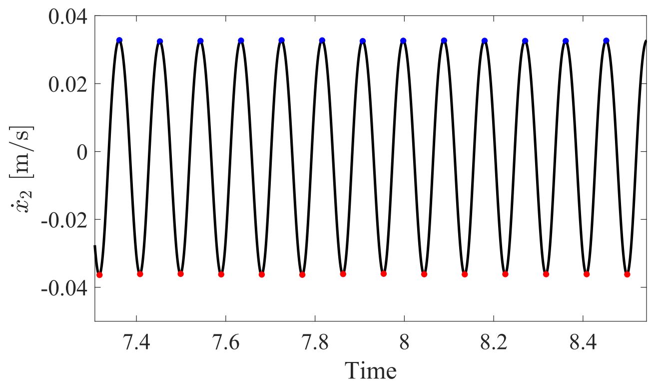

Figure 4.19: Averaging process: time history of the second mass at $\Omega = 11$ Hz. The blue and red dots indicate the identified maxima and minima of the signal that are then averaged to obtain the amplitude of the signal.

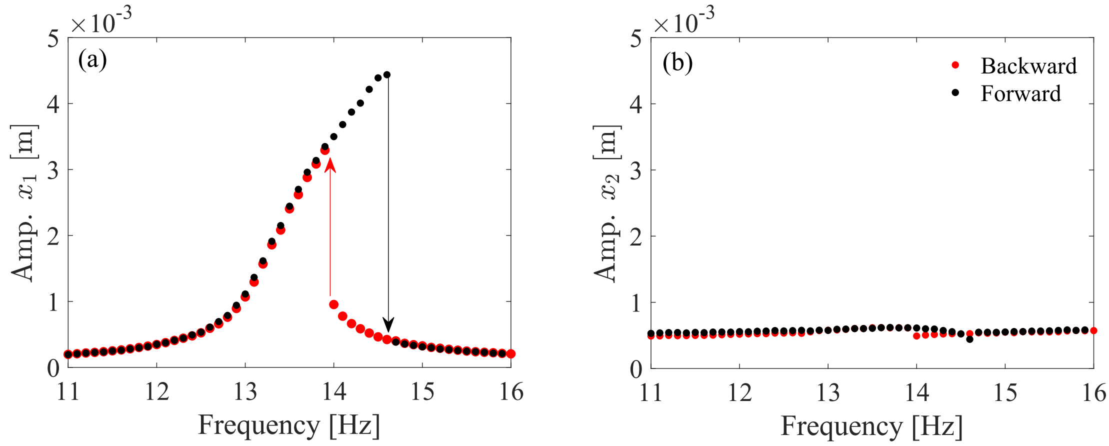

Figure 4.20: FRC for the experimental model with suspended shaker.

of response. During the averaging process, it is important to select a suitable number of periods N_p. This must be equal or larger than the number of periods required to complete an entire limit cycle. In this way, subtle bifurcations such as period-doubling bifurcations are not missed. In the case of Fig. 4.19, the periodic steady-state response is completed after one excitation period, therefore $N_p \geq 1$ allows to correctly average the amplitude of the system. Numerical integration is used to obtain displacement and the velocity of the two masses, from the measured accelerations. The described procedure is used to compute the FRC of the experimental test rig with the suspended shaker. The resulting FRCs in terms of the amplitude of the first and second mass are reported in Fig. 4.20. The FRC is reported on the same scale to emphasise the difference in amplitude between the two masses. Two different aspects should be noted: the FRC of the first mass shows the presence of a single peak and the amplitude of the FRC of the second mass is practically constant. This behaviour is caused by the presence of the shaker which constrains the excited mass and does not allow it to reach a large amplitude of response, capable of triggering nonlinear dynamic behaviour. This results in the presence of a single peak in the FRC, and in the impossibility of evaluating the behaviour of both the system modes in the nonlinear regime.

The presented preliminary experimental analyses provided important information about the dynamics and the problems of the experimental test rigs. Firstly, the system behaves as expected in the linear regime, showing two peaks in the frequency range of interest and experimental resonant frequencies close to the ones predicted by the FE model. This is demonstrated by the analyses of the underlying linear system reported in Fig. 4.18. On the other hand, the preliminary nonlinear analysis showed the presence of desired and unwanted dynamic behaviours. Fig. 4.20 (a) shows the presence of the desired nonlinear hardening response in the FRCs. This is demonstrated by the presence of jumps and bending of the first resonant peak towards higher frequencies of excitation. Nonetheless, unwanted behaviours are also present in the FRCs and are mainly associated with the over-constrained motion of the excited mass: the selected excitation mode, indeed, requires a direct connection between the mass and the shaker, causing the shaker to influence the dynamics of the system. Although a certain degree of dynamic interference from the shaker is expected, especially when no dedicated controllers are implemented, the effect of the shaker on the experimental test rig is so strong that the second resonant peak is practically removed from the considered FRC. This is especially true if only the amplitude of response of the masses is considered. The presence of a second mode can only be revealed by analysing the amplitude of the force (see Fig. B.4) during the frequency sweep. The amplitude of force is substantially reduced at the two linear natural frequencies of the test rig, indicating the presence of the resonance condition. Although this is sufficient to obtain a TF with two peaks in the linear regime, this condition can not be extended to the nonlinear regime of the structure as the response of the system changes with the excitation amplitude,

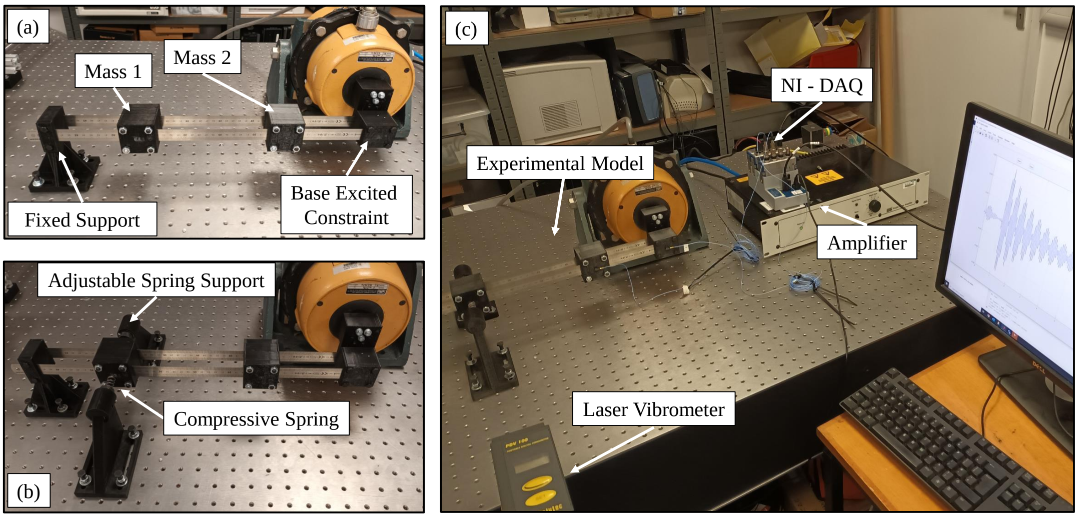

Figure 4.21: Experimental Test Rig #1. The figure represents the version of the experimental model without (a) and with the motion limiting constraints (b). Panel (c) shows the experimental setup [2].

leading to a distorted equivalent nonlinear TF. Therefore, it is necessary to change the excitation mode, so that the excited mass is not over-constrained by the shaker and can reach large amplitudes of response, capable of triggering nonlinear dynamic phenomena.

4.4.2 Base Excited System

To solve these problems, the experimental test rig is modified so that the excitation of the shaker does not directly interfere with the motion of the mass. To this end, the base excitation is chosen as a possible candidate to solve this problem. One of the supports is modified and the new configuration of the experimental test rig, named *Test Rig #1* is shown in Fig. 4.21. The figure shows the experimental model with and without motion limiting constraints (Fig. 4.21(a,b)), and the experimental setup which consists of two unidirectional accelerometers, a point laser vibrometer, and National Instrument (NI) Data Acquisition System (DAQ). The shaker (LDS-V403) is now used to support the loads and the weight of the experimental model. The new support excites the system from one end: this avoids constraining the natural motion of the second mass at large amplitudes of response and, at the same time, it allows

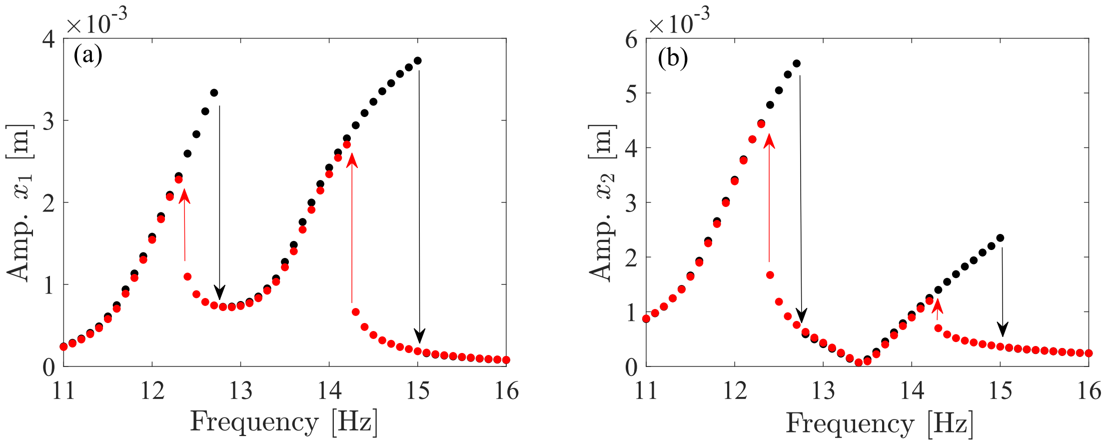

Figure 4.22: FRC of Test Rig #1 in terms of displacement of (a) first and (b) second mass for forward and backward frequency sweeps. The FRCs are obtained by applying a constant voltage amplitude equal to 0.4 V.

preserving the general design of the structure. The nonlinear experimental analysis with forward/backward frequency sweeps is now repeated with the new experimental model. This experimental test rig has the same dimensions as the previous one (see Tab 4.4), except for a_m and b_m which are set, respectively, equal to 90 mm and 160 mm. Finally, the mass of the block has changed and is set equal to 113.0 g. The resulting FRC is reported in Fig. 4.22; the FRC curve is obtained by applying a sinusoidal voltage with an amplitude equal to 0.4 V, and in the new excitation configuration, shows the presence of two peaks. The nonlinear hardening behaviour is testified by the jumps experienced by the system in both forward and backward analyses. In addition, the system responds as a two DOF nonlinear system showing comparable amplitude of response on both masses. At this stage all the product design specifications are satisfied, therefore the proposed configuration is used to carry out a full experimental analysis whose results are discussed in Chapter 5.

4.5 Summary

This chapter discusses the numerical design and experimental adjustment of an experimental test rig. Firstly the product design specifications are described and then a preliminary design of the system is proposed, using numerical simulations. The design exploits common tools for the analysis of mechanical systems like FEA and CAD, as well as more advanced ones like numerical continuation. FEA is used to obtain the required system dimensions, paying attention to the functional requirements. Nonetheless, to reduce the computational effort of simulations, FEAs are limited to investigating the linear behaviour of the system in the frequency domain. CAD is used in parallel to check that the designed system is compliant with practical requirements, such as compatibility in terms of space for shakers, motion limiting constraints, sensors, etc. The nonlinear behaviour of the system in the frequency domain is analysed with a ROM. This model is derived and its parameters are identified by using the analyses of the FE model and the knowledge of the geometry and inertia properties of the system. The ROM is then used to conduct the design of the experimental test rig from a nonlinear perspective: to this end, the numerical continuation is employed and the sought nonlinear features, i.e. isolas and bifurcation of the backbone curves, are investigated through parametric analyses for three different versions of the initial design. The results show that the bifurcation of the backbone curve is affected by the cubic nonlinearities (μ and μ_d), the stiffness of the piecewise characteristics (k_p), and the non-contact gap (a). In addition, the parametric study reveals that large smooth hardening stiffness does not lead to the generation of a bifurcation on the backbone curve. On the other hand, the piecewise stiffness characteristic is shown to have an opposite effect on the bifurcation of the backbone curve, inducing the bifurcation when its effect is predominant in the dynamics of the system, e.g. when small non-contact gaps and large contact stiffness are present. After accurate dynamics analyses and engineering evaluations, the final version (model Version 3) of the test rig is obtained from the preliminary design. This version of the system satisfies all the product design specifications, including the constraint in terms of resources (time and budget) available. This model is then manufactured and tested experimentally in different experimental conditions, to check that all the product design specifications are satisfied. Firstly, the shaker is placed in contact with the excited mass using two possible configurations: fixed or suspended. In these conditions, the second mass is not able to generate a large amplitude of response, as it is constrained in its motion by the shaker. To solve this problem, a re-design of the excitation conditions is taken into account: the excitation point is moved from the second mass to one of the supports to simulate a based-excited system. The required dynamic behaviour of the system is proven by the experimental FRC which is measured again in the new configuration. The test demonstrates that both the masses are free to reach amplitudes of response capable of triggering nonlinear dynamic behaviours, satisfying the product design specifications in actual experiments.

Chapter 5

Experimental Dynamic Behaviour of Multi-Degree-of-Freedom Non-Smooth Systems

5.1 Introduction

This chapter introduces the experimental analysis of the previously designed and tested nonlinear test rig. The following points are discussed:

- Section 5.2 shows the results of the experimental Test Rig #1 with and without motion limiting constraints. The experimental analyses demonstrated the presence of complex dynamic behaviours with quasi-periodic, chaotic, and multi-periodic steady-state responses when the motion limiting constraints are used. Evidence about the presence of detached isolas and bifurcation of the backbone curve is highlighted by comparing experimental features with the previous numerical analyses.

- Section 5.3 introduces the problems and the limitations of Test Rig #1, in particular regarding the amplitude of excitation of the base. To this end, a vibrating table is built and added to the experimental setup, and a control algorithm is implemented to control the amplitude of excitation when frequency sweep tests are performed. The resulting test rig, named Test Rig #2, is experimentally studied. The section terminates by discussing the results of the experimental analysis when the amplitude of displacement is controlled.

5.2 Experimental Results: Test Rig #1

In this section, the experimental analysis of Test Rig #1 is described and analysed to obtain more insights into the dynamics of the system. The test rig is obtained from the design study conducted in the previous chapter, and it is shown in two configurations in Fig 4.21. During the experimental analyses, the model is mounted on a vibration isolation table to avoid interference from external sources.

5.2.1 Underlying Linear Behaviour of Test Rig #1

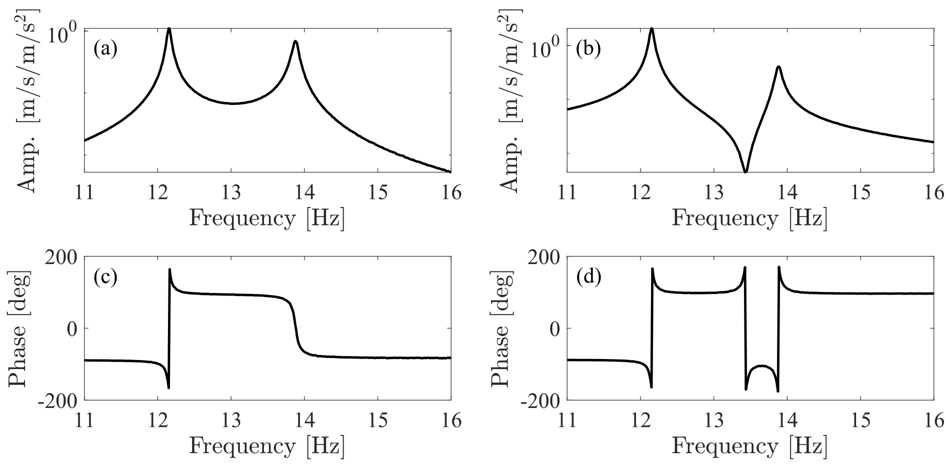

Figure 5.1: Experimental averaged mobility of the two masses in terms of amplitude (a,b) and phase (c,d). Panels are associated with the first (a,c) and second (b,d) degree of freedom.

The underlying linear behaviour of the system is obtained by applying random excitation with low amplitude, as it allows reducing the effect of the nonlinearities, resulting in an averaged linear FRF [7, 74]. As described in the previous section, the underlying

Table 5.1: Sensors configurations in the experimental analyses of the test-rig #1.

Experimental Set-up	Mass 1	Mass 2	Base
Without Motion Constraints	Acc. n.44	Acc. n.46.	Laser Vib.
With Motion Constraints	Laser Vib.	Acc. n.46.	Acc. n.44

linear behaviour is experimentally measured using the commercial software *SignalCalc 900 Series* along with the unit *DataPhysics Abacus 901* (DP-901). This allows obtaining an averaged TF which is measured multiple times during the experimental test. The linear TFs are evaluated with the estimator H2, considering the acceleration of the excited extremity as input and the velocity of the masses as output. A laser-vibrometer (Polytec PVD 100) and two accelerometers (PCB Piezotronics Model: 352C22, n.44 and n.46) are utilised to measure the velocity and the acceleration of the masses and the exciting support in different configurations, as described by Tab 5.1. During the measurement of the underlying linear behaviour, the motion limiting constraints are removed to facilitate the experimental analysis. The resulting linear TFs are shown in Fig. 5.1 in terms of amplitude and phase. As expected, two peaks are found in the TFs testifying to the presence of multiple excited modes in the considered frequency range. The coherence of the TFs is steady and close to one in the frequency range of investigation with minimum values of 0.97 and 0.87 for the TF associated with the first and second mass (see Fig. B.5). This guarantees that the noise is low, the effect of the nonlinearities is limited, and the obtained TFs are representative of the underlying linear system.

5.2.2 Smooth Nonlinear Behaviour of Test Rig #1

To understand the nonlinear behaviour of Test Rig #1, forward/backward sinusoidal frequency sweeps are applied to the structure. The analysis is carried out at diverse excitation amplitudes: these amplitudes are used to obtain the FRCs of the two-mass system at different excitation conditions. During the experiments, the physical amplitude of the shaker (LDS-V403) is not directly controlled, therefore, the input voltage

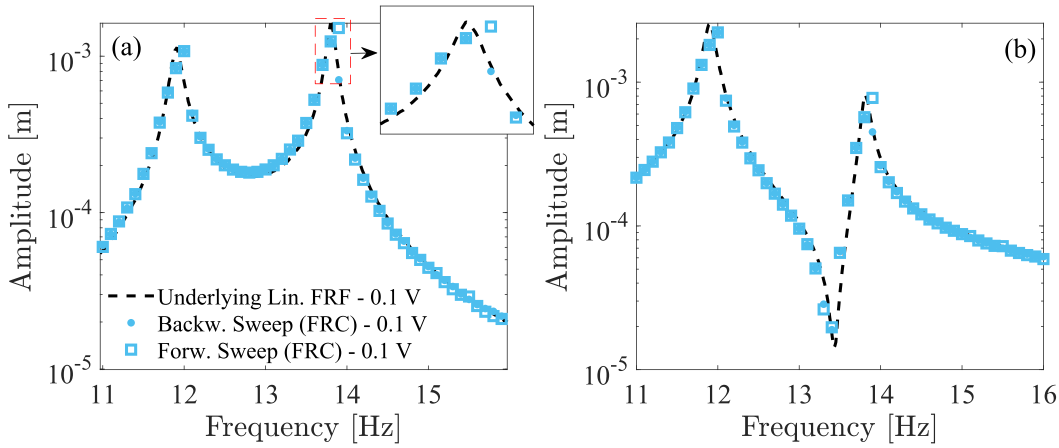

Figure 5.2: Comparison between the underlying linear FRF (dashed black line) and the nonlinear FRC (square and circular markers). To compare the two frequency responses, the TF obtained with low-amplitude and random excitation is multiplied by an amplitude of 0.1 V, the same utilised to obtain the associated FRC. The frequency responses are reported in terms of displacement of the first (a) and second (b) mass.

of the shaker is considered as the excitation control parameter [1]. For each experiment, the frequency range of 11 - 16 Hz is investigated, applying a frequency variation of 0.1 Hz. To reach the steady-state condition, the input signal is maintained for 30 seconds. The experiments consist of recording the time histories of the two masses and the base. The FRCs are obtained via time-history post-processing which involves operations of integration, time cropping, filtering, and averaging, as as previously outlined in Chapter 4. The *National Instrument* data acquisition system (NI cDAQ-9174, NI 9234) and the analogue output module (NI 9263) are used to produce the voltage signal and to record the system responses. Differently from the linear TFs, the dynamics of the shaker are not removed in this case, but they are included in the experimental measurements of the FRC. Therefore, subsequent numerical analyses should consider this problem and utilise the experimental motion of the exciting constraint as input signals for the simulations. The experimental measurements are performed in two stages: in the first one, the FRCs of the test rig are measured without motion limiting constraints at different levels of excitation amplitude, namely 0.1 V, 0.2 V, 0.3 V, and 0.4 V, for

[1] As shown in Fig 4.21, the experimental set-up utilises an amplifier. To know the exact voltage input the amplified value is kept constant and equal to one during the experimental tests.

forward and backward frequency sweeps. This permits the analysis of the nonlinear behaviour of the system in the presence of only smooth nonlinear characteristics. The resulting FRCs are reported in Fig. 5.2 and Fig. 5.3. Fig. 5.2 shows the comparison between experimental frequency responses when an amplitude of excitation of 0.1 V is considered: the dashed line indicates the underlying linear FRF while the markers denote the FRC, obtained from forward and backward frequency sweeps. The FRF is derived from the TF between the voltage input and the displacement output of the two masses. To obtain an amplitude of response in meters, the TF is multiplied by 0.1 V. In this way, the obtained FRF represents the linear dynamic behaviour of the system at the amplitude of 0.1 V. The FRC, instead, shows the full nonlinear response of the system at 0.1 V, as it is obtained with sinusoidal excitation. Fig. 5.2 shows that the amplitude of the FRC is very close to the amplitude of the linear FRF in the whole investigated frequency domain, except at the resonance peaks, where the amplitude of the response is large enough to develop the nonlinear response of the structure. The good match between the two independent experimental measurements, i.e. the FRF and the FRC at 0.1 V, in terms of qualitative and quantitative behaviour highlights the robustness of the experimental study and shows the high quality of the experimental results. To have a clear understanding of the system dynamics, the FRCs are measured at higher excitation amplitudes, namely 0.2 V, 0.3 V, and 0.4 V. The results are reported in Fig. 5.3: by increasing the amplitude of excitation the system shows the presence of jumps and regions of frequency where high- and low-amplitude responses co-exist. The presence of hardening stiffness limits the amplitude of the response, bending the peaks towards higher frequencies. The backward frequency sweep measurements allow measuring the low-amplitude responses which did not emerge with forward-frequency sweep experiments.

5.2.3 Non-Smooth Nonlinear Behaviour of Test Rig #1

In the second phase of the experimental analysis, the dynamic response of the test rig is measured when a piecewise stiffness characteristic is present. To this end, the motion limiting constraints are mounted on the experimental test rig so that the contact be-

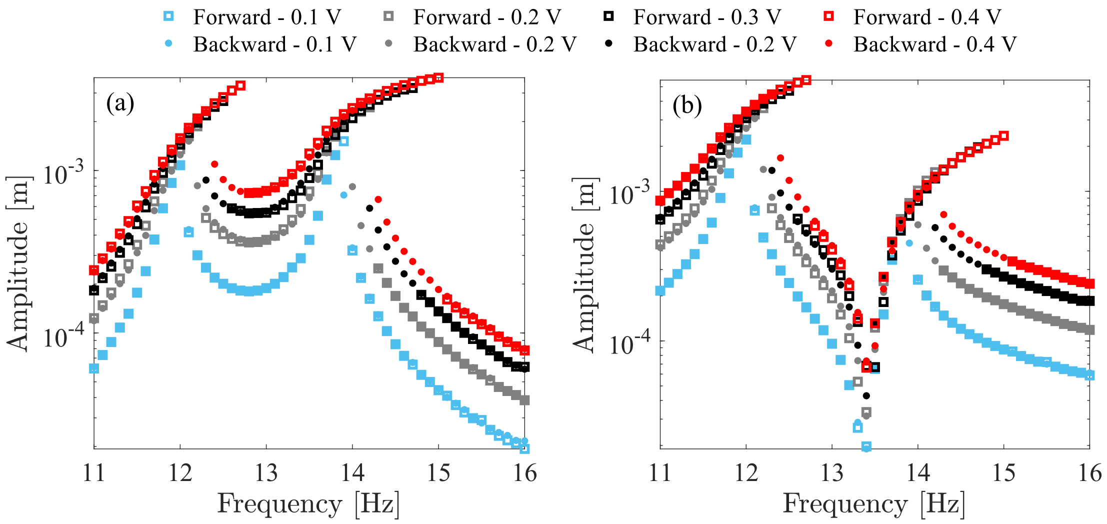

Figure 5.3: Nonlinear frequency response curves for different excitation amplitude (smooth system - Test Rig #1). The frequency responses are reported in terms of amplitude of displacement of the first (a) and second (b) mass.

tween the mass and impact springs occurs at an amplitude of response equal to 0.4 mm. This amplitude represents the non-contact gap, which is set symmetrically on both sides of the impact mass. Two elastic linear springs, with a stiffness of 11.96 N/mm, are mounted on the external supports to simulate the presence of a medium/hard contact. The FRC of the experimental test rig, under harmonic excitation, is measured again using the procedure outlined before and imposing three different levels of excitation amplitude: 0.2 V, 0.3 V, and 0.35 V. Fig. 5.4(a) shows the resulting nonlinear FRCs of the impacting mass (mass 1) for the three considered levels of excitation amplitude. The amplitude of excitation is limited to 0.35 V to avoid damaging the experimental test rig. The three FRCs of Fig. 5.4(a) show that the presence of the piecewise stiffness characteristics deeply affects the dynamics of the experimental test rig, limiting the amplitude of response of the impacting mass and introducing complex dynamics. To better understand the dynamics of the system, the orbits of the impacting mass are shown at different frequencies of excitation Ω, for the three considered levels of excitation. For the sake of simplicity, only the orbits associated with the forward frequency sweep experiments are shown. The orbits are reported in the bottom part of Fig. 5.4: each column shows the phase-portraits of the first mass for four different

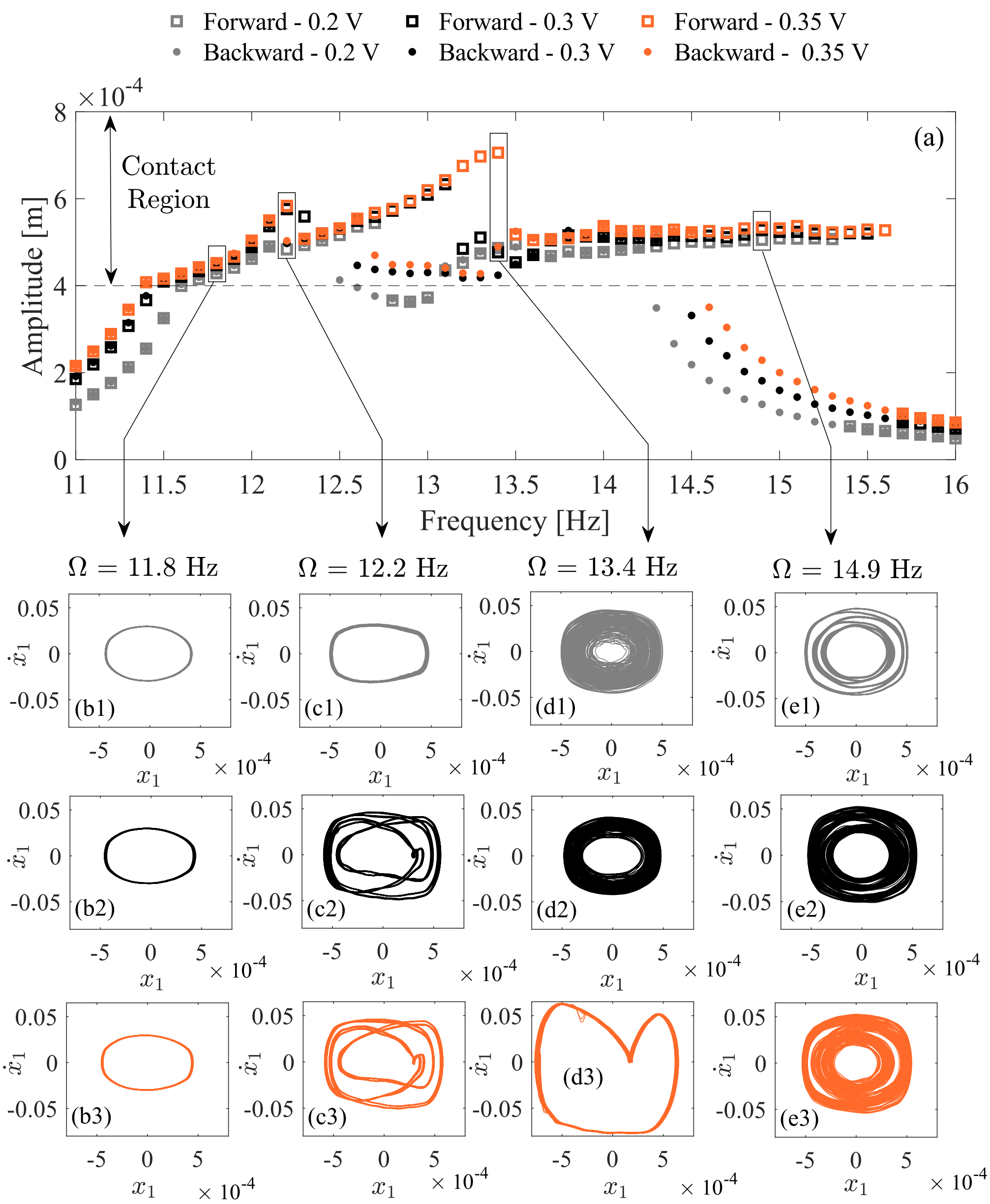

Figure 5.4: Experimental FRCs of the Test Rig #1 with motion limiting constraints . The amplitude of the first mass for forward/backward frequency sweeps is reported in panel (a). The remaining panels (b1-e1) show the orbits of the first mass for forward frequency sweeps [2].

excitation frequencies, namely 11.8 Hz, 12.2 Hz, 13.4 Hz, and 14.9 Hz, while each row illustrates the orbits for a certain excitation amplitude, i.e 0.2 V (grey), 0.3 V (black), and 0.35 V (orange). When the excitation frequency Ω is set equal to 11.8 Hz, the system responds with circular (deformed) single-period orbits for the three excitation levels, as shown in Fig. 5.4 (b1, b2, b3). At $\Omega = 12.2$ Hz, the single-period circular orbit is found only for the first excitation level (0.2 V). The associated phase portrait (Fig. 5.4 (c1)) shows a particularly deformed orbit which is limited in displacement by the presence of the motion constraints. When higher excitation amplitudes are applied to the system, multi-periodic dynamic responses appear, as shown by phase portraits of Fig. 5.4 (c2,c3). The new multi-periodic orbits are associated with an increased amplitude of response of the system in the FRCs, between 12-12.4 Hz. In that region of the frequency domain, the FRCs of Fig. 5.4 (a) shows the presence of co-existing steady-state responses. The low-amplitude branch represents the evolution in frequency of the single-period dynamic response as suggested by phase portraits in panels (b1) and (c1). The high-amplitude branch, instead, is associated with the multi-periodic dynamic responses and it might be due to the presence of a detached isola or bifurcating branch of the FRC. At further higher frequencies of excitation, the experimental test rig shows different dynamics. When the excitation frequency Ω is equal to 13.4 Hz, the low amplitudes of excitation induce quasi-periodic/chaotic responses in the experimental system, as shown by panels (d1) and (d2). This behaviour is triggered by the interaction of the second mode of the system and the contact stiffness. At the highest excitation amplitude (0.35 V), instead, the system responds with a severely deformed single-period response (named degenerate orbit) as depicted in Fig. 5.4 (d3). This dynamic response is associated with the first resonance peak of the FRC and it is very similar to certain dynamic features encountered during the numerical analysis of Chapter 3. Specifically, the phase portrait of panel (d3) shows an experimental dynamic orbit that is very close to the numerical one named PO_2 (see Fig. 3.10). As demonstrated in Chapter 3, PO_2 belongs to the branch B_2 which originates from branch B_1 and exists only when the backbone curve presents a bifurcation point. In addition, the change of shape of the experimental orbit suggests the presence of a bifurcation in the stable branch described by single-period impacting orbits. Once again, this behaviour is very similar to the one encountered in Chapter 3, and underlines the presence of a bifurcation of the backbone curve (see also [1]). Therefore, the presence of the degenerate orbit is considered

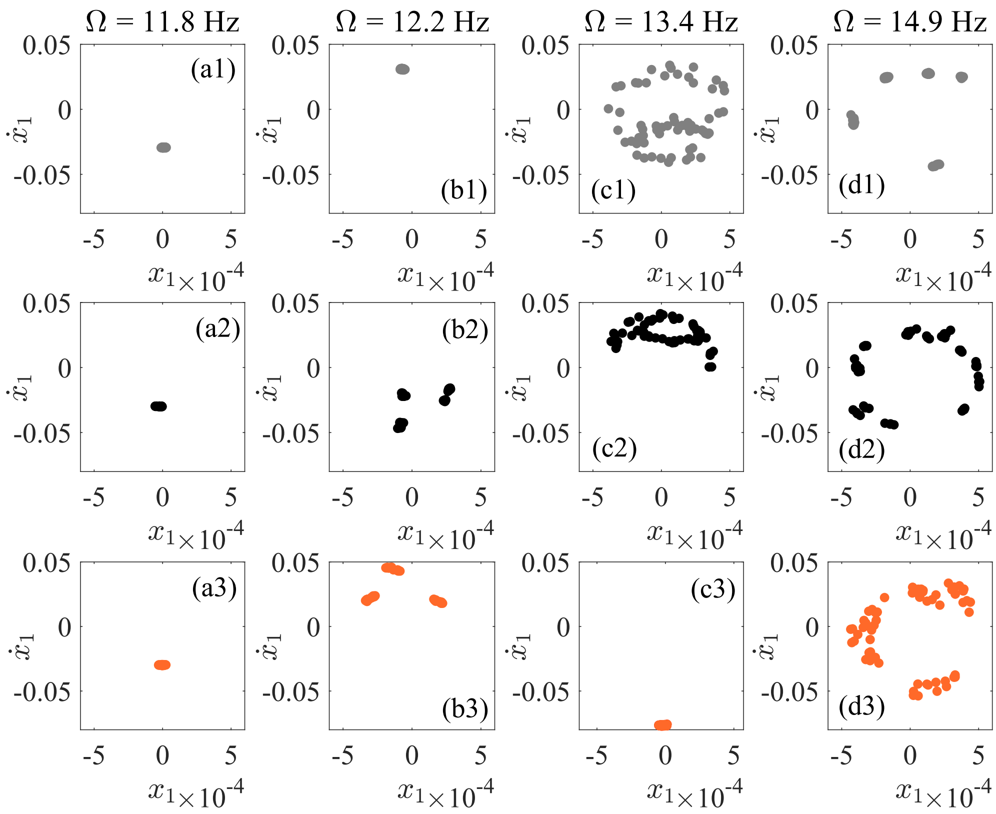

Figure 5.5: Poincaré sections of the steady-state dynamic orbits described in Fig. 5.4 (b1-e3). The sections are obtained by considering the plane $x_2 = 0$ [2].

strong evidence of the presence of a bifurcation of the backbone curve in the investigated experimental test rig. Finally, when $\Omega = 14.9$ Hz, the FRCs show the presence of multi-periodic and torus co-existing attractors, as revealed by panels (e1), (e2), and (e3) of Fig. 5.4. In this case, the analysis of the phase portraits does not provide a clear understanding of the dynamics of the system. Therefore, the Poincaré sections of the previously analysed orbits are computed and reported in Fig. 5.5. The figure shows 12 panels whose organisation in rows and columns is equivalent to the panels (b1-e3) of Fig. 5.4.

In the Poincaré diagrams, single-period orbits generate a single point, as shown in Fig. 5.5 (a1, a2, a3, b1, c3). Differently, multi-periodic responses result in multiple points in the Poincaré sections, as demonstrated by panels (b2, b3) of Fig. 5.5. The remaining dynamic orbits are associated with the second resonance peak of the FRC and can be found in the range between 13 Hz and 16 Hz. In that portion of the frequency domain, the second mode of the system is mainly excited and leads to quasi-periodic and chaotic regimes when contact occurs. This dynamic behaviour is aligned with the numerical analyses conducted in Chapter 3 which demonstrated the presence of a Neimark-Sacker bifurcation in the second resonant peak. In particular, panels (c1) and (c2) of Fig. 5.5 show the presence of distorted invariant circles in the Poincaré sections: this suggests the presence of quasi-periodic dynamics in the experimental system when the second mode is excited. Furthermore, Fig. 5.5 (d1), illustrates a phase-locked condition [127] for which the invariant circle degenerates in multi-periodic orbits. This phenomenon typically happens in structures that exhibit quasi-periodic oscillations due to contact [127] and consists of the formation of multi-periodic responses that live on a torus. Interestingly, these multi-periodic dynamics may generate a complex network of detached isolas in an MDOF piecewise system, as demonstrated in [1] and in the previous chapters. Finally, panels (d2) and (d3) of Fig. 5.5 show experimental Poincaré sections that represent the phase-locked condition. In this case, differently from before, the phase-lock condition is not fully developed but rather the dynamic of the system is stuck into an intermediate state between quasi-periodic/chaotic behaviour and multi-periodic response. To investigate the route to chaos and the phase-locking phenomena [127], other steady-state dynamic responses of the experimental test rig are analysed via Poincaré sections. Specifically, the experimental dynamic responses obtained with an excitation amplitude equal to 0.2 V and an excitation frequency comprised between 13.3 - 13.6 Hz and 14.7- 15.0 Hz are considered. The results are reported in Fig. 5.6 where phase-portraits and the Poincaré sections are shown for the first mass. The route to chaos is represented in the panels (a, b, c, d) of Fig. 5.6: at $\Omega = 13.6$ Hz the system shows the presence of an invariant circle; then reducing the frequency of excitation a torus-doubling (panel (c)) is found at 13.5 Hz. A further decrement in the excitation frequency leads to the generation of chaos in the system as shown by Fig. 5.6 (a) and (b). The phase-locking mechanism is instead described by panels (e, f, g, h) of Fig. 5.6: moving from low to high frequency of excitation, the experimental system transitions from quasi-periodic dynamics (panels (e) and (f)) to a multi-periodic attractor (panel (g)) to a quasi-periodic dynamics (panel (h)) again.

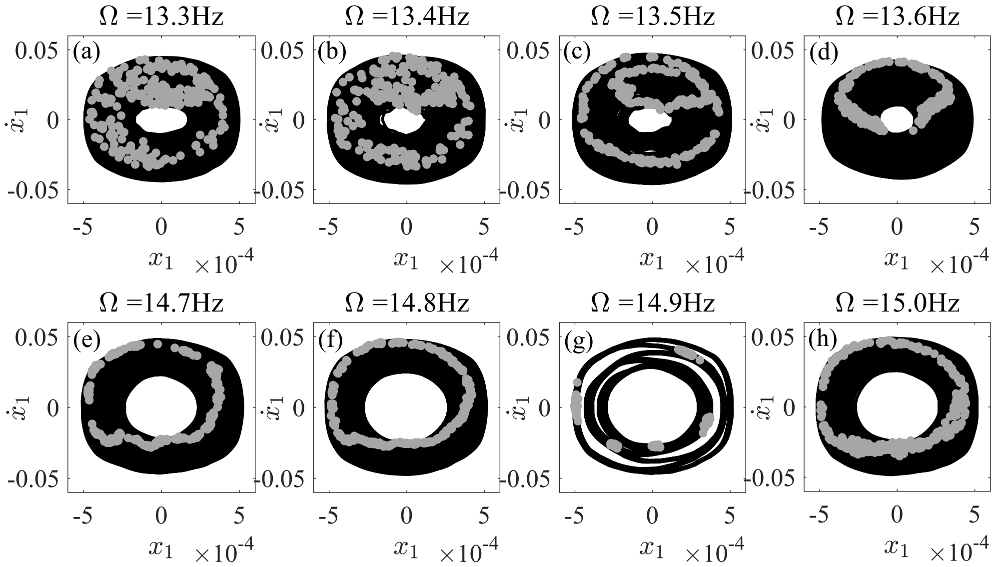

Figure 5.6: Poincaré sections (gray dots) and periodic orbits (black line) of the experimental test rig (first mass) at different frequencies of excitation. All sections are obtained by considering the plane $x_2 = 0$ [2].

When the system is 'locked' into the multi-periodic dynamics, the associated Poincaré section is characterised by the presence of multiple points and the invariant circle disappears as shown in Fig. 5.6 (g).

The experimental analysis of the system revealed the presence of a complex and rich dynamic scenario with multi-periodic, chaotic, and quasi-periodic responses. More importantly, experimental evidence about the presence of detached multi-periodic isolas and bifurcation of the backbone curves are found. Nonetheless, only through the identification, validation, and analysis of an equivalent mathematical model is possible to demonstrate the presence of these phenomena.

5.3 Experimental Results: Test Rig #2

Although the previous experimental analysis provided useful insights into the dynamics of the system, the dynamics of the shaker cannot be removed from the nonlinear response of the system. This makes particularly challenging the comparison between experimental data and numerical simulations, especially when numerical continuation techniques are employed. The presence of the shaker dynamics affects the physical excitation amplitude of the system, making the amplitude of motion of the base non-constant (see Fig B.6) [2, 4].

To solve this problem a control system is developed and implemented in the designed test rig. To distinguish the experimental results, the modified test rig is called Test Rig #2. Fig. 5.7 shows the modified test rig: different dimensions of the system are used to accommodate the presence of a vibrating table, which is used to provide the excitation to the system. The vibrating table is constituted of a metallic structure

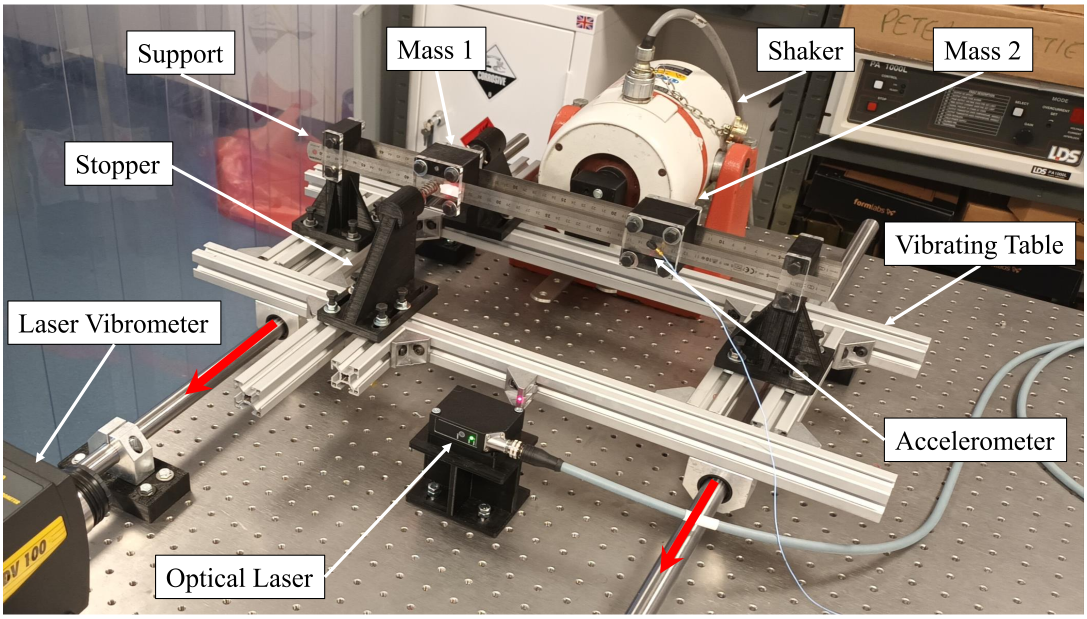

Figure 5.7: Experimental Test Rig #2.

and is supported by bearings which allow the transversal motion of the system. This motion is close to a modal excitation for the considered system, thus it is expected that it mainly excites the first motion of the structure. In the new configuration, each block (mass 1 and mass 2) has a mass of 136.5 g. The blocks are separated by 165.0 mm while the distance between the support and each block is equal to 85.0 mm (symmetric configuration). This leads to a slight change in the natural frequencies of the system which need to be identified once again.

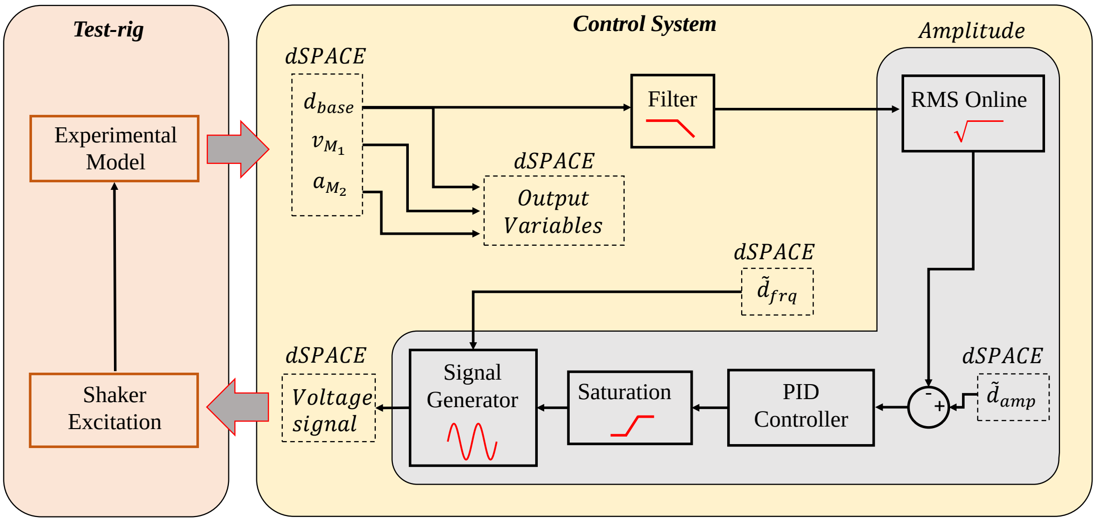

Figure 5.8: Control architecture for Test Rig #2 [3].

5.3.1 Control System Architecture of Test Rig #2

The experimental measurements are performed using an accelerometer (PCB Piezotronics Model: 352C22) and two lasers: a single-point vibrometer (Polytec PVD 100) and a single-point optical laser (Micro-Epsilon optoNCDT 1402). The accelerometer is used to measure the response of the second mass (not subjected to impact), the laser vibrometer is used to measure the velocity of the first mass (subjected to impact in the non-smooth configuration of the test rig), and the optical laser is used to measure the displacement of the vibrating table. The latter sensor is also used as a feedback sensor for controlling the amplitude of the displacement of the vibration table. The closed-loop control system is implemented in the experimental setup by using the control unit dSPACE (CP1104). The designed control system is schematically represented in Fig. 5.8 where dashed boxes indicate inputs/outputs of the control unit. As a first step, the unit reads the displacement of the vibrating table (d_{base}), the velocity of the first mass (v_{M_1}), and the acceleration of the second mass (a_{M_2}) and display them for user inspection. The displacement of the vibrating table is then filtered and a Root Mean Square (RMS) online function is used to estimate its amplitude. The online function estimates the amplitude of the fundamental sinusoidal component of the signal, using the RMS operator. The control system tries to control the measured amplitude by com-

Table 5.2: Experimental displacement amplitudes of the vibrating table in closed-loop control mode.

Experiment	Mean	Standard dev.
Forward Sweep (0.03 mm)	3.02×10^{-5} m	1.47×10^{-6} m
Backward Sweep (0.03 mm)	3.01×10^{-5} m	2.48×10^{-8} m
Forward Sweep (0.04 mm)	4.00×10^{-5} m	1.03×10^{-6} m
Backward Sweep (0.04 mm)	4.02×10^{-5} m	3.11×10^{-8} m
Forward Sweep (0.05 mm)	5.01×10^{-5} m	6.41×10^{-7} m
Backward Sweep (0.05 mm)	5.02×10^{-5} m	3.81×10^{-8} m

paring it with the imposed one ($\tilde{d}_{amp}$). To this end, a Proportional-Integral-Derivative (PID) controller is utilised. The control of the RMS-based amplitude requires significantly lower control effort than controlling the actual sinusoidal signal. In addition, as demonstrated by previous studies [6, 128], the control of the RMS-based amplitude produces good results and enables the comparison between experimental data and numerical simulations obtained from perfect sinusoidal excitation. The output of the PID controller represents the amplitude of the voltage signal that is passed to the shaker: in order to prevent excessively large amplitudes of excitation, the amplitude is limited by a saturation function. Finally, a signal generator is used to create a sinusoidal signal with the required frequency ($\tilde{d}_{frq}$) which is passed to the shaker as voltage input.

To evaluate the capabilities of the controller, the amplitude of the vibrating table during sinuoidal frequency sweep tests is computed from experimental data for three excitation conditions, namely when the base amplitude is imposed equal to 0.03 mm, 0.04 mm, and 0.05 mm. At each frequency of excitation, the amplitude of the vibrating table is computed using the following expression:

$$A_{vt}(\Omega) = \sqrt{2}\sqrt{\frac{1}{n}\sum_{i=1}^{P} x_{vt}(t_i)^2}, \tag{5.1}$$

where $x_{vt}(t_i)$ represents the i-th component of the time history of the displacement, $A_{vt}(\Omega)$ is the amplitude of the vibrating table at the frequency Ω, and P is the number of elements of the considered time history. Following the definition of amplitude used in the control system, Eq. 5.1 estimates the amplitude of the signal, assuming that the signal is perfectly sinusoidal. This allows obtaining the actual amplitude that is controlled by the proposed control system. Eq. 5.1 is used to compute the amplitude of the vibrating table at each frequency of excitation. These amplitudes are then used to compute the mean and standard deviations for an entire frequency sweep. Tab. 5.2 shows the mean and standard deviation of the base amplitude for forward and backward frequency sweeps experiments for three different imposed excitation amplitude. For the sake of simplicity, only the experiments without the motion limiting constraints are considered. The results demonstrate that the proposed control system controls accurately the amplitude of displacement of the vibrating table as the measured mean input amplitudes are very close to the imposed ones (reported in brackets) for the three considered excitation levels. Furthermore, the very small standard deviation proves that the amplitude has a very low fluctuation during the frequency sweep.

5.3.2 Dynamic Behaviour of Test Rig #2

At this stage, it is possible to perform the experimental analysis of Test Rig #2. As usual, the underlying linear behaviour is first measured. The linear TFs are obtained by using the displacement of the masses as the output signal and the acceleration of the base as the input signal. The measured TFs are obtained through the same procedure outlined before for Test Rig #1 and the results are shown in Fig. 5.9. The figure shows the amplitude, phase, and coherence of the measured signal. From Fig. 5.9 (a,b) it is clear that, in the investigated frequency range (12-20 Hz), two resonances are present with the first one producing the largest response. This is due to the vibrating table motion which mostly excites the in-phase motion of the two masses, i.e. the first mode, generating a larger response around the first natural frequency (15.2 Hz). The change of natural frequencies, with respect to test #1, is justified by the change in dimensions and mass of the system. Fig. 5.9 (e) and (f) show the coherence of the measured signals: this measure is typically used in industrial procedures to estimate and understand the repeatability of a signal along the considered frequency span. It is worth noting that the minimum value of the coherence for both resonances is higher than 0.87: this demonstrates that the system is behaving linearly at the considered level of excitation,

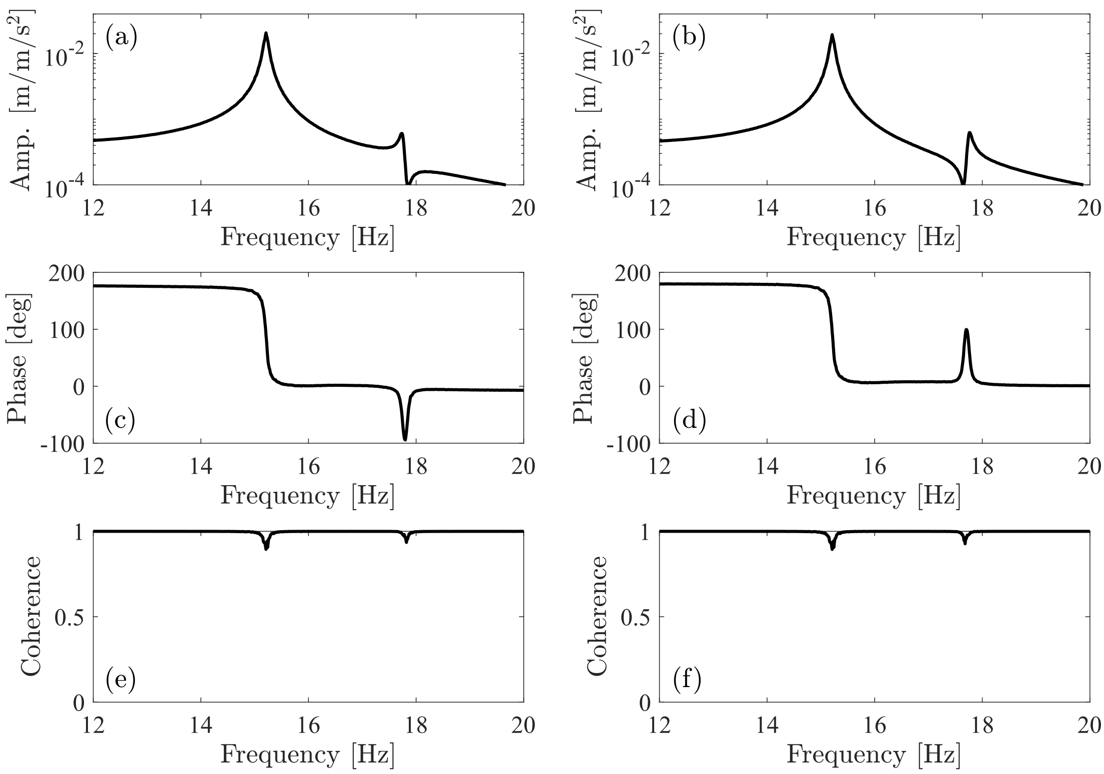

Figure 5.9: Transfer functions of the underlying linear system (Test Rig #2). The measured transfer function is reported in terms of amplitude (a,b), phase (c,d), and coherence (e,f). Panels on the left and right represent the measured quantities for, respectively, first and second mass.

demonstrating that the identified TFs are a good and robust representation of the underlying linear behaviour of Test Rig #2.

To trigger the nonlinear behaviour, sinusoidal frequency sweeps are applied to the experimental system. The nonlinear analysis of the system is initially performed without motion limiting constraints , i.e. using the smooth version of the system, by controlling the amplitude of the displacement of the vibrating table. Three different excitation levels, namely, 0.03 mm, 0.04 mm, and 0.05 mm are used to generate the FRCs of the system. The system is investigated in the frequency range between 14.5 Hz to 19.5 Hz where the first two resonant peaks of the underlying linear system are found from the previous linear analysis. The system is excited with a discrete frequency sweep whose frequency of excitation is incremented/decremented by 0.1 Hz. For each frequency, the excitation signal is maintained for 45 seconds to let the transient response die. The

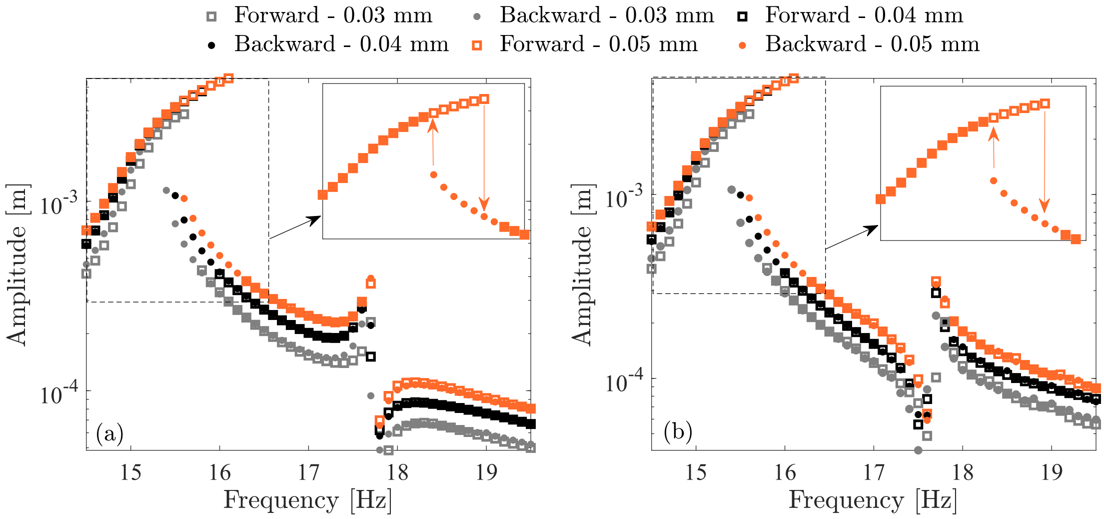

Figure 5.10: Experimental frequency response curve of Test Rig #2 in the nonlinear regime without motion limiting constraints . The FRCs are reported in terms of absolute displacement of the first (a) and the second mass (b) [3].

same post-processing used for Test Rig #1 is now applied: the time signal is filtered with a low pass (150 Hz) and a high pass (2 Hz) filter and then it is divided into blocks of 45 seconds where the excitation has a constant frequency. Then, averaging and numerical integration/derivation procedures are used to obtain the FRCs. Fig. 5.10 shows the FRC of the nonlinear system for the three excitation conditions in terms of absolute displacement of the first and second mass. Once again, the parallel beams induce a hardening effect on the stiffness of the system which results in the typical hysteresis loops with resonance peaks bent towards higher frequencies. Differently from Test Rig #1, the system is controlled in amplitude via a feedback sensor; this might slow down this transition from high- to low- amplitude of response in the hysteresis loop, therefore it is important to check that appropriate PID gains are applied before conducting any experimental tests. During the experiments the transition from high- to low- amplitude of response is shown to be fast enough to guarantee the recording of the whole FRC. In addition, the forward and backward amplitude of responses, away from the hysteresis loop, are very similar, demonstrating the robustness of the experimental analysis and the obtained FRCs.

The Test Rig #2 is also tested in its non-smooth version using the motion limiting

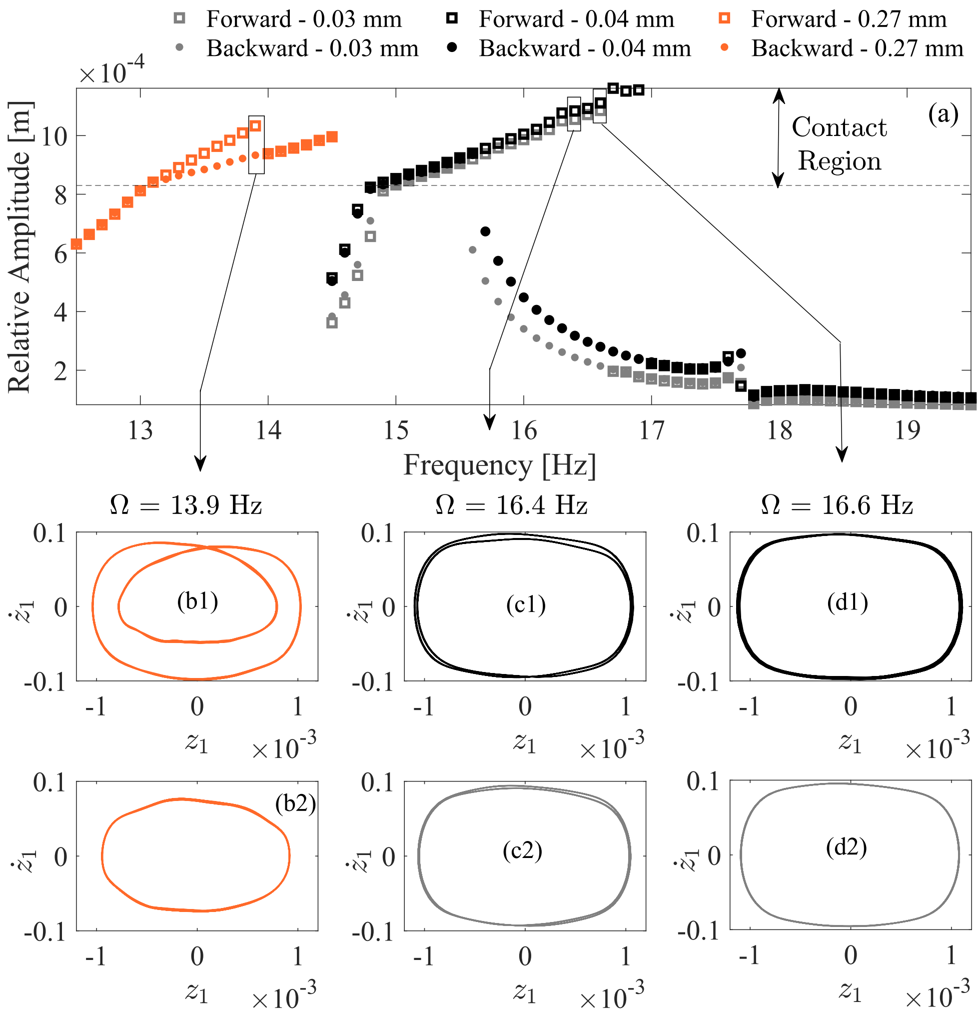

Figure 5.11: Experimental frequency response curves of Test Rig #2 when contact springs with stiffness of 7.87 N/mm and a non-contact gap equal to 0.83 mm are used in the experimental set-up. The FRC of the first mass is reported in panel (a) in terms of relative displacement while panel (b1-d2) show different steady-state orbits of the system in terms of relative coordinates.

constraints reported illustrated in Fig. 5.7. Differently from Test Rig #1, the motion limiting constraints are moving with the vibrating table, imposing a piecewise stiffness characteristic on the relative displacement of the masses. Two different conditions are tested: in the first case, the impacting spring is chosen with a nominal stiffness of 7.87 N/mm while the second experiment adopts a spring with a nominal stiffness equal to 11.97 N/mm. The symmetric non-contact gap is set equal to 0.83 mm in the first case and to 0.82 mm in the second case. Similar results are obtained in the two analyses: the two-DOF system response is driven by the first mode therefore only the first peak of the frequency response reaches an amplitude large enough to trigger the contact condition. However, when the contact occurs both the modes contribute to the steady-state response of the system and evidence of the presence of a bifurcation of the first peak is found in both the analysed configurations. Fig. 5.11 shows the dynamic steady-state response of the first non-smooth configuration (the same analysis can be found in Appendix B.1 for the second configuration (Fig B.7)). After the grazing bifurcation, the system experiences a sudden increase in stiffness which leads to a reduction in the steepness of the FRC (Fig. 5.11(a)), clearly visible in the forward frequency sweep analyses. The classical deformed single-period orbit appears in the experimental test rig, as shown by panels (b2), (d1), and (d2) of Fig. 5.11. In addition, the system shows the presence of orbits typically found on the bifurcating branch of the first peak, i.e. branch B_2 according to the numerical analysis of Chapter 3. They are illustrated in Fig. 5.11 (c1,c2) for the amplitude of excitation equal to 0.04 and 0.03 mm. At this low amplitude of excitation, this condition appears only at the highest frequencies of excitation of the first resonance peak. Nonetheless, the presence of a fully developed bifurcating branch is not visible. To solve this problem the analysis is repeated at a higher excitation amplitude, equal to 0.27 mm: at this amplitude, the grazing condition occurs at lower frequencies thus the analysis is conducted in the frequency range between 12.5 Hz and 14.5 Hz. The analysis is interrupted at 14.5 Hz to not damage the experimental model. In particular, the experimental tests at high amplitude are performed so that the forces and the deformations in the experimental test rig do not induce structural changes in the system, e.g. movement of the masses or the motion limiting constraints . This is fundamental to guaranteeing the comparison between different experiments.

The analysis at high amplitude of excitation shows the presence of a visible bifurcation whose amplitude of response is significantly different from the main branch. The associated orbits at $\Omega = 13.9$ Hz are reported in panels (b1) and (b2) of Fig. 5.11, showing the co-existence of different attractors. The first one, reported in panel (b1), demonstrates the presence of a degenerate orbit similar to the one associated with the bifurcation of the first peak (branch B_2 in Fig 3.10). The second orbit, instead, has the typical shape of a single-period orbit subjected to symmetric piecewise stiffness and it is associated with the main branch of the first peak. Although the numerical analyses of Chapter 3 showed the presence of these steady-state orbits in the system, they appeared with different stability. Specifically, in the numerical analysis, the bifurcation of the first peak branch induces the main single-period orbit to become unstable, while the degenerate one is gaining stability. Further analysis should be performed to demonstrate if the experimental degenerate orbit of Fig. 5.11 (b1) is associated with a bifurcating branch or a detached isola.

5.4 Summary

This chapter describes the experimental analysis of the designed test rig (Test Rig #1) and its controlled version (Test Rig #2). Firstly, the dynamics of Test Rig #1 are investigated in terms of underlying linear behaviour, nonlinear frequency response, limit cycle oscillations, and Poincaré sections. The analysis of the smooth version of the system shows the presence of a hardening stiffness behaviour in the system, characterised by the presence of jumps in the FRCs near the system resonances. The test rig is also analysed in the presence of non-smooth characteristics. To this end, the external motion limiting constraints are mounted on the table and the experimental analyses are repeated for different levels of excitation amplitudes. In this case, the test rig shows the presence of a rich dynamic behaviour, dominated by nonlinear features like multi-periodic, quasi-periodic, and chaotic responses. The obtained FRCs show the presence of steady-state multi-periodic orbits which might be associated with isolas or bifurcating branches. Degenerate single-period impacting orbits are also experimentally encountered: this orbit was found in previous numerical analyses of Chapter 3 and thus represents evidence of the possible presence of a bifurcation of the backbone curve. The analysis of the Poincaré sections confirms the presence of quasi-periodic and chaotic behaviour, demonstrating that the system reaches chaos via period-doubling tori. In addition, it is shown that the multi-periodic responses in the second resonant peak are generated by lock-in conditions of the quasi-periodic behaviour of the system.

The experimental analyses are repeated using the second test rig: the experimental model is practically equivalent to the previous one but it is excited by a vibrating table whose motion is controlled in displacement. This allows to overcome some of the limitations of the previous test rig. The new test rig, named Test Rig #2, demonstrates the presence of degenerate orbits and multi-periodic responses similar to the previous test rig. Once more, these orbits provide further evidence of the presence of induced bifurcation in the backbone curves and detached isolas in piecewise nonlinear mechanical systems. Nonetheless, these promising experimental results represent only evidence of the presence of the above-mentioned nonlinear phenomena in the system and further analyses are necessary to formally prove their existence. To this end in the next chapters, the experimental data are used to identify and validate equivalent nonlinear systems which are then used to conduct detailed numerical analyses.

Chapter 6

Identification of Multi Degree of Freedom Systems: The Nonlinear Restoring Force Approach

6.1 Introduction

This chapter discusses the identification of equivalent mathematical models representing the dynamics of the experimental test rigs previously introduced. In particular, the following points are discussed in the sections:

- In Section 6.2, Test Rigs #1 and #2 are experimentally identified when the motion limiting constraints are removed. The separate identification of linear and nonlinear contributions in mechanical systems is presented and discussed. Specifically, the identification of the nonlinear contributions is performed by exploiting meta-heuristic optimisation methods and the knowledge of the experimental frequency response curve. The section provides a discussion about the efficacy of two meta-heuristic optimisation techniques, i.e. the particle swarm optimisation (PSO) and the genetic algorithm (GA), in identifying nonlinear systems, using the experimental data. At the end of the section, the limits of the proposed identification approach are discussed by assessing the capabilities of the identified model in capturing the the qualitative and quantitative nonlinear dynamic behaviour of Test Rig #2.

- Section 6.3 introduces the Nonlinear Restoring Force (NLRF) method: the method is developed to overcome some of the difficulties encountered when meta-heuristic optimisation methods are used. Firstly the mathematical structure of the method is presented and then numerical examples are provided. Particular attention is paid to the graphical representation of the nonlinear restoring force surfaces of the MDOF system, highlighting the advantages and implications in the subsequent identification process. Finally, the NLRF method is utilised to identify the nonlinear characteristics of the two test rigs in different configurations using experimental data: firstly the method is used to identify a reduced order model representing the smooth version of Test Rig #2 and then the method is used to identify the piecewise nonlinear characteristic of the Test Rig #1.

6.2 Experimental Identification via Meta-Heuristic Optimisation Methods

In this section, the models representing the linear and nonlinear behaviour of Test Rigs #1 and #2 are identified. The experimental models are graphically shown in Fig. 4.21 and Fig. 5.7 in two configurations: with and without the motion limiting constraints . This section focuses on the identification of the experimental test rigs when the motion limiting constraints are removed. The smooth behaviour of the two-mass system is identified and the associated nonlinearities are characterised, following the procedure outlined in [4].

6.2.1 Identification of the Underlying Linear System - Test Rig #1

In Chapter 4, a ROM representing the investigated two-mass system was developed and validated against the numerical results of a 3D finite element model. Building on this knowledge, a modified ROM is used to identify the experimental Test Rig #1. The ROM aims to identify the nonlinear behaviour of the test rig when the motion limiting constraints are not present, thus it can be represented with a lumped parameter model

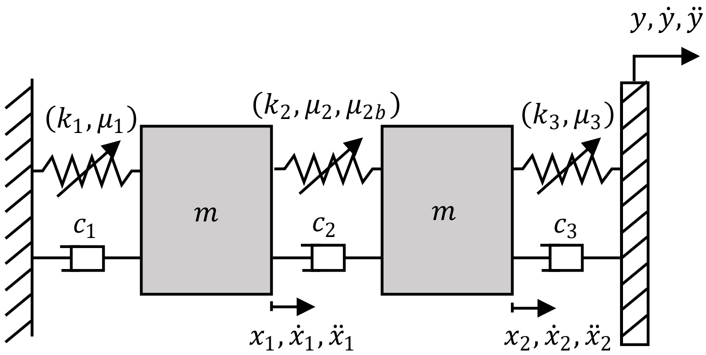

Figure 6.1: Reduced order model representing experimental Test Rig #1 [4].

with cubic stiffness coefficients, as shown in Fig. 6.1. To replicate the experimental excitation conditions, the model is base excited on one single side. Fig. 6.1 shows also the locations of the connection elements where μ_1, μ_2, $\mu_{2,b}$, and μ_3 are the cubic stiffness coefficients, k_1, k_2, and k_3 indicate the linear stiffness coefficients, c_1, c_2, and c_3 denote the viscous damping coefficients, m is the mass of the system, and y is the displacement of the moving constraint. The associated equation of motion is represented by the following expression:

$$\begin{aligned} &m\ddot{x}_1 + c_1\dot{x}_1 + k_1x_1 + \mu_1x_1^3 + c_2(\dot{x}_1 - \dot{x}_2) + k_2(x_1 - x_2) + \mu_2x_1^3 - \mu_{2,b}x_1^2x_2 + \\ &+ \mu_{2,b}x_1x_2^2 - \mu_2x_2^3 = 0 \end{aligned} \tag{6.1a}$$

$$\begin{aligned} &m\ddot{x}_2 + c_3(\dot{x}_2 - \dot{y}) + k_3(x_2 - y) + \mu_3(x_2 - y)^3 - c_2(\dot{x}_1 - \dot{x}_2) - k_2(x_1 - x_2) + \\ &- \mu_2x_1^3 + \mu_{2,b}x_1^2x_2 - \mu_{2,b}x_1x_2^2 + \mu_2x_2^3 = 0 \end{aligned} \tag{6.1b}$$

The equation of motion representing the system presents unsymmetrical cubic nonlinearities. These are introduced to account for the hardening behaviour, demonstrated by the experimental test rig in the previous experimental analyses, and for facilitating the identification of the nonlinear characteristics.

The linear behaviour of the system is defined by the linear part of Eq. 6.1; by considering a sinusoidal input signal y with constant acceleration amplitude, the linear receptance H can be expressed as follows:

$$H_{A,1} = \frac{X_1}{\ddot{Y}} = \frac{X_2 k_2 + i\Omega X_2 c_2}{\ddot{Y}(k_1 + k_2 - \Omega^2 m + \Omega i(c_2 + c_1))} \tag{6.2a}$$

$$H_{A,1} = \frac{X_2}{\ddot{Y}} = \frac{X_1 k_2 - \frac{\ddot{Y} k_3}{\Omega^2} + i\Omega X_1 c_2 - \frac{i\ddot{Y} c_3}{\Omega}}{\ddot{Y}(k_2 + k_3 - \Omega^2 m + \Omega i(c_2 + c_3))} \tag{6.2b}$$

where $\ddot{Y}$ is the complex amplitude of the acceleration input, X_1 and X_2 denote the complex amplitudes of the masses displacement, and Ω indicates the forcing frequency of the excitation. The linear transfer functions, $H_{A,1}$ and $H_{A,2}$, represent the numerical counterpart of the receptance experimentally obtained in Chapter 5 for the Test Rig #1 and graphically described in Fig. 5.1. To identify the linear coefficients of the system, the experimental linear receptances are utilised; the circle-fit and half power methods [7] are a straightforward and effective tool to estimate the natural frequencies ω_n, modal damping ratios ζ, and the modal matrix Ψ of an MDOF mechanical system. It is worth noting, that this method can be applied for the extraction of modal parameters because the FRF shows that there are two well-separated resonant peaks in the frequency range of interest. Following this approach, the modal damping ratios and the natural frequencies can be organised in matrix form:

$$\mathbf{Z} = \begin{bmatrix} 2\zeta_1\omega_1 & 0 \\ 0 & 2\zeta_2\omega_2 \end{bmatrix} \tag{6.3a}$$

$$\mathbf{W}_n = \begin{bmatrix} \omega_1^2 & 0 \\ 0 & \omega_2^2 \end{bmatrix} \tag{6.3b}$$

The modal matrices of Eq. 6.3 are then used to estimate the actual stiffness and damping linear coefficients, using the following approach:

$$\mathbf{M} = \begin{bmatrix} m & 0 \\ 0 & m \end{bmatrix} \tag{6.4a}$$

$$\mathbf{C} = \begin{bmatrix} c_1 + c_2 & -c_2 \\ -c_2 & c_2 + c_3 \end{bmatrix} = (\Psi^T)^{-1}(\Psi^T \mathbf{M} \Psi \mathbf{Z})(\Psi)^{-1} \tag{6.4b}$$

$$\mathbf{K} = \begin{bmatrix} k_1 + k_2 & -k_2 \\ -k_2 & k_2 + k_3 \end{bmatrix} = (\Psi^T)^{-1}(\Psi^T \mathbf{M} \Psi \mathbf{W}_n)(\Psi)^{-1} \tag{6.4c}$$

where M represents the diagonal mass matrix, C is the linear damping matrix, and K denotes the linear stiffness matrix. The mass matrix M is estimated by measuring the weight of the two blocks. Each block has a mass of 0.113 kg which is much larger than the mass of the supporting beams. Following this observation, the system mass matrix M is estimated on the base of the mass of the two blocks, neglecting the inertia contribution of the beams. The simple geometry of the investigated test rig allows us to directly measure the mass of the system. Nonetheless, more sophisticated methods for the identification of the modal mass are available in the literature [7, 129]. Such methods can be applied to obtain an estimation of the mass when the approach here proposed is not feasible. The remaining unknown coefficients are evaluated using the above-mentioned linear identification methods. Specifically, the circle fit and half-power methods are used to estimate the natural frequencies ω_1, ω_2, the damping ratio ζ_1, ζ_2, and the modal matrix Ψ of Test Rig #1. Then, Eq. 6.4 are used to estimate the stiffness $\mathbf{K}$ and damping $\mathbf{C}$ matrices of the system, from which the linear coefficient of the system are retrieved.

The obtained set of coefficients represents a preliminary estimation of the linear dynamics of the system. To further improve the identification of the underlying linear system, the identified linear coefficients are used as an initial guess for an optimisation procedure which aims to minimise the difference between the experimental and analytical transfer functions. Specifically, the amplitude and phase of the analytical transfer functions are obtained by solving Eq. 6.2a and 6.2b. Then the numerical results are compared against the experimental counterparts and their difference is minimised to

Table 6.1: Identified linear coefficients representing the underlying linear system of Test Rig #1: the estimated coefficients are obtained using well-established linear identification methods while the optimised coefficients are obtained through a minimisation procedure.

Coeff.	c_1 [Ns/m]	c_2 [Ns/m]	c_3 [Ns/m]	k_1 [N/m]	k_2 [N/m]	k_3 [N/m]
Estimated	0.0454	0.0069	0.0370	726.3	85.5	621.5
Optimised	0.0454	0.0075	0.0366	714.9	89.6	624.9

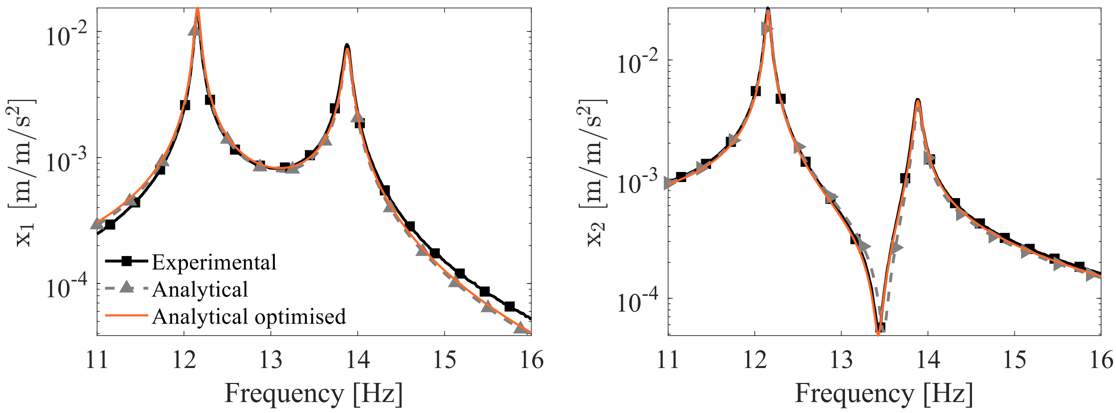

Figure 6.2: Comparison between the experimental and analytical linear transfer function for Test Rig #1. The amplitude of the TFs associated with the first and second DOF are reported, respectively, in the left and right panels [4].

reach a more accurate definition of the linear coefficients of the system. The minimisation procedure is performed with the aid of the MATLAB function *lsqnonlin*; this function implements the Levenberg–Marquardt algorithm, which is suitable for the optimisation of similar problems. The final results of the optimisation process are reported in Tab. 6.1. As shown by Tab. 6.1, only the linear stiffness and damping coefficients are optimised in the proposed optimisation process. The mass m can be also considered in the proposed optimisation nonetheless, to reduce the search space of the optimisation procedure, the mass has not been included. The table demonstrates that the optimisation process does not induce significant changes in the numerical values of the linear coefficients, proving the accuracy of well-established linear identification methods. Fig. 6.2 shows the experimental and analytical receptances for the two sets of coefficients: the figure demonstrates that the initial estimation with the circle-fit method is very close to the optimal configuration. Nonetheless, small differences between the analytical and the experimental TFs are found in the anti-resonance of the second FRF. The optimised TFs, instead, provide a slightly better fit of the experimental data. The comparison between experimental and optimised transfer functions demonstrated that the chosen ROM and the identified linear coefficients provide a good prediction of the linear behaviour of the test rig. Based on these results, the identified linear ROM is considered sufficiently accurate and it is used in the next steps of the identification process.

6.2.2 Identification of the Nonlinear Parameters - Test Rig #1

The identification of a nonlinear model representing Test Rig #1 is based on the previous linear identification procedure. The idea is to exploit all the available experimental data, i.e. the linear TFs and nonlinear FRCs, to identify a nonlinear system capable of capturing the full dynamics of the test rig. The literature offers a plethora of identification methods for nonlinear systems [70, 71]: between them, identification methods based on optimisation procedures are particularly useful when multiple experimental data are available, like in the considered case. These methods can be used to optimise an user-defined objective function, reducing the identification procedure to a minimisation problem. Meta-heuristics methods, such as the Particles Swarm Optimisation (PSO) and the Genetic Algorithm (GA), try to exploit and explore the search space optimally and are often used to solve similar identification problems [130]. In this work, the aforementioned meta-heuristic optimisation methods, PSO and GA, are used to identify the nonlinear parameters of the ROM representing Test Rig #1. The GA and PSO algorithms belong to the population-based methods and try to emulate natural processes :

- **GA**: The genetic algorithm [131] initialises the domain with a random initial population, whose size is defined by the user. Following the analogy with nature, the population is represented by individuals who try to survive at each evaluation of the objective function. Each individual, indeed, represents a possible configuration of the system parameters which is used to evaluate the objective function. At each step, the algorithm creates the next generation of individuals starting from the current available population. Some individuals, the ones associated with low objective function values, are selected as parents according to the selection criteria and used to create new individuals. The children, i.e. individuals created from the parents, are generated in three different ways: elite individuals survive the generational change as they have the lowest values of the objective function, crossover children are obtained by combining the genes of the parents according to the selected crossover function, and mutated children are generated by introducing random mutation to a single parent. The algorithm stops when the change in the objective function is less than the prescribed tolerance.

- **PSO**: The particle swarm optimisation method [132, 133], instead, is based on swarm intelligence. Similarly to the GA, the PSO begins uniformly populating the entire search domain with a certain number of particles. The number of particles, generally called swarm size, is selected by the user and each particle, similarly to the individuals, represents a possible configuration of the system parameters. Each particle possesses a position x_{PSO} and a velocity v_{PSO}. The algorithm randomly assigns the initial position and velocity to the particles and computes the value of the objective function for each particle. Then, the most performing particle, i.e. the particle with the best position d and the best function value b, is identified, and all the particle positions are stored in a matrix. After these preliminary steps, the iteration process starts: for each particle i, a random subset S of particles is chosen. This set does not include the i-th particle. The best position g and the best function value f are identified in the subset S. Using this information, the algorithm can compute the new velocity and position of the i-th particle, utilising the following expressions:

$$v_{PSO}(i) = Wv_{PSO}(i) + y_1u_1(p(i) - x_{PSO}(i)) + y_2u_2(g - x_{PSO}(i)) \tag{6.5a}$$

$$x_{PSO}(i) = x_{PSO}(i) + v_{PSO}(i) \tag{6.5b}$$

where $x_{PSO}(i)$ and $v_{PSO}(i)$ are the position and the velocity of the i-th particle, y_1, y_2, u_1, and u_2 denote the PSO tuning coefficients, and W indicates the inertia

Table 6.2: Identified nonlinear coefficients using the PSO algorithm (Test Rig #1). A swarm size of 40 particles is used to carry out the identification.

PSO	Time [min]	Iterations	Func. Counts	μ_1 [N/m^3]	μ_2 [N/m^3]	$\mu_{2,b}$ [N/m^3]	μ_3 [N/m^3]	Func. Value
Test 1	566.1	77	3120	2.653e6	1.314e6	8.889e6	7.071e6	2.461e-3
Test 2	524.7	74	3000	2.732e6	1.324e6	8.850e6	7.069e6	2.458e-3
Test 3	591.8	87	3520	2.651e6	1.312e6	8.891e6	7.074e6	2.461e-3

coefficient. At this stage another iteration is performed: the updated position $x_{PSO}(i)$ is utilised to re-evaluate the objective function $F(x_{PSO})$. If the objective function value is lower than $F(p)$ the optimal position p is updated with the newly identified position $x_{PSO}(i)$. Finally, if $F(x_{PSO}(i)) < b$ then the optimal value b is updated. At each iteration, the bounds are enforced, and the process is repeated until the change in the objective function is less than the prescribed tolerance.

The identification procedure with meta-heuristic optimisation methods is performed using the following objective function:

$$F(s) = \sum_{j=1}^{P} \sum_{i=1}^{R} (|FRC_{num}(s) - FRC_{exp}|) \tag{6.6}$$

where s is the design variables vector, constituted of the nonlinear unknown coefficients μ_1, μ_2, $\mu_{2,b}$, and μ_3 (see Eq. 6.1), R is the number of discrete frequencies at which the function is evaluated, P is the number of degrees of freedom of the problem, and FRC_{exp} and FRC_{num} represent, respectively, the experimental and numerical frequency response curves associated with the masses displacement, when a constant voltage amplitude is applied to the shaker. The numerical frequency response curve FRC_{num} is obtained by numerically integrating Eq. 6.1, using the MATLAB built-in function *ode45*, a Runge-Kutta scheme. In the experimental measurements, the motion of the shaker is not controlled and it affects the output signals of the system. Specifically, the amplitude of excitation of the shaker might vary in amplitude along the frequency sweeps. To overcome this problem the measured displacement and velocity of the moving constraint are used as forcing input in the numerical integration procedures. The optimisation process is carried out with the aid of the MATLAB built-in functions *ga* and *particleswarm* using the default options. The functions utilised the

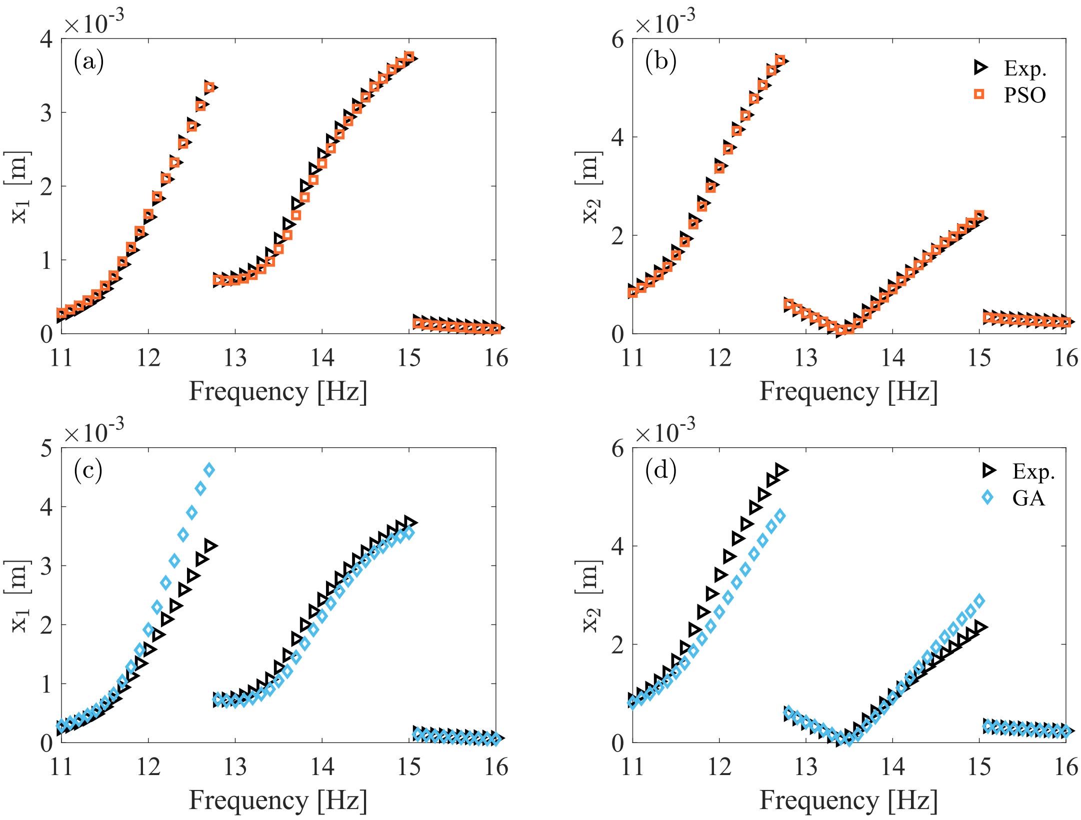

Figure 6.3: Experimental and numerical optimised frequency response curves, representing Test Rig #1. Panels (a-b) show the results obtained with PSO while panels (c) and (d) illustrate the results achieved using the GA [4].

GA and the PSO algorithm previously discussed. For both the optimisation methods, the identification is repeated three times to obtain more robust results, and a multi-core computer (32 cores - Intel(R) Xeon(R) Silver 4214 CPU @ 2.10 GHz, RAM 129 Gb) is utilised to perform the analyses with parallel computing. The objective function is computed considering the experimental FRC with the largest amplitudes of excitation, i.e. 0.4 V. In addition, the computation of the objective function is limited to the following frequency ranges: 11.6 Hz to 12.7 Hz and 13.6 Hz to 15.0 Hz. This allows the optimisation procedure to evaluate the objective function near the resonances, where the density of information about the nonlinear characteristic is higher. The lower and upper boundaries of the optimisation are set, respectively, at $\mu = 10^3$ N/m^3 and $\mu = 10^8$ N/m^3, for all the design variables. The results of the identification procedures are re-

Table 6.3: Identified nonlinear coefficients using the GA algorithm (Test Rig #1). A population of 50 individuals is used to carry out the identification.

GA	Time [min]	Iterations	Func. Counts	μ_1 [N/m^3]	μ_2 [N/m^3]	$\mu_{2,b}$ [N/m^3]	μ_3 [N/m^3]	Func. Value
Test 1	471.8	55	2638	1.259e7	1.685e7	9.162e6	3.104e6	40.705e-3
Test 2	489.3	54	2591	8.093e6	1.785e7	1.446e6	3.363e6	38.705e-3
Test 3	497.5	57	2732	1.002e3	8.612e6	3.537e5	1.296e7	22.668e-3

ported in Tab. 6.2 and 6.3: the tables demonstrate that the PSO have a higher accuracy and tends to converge to the same optimal combination of nonlinear coefficients for the three tests. The associated lowest value of the objective function is 2.458e-3 which represents the best-optimal identified condition. The PSO requires around 550 minutes (9.2 hours) to complete the optimisation procedure. The GA, instead, is faster and converges to an optimal solution in about 490 minutes (8.2 hours). Nonetheless, the algorithm struggles to find an optimal solution and tends to converge to very different combinations of optimal nonlinear coefficients μ. In addition, the optimal solutions are associated with higher values of the objective function. Fig. 6.3 provides a graphical interpretation of the optimisation results of Tab. 6.2 and 6.3, showing the comparison between numerical and experimental FRCs. The numerical FRCs are computed using the linear coefficients previously identified (see Tab. 6.1) and the nonlinear coefficients associated with the best results of PSO and GA. When the nonlinear coefficients obtained with the PSO are used to compute the FRCs, the numerical and experimental frequency responses are in good agreement, as shown by Fig. 6.3 (a) and (b). In this case, the numerical model captures the qualitative and quantitative dynamic behaviour of the experimental test rig, i.e. the model can predict where jumps occur and the amplitude of response of the experimental system along the entire frequency domain. Conversely, the numerical FRCs associated to GA optimal coefficients poorly capture the nonlinear dynamics of the experimental test rig, as shown in Fig. 6.3 (c) and (d), especially in terms of the amplitude of response. The results of Tab. 6.2, Tab. 6.3, and Fig. 6.3 demonstrate the robustness of the PSO and its ability to solve identification problems of nonlinear systems. In addition, it is shown that GA struggles to identify optimal nonlinear coefficients. This suggests that the PSO perform slightly better than the GA when common default options are used in the identification procedure. This

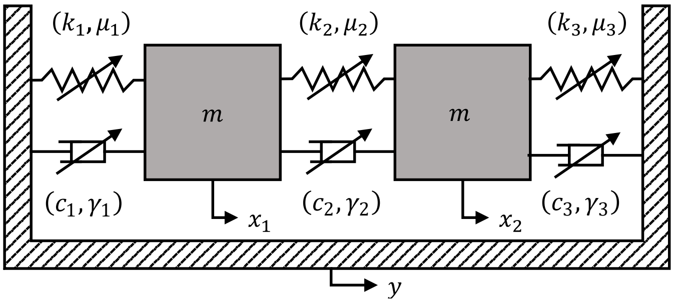

Figure 6.4: Reduced order model with two degrees of freedom and base excitation, representing Test Rig #2. The presence of the arrow indicates a nonlinear behaviour in the connecting element. The letters μ and γ indicate nonlinear stiffness and damping coefficients [3].

result is also in agreement with previous studies [134–136] which, differently from this case, utilised time data to identify the system parameters.

Despite the complexity and the computational cost of the optimisation process, the identification procedure with PSO has been successful, requiring relatively few iterations and particles. This is due to the low number of design variables in the optimisation procedure which simplified the problem. In fact, the linear parameters of the system are identified in a separate way using linear identification methods which are faster and simpler to implement. This improves the capability of the nonlinear identification process, reducing its complexity, and simplifying the overall procedure. This approach is based on the good performance of linear models and identification procedures of linear systems and requires that the investigated nonlinear system possesses an underlying linear system. Despite this limitation, this approach seems to be particularly effective in identifying the parameters associated with strongly nonlinear systems, thus it is better investigated in the following sections.

6.2.3 Identification of a Nonlinear Model - Test Rig #2

In this section, a nonlinear mathematical model representing the nonlinear dynamic behaviour Test Rig #2 is identified. The same procedure utilised in Sections 6.2.1 and 6.2.2 are utilised to identify a model that represents the linear and nonlinear behaviour of the test rig. As for the previous case, a ROM model is selected based on the available experimental data. The Test Rig #2 utilises the two-mass system designed in Chapter 4 for which a two-DOF model has been demonstrated to be sufficiently accurate to capture the underlying linear behaviour of Test Rig #1. Nonetheless, Test Rig #2 is excited differently, as the vibrating table moves both supports. To take into account this change, the ROM represented by Fig. 6.4 is utilised in the identification procedure whose equation of motion is represented by the following expression:

$$m\ddot{z}_1 + c_1\dot{z}_1 + c_2(\dot{z}_1 - \dot{z}_2) + k_1 z_1 + k_2(z_1 - z_2) + \mu_1 z_1^3 + (\mu_2 z_1^3 - \mu_{2b} z_1^2 z_2 + \\ + \mu_{2b} z_1 z_2^2 - \mu_2 z_2^3) = -m\ddot{y} \tag{6.7a}$$

$$m\ddot{z}_2 + c_3\dot{z}_2 - c_2(\dot{z}_1 - \dot{z}_2) + k_3 z_2 - k_2(z_1 - z_2) + \mu_3 z_2^3 - (\mu_2 z_1^3 - \mu_{2b} z_1^2 z_2 + \\ + \mu_{2b} z_1 z_2^2 - \mu_2 z_2^3) = -m\ddot{y} \tag{6.7b}$$

To create a parallelism with the previous section the same cubic nonlinear characteristic is utilised and no nonlinear damping contributions (γ) are considered at this stage. Linear stiffness, damping, and mass matrices are identified again. The estimated

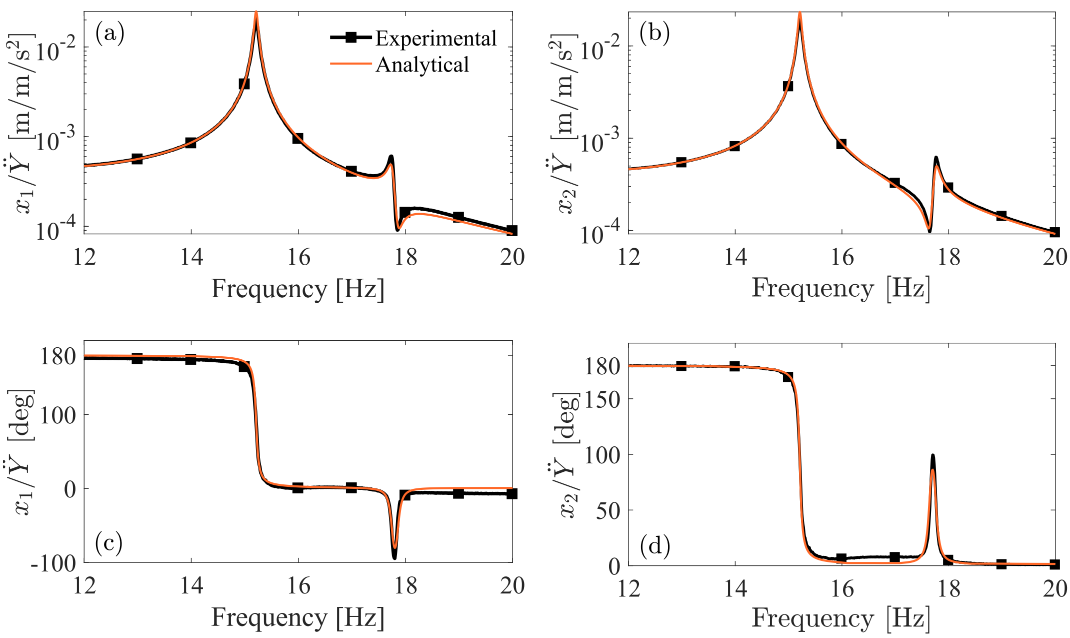

Figure 6.5: Experimental (black line) and the analytical optimised (orange line) transfer functions representing Test Rig #2. The transfer functions are shown in terms of amplitude (a,b) and phase (c,d) of the two degrees of freedom [3].

coefficients are then improved via an optimisation procedure, minimising the difference between the experimental and the analytical transfer functions in terms of amplitude and phase. Once again, the MATLAB function *lsqnonlin* is used and the receptance is adopted as a reference transfer function for the minimisation procedure. The analytical formulation of the receptance (linear transfer function) for the considered ROM is represented by the following expressions:

$$H_{B,1} = \frac{X_1}{\ddot{Y}} = \frac{X_2\,k_2 - \frac{\ddot{Y}\,k_1}{\Omega^2} + \Omega\,X_2\,c_2\,i - \frac{\ddot{Y}\,c_1\,i}{\Omega}}{\ddot{Y}\,(k_1 + k_2 - \Omega^2\,m + \Omega\,(c_1 + c_2)\,i)} \tag{6.8a}$$

$$H_{B,2} = \frac{X_2}{\ddot{Y}} = \frac{X_1\,k_2 - \frac{\ddot{Y}\,k_3}{\Omega^2} + \Omega\,X_1\,c_2\,i - \frac{\ddot{Y}\,c_3\,i}{\Omega}}{\ddot{Y}\,(k_2 + k_3 - \Omega^2\,m + \Omega\,(c_2 + c_3)\,i)} \tag{6.8b}$$

where, X_1 and X_2 are the complex amplitudes of the absolute displacements of the two degrees of freedom, $\ddot{Y}$ represents the complex amplitude of the acceleration input, Ω denotes the forcing frequency of the excitation, and H_B is the transfer function (receptance) of the Test Rig #2. The estimated and optimised linear coefficients are reported in Tab. 6.4. The mass matrix, as discussed in Section 6.2.1, is estimated via direct measurement of the mass of each block which is found equal to 0.1365 Kg. Fig. 6.5

Table 6.4: Linear coefficients representing Test Rig #2. The coefficients are identified using the procedure outlined in Section 6.2.1.

Coefficients	c_1 [Ns/m]	c_2 [Ns/m]	c_3 [Ns/m]	k_1 [N/m]	k_2 [N/m]	k_3 [N/m]
Estimated	0.0727	0.0256	0.0750	1235.8	225.3	1256.3
Optimised	0.0582	0.0205	0.0600	1232.9	225.1	1261.9

shows the comparison between the experimental and optimised transfer functions in terms of amplitude (panel (a) and (b)) and phase (panels (c) and (d)) for the two considered degrees of freedom. The figure highlights the good match between the analytical and experimental TFs, demonstrating that the chosen ROM captures the dynamics of the experimental test rig in the linear regime.

The nonlinear parameters of the system are identified using meta-heuristic optimisation. The frequency range where there is the largest experimental amplitude of response, i.e. 14.5 - 16.2 Hz, is used in the minimisation process. Given its good performance, only the PSO algorithm is used in the identification process. The identification

Table 6.5: Identified nonlinear coefficients using the PSO algorithm (Test Rig #2). A population of 40 individuals is used to carry out the identification.

PSO	Time [min]	Iterations	Func. Counts	μ_1 [N/m^3]	μ_2 [N/m^3]	$\mu_{2,b}$ [N/m^3]	μ_3 [N/m^3]	Func. Value
Test 1	138.3	144	5800	3.298e+07	4.281e+07	8.882e+07	1.000e+03	37.758e-3
Test 2	79.7	49	2000	3.303e+07	2.797e+07	4.554e+07	1.000e+03	37.581e-3
Test 3	77.1	41	1680	3.310e+07	2.770e+07	4.687e+07	1.000e+03	37.581e-3
Test 4	89.7	46	1880	3.263e+07	4.992e+07	9.999e+07	3.136e+04	37.580e-3
Test 5	76.2	68	2760	2.823e+07	1.075e+07	1.123e+07	3.262e+06	37.646e-3
Test 6	47.8	68	2760	2.823e+07	1.075e+07	1.123e+07	3.262e+06	37.646e-3
Test 7	55.2	68	2760	2.823e+07	1.075e+07	1.123e+07	3.262e+06	37.646e-3
Test 8	35.3	44	1800	4.997e+06	3.319e+07	1.435e+06	1.444e+07	38.428e-3

is repeated 8 times to obtain robust results which are reported in Tab. 6.5. Using perfect sinusoidal excitation loads, the identification process becomes much faster than the case of Test Rig #1 [1]. However, this results in passing less information to the PSO which in turn affects the identification procedure, increasing the obtained minimum function values (see Tab. 6.5). The best nonlinear coefficients, i.e. the coefficients associated

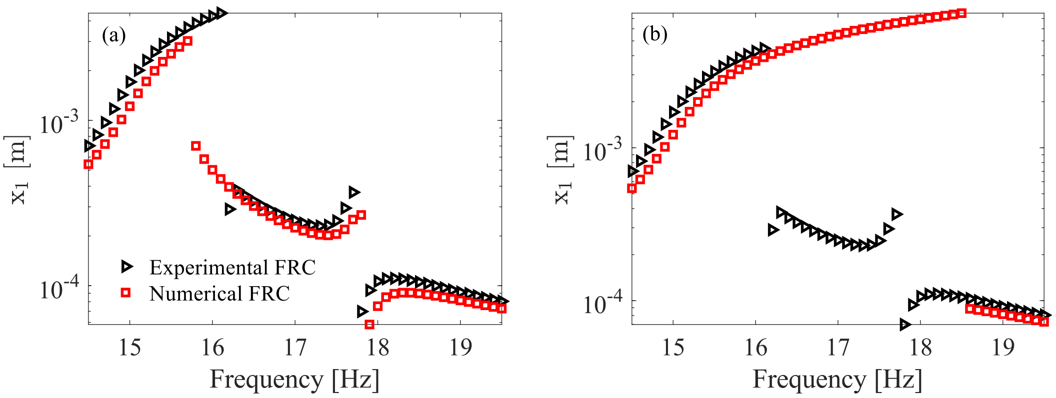

Figure 6.6: Comparison between numerical and experimental FRC representing Test Rig #2: the numerical FRC is computed resetting (a) and non-resetting (b) the initial conditions.

with the minimum objective function value in Tab. 6.5, are then used to perform a comparison between numerical and experimental FRCs. The numerical FRCs are computed with a forward frequency sweep with and without resetting the initial conditions at each frequency of excitation. In the first case, the initial conditions are imposed equal to zero for each frequency of excitation. Instead, when the initial conditions are

[1] For practical reasons, the simulations were performed using a different multi-core computer (10 cores - 12th Gen Intel(R) Core(TM) i7-12700H @ 2.30 GHz, RAM 16 Gb)

not reset, the last state of the numerical simulation at the previous frequency of excitation is used as initial conditions for the next simulation. The comparison between numerical and experimental FRCs of the first mass is shown in Fig. 6.6.

Although the hardening nonlinear behaviour is caught, the identified nonlinear model is not able to predict the qualitative dynamic behaviour of the experimental test rig, i.e. the model does not identify the frequency at which the experimental system shows jumps from high-amplitude to low-amplitude response. When the initial conditions are reset (Fig. 6.6(a)) jumps occur prematurely in the numerical FRC. When the numerical FRC is 'continued', (Fig. 6.6(b)), the jump occurs at a very high frequency. This indicates that the identification of the system has not been successful as the identified nonlinear model is not able to capture the qualitative dynamic behaviour of the experimental test rig. To solve this problem, a novel method for the identification of the MDOF nonlinear system is proposed and applied to Test Rig #2 in the following section.

6.3 Experimental Identification via Nonlinear Restoring Force Method

The previous section demonstrated that the separation of linear and nonlinear contributions is particularly effective for the identification of equivalent mathematical models that represent strongly nonlinear systems. Nonetheless, direct optimisation of predetermined nonlinear systems might lead to inaccurate models. Building upon this knowledge, this section introduces a novel methodology for the identification of nonlinear systems with strong nonlinear characteristics, named the Nonlinear Restoring Force (NLRF) Method. This method is based on the well-established Restoring Force Surface (RFS) method [137–139] and exploits the separation between linear and nonlinear behaviour of the system. The method applies to any mechanical system which shows an underlying linear behaviour, it allows the nonlinear properties of MDOF mechanical systems to be characterised, and it does not require the selection of the form of nonlinear characteristics, before the identification. In this section, the method is introduced and applied to a numerical example. Then the technique is applied to identify the smooth nonlinear characteristics of the Test Rig #2. Finally, using the successful identification of Test Rig #1, the non-smooth characteristics of Test Rig #1 are graphically reconstructed and identified using the proposed method.

6.3.1 Nonlinear Restoring Force Method: Introduction

Since the 60s, different identification methods for nonlinear systems have been proposed in the literature. Kerschen at al. [70,71] reviewed the various identification methods and provided guidelines for their usage. Among the different methods, the Restoring Force Surface (RFS) method is considered one of the most suitable and effective methods for the identification of nonlinear systems [138]. Thanks to its simplicity, the RFS has been used for the identification of very different mechanical systems: Bonisoli et al. [140] utilized the RFS method to identify the nonlinear parameters of a passive magneto-elastic suspension. Cammarano et al. [6] effectively employed the RFS method to extract the nonlinear characteristics of a vibration energy harvester with two potential wells, whereas Rizos et al. [141] applied the method to a leaf-spring-based tuned mass damper. Considering a real-life scenario, Noël et al. [12] employed the RFS method to identify trilinear characteristics of a small real satellite. They demonstrated that the identified system accurately reproduced the nonlinear behaviour of the satellite with high precision, even within such a complex structure. In another practical scenario, Kerschen et al. [11] utilised the RFS method to identify the nonlinear properties associated with a wing of an aircraft. The authors successfully identified the nonlinear properties and applied them to conduct a numerical analysis of the NNMs associated with a ROM. In a recent work, Anastasio et al. [142] employed the RFS method to determine the nonlinear stiffness properties of a Duffing-like negative stiffness oscillator. These examples collectively demonstrate the robust capabilities and reliability of the method in identifying nonlinear characteristics of mechanical systems.

A modified version of the RFS method for the identification of MDOF-ROM systems is here presented: the method, named the Nonlinear Restoring Force (NLRF) method, builds on the work of Masri et al. [139,143] and it is based on the assumption that the restoring force is composed of linear and nonlinear components. Taking into account a previous linear identification, the method is able to identify the nonlinear characteristics of a chosen ROM. The separation in linear and nonlinear restoring forces components is not new to literature; e.g., in the Condition Reversed Path (CRP) method proposed by Richard and Singh [144], the linear and nonlinear parts of the system are identified separately in the frequency domain. Likewise, in [145, 146], authors resorted to the same concept, separating the linear and the nonlinear contributions to apply different identification methods. Nonetheless, unlike the previously listed methods, the proposed NLRF method allows one to obtain a graphical representation of the nonlinear restoring force in the form of a surface. This is then used to identify the nonlinear characteristic of the system. The graphical representation has the intrinsic advantage of showing the minimal dimensional space that fully describes the surface, i.e., it shows the dependence of the nonlinear restoring force on the different DOFs. This allows for establishing engineering considerations which can simplify and improve the identification of the unknown nonlinear function.

The proposed NLRF method is schematically reported in Fig. 6.7. The method

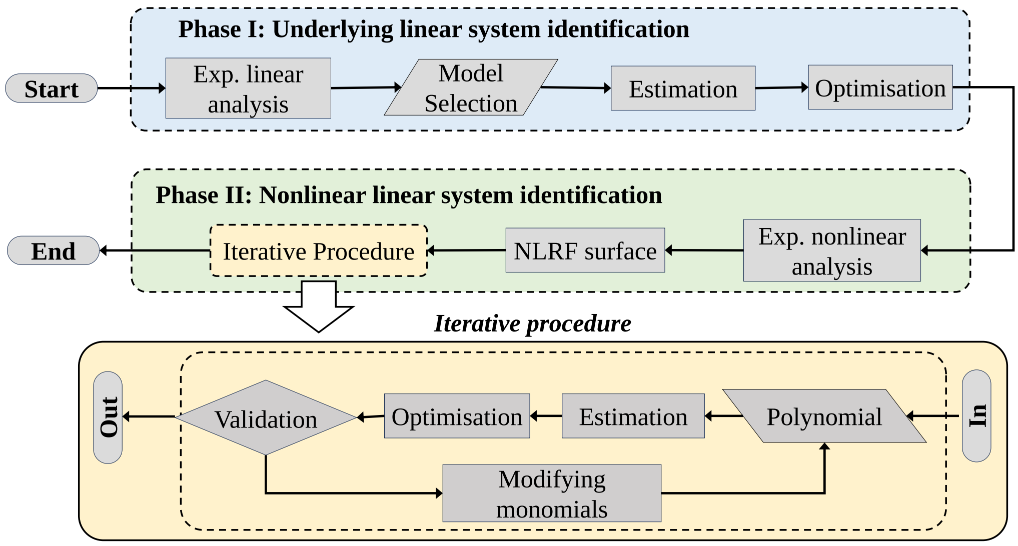

Figure 6.7: Flowchart of the identification procedure. The main phases (linear identification and nonlinear identification) are described in different blocks.

is constituted of two phases: in the first phase an underlying linear system is identified using the procedure outlined in Section 6.2. The second phase, instead, tries to identify nonlinear characteristics of the investigated nonlinear system. To this end, an experimental nonlinear analysis with sinusoidal frequency sweeps is performed and the NLRF surfaces are created. The obtained surfaces are then used to perform engineering considerations, identifying a suitable polynomial function capable of representing the nonlinear contributions of the system. The degree of the polynomial is chosen through an iterative procedure. Specifically, a polynomial is assumed and then the associated coefficients are identified via a Least Mean Square (LMS) process. This results in a first estimation of the nonlinear coefficients which are then used as a starting point for a minimisation process. The optimised coefficients are then utilised, along with the identified linear ROM, to perform numerical predictions of the identified model and are compared against sets of experimental data. The reference experimental data must be different from the one adopted in the identification process, i.e. the one used to generate the NLRF. If the validation is successful, then the linear and nonlinear contributions are considered to be identified.

Mathematically, the NLRF method is applied by manipulating the general equation of motion of an n-DOF reduced-order mechanical system in matrix form, resulting in the following equation:

$$\mathbf{N}_{RF} = \mathbf{N}(\dot{\mathbf{x}}, \mathbf{x}) = \mathbf{F} - \mathbf{M}\ddot{\mathbf{x}} - \mathbf{C}\dot{\mathbf{x}} - \mathbf{K}\mathbf{x} \tag{6.9}$$

where $\mathbf{x} \in \mathbb{R}^{n\times 1}$ is the displacement vector, $\mathbf{M}$, $\mathbf{C}$, and $\mathbf{K} \in \mathbb{R}^{n\times n}$, represent the mass, damping, and stiffness matrices of the linear system, while $\mathbf{N}(\dot{\mathbf{x}}, \mathbf{x})$ and $\mathbf{F} \in \mathbb{R}^{n\times 1}$ are the nonlinear contribution and forcing function. Eq. 6.9 allows to obtain the nonlinear restoring force $\mathbf{N}_{RF}$. This term contains all the nonlinear contributions of the system and the NLRF method aims to identify a nonlinear function which correctly describes this term. Building on the previous identification of the underlying linear system (see Section 6.2.3), the left-hand side of Eq. 6.9 is known for any time instant experimentally measured. This permits to plot the experimental nonlinear restoring force surface for each degree of freedom of the ROM. It is worth mentioning that: (1)

the method needs a ROM for its application and (2) utilises physical coordinates. The usage of a ROM is fundamental to limiting the number of NLRF surfaces and the complexity of the subsequent identification process. Real coordinates are selected for their straightforward nature, which enables easy integration with experimental sensors and facilitates a clear understanding of the resulting surfaces in a physical context.

The original version of the RFS method utilises Chebyshev series [138] for the identification procedure, but simple polynomial expansions have been demonstrated to be superior in terms of simplicity, accuracy, and speed in the estimation of the nonlinear contributions [70]. Nevertheless, the utilisation of such polynomials without prior knowledge of the system might lead to erroneous results, as the restoring force may not be governed by integer-power polynomials. In this work, the attention is focused on mechanical structures with geometric nonlinearities subjected to large deformations for which integer-order polynomials are found to be a good approximation, as shown in [4, 27–29]. Based on the above considerations, a least mean square problem can be formulated for each degree of freedom when a time series is available, using the following linear system of equations:

$$\mathbf{N}_{RF,n} = \mathbf{p}(\mathbf{x}, \dot{\mathbf{x}}, a_1, ..., a_k) = \mathbf{A}(\mathbf{x}, \dot{\mathbf{x}})\mathbf{b} \tag{6.10}$$

where n represents the number of reduced-DOF, v indicates the time instant, $\mathbf{N}_{RF,n}$ is a vector which varies in time and represents the nonlinear restoring force of a single DOF, $\mathbf{p}$ is a vector representing the values of a polynomial which depends on the coefficients a_k and the displacement/velocities of each DOF, A is a matrix with dimensions $v \times k$, and $\mathbf{b} = [a_1, ..., a_k]$ is a vector $k \times 1$. By solving Eq. 6.10, it is possible to obtain an estimation of the polynomial coefficients which are then used as a starting point for a minimisation procedure. During the minimisation process the following objective function $\mathbf{G}$ is used :

$$\mathbf{G}(\mathbf{b}) = \mathbf{N}_{RF,n} - \mathbf{p}(\mathbf{x}, \dot{\mathbf{x}}, \mathbf{b}) \tag{6.11}$$

Eq. 6.10 and 6.11 are adopted in the iterative procedure illustrated in Fig. 6.7. The procedure is repeated until the validation conditions are not satisfied.

6.3.2 Nonlinear Restoring Force Method: Numerical Example

In order to show how the method works, a numerical example is described in this section. The example serves to explain how the NLRF surfaces can help and improve the identification of the nonlinear ROM: the idea is to exploit the generated NLRF surfaces to obtain additional information on the nonlinear dynamics of the system. Such information enables engineering considerations that can simplify the polynomial representation of the nonlinear restoring force.

To provide parallelism with the investigated test rig, the numerical example considers a two-DOF ROM with generic smooth nonlinear characteristics. Specifically, the considered model is schematically represented in Fig. 6.4 where the mass is indicates by m, the linear stiffness/damping coefficients are denoted by k_1, k_2, k_3 and c_1, c_2, c_3, while the nonlinear stiffness and damping characteristics are symbolised by μ_1, μ_2, μ_3 and γ_1, γ_2, γ_3. This system is mathematically represented by the following set of ODEs:

$$m\ddot{z}_1 + c_1\dot{z}_1 + c_2(\dot{z}_1 - \dot{z}_2) + k_1 z_1 + k_2(z_1 - z_2) + N_{RF,1}(z_1, z_2, \dot{z}_1, \dot{z}_2) = -m\ddot{y} \quad (6.12a)$$

$$m\ddot{z}_2 + c_3\dot{z}_2 - c_2(\dot{z}_1 - \dot{z}_2) + k_3 z_2 - k_2(z_1 - z_2) + N_{RF,2}(z_1, z_2, \dot{z}_1, \dot{z}_2) = -m\ddot{y} \quad (6.12b)$$

where $\ddot{y}$ indicate the base acceleration, $z = x - y$ is the relative displacement, and $N_{RF,1}$ and $N_{RF,2}$, instead, define the nonlinear restoring terms associated with the first and second DOF. Considering the absolute acceleration $\ddot{x}$, the nonlinear restoring force $\mathbf{N}_{RF}$ is expressed by:

$$\mathbf{N}_{RF} = \begin{cases} N_{RF,1}(z_1, z_2, \dot{z}_1, \dot{z}_2) = -m\ddot{x}_1 - c_1\dot{z}_1 - c_2(\dot{z}_1 - \dot{z}_2) - k_1 z_1 - k_2(z_1 - z_2) \\ N_{RF,2}(z_1, z_2, \dot{z}_1, \dot{z}_2) = -m\ddot{x}_2 - c_3\dot{z}_2 + c_2(\dot{z}_1 - \dot{z}_2) - k_3 z_2 + k_2(z_1 - z_2) \end{cases} \quad (6.13)$$

The general form of the sought polynomial is represented by the following equation:

$$p(z_1, z_2, \dot{z}_1, \dot{z}_2, a_1, ..., a_j) = a_1 z_1^2 + a_2 z_2^2 + a_3 \dot{z}_1^2 + ... + a_{11} z_1^3 + a_{12} z_2^3 + a_{13} \dot{z}_1^3 + ... \quad (6.14)$$

where j represents the number of coefficients. Because the method wants to identify the restoring forced purified by the linear components, the polynomial starts from the second degree. The nonlinear MDOF-ROM is considered in two different configurations: in the first version (configuration-A) the nonlinearities are applied only to the external elements. In the second version (configuration-B), the nonlinearities are applied to every connecting element of the system. Tab. 6.6 and Tab. 6.7 resume the property utilised in the two numerical examples: for the sake of simplicity, only nonlinear stiffness elements are applied to the model. Thus, the equation of motion can be rewritten as follows:

$$m\ddot{z}_1 + c_1\dot{z}_1 + c_2(\dot{z}_1 - \dot{z}_2) + k_1 z_1 + k_2(z_1 - z_2) + \mu_1 z_1^3 + \mu_2(z_1 - z_2)^3 = -m\ddot{y} \quad (6.15a)$$

$$m\ddot{z}_2 + c_3\dot{z}_2 - c_2(\dot{z}_1 - \dot{z}_2) + k_3 z_2 - k_2(z_1 - z_2) + \mu_3 z_2^3 - \mu_2(z_1 - z_2)^3 = -m\ddot{y} \quad (6.15b)$$

The numerical data are generated by numerically integrating Eq. 6.15. To this end, the MATLAB built-in function *ode45*, a classical Runge-Kutta integration scheme, is utilised. The numerical results are collected similarly to the experimental data by performing forward frequency sweeps from 15.5 to 23.5 Hz and recording the entire time history for the two DOFs. The discrete increase of excitation frequency is set to 0.16 Hz so that the FRC is evaluated on 51 excitation frequencies. Fig. 6.8 shows the absolute displacements of the two DOFs for configuration A. The figure shows the

Table 6.6: Linear parameters adopted in the numerical example.

Config.	m [kg]	k_1 [N/m]	k_2 [N/m]	k_3 [N/m]	c_1 [Ns/m]	c_2 [Ns/m]	c_3 [Ns/m]
A	1.0×10^{-1}	1.5×10^{3}	2.5×10^{2}	1.0×10^{3}	3.0×10^{-2}	2.5×10^{-2}	6.5×10^{-2}
B	1.0×10^{-1}	1.5×10^{3}	2.5×10^{2}	1.0×10^{3}	3.0×10^{-2}	2.5×10^{-2}	6.5×10^{-2}

Table 6.7: Nonlinear parameters and excitation amplitude utilised in the numerical example.

Config.	μ_1 [N/m^3]	μ_2 [N/m^3]	μ_3 [N/m^3]	Y [mm]
A	5.0×10^{6}	0.0	2.8×10^{6}	5×10^{-2}
B	5.0×10^{6}	1.0×10^{6}	2.8×10^{6}	5×10^{-2}

presence of two bent resonance peaks just after the linear resonance of the system, which leads to the typical jumping phenomena of nonlinear hardening structures. Despite the nonlinearities being applied only between the masses and the supports (external

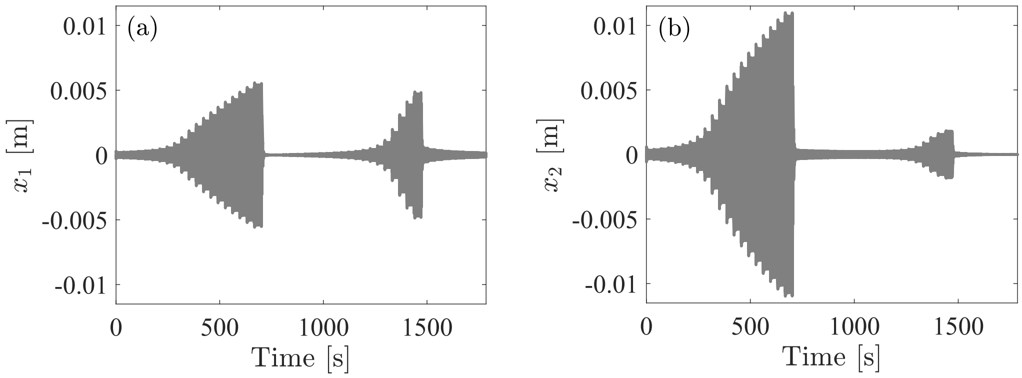

Figure 6.8: Numerical time history of the first (a) and second (b) DOF. The numerical results are obtained with the reduced order model described by Eq. 6.15 and the parameters reported in Tab. 6.6 and Tab. 6.7 for only configuration A [3].

elements), the time histories and the associated FRCs of the two DOFs are not able to provide any information about the location of the nonlinearities of the system, as the jumps are found on both peaks for both the DOFs. On the contrary, using the NLRF surfaces, it is possible to obtain additional information on the system dynamics. The obtained NLRF surfaces (configuration A and B) are reported in Fig. 6.9 considering two different reduced nonlinear spaces, i.e. z_1 and $\dot{z}_1$ for $N_{RF,1}$ and z_2 and $\dot{z}_2$ for $N_{RF,2}$. When the full nonlinear system (configuration B) is taken into account, the NLRF surfaces appear as illustrated by panels (g-h) of Fig. 6.9. The surfaces are not a function in the considered 3D space, i.e., they are hyper-surfaces [2] as the nonlinear contribution on each DOF depends on more than one mechanical DOF and thus it cannot be fully represented in the reduced subspace. This is clearly illustrated by the lateral views in the panels (e,f), where it is shown that for some elements of the nonlinear domain, there exists more than one value of the NLRF. The NLRF surfaces associated with configuration A are reported in panels (c) and (d), with the lateral view shown in panels (a) and (b) of Fig. 6.9. In this case, the entire recorded time history lies on a single surface that is graphically representable as a function in the considered 3D space, i.e. in the reduced subspace. This can be achieved because the

[2] For hyper-surface it is intended a surface function that depends on a number of parameters larger than two, hence that is not representable as a function in a 3D space. On the contrary, surfaces are a function of two parameters which enables the representation in a 3D space.

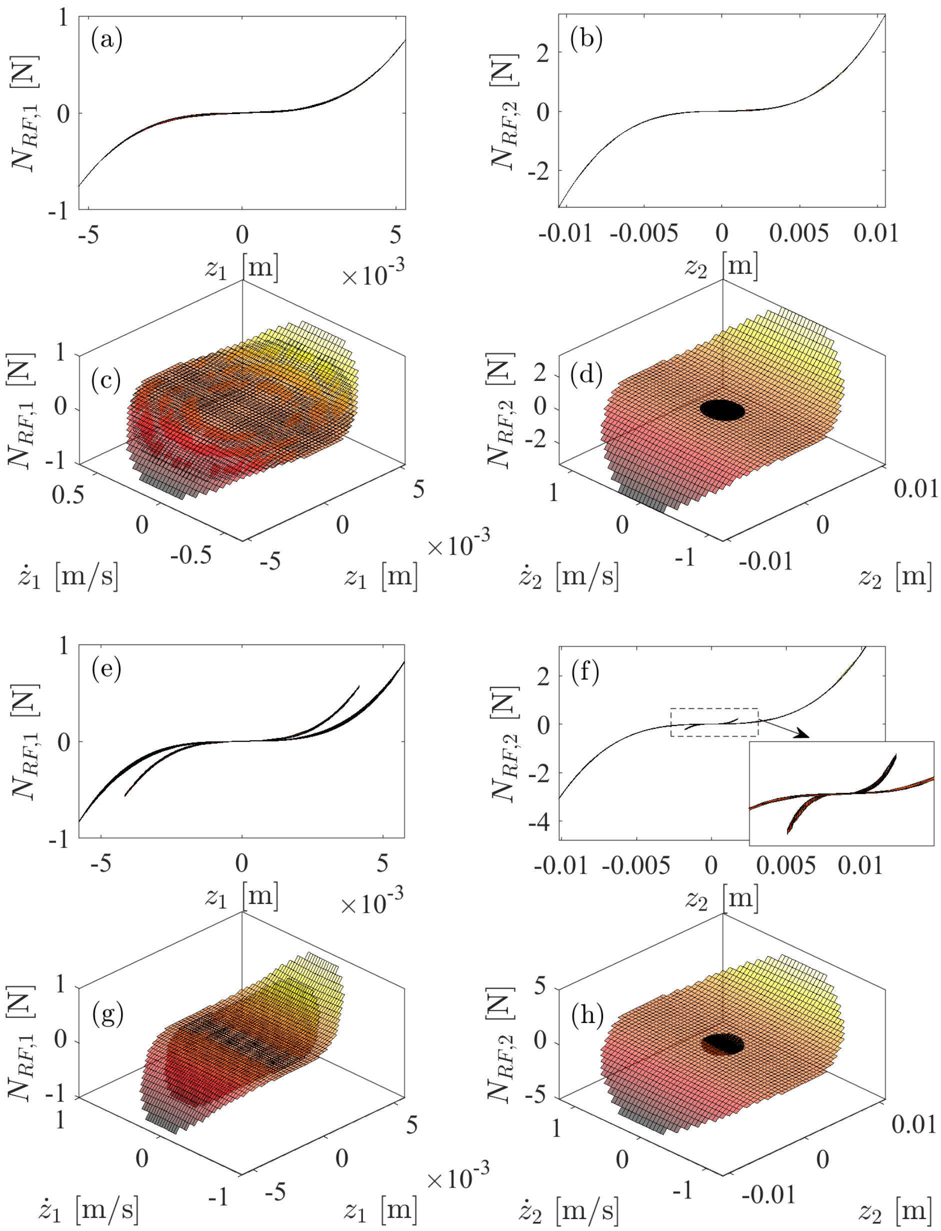

Figure 6.9: Numerical nonlinear restoring force surfaces of the first and second DOF for case A (a,b,c,d) and case B (e,f,g,h). Zooms in the plane relative displacement-restoring force are reported for each diagram in panels (a), (b), (e), and (f) [3].

Table 6.8: Nonlinear coefficients identified in the numerical test (configuration A). The numerical zeros values are represented with the symbol $\varnothing$. For each restoring force surface, a different polynomial is used.

Monom. (M_1)	Coeff.	Value	Monom. (M_2)	Coeff.	Value
z_1^2	a_1	$\varnothing$	z_2^2	b_1	$\varnothing$
$z_1\dot{z}_1$	a_2	$\varnothing$	$z_2\dot{z}_2$	b_2	$\varnothing$
$\dot{z}_1^2$	a_3	$\varnothing$	$\dot{z}_2^2$	b_3	$\varnothing$
z_1^3	a_4	5.00×10^6 N/m^3	z_2^3	b_4	2.80×10^6 N/m^3
$\dot{z}_1^3$	a_5	$\varnothing$	$\dot{z}_2^3$	b_5	$\varnothing$
$z_1\dot{z}_1^2$	a_6	$\varnothing$	$z_2\dot{z}_2^2$	b_6	$\varnothing$
$z_1^2\dot{z}_1$	a_7	$\varnothing$	$z_2^2\dot{z}_2$	b_7	$\varnothing$

linear contribution of the restoring force has been removed and the nonlinearities are localised, i.e. they only depend on the local degree of freedom. It is worth noticing that, given a general mechanical MDOF system, the classical definition of the restoring force surface, with linear and nonlinear contributions, always leads to a hyper-surface. This is a consequence of the definition of the system, as the minimal dimensional space for mechanical MDOF is composed of two displacements and two velocities. Nonetheless, moving to a space dominated only by the nonlinear contributions of the restoring force, it is possible to represent the restoring force surfaces as a function in a 3D space if the nonlinearities are localised in the mechanical system. This fact has important consequences for the identification of nonlinear characteristics. Indeed, considering the obtained NLRF surfaces, the sought polynomial for the system in configuration A can be simplified by accounting for only a local mechanical DOF. Eq. 6.14 is thus modified as follows:

$$\mathbf{N}_{RF} = \begin{cases} N_{RF,1}(z_1, \dot{z}_1) = a_1 z_1^2 + a_2 \dot{z}_1^2 + a_3 z_1 \dot{z}_1 + a_4 z_1^3 + a_5 \dot{z}_1^3 + a_6 z_1^2 \dot{z}_1 + ... \\ N_{RF,2}(z_2, \dot{z}_2) = b_1 z_2^2 + b_2 \dot{z}_2^2 + b_3 z_2 \dot{z}_2 + b_4 z_2^3 + b_5 \dot{z}_2^3 + b_6 z_2^2 \dot{z}_2 + ... \end{cases} \tag{6.16}$$

Assuming that the linear properties are known, the nonlinear contribution is identified using Eq. 6.10 and 6.11. The identification is performed only for configuration A and the obtained nonlinear parameters are reported in Tab. 6.8 for a full third-order polynomial. The table demonstrates that the nonlinear coefficients are correctly identified and, thanks to the absence of noise, a very close match between the assumed polynomials and the numerical data is achieved.

6.3.3 Nonlinear Restoring Force Method: Experimental Identification of Smooth Nonlinear Characteristics

The NLRF is now utilised to identify smooth nonlinear characteristics from experimental data. To this end, the experimental data associated with Test Rig #2 (without the motion limiting constraints) are used in the identification procedure. Although it would be ideal to directly measure the acceleration, velocity, and displacement of each measurement point [147], numerical integration/derivation procedures have been demonstrated to generate sufficiently accurate RFS [6]. In the considered experimental setup, the velocity and displacement of the two main blocks are obtained via numerical integration of the accelerometer and laser vibrometer signals. The velocity of the vibrating table, instead, is obtained via numerical differentiation of the displacement signal. The time data are then filtered with a high-pass filter (5 Hz) and a low-pass filter (75 Hz) to remove high-frequency components and the drifting introduced by the numerical integration/derivation procedure. In addition, the band filter allows obtaining smooth NLRF surfaces which facilitate the identification of the unknown polynomial coefficients.

The linear coefficients representing the underlying linear behaviour of the system can be retrieved from Tab. 6.4 and Eq. 6.13 can be used to compute the experimental nonlinear restoring force. The experimental NLRF surfaces are graphically represented in a reduced nonlinear space constituted of the displacement of the velocity of each DOF. The experimental NLRF surfaces are reported in Fig. 6.10. The figure shows that, in the reduced nonlinear space, the restoring force surfaces are representable as a 3D surface. This indicates that the nonlinear behaviour of each DOF can be fully described by a single local mechanical DOF, e.g., $N_{RF,1}$ is a function of z_1 and $\dot{z}_1$. In other words, the majority of the nonlinear contributions of the experimental test rig are provided by the parallel beams that connect the two blocks to the supports. This does not mean that parallel beams in between the two blocks behave linearly, but that their nonlinear contribution is negligible in the considered dynamic configuration.

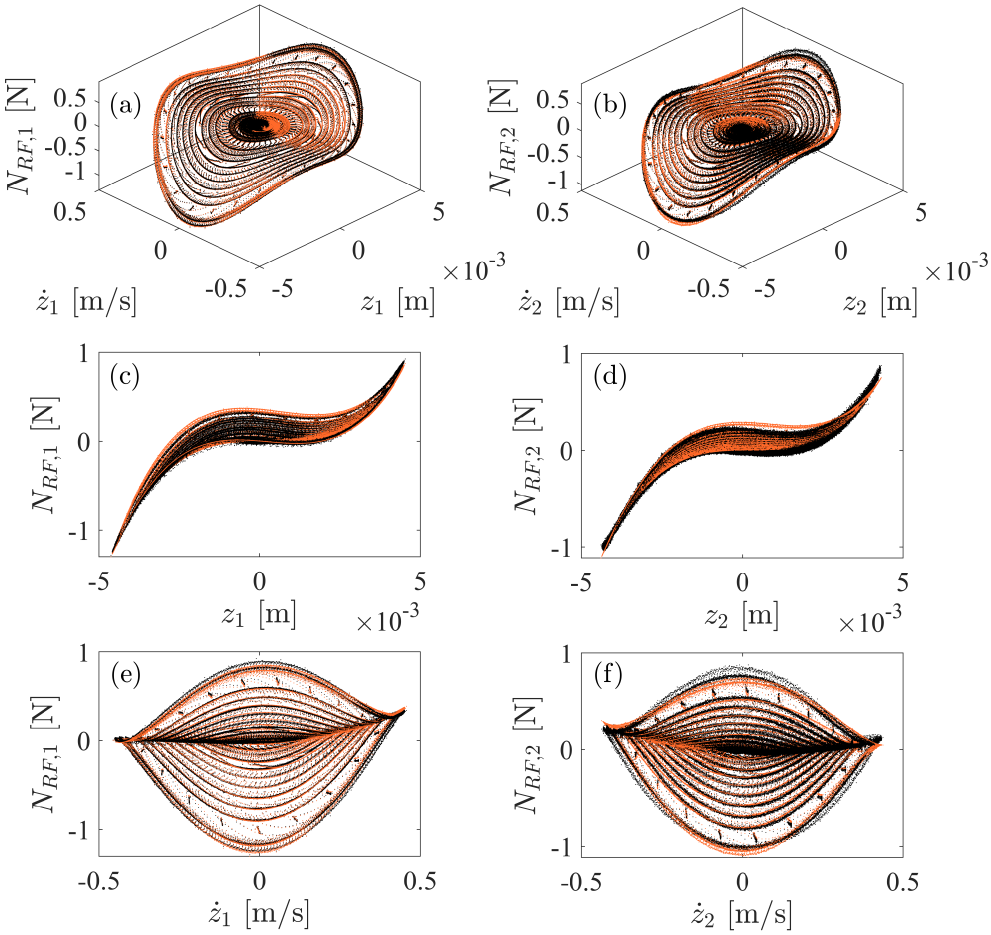

Figure 6.10: Identified (orange) and the experimental (black) nonlinear restoring force surfaces of Test Rig #2 (without motion limiting constraints). Forward frequency sweeps with 0.05 mm excitation amplitude are utilised to generate the data. The left and right panels show the NLRF surfaces associated with the first and second DOF, respectively [3].

The experimental data generated from forward frequency sweep at an amplitude equal to 0.05 mm are used to generate the NLRF surfaces and to identify the nonlinear characteristics. The prediction capabilities of the identified model, instead, are tested against different sets of experimental data, namely against the FRCs obtained with base amplitude equal to 0.04 and 0.03 mm.

In order to identify the experimental nonlinear contributions of the test rig, different polynomials are tested: by increasing the complexity of the chosen polynomial,

Table 6.9: Nonlinear characteristics identified from the experimental data (smooth version of Test Rig #2). For each degree of freedom, a different polynomial is utilised (as prescribed in the table).

Monom. (M_1)	Coeff.	Value	Monom. (M_2)	Coeff.	Value
z_1^2	a_1	$-8.4608 \times 10^3\,\mathrm{N/m^2}$	z_2^2	b_1	$-8.3989 \times 10^3\,\mathrm{N/m^2}$
$z_1\dot{z}_1$	a_2	$5.3189\,\mathrm{Ns/m^2}$	$z_2\dot{z}_2$	b_2	$-4.8546\,\mathrm{Ns/m^2}$
$\dot{z}_1^2$	a_3	$0.9055\,\mathrm{Ns^2/m^2}$	$\dot{z}_2^2$	b_3	$0.904\,66\,\mathrm{Ns^2/m^2}$
z_1^3	a_4	$1.1237 \times 10^7\,\mathrm{N/m^3}$	z_2^3	b_4	$1.1231 \times 10^7\,\mathrm{N/m^3}$
$\dot{z}_1^3$	a_5	$1.9777\,\mathrm{Ns^3/m^3}$	$\dot{z}_2^5$	b_5	$-8.0214\,\mathrm{Ns^5/m^5}$
$z_1\dot{z}_1^2$	a_6	$-1.3876 \times 10^2\,\mathrm{Ns^2/m^3}$	–	–	–
$z_1^2\dot{z}_1$	a_7	$1.0495 \times 10^4\,\mathrm{Ns/m^3}$	–	–	–

i.e., the number of monomials that compose the polynomial and the associated order, the number of unknowns increases exponentially, leading to high computation burden and expensive calculations. Nonetheless, exploiting the information of localised nonlinearities provided by the NLRF surfaces, the number of variables for each polynomial can be considerably reduced because the polynomial for each degree of freedom can be written using local coordinates, i.e. z_1, $\dot{z}_1$ for the first surface and z_2, and $\dot{z}_2$ for the second one. This enables the usage of Eq. 6.16 to represent the nonlinear polynomials.

The polynomial order, instead, is selected by applying the iterative procedure reported in Fig. 6.7: initially, a polynomial is chosen and the associated coefficients are identified using the LMS and optimisation procedures previously described. Finally, the numerical predictions of the identified model are compared against sets of experimental data that have not been used in the identification process. The numerical time histories are computed by exciting the system with perfect sinusoidal excitation and using the same discrete frequency sweep adopted in the experimental measurements. Such simulations provide important insights into the dynamics of the system: firstly they tell us the amplitude of response of the system along the frequency sweep, then they show when the passage from high- to low- amplitude of response (jumps) occurs. If the identified model captures the quantitative dynamic behaviour, i.e. the amplitude of the response, and the qualitative dynamic behaviour, i.e. the jumps, of the experimental test rig, the selected polynomial is considered to be validated. If the validation does not produce satisfactory results, then the polynomial is modified by removing monomials with a low contribution and/or increasing the order, until all the required nonlinear

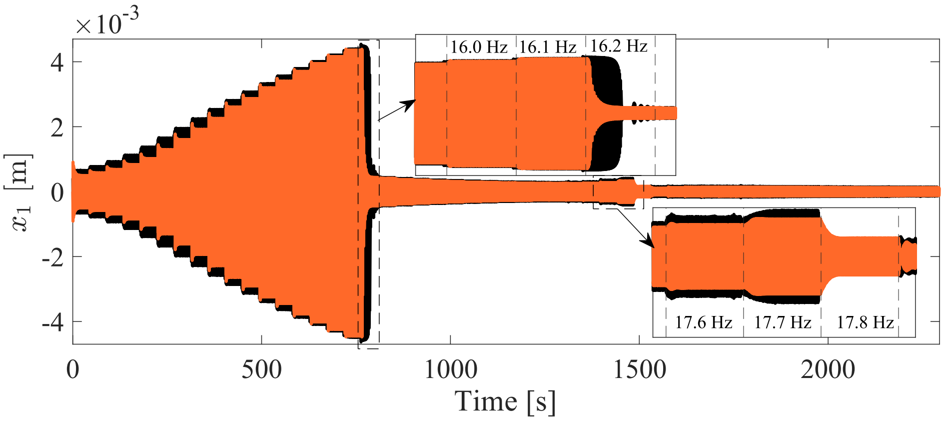

Figure 6.11: Comparison between the experimental (black line) and the numerical (orange line) time histories at excitation amplitudes equal to 0.05 mm. Zooms in correspondence of the first and second resonance are reported.

features are captured by the identified model. It should be noted that the usage of ideal sinusoidal excitation and a ROM greatly reduces the computational burden of the simulations and allows for many polynomials to be tested in a short amount of time.

The results of the identification procedure are shown in Tab. 6.9: the first polynomial is correctly identified using a full polynomial of order 3. The second polynomial, instead, requires adding/removing some monomials to achieve good accuracy in the jump predictions, during the numerical simulations. Fig. 6.10 shows with different views the comparison between numerical and experimental NLRF surfaces for the two DOFs. The identified numerical NLRF surfaces match very well the experimental data, thus the identified polynomial is considered accurate enough to describe correctly the dynamics of the test rig.

Numerical and experimental time histories are also compared for the largest level of excitation amplitude, i.e. 0.05 mm. The results are reported in Fig. 6.11 in terms of displacement of the first DOF: the figure demonstrates that the identified nonlinear MDOF-ROM captures the qualitative and quantitative dynamic behaviour of the experimental Test Rig #2 for the considered amplitude of excitation. Given the very good match between experimental and numerical results, the nonlinear MDOF-ROM representing the Test Rig #2 (without motion limiting constraints) is considered to be identified. The complete validation of the identified ROM against different sets of experimental data is reported in Chapter 7.

6.3.4 Nonlinear Restoring Force Method: Experimental Identification of a Localised Piecewise Characteristic

In the previous section, the NLRF method was introduced and applied to identify a nonlinear MDOF-ROM capable of representing the dynamic behaviour of Test Rig #2 without the motion limiting constraints . In this section, instead, the NLRF method is used to identify a piecewise characteristic. The identification process utilises the experimental data associated with the non-smooth version of Test Rig #1 because, as shown in Chapter 5, it presents very a rich dynamic behaviour, including chaotic, quasi-periodic, and multi-periodic dynamic responses. The linear and smooth nonlinear characteristics of an associated ROM have been already identified in Section 6.2.1 and 6.2.2, utilising linear identification methods and meta-heuristic optimisation methods. The equation of motion of the identified nonlinear ROM is shown in Eq. 6.1 whose linear and nonlinear coefficients are reported in Tab. 6.10 for the sake of completeness. The NLRF method is applied following a slightly modified procedure to the original

Table 6.10: Linear and nonlinear parameters of Test Rig #1 without motion limiting constraints . The parameters are identified in Section 6.2.

Parameter	Value
m	$0.113\,\mathrm{kg}$
k_1	$714.9\,\mathrm{N/m}$
k_2	$89.6\,\mathrm{N/m}$
k_3	$624.9\,\mathrm{N/m}$
c_1	$0.0454\,\mathrm{Ns/m}$
c_2	$0.0075\,\mathrm{Ns/m}$
c_3	$0.0366\,\mathrm{Ns/m}$
μ_1	$2.732 \times 10^6\,\mathrm{N/m^3}$
μ_2	$1.324 \times 10^6\,\mathrm{N/m^3}$
$\mu_{2,b}$	$8.850 \times 10^6\,\mathrm{N/m^3}$
μ_3	$7.069 \times 10^6\,\mathrm{N/m^3}$

version. In this case, the sought characteristic cannot be correctly represented by polynomial functions, but piecewise functions are necessary to perform the identification. This simplifies the process, as there is no need for searching a suitable order of the polynomial. The NLRF method reduces to the scheme outlined in Fig. 6.12, which

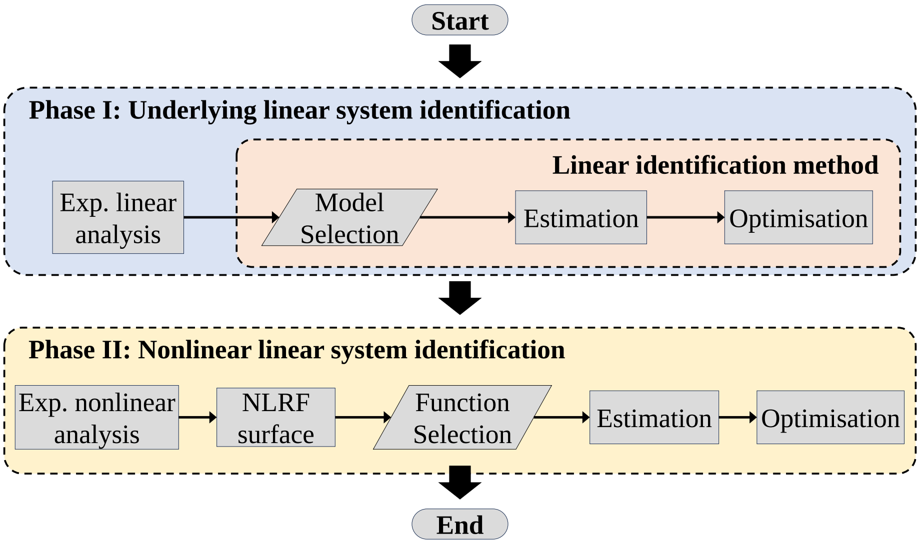

Figure 6.12: NLRF method: simplified procedure for the identification of non-smooth characteristics

involves the selection of an appropriate ROM, the identification of the underlying linear system, the computation of the NLRF surfaces, and the identification of nonlinear parameters. To account for the presence of a piecewise characteristic, the following set of ODEs is utilised:

$$m\ddot{x}_1 + c_1\dot{x}_1 + k_1x_1 + c_2(\dot{x}_1 - \dot{x}_2) + k_2(x_1 - x_2) + \mu_1x_1^3 + \mu_2x_1^3 - \mu_{2,b}x_1^2x_2 + \\ + \mu_{2,b}x_1x_2^2 - \mu_2x_2^3 + F_p(x_1) = 0 \tag{6.17a}$$

$$m\ddot{x}_2 + c_3(\dot{x}_2 - \dot{y}) + k_3(x_2 - y) - c_2(\dot{x}_1 - \dot{x}_2) - k_2(x_1 - x_2) + \mu_3(x_2 - y)^3 + \\ - \mu_2x_1^3 + \mu_{2,b}x_1^2x_2 - \mu_{2,b}x_1x_2^2 + \mu_2x_2^3 = 0 \tag{6.17b}$$

Eq. 6.17 is an extension of Eq. 6.1 and incorporates an extra term to explicitly represent the influence of a piecewise stiffness restoring force, denoted by F_p. Despite efforts, a perfectly symmetric gap is difficult to archive in a real experimental setup, thus the sought piecewise characteristic is more general and it allows for having asymmetric non-contact gaps. The characteristic is mathematically represented by the following

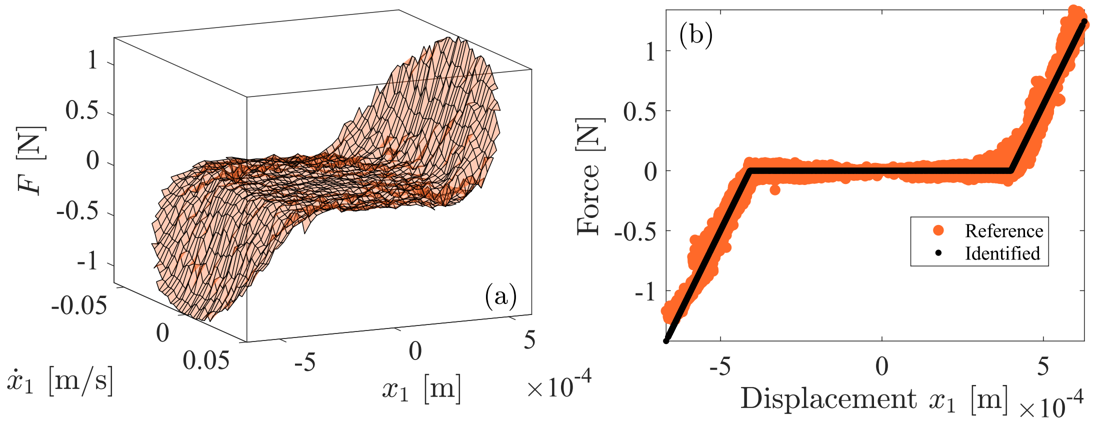

Figure 6.13: Experimental NLRF surface of Test Rig #1 (a) in the reduced sub-space $x_1 - \dot{x}_1$. The section cut of the experimental NLRF surface at $\dot{x}_1 = 0$ and the identified properties are graphically shown in panel (b)

expression:

$$F_p = \begin{cases} k_p(x_1 - a_2) & \text{if } x_1 > a_2 \\ 0 & \text{if } -a_1 < x_1 < a_2 \\ k_p(x_1 + a_1) & \text{if } x_1 < -a_1 \end{cases} \tag{6.18}$$

where k_p is the piecewise stiffness and, a_1 and a_2 are the lower and upper limits of the free-play gap.

Considering that the linear and nonlinear smooth parameters of the equation of motion are known, the identification procedure is reduced to the identification of the piecewise characteristic. The idea is to remove the linear and the smooth nonlinear restoring force contributions from the global restoring force to obtain an NLRF surface representing the piecewise stiffness characteristic. This can be used to identify the non-smooth property of Test Rig #1. The NLRF, representing the piecewise stiffness contribution, is obtained by manipulating the equation of motion associated with the first DOF of the system (Eq. 6.17a) as follows:

$$N_{RF} = -m\ddot{x}_1 - c_1\dot{x}_1 - k_1x_1 - c_2(\dot{x}_1 - \dot{x}_2) - k_2(x_1 - x_2) - \mu_1 x_1^3 - \mu_2 x_1^3 + \mu_{2,b} x_1^2 x_2 - \mu_{2,b} x_1 x_2^2 + \mu_2 x_2^3 \tag{6.19}$$

The experimental NLRF is then computed using the time histories obtained from forward sine sweeps with an amplitude of 0.3 V. Fig. 6.13 (a) shows the experimental NLRF surface in the reduced subspace of nonlinear coordinates associated with the

Table 6.11: Identified piecewise function parameters.

a_1 [m]	a_2 [m]	k_p [N/m]
4.091×10^{-4}	3.995×10^{-4}	5.472×10^{3}

first DOF. The figure demonstrates that, in a reduced subspace, the restoring force surface of a localised nonlinearity can be graphically reconstructed even in the case of an MDOF nonlinear system. Most of the variation of the surface is concentrated along the axis x_1; this suggests that no significant nonlinear damping contribution is present in the experimental NLRF. Following this consideration, every cutting section of the surface along the axis x_1 is suitable for identifying the sought piecewise characteristic. Fig. 6.13 (b) shows the cutting section of the experimental NLRF surface at $\dot{x}_1 = 0$, denoted by the orange large dot. The unknown coefficients of the nonlinear property are obtained by minimising the difference between the experimental and the analytical piecewise characteristics. Once again, the MATLAB function *lsqnonlin* is utilised to solve the optimisation problem, using the following piecewise function:

$$F_p = k_p[(x_1 + a_1)/2(sign(-x_1 - a_1) + 1) + (x_1 - a_2)/2(sign(x_1 - a_2) + 1)] \quad (6.20)$$

The results of the optimisation process are reported in Tab. 6.11. The non-contact gaps a_1 and a_2 are close but not identical, as it is challenging to obtain a perfect symmetric characteristic in the experimental setup. Fig. 6.13 (b) shows the comparison between the experimental cutting section of the NLRF and the identified piecewise characteristic. The identified property reproduces very well the experimental data and therefore is considered sufficiently accurate to proceed with the validation of the model. The validation is carried out using different sets of experimental data and is described in detail in the Chapter 7.

6.4 Summary

In this chapter, Test Rigs #1 and #2 are identified from experimental data. Reduced order models are derived and equivalent parameters are identified using two diverse procedures: meta-heuristic optimisation and the NLRF method. Initially, the test rigs are identified in their smooth configuration, i.e. in the absence of the motion limiting constraints. The linear and nonlinear behaviour of the system are identified separately: the first one is identified using classical identification methods such as circle fit and half power methods which allow obtaining an estimation of the system modal parameters. The estimated parameters are then used as an initial guess for an optimisation procedure which aims to minimise the difference between analytical and experimental transfer functions representing the underlying linear system. Then meta-heuristic optimisation methods, such as PSO and GA, are used to identify the nonlinear smooth characteristics of the system. In this specific case, the knowledge of the FRC is exploited to create an objective function and extract useful information from the experimental measurements. Test Rig #1 is successfully identified using the meta-heuristic optimisation approach, as demonstrated by the comparison between the experimental and numerical data. On the contrary, using the same approach, the ROM identified from the experimental data of Test Rig #2 does not capture the qualitative dynamic behaviour of the experimental system, failing to locate the frequency at which jumps occur. This is caused by the usage of a perfect sinusoidal excitation in the numerical simulations which reduces the amount of information passed to the optimisation process.

The successful identification of Test Rig #1 is taken as inspiration to develop a novel method for the identification of nonlinear MDOF systems. The method incorporates the identification of the underlying linear and nonlinear behaviour of the mechanical system in a separate way as previously done for Test Rig #1. The proposed method is a modified version of the RFS method, named the NLRF method, which tries to identify the nonlinear characteristics of the system in the real coordinate space using the nonlinear components of the restoring force. The capabilities of the method are shown numerically and experimentally. The method can extract information from the NLRF surfaces associated with each DOF of the system; this information is then used to develop engineering considerations which reduces the mathematical complexity of the identification procedure. For example, knowing that the NLRF is fully represented by only two states of the system, e.g. x_1 and $\dot{x}_1$, it is possible to simply the definition of the general polynomial for the identification of the nonlinear characteristic, saving time and reducing the computational effort of the procedure in comparison to the meta-heuristic optimisation approach. The method is applied to identify the smooth and non-smooth characteristics of the experimental test rigs, introduced in the previous chapters. The successful identification of the nonlinear characteristics is proven by the good match between the experimental and numerical data, posing the basis for the subsequent validation process, reported in Chapter 7.

Chapter 7

From Identification to Extrapolation: Validation of the Identified Nonlinear Systems

7.1 Introduction

This chapter discusses the validation of the reduced-order models previously identified. Particular attention is given to the extrapolation capabilities of the models, i.e. their capability to predict dynamic behaviours of the test rig. Specifically, the sections are organised as follows:

- Section 7.2 shows the validation process of the identified reduced-order models. To this end, the comparison between experimental data and the numerical predictions is carried out considering experimental data sets that are different from the ones used during the identification process. In particular, FRCs, time histories, and steady-state orbits are utilised to assess the prediction capabilities of the identified ROMs. The validation is performed for the ROMs associated with the smooth version of Test Rig #1 and #2 and for the non-smooth version of Test Rig #1.
- Section 7.3 discusses the differences between a full FE nonlinear model and a

ROM. To this end, a nonlinear FE model representing Test Rig #2 is updated using the NLRF method and validated against a different set of experimental data. The updated model is then used to carry out the comparison with the equivalent ROM, previously identified. The section discusses the difference between the two models in terms of the accuracy of the solution and the computational burden of the calculations, highlighting the advantages and disadvantages of the two approaches.

- Section 7.4 utilises the identified non-smooth ROM of Test Rig #1 to perform numerical predictions of the system dynamics at different levels of excitation. Path-following continuation is utilised to obtain a clear picture of the bifurcation scenario associated with the identified ROM. The numerical analyses are performed paying attention to the similarities between the dynamic features of the identified model and the general model investigated in Chapter 3. The section concludes by showing the presence of isolas and bifurcation of the backbone in the identified non-smooth ROM and suggesting a procedure for the detection of bifurcation of the backbone curve from experimental data.

7.2 Validation of the Identified Reduced Order Models

This section discusses the validation of the nonlinear ROMs identified in Chapter 6. The validation process is carried out by comparing the numerical predictions of the identified models against different sets of experimental data. These sets include experimental data obtained at excitation levels that are different from the one used during the identification process. This consents to demonstrate the robustness of the identified models and their suitability in predicting the global dynamic behaviour of the investigated structures. It should be pointed out, that this is particularly important in industrial applications, where the identified models are used to predict the behaviour of systems and structures in operational conditions that are generally different from the identification ones.

7.2.1 Validation of the Reduced Order Model representing the Smooth Behaviour of Test Rig #1

The nonlinear ROM representing the dynamic behaviour of Test Rig #1 without motion limiting constraints is now validated against experimental data. To this end, Eq. 6.1 and its linear and nonlinear coefficients (Tab. 6.10) are used to simulate the dynamic response of the system via numerical integration and the predicted dynamic behaviour is tested against a different set of experimental data. In particular, the FRCs associated with an input voltage amplitude of 0.3 V and 0.4 V, are used to validate the identified

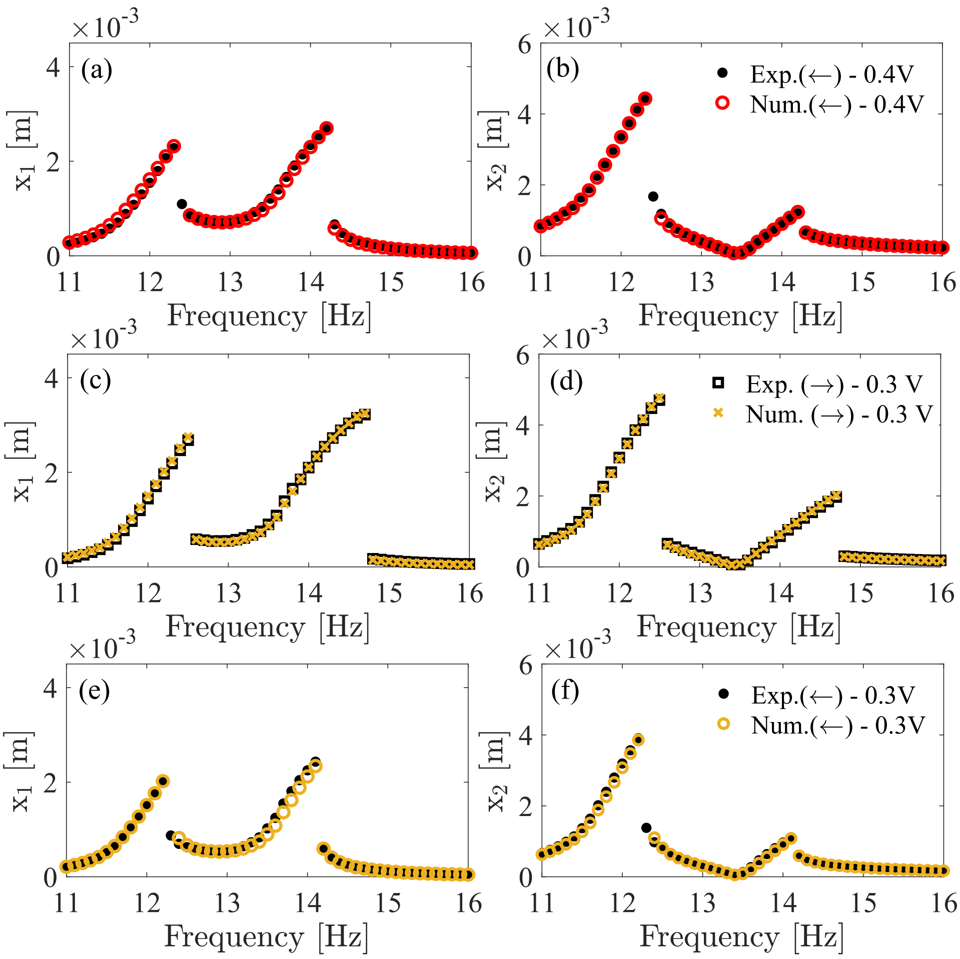

Figure 7.1: Validation of the identified nonlinear ROM representing the smooth behaviour of Test Rig #1. The arrows in the legends indicate the direction of the frequency sweep [4].

nonlinear model. The numerical simulations are carried out at the same frequency of excitation at which the experiments are performed. To mitigate the shaker interaction with the structure at resonance, the experimental input amplitude of excitation, i.e. the velocity and displacement of the base, are used as input in the simulations. This is necessary because the base motion of Test Rig #1 is not controlled via feedback control loop. Fig. 7.1 shows the comparison between the experimental data and numerical simulations: the identified ROM captures the dynamic behaviour of the experimental system with good accuracy at different levels of excitation. In addition, the ROM accurately predict the dynamic response of the experimental test rig when forward and backward frequency sweeps are used to excite the structure, identifying high-amplitude and low-amplitude responses in both the excitation conditions. This validates the identified ROM and the associated smooth nonlinear characteristics and demonstrates the good extrapolation capabilities of the identified model.

7.2.2 Validation of the Reduced Order Model representing the Smooth Behaviour of Test Rig #2

The ROM representing Test Rig #2 (Eq. 6.12) and the identified parameters (Tab. 6.4 and Tab. 6.9) are validated against different sets of experimental results. Differently from the previous case, the nonlinear dynamic behaviour of the system is fully tested. In the previous case, the usage of experimental input did not allow for testing the destabilisation of high-amplitude responses. In particular, it was not possible to validate the capability of the ROM to identify the jump-up and jump-down phenomena, i.e. the transition from low- to high-amplitude of response, as the input is partially driven this phenomenon. This feature is particularly important to correctly represent the dynamic behaviour of nonlinear systems and it is directly linked to their basins of attraction of the stable dynamic solutions. Validating similar features, the identified ROM reaches a high degree of confidence, suitable for performing extrapolation of dynamic features. In the considered case, the control system tries to eliminate the dynamics of the shaker from measured signals allowing for the direct comparison between numerical continuation analyses and experimental results. Specifically, the numerical simulations are

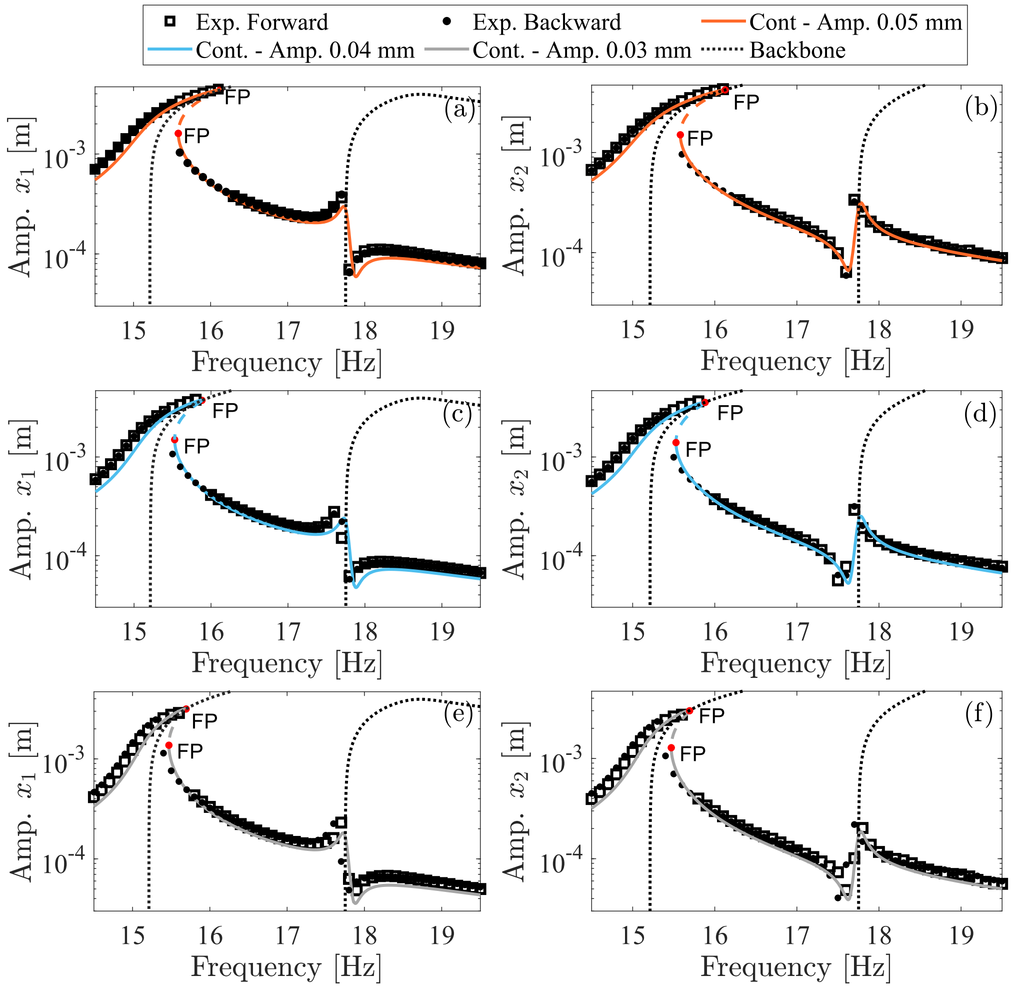

Figure 7.2: Numerically continued (continuous and dashed lines) and experimental (markers) FRCs. The numerical backbone curves are indicated by dotted lines. Numerical and experimental data are associated with the smooth version of Test Rig #2

carried out at constant amplitude displacement of the base, as imposed experimentally. The results of the comparison between experimental and numerical FRCs are shown in Fig. 7.2: the numerical FRCs are obtained from the identified ROM and the results are compared with the experiments using input amplitude equal to: 0.05 mm, 0.04 mm, and 0.03 mm. The panels on the left describe the FRCs associated with the displacement of the first DOF (panels (a), (c) and (e)), while the panels on the right illustrate the FRCs obtained from the displacement of the second DOF (panels (b), (d) and (f)). All the numerical simulations are in good agreement with the experimental data: in particular, the identified model can reproduce the qualitative and quantitative dynamic behaviour of the test rig, at all the considered excitation levels. In addition, the model effectively scales the amplitude of the response and the jumps following the varying levels of excitation. This is particularly important because it demonstrates that the identified model has correctly captured the nonlinear dynamics features of the experimental system like the destabilisation of high-amplitude responses. The good match between numerical and experimental FRCs demonstrates that the chosen ROM captures the complex nonlinear behaviour of the experimental test rig, characterised by the presence of stiffness and damping nonlinear properties. In addition, it is shown that the ROM can extrapolate information from the experimental data and predict the nonlinear dynamics behaviour of the experimental system at different excitation conditions. Fig. 7.2 shows the numerical backbone curve of the system. These curves represent the undamped unforced dynamic response [1] of the system in the frequency-amplitude plot. The backbone curves behave as expected, showing nonlinear features that are aligned with the previous experimental analysis and identification process. Specifically, both the backbone curves show the hardening effect, bending towards higher frequencies when large amplitudes of responses are reached. In addition, no bifurcation or flipping points are found in the backbone curves, demonstrating the absence of internal resonances in the considered range of amplitude of the response. Nonetheless, the second backbone curve shows an unexpected bending towards lower amplitudes of response when very large amplitudes of response are achieved in the second mode: this is due to the extreme difference between the amplitude of the available experimental data, utilised to identify the model, and the predictions that are attempted. At high amplitude of response, the ROMs probably fail to predict the dynamics of the experimental test rig: however, such conditions are not easy to reach in a real experimental set-up, as the vibration table of Test Rig #2 allows for exciting the first mode effectively, and therefore they do not represent an issue for the validation process reported in this chapter.

[1] Differently from Chapter 3 the continuation of the conservative periodic solutions is achieved using an unfolding parameter and numerical corrections, as proposed in [125].

7.2.3 Validation of the Reduced Order Model representing the Non-Smooth Behaviour of Test Rig #1

In Section 7.2.1, the ROM representing Test Rig #1 in the smooth configuration is identified and validated. The model demonstrated to predict the experimental dynamic behaviour of the test rig when excitation conditions, different from the one used during the identification process, are used.. Building on these results, it is now possible to validate the ROM representing the non-smooth dynamics behaviour of Test Rig #1. The associated piecewise characteristic is identified in Chapter 6 with the NLRF method. To this end, the mathematical model of Eq. 6.17 is used for the validation process. The validation is carried out by comparing steady-state orbits and the time histories of the experimental and numerical models. Firstly, the forward sweep at 0.3 V, is used in the validation process. These data correspond to the data used in the NLRF method for the identification of the system, nonetheless, the comparison of different orbits provides a cross-validation of the identified model. The results of the comparison are reported in Fig. 7.3. The panels in the first column show a comparison between experimental and numerical time histories while the panels in the second column illustrate the comparison between experimental and numerical dynamic orbits. The comparison is carried out by considering three different dynamic conditions, namely, a single-period attractor, a multi-periodic attractor, and a quasi-periodic attractor. The single-period attractor is identified at $\Omega = 12.7$ Hz and the comparison between numerical and experimental data is reported in Fig. 7.3 (a1-a4) for the first and second DOF. The multi-periodic attractor, instead, is experimentally observed at $\Omega = 12.2$ Hz while the quasi-periodic attractor is found at $\Omega = 14.8$ Hz. Fig. 7.3 (b1-b4) and Fig. 7.3 (c1-c4) show the comparison between the numerical and experimental time-histories/steady-state orbits for the two remaining attractors. The numerical simulations are computed via numerical integration with the aid of the MATLAB function *ode45*. As suggested in [2], the measured base motion is used as input in the numerical simulations according to the

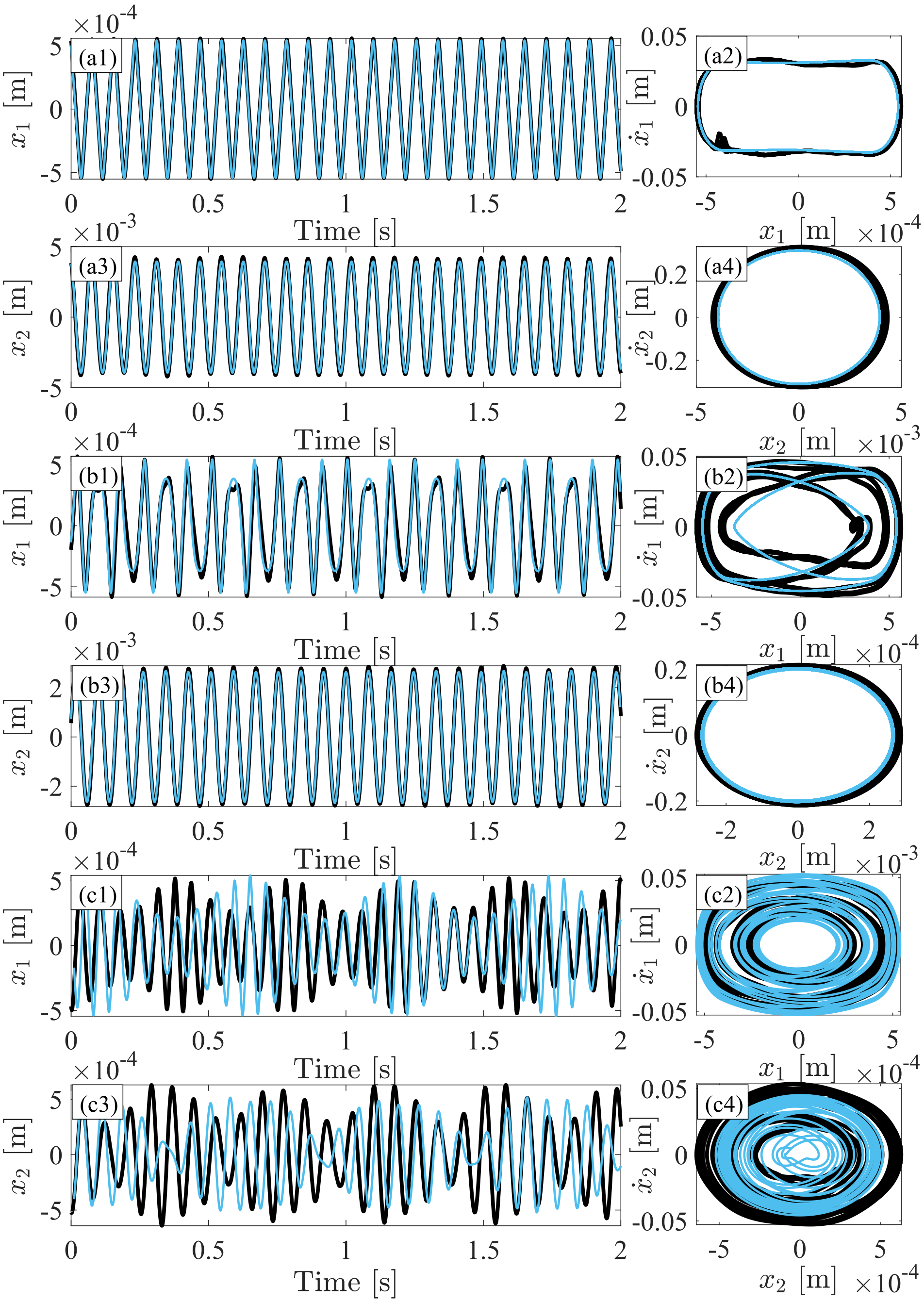

Figure 7.3: Comparison between the experimental data (black line) and the numerical solutions (light blue line) at the steady-state conditions (non-smooth version of Test Rig #1). Experimental forward sweep data at 0.3 V amplitude are utilised for the comparison.

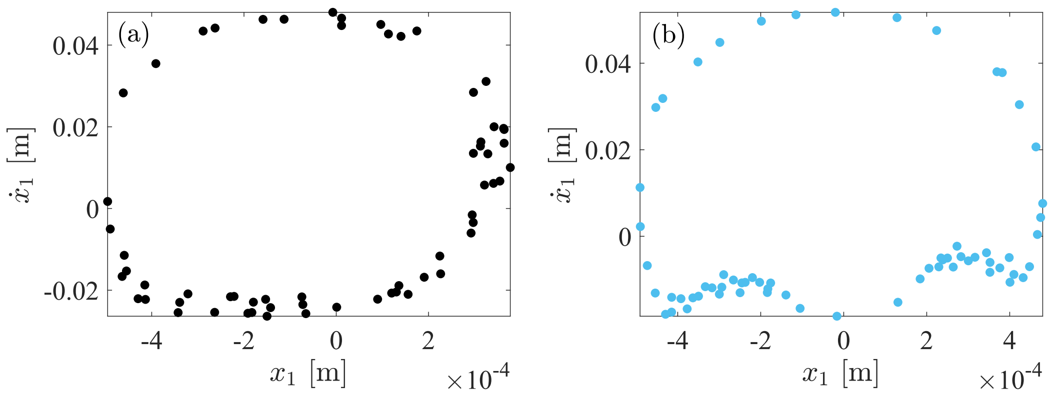

Figure 7.4: Experimental (a) and numerical (b) Poincaré sections for $\Omega = 14.8$ Hz. The sections are obtained using the section plane $x_2 = 0$.

following expressions:

$$y(t) = Y_{exp}(\Omega)\cos(\Omega t) \tag{7.1a}$$

$$\dot{y(t)} = -\dot{Y}_{exp}(\Omega)\sin(\Omega t) \tag{7.1b}$$

where Y_{exp} and $\dot{Y}_{exp}$ are the experimental displacement and velocity amplitude of the base at a specific excitation frequency Ω. The comparison between numerical and experimental time histories/steady-state orbits demonstrates that the identified ROM can accurately predict the dynamic response of the experimental test rig, especially when periodic attractors are considered. This is evident from the comparison carried out in Fig. 7.3 (a1-a4) and Fig. 7.3 (b1-b4) where the numerical solutions associated with single-period and multi-periodic attractors are shown to be in good agreement with the experimental data. Good results are also achieved in the presence of a quasi-periodic attractor: in this case, numerical and experimental time-histories are not perfectly matched in terms of amplitude, nonetheless, the general qualitative behaviour of the experimental system is captured by the numerical model, as shown by Fig. 7.3 (c2,c4). To further prove this aspect, the Poincaré sections of the experimental and the numerical attractors are compared: Fig. 7.4 shows that in both cases the attractors are associated with an invariant circle. This demonstrates that the ROM can correctly predict the presence of a quasi-periodic attractor, i.e. the qualitative dynamic behaviour of the experimental test rig.

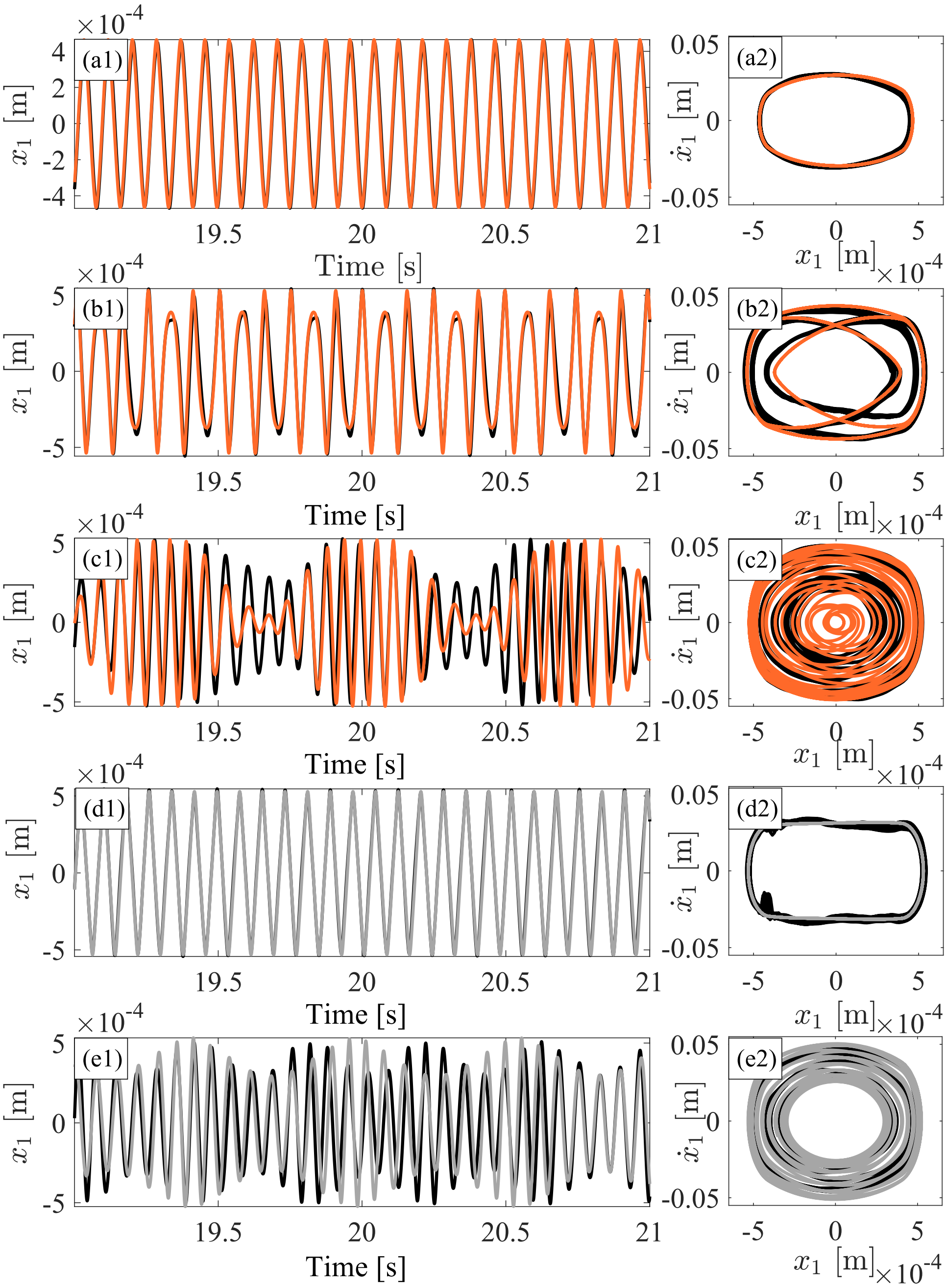

Figure 7.5: Comparison between the experimental data (black line) and the numerical solutions (coloured lines) at the steady-state conditions (non-smooth version of Test Rig #1). Experimental forward sweep data at 0.35 V and 0.2 V amplitude are used. The numerical solutions for amplitude equal to 0.35 V are indicated with orange lines and for amplitude equal to 0.2 V are indicated with gray lines.

To finalise the validation, the identified non-smooth model is used to compute dynamic responses at different excitation conditions. Specifically, the experimental excitation measured during forward sweep with amplitude equal to 0.35V and 0.2 V are used to carry out additional numerical simulations and the results are compared against experimental data. The results are shown in Fig. 7.5 for a single periodic attractor (panels (a1-a2)) at 0.35 V ($\Omega = 11.9$Hz), a multi periodic attractor (panels (b1-b2)) at 0.35 V ($\Omega = 12.1$Hz), an aperiodic attractor (panels (c1-c2)) at 0.35 V ($\Omega = 15.3$Hz), a single periodic attractor (panels (d1-d2)) at 0.2 V ($\Omega = 12.7$Hz), and a multi-periodic attractor (panels (e1-e2)) at 0.2 V ($\Omega = 14.9$Hz). Once again, the predicted orbits are very close to the experimental ones in all the considered cases. The identified model captures very well the qualitative dynamics of all the considered experimental attractors and predicts accurately the quantitative steady-state dynamics of the test rig when single and multi-periodic attractors are considered. This demonstrates the accuracy of the identified model in predicting the dynamic behaviour of the experimental test rig and validates the model.

7.3 Finite Element Model vs Reduced Order Model

The previous section presented the validation of the ROM representing the test-rig #2. In this section, a nonlinear FE model, representing the same test rig, is updated using the NLRF method and the resulting model is validated against experimental data. Then the FE and reduced models are compared in terms of the accuracy of the predicted dynamic response.

7.3.1 Nonlinear Finite Element Model: Model Updating

An FE model representing the experimental Test Rig #2 is modelled and analysed with the FE package Abaqus (Dassault Systeḿes). The FE model is shown in Fig. 7.6: it consists of parallel steel beams (S_1, S_2, and S_3), modelled with shell elements, and two blocks (B_1 and B_2), modelled with cubic elements. The two blocks are modelled considering the presence of polymeric and metallic components: a core mass in the

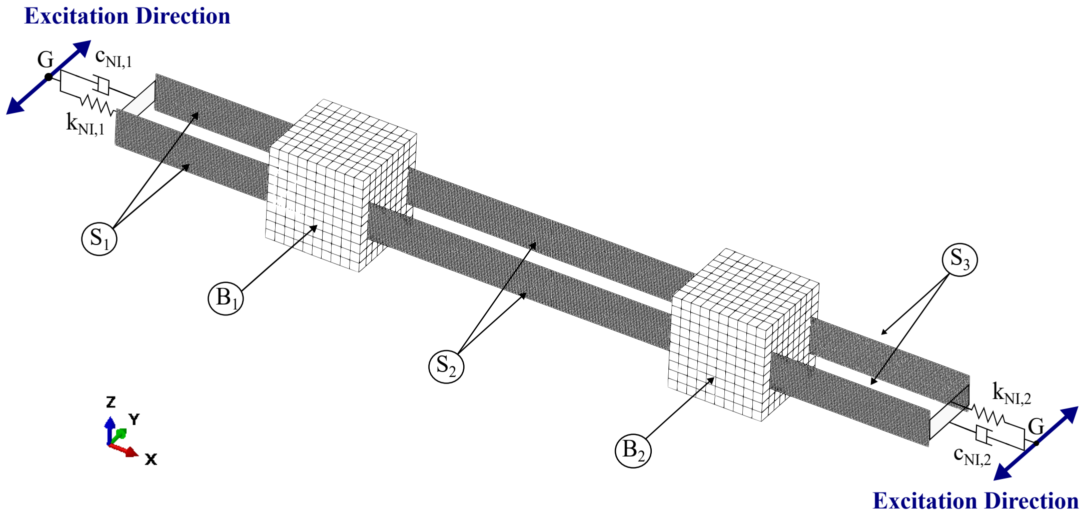

Figure 7.6: FE model representing the experimental Test Rig #2. Spring-dashpot elements ($k_{NI,1}$, $c_{NI,1}$ and $k_{NI,2}$, $c_{NI,2}$) are applied between the extremities of the FE model and the ground G to simulate the non-ideal boundary conditions. The arrows show the direction of excitation.

middle of each block is used to take into account the presence of heavier components, e.g. fastening elements. This permits us to properly tune the mass of each block with respect to the experimental measurements. Non-ideal boundary conditions are applied at the extremities of the FE model: such conditions are generally modelled using linear or torsional spring/damping elements [26]. The nonlinear dynamic behaviour of the FE model is affected by the non-ideal boundary conditions and by the deformation of the parallel beams. To correctly estimate the deformation of the beams, the number of shell elements is selected via a convergence study. The non-ideal boundary conditions are modelled with spring-dashpot elements applied along the longitudinal direction. These elements are applied at the extremities of the model, as shown by Fig. 7.6 where $k_{NI,1}$, $c_{NI,1}$, $k_{NI,2}$, and $c_{NI,2}$ denote the linear coefficients of the aforementioned elements. The presence of the spring-dashpot elements allows modelling the complex interaction between different materials and the presence of friction and relative motions between the beams and the supports.

To update the FE model, the parameters that mostly affect the dynamics of the system must be identified and selected. These parameters are divided into two sets: the first one is constituted of the mechanical properties of the materials, i.e. the Poisson coefficient (ν), the elastic modulus (E), the density (ρ), and the damping (modelled as proportional damping, using the coefficients α and β), while the second one is constituted of the parameters that represent the non-ideal boundary conditions, i.e. $k_{NI,1}$, $k_{NI,2}$, $c_{NI,1}$, and $c_{NI,2}$. The first set of parameters strongly influences the linear dynamic response of the system and the associated modes. The second one, instead, mostly affects its nonlinear dynamic response. A linear model updating procedure from an initial guess of the parameters is performed. During the updating procedure, modal and linear steady-state analyses are carried out via numerical FE simulations. The linear dynamic simulations have quite a low computational burden, thus multiple iterations can be done until the convergence between numerical and experimental dynamic behaviour is not reached. In this case, two comparisons are carried out: firstly a Modal Assurance Criterion (MAC) against experimental data is performed by considering the first two modes of the system, and then the numerical and experimental receptances, i.e. the system transfer functions, are compared. These analyses account for the presence of non-ideal boundary conditions, assuming an initial guess for the parameters $k_{NI,1}$, $k_{NI,2}$, $c_{NI,1}$, and $c_{NI,1}$. The first set of parameters is then modified to improve the match between experimental and numerical results and the process is repeated until the difference between the experimental and numerical TFs is considered negligible. The linear model update is initialised as shown in Appendix C and is repeated for each change of the non-ideal boundary conditions.

After the linear model update, the nonlinear response of the FE model is updated by modifying the non-ideal boundary conditions. Direct numerical integration is performed in an iterative updating procedure and the simulations are compared against experimental results. Non-ideal spring and damping elements are updated separately. To limit the computational burden, the updating procedure is performed by considering only certain excitation conditions rather than an entire frequency sweep; two conditions are identified, namely, the first linear resonance and the jumps from high- to low-amplitude of response. The first condition allows tuning the stiffness $k_{NI,1}$ and $k_{NI,2}$ since high-amplitude responses are accessible without the need to impose complicated

Table 7.1: Iterative procedure for tuning the non-ideal constraints (stiffness $k_{NI,1}$ and $k_{NI,2}$) at an excitation frequency of 15.2 Hz (first natural frequency). The updated properties are shown on the left side of the table, while the associated dynamic responses are reported on the right. The top row indicates the initial guess, while the bottom row denotes the end of the identification procedure. Experimental targets are reported in brackets.

k_{NI} [N/m]	E_{S_1} [GPa]	E_{S_2} [GPa]	E_{S_3} [GPa]	F_1 [Hz]	F_2 [Hz]	Mode 1 ($u_{2,1}/u_{1,1}$)	Mode 2 ($u_{2,2}/u_{1,2}$)	$A_{M,1}$ [mm]	$A_{M,2}$ [mm]
5000	199.6	242.0	202.6	15.21 (15.20)	17.75 (17.75)	0.960 (0.956)	-1.040 (-1.046)	1.84 (2.31)	1.78 (2.20)
4500	199.6	242.0	202.6	15.21 (15.20)	17.74 (17.75)	0.960 (0.956)	-1.040 (-1.046)	1.91 (2.31)	1.85 (2.20)
2390	199.3	251.0	202.6	15.21 (15.20)	17.75 (17.75)	0.957 (0.956)	-1.043 (-1.046)	2.40 (2.31)	2.31 (2.20)
2450	199.3	251.0	202.6	15.21 (15.20)	17.75 (17.75)	0.957 (0.956)	-1.043 (-1.046)	2.37 (2.31)	2.29 (2.20)
2510	199.3	250.0	202.6	15.21 (15.20)	17.74 (17.75)	0.958 (0.956)	-1.043 (-1.046)	2.36 (2.31)	2.27 (2.20)
2560	199.3	250.0	202.6	15.21 (15.20)	17.75 (17.75)	0.957 (0.956)	-1.043 (-1.046)	2.34 (2.31)	2.26 (2.20)
2610	199.3	250.0	202.6	15.21 (15.20)	17.75 (17.75)	0.957 (0.956)	-1.043 (-1.046)	2.32 (2.31)	2.24 (2.20)

Table 7.2: Iterative procedure for the tuning of the non-ideal constraints (damping $c_{NI,1}$ and $c_{NI,2}$). The updated properties are shown on the left side of the table, while the associated dynamic responses are reported on the right. The top row indicates the initial guess, while the bottom row denotes the identified properties. The experimental targets are denoted in brackets

$c_{NI,1}$ [Ns/m]	$c_{NI,2}$ [Ns/m]	MSE 1	MSE 2	Jump [Hz]
0.0	0.0	5.6e-08	5.1e-08	18.5 (16.1)
2.0	1.58	5.7e-08	5.1e-08	16.1 (16.1)

initial conditions. The damping associated with the non-ideal boundary conditions ($c_{NI,1}$, and $c_{NI,2}$) has a strong effect on the destabilisation of high-amplitude responses and influences the occurrence of the jump phenomenon in a classical frequency sweep excitation. Therefore, the frequencies of excitation near the jumps are the best candidates for performing direct integration simulations and tuning the damping coefficients of the boundary conditions. The identification process ends when both the damping and stiffness coefficients of the non-ideal boundary conditions are correctly updated. Finally, the updating process is concluded with the validation phase which compares numerical and experimental FRCs in the frequency range of interest.

The results of the nonlinear model updating are reported in Tab. 7.1, for the non-ideal springs and Tab. 7.2, for the non-ideal damping elements. In the first nonlinear updating procedure, only the stiffness $k_{NI,1}$ and $k_{NI,2}$ of the non-ideal constraints and the elastic moduli E_{S_1}, E_{S_2}, and E_{S_3} associated with the supporting beams are updated: the idea behind is to update only the parameters that have most of the effect on the nonlinear response of the system, neglecting for the moment the effect of the non-ideal boundary damping. The remaining parameters, i.e., the Poisson coefficients

ν, density ρ, and proportional damping properties α and β are kept fixed during the model updating. The nonlinear FE model is updated by minimising the difference between the numerical and experimental displacement amplitude of the two masses $A_{M,1}$ and $A_{M,2}$, which are respectively retrieved from the nonlinear numerical simulations and experimental analyses. The linear behaviour, instead, is updated by adjusting the modal characteristics of the numerical system. Fig. 7.7 shows the comparison between the numerical and experimental FRC in terms of the amplitude of response, after the first nonlinear updating procedure, i.e. considering only the presence of non-ideal springs; the figure demonstrates that the updated FE model captures nonlinear hardening behaviour of the experimental system, but fails to identify when the jump occurs.

To solve this problem, a second iterative procedure for updating the non-ideal boundary damping is carried out. The idea is to increase the value of the two boundary dampers until the jump occurs at the correct frequency of excitation. Nevertheless, this time, instead of updating the coefficients with an iterative procedure, the knowledge of the Nonlinear Restoring Force (NLRF) surface is leveraged to obtain optimal values and reduce the number of iterations. Since the experimental and the FE models showed the presence of only two modes in the investigated frequency range, a good analytical approximation of the system dynamics is provided by Eq. 6.12. This equation represents the ROM that was identified and validated in the previous chapters and sections. Eq. 6.12 and the knowledge of the underlying linear parameters, reported in Tab. 6.4 are then exploited to compute the experimental and numerical NLRF surfaces. Thus, the $N_{RF,1}$ and $N_{RF,2}$ are computed using the experimental and numerical displacement, velocity, and accelerations. The numerical and experimental NLRF surfaces are shown in Fig. 7.8 (a,b). Two important aspects must be noted: first, the experimental and numerical NLRF surfaces are representable with a 3D function in considered reduced sub-spaces; this consents to assume that the nonlinear restoring force contribution on each mass depends only on the local coordinate, e.g. the first surface depends only on the states z_1 and $\dot{z}_1$. Secondly, the numerical NLRF surfaces are tilted with respect to the experimental one; this second aspect provides information

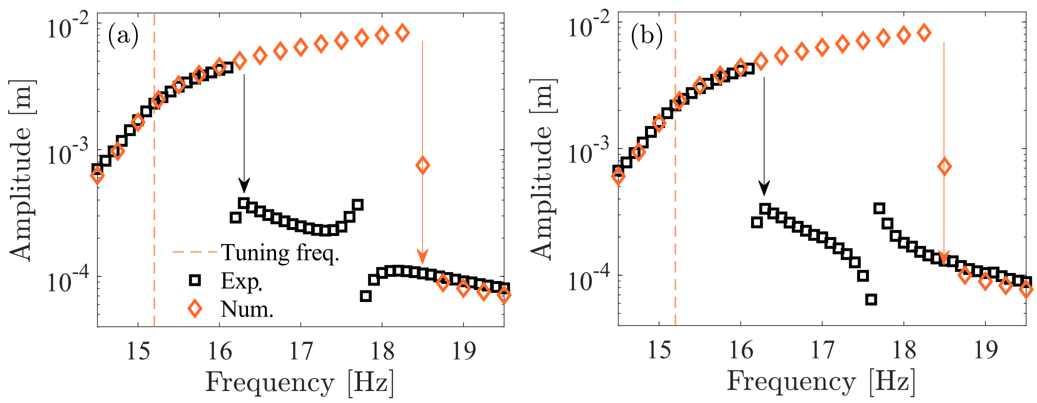

Figure 7.7: Comparison between the experimental and numerical FRCs, after the first nonlinear updating procedure, i.e. considering the presence of only the non-ideal springs and the properties shown in the bottom row of Tab. 7.1. The comparison is performed in terms of amplitudes of the response for the first (a) and second (b) mass.

about the missing contribution to match the experimental conditions. By adding a linear damping contribution in the non-ideal boundary conditions, the numerical NLRF surface can be rotated around the displacement axes (i.e. z_1 and z_2), matching the experimental conditions. Fig. 7.8 (c,d) shows the difference between the numerical and experimental NLRF surfaces which results in a straight inclined plane for both the masses. These surfaces are cut along the plane passing for $z = 0$ to obtain a line which is used to estimate the value of the damping to be added to the non-ideal boundary conditions. Tab. 7.2 shows the results of the proposed procedure which reaches the convergence with just one step.

At this point, it is possible to verify the dynamic behaviour of the FE model by comparing its amplitude and phase of response with the experimental data. Fig. 7.9 reveals a good agreement between the experimental data and the numerical results, not only in terms of the curvature of amplitude and phase at the first resonance but also in terms of jumps, demonstrating that the identified FE model capture the qualitative and quantitative dynamics of the test-rig. The comparison is performed against the forward/backward frequency sweep experimental data that were used in the identification process. In particular, the experimental data and the numerical results were obtained by imposing a constant amplitude of excitation equal to 0.05 mm. To further

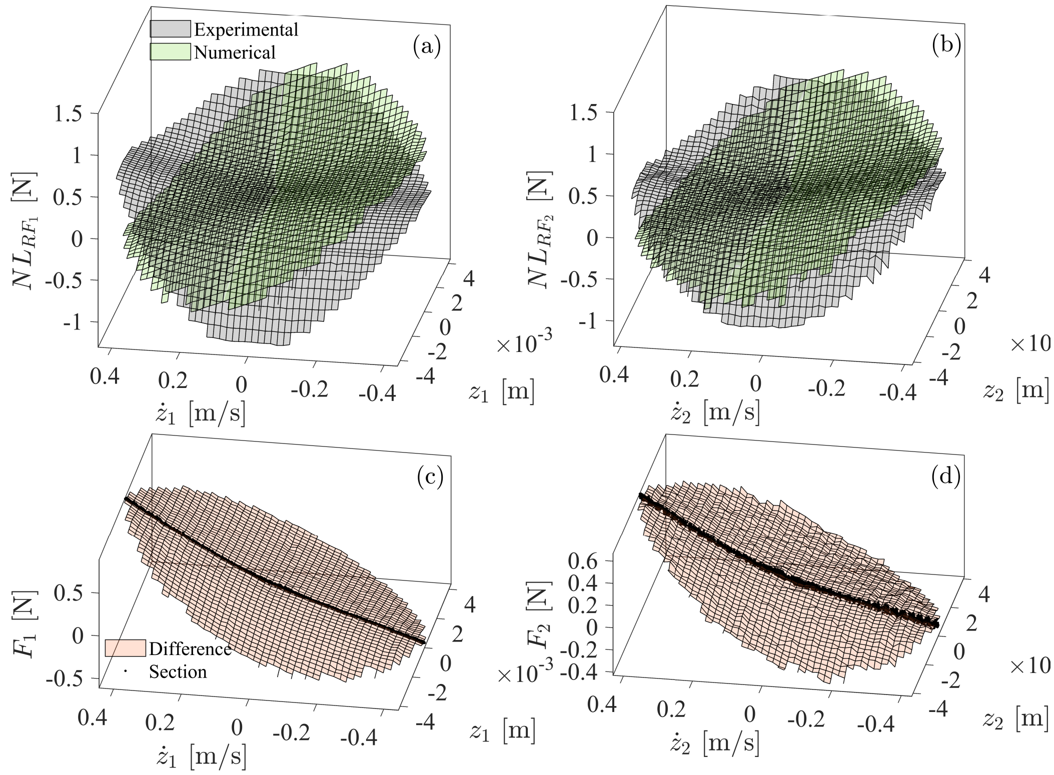

Figure 7.8: Graphical representation of the NLRF surfaces. The comparison between the numerical and experimental NLRF surfaces is reported in panels (a) for the first mass and (b) for the second mass. The difference between the surfaces is shown in panels (c,d) where symbol $\cdot$ denotes the cutting sections at $z = 0$.

demonstrate the capabilities of the proposed updating procedure, the identified nonlinear FE model is validated against a different experimental data set, obtained with an amplitude of excitation equal to 0.04 mm. Fig. 7.10 describes the validation process and demonstrates the excellent match between the experimental data and the numerical simulations in terms of nonlinear hardening behaviour and jumps. This shows that the identified FE model is capable of predicting with good accuracy the dynamics of the experimental test rig at diverse excitation conditions, demonstrating the efficacy of the proposed model updating procedure.

Fig. 7.11 shows the comparison between experimental and numerical FRCs in terms of displacement of the first mass. Specifically, the comparison accounts for FRCs obtained from the updated nonlinear FE model and the previously identified ROM (see

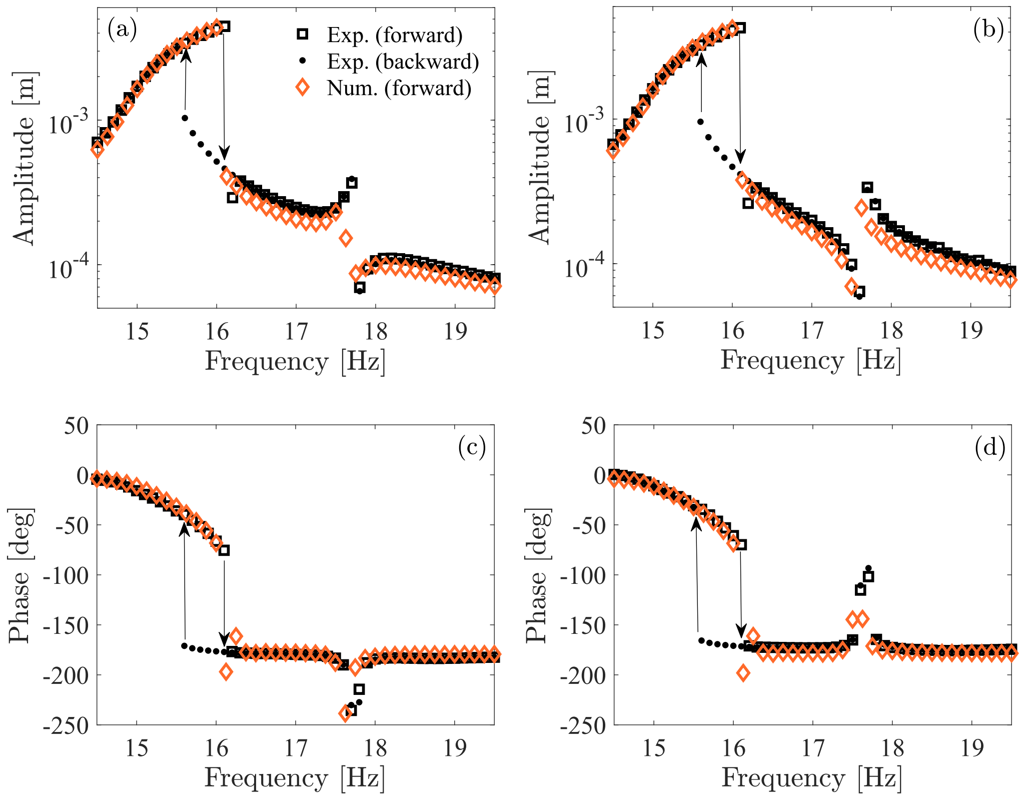

Figure 7.9: Comparison between the experimental and numerical (FE model) FRCs with excitation amplitude equal to 0.05 mm (smooth version of Test Rig #2). Upper panels (a,b) represent the absolute amplitudes while lower panels (c,d) illustrate the phase between the displacement of the vibrating table and the displacement of the masses. The left and right panels denote the quantities associated with, respectively, the first and second mass.

Section 7.2.2). The figure shows that both models provide a very good representation of the dynamic response of Test Rig #2. The FE model is slightly more accurate in capturing the amplitude of response of the experimental model, especially near the jump. This is justified by the higher degree of complexities of the FE model which not only utilises distributed elements to compute the nonlinear stiffening effect of the parallel beams but also introduces non-ideal boundary conditions to correctly catch the interaction between the supports and the system dynamics. Nonetheless, this small increase in accuracy does not justify the more complicated iterative procedure for updating the FE model and the large increment of computational burden to perform

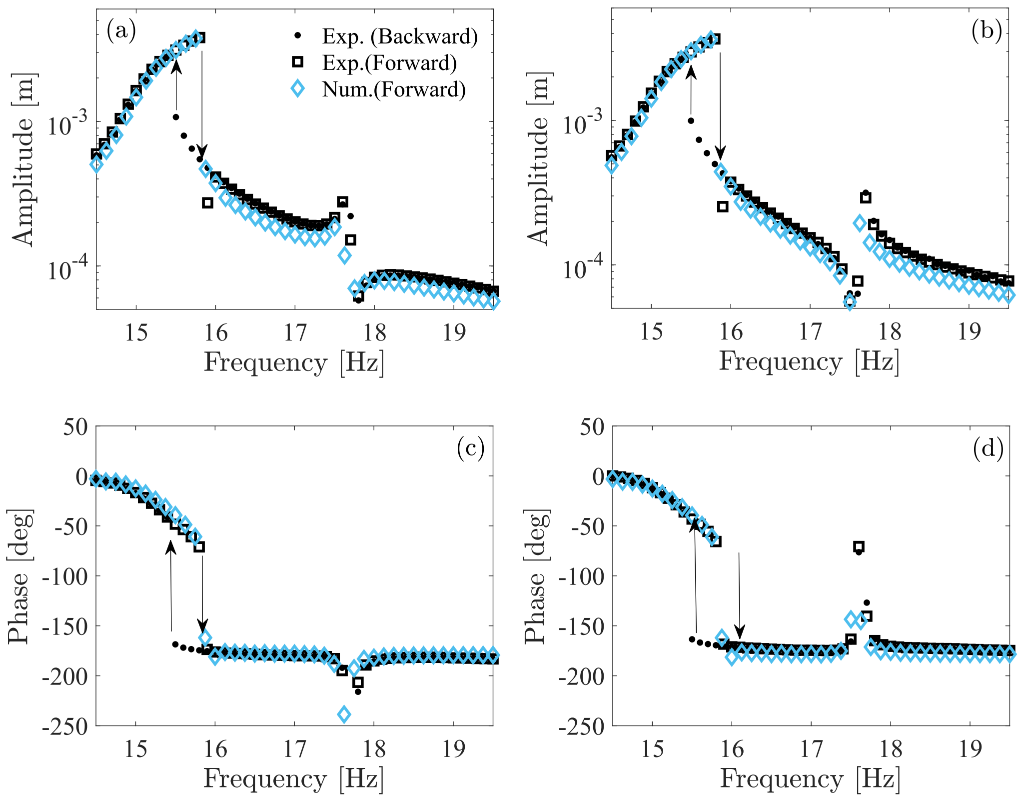

Figure 7.10: Comparison between the experimental and numerical (FE model) FRCs with excitation amplitude equal to 0.04 mm (smooth version of Test Rig #2). Upper panels (a,b) represent the absolute amplitudes while lower panels (c,d) illustrate the phase between the displacement of the vibrating table and the displacement of the masses. The left and right panels denote the quantities associated with, respectively, the first and second mass

the analysis. Using direct numerical integration, the computation of the FRCs with the FE models is extremely long and computationally demanding as demonstrated by Tab. 7.3 [2]. This represents the most critical aspect in practical industrial applications as it does not allow for achieving a solution in reasonable times. The proposed comparison demonstrated that the identified ROM captures the dynamics of the experimental rig, requiring relatively low computational efforts, performing the analysis in a few minutes, and allowing the calculation of stable and unstable solutions via path-following continuation techniques. For all these reasons, the ROMs are strongly preferred to FE

[2]Direct integrations of FE model are performed with maximum time step equal to 0.0025 sec, while numerical continuation is performed with NCOL = 4, NTST = 80, and maximum step equal to 0.05.

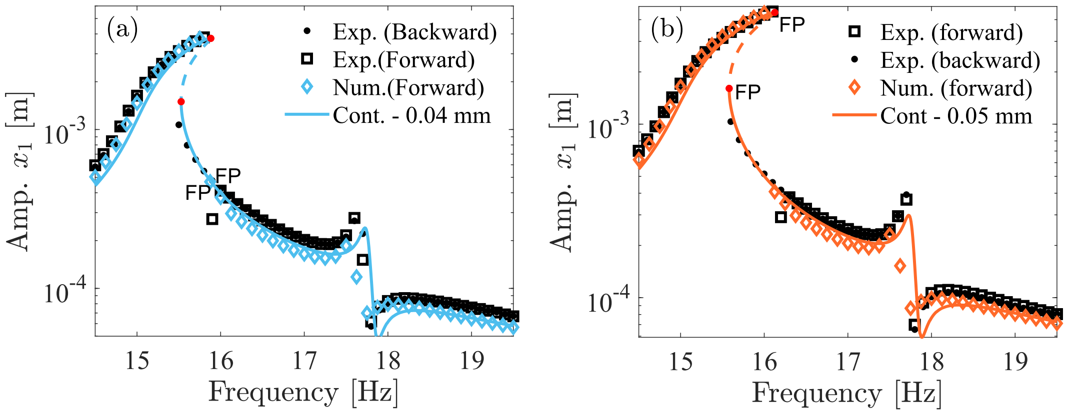

Figure 7.11: Comparison between the experimental and numerical FRCs with excitation amplitude equal to 0.05 mm (a) and 0.04 mm (b). The numerical FRCs are obtained with the nonlinear FE model (marker $\Diamond$) and with the ROM (line $-$).

Table 7.3: Duration of the forward sweep numerical simulations.

Amplitude	0.04 mm	0.05 mm
Reduced Order Model	1456 (24.3 mins)	1638 (27.0 mins)
Finite Element Model	501124 s (5.8 days)	539668 (6.2 days)

models to perform the analysis of strongly nonlinear systems.

7.4 Extrapolation of Dynamic Features

The validated ROM representing the Test Rig #1 is utilised to extrapolate additional dynamic features and obtain more information about the dynamic behaviour of the investigated system. To this end, numerical continuation is used to assess the dynamic response of the system focusing on the investigation of isolas and bifurcation of backbone curves. The idea is to unveil the nature of the multi-periodic stable attractors found in the experimental analysis (see Fig. 5.4), understanding if this dynamic condition is associated with a branch or a detached isola. In addition, the numerical analysis aims to demonstrate that it is possible to identify the presence of bifurcation of the backbone curve using only forced responses. It is worth noting that the base excitation of Test Rig #1 is not controlled via feedback control loop, thus the experimental results are not directly comparable with the numerical simulation based on path-following

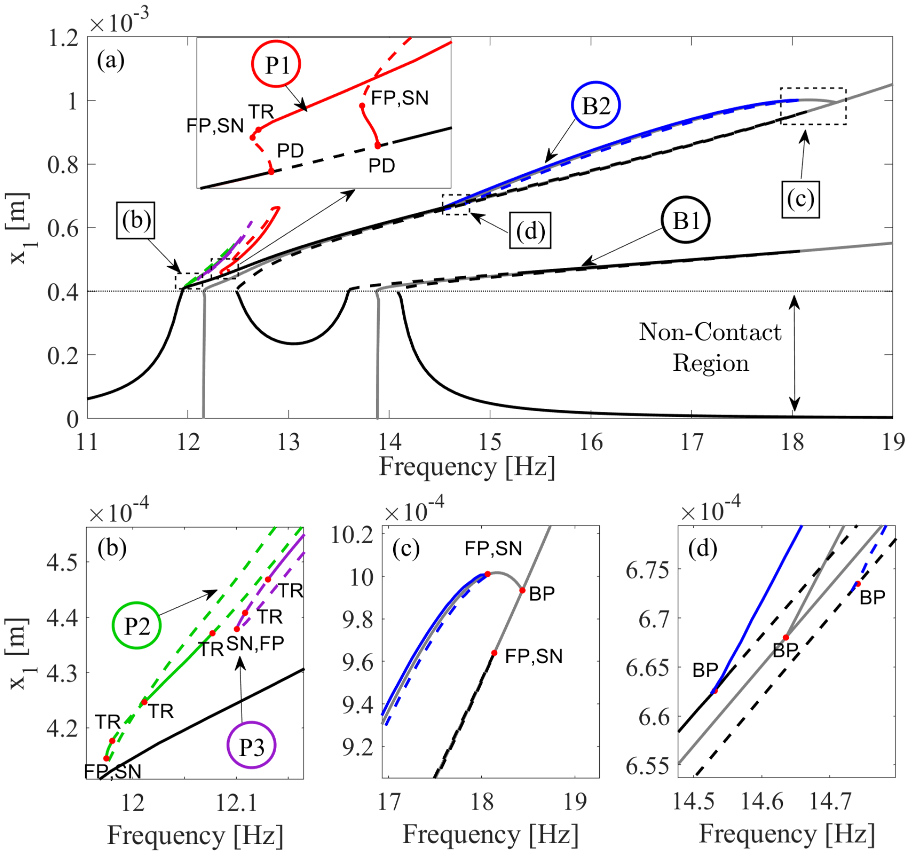

Figure 7.12: Numerical FRC of the validated model in terms of first mass amplitude. The considered ROM represents the non-smooth behaviour of Test Rig #1. The system is excited with a sinusoidal base displacement (amplitude $A = 4.22e-05$ m) and a smoothing parameter $\delta = 2e5$ is utilised to approximate the piecewise characteristic. The remaining properties can be found in Tab. 6.10 and Tab. 6.11.

methods as they utilise an ideal sinusoidal excitation. To be consistent with the experimental measurements, averaged experimental amplitudes of the base motion are used in the numerical analysis. The model is excited with a constant amplitude displacement, equal to 4.22e-05 m; this amplitude represents the mean experimental amplitude of displacement of the base during the forward frequency sweep at 0.1 V without motion limiting constraints. This amplitude is chosen as it represents the lowest experimental excitation amplitude applied to the test rig. The piecewise stiffness is approximated with a sigmoid function whose approximation parameter is chosen imposing an error of 3.24 % (parameter $\delta = 2e5$). The results of numerical analysis are reported in

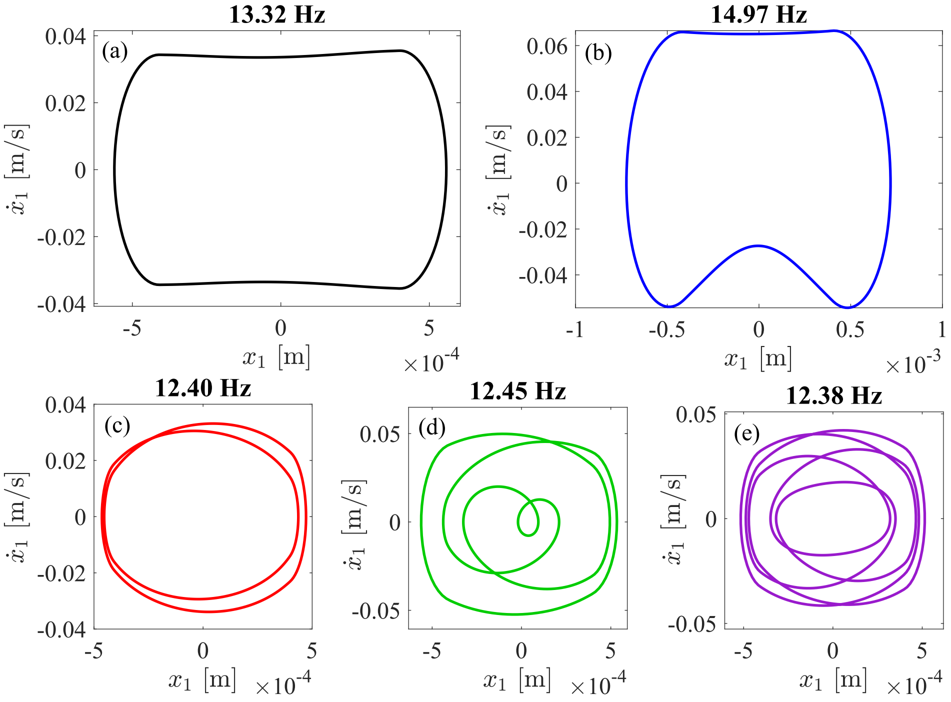

Figure 7.13: Orbits of the first mass associated with the stable branches/isolas identified during the numerical analysis, i.e. branches/isolas B1 (a), B2 (b), P1 (c), P2 (d), P3 (e) of Fig. 7.12. The same colours are used to indicate periodic orbits and the associated branches/isolas.

Fig. 7.12: the analysis of the identified non-smooth model shows the presence of isolas and bifurcation of the backbone curve, demonstrating the presence of a dynamic behaviour qualitatively similar to the one obtained in Chapter 3. Despite the low excitation amplitude, the main branch B1 presents a bifurcating branch, named B2. Once again, the bifurcation of the forced response is generated by the bifurcation of the first backbone curve as shown in the detail of Fig. 7.12 (d). The bifurcating branch of the backbone reconnects to the main branch at high amplitudes of response as illustrated in Fig. 7.12 (c). The analysis of the frequency response unveils the presence of period-doubling bifurcations of the main branch B1: this induces the destabilisation of B1 and the generation of a closed branches P1, as shown in the zoom of Fig. 7.12 (a). This branch is associated with period-doubling stable orbits which persist at amplitudes of response that are sensible larger than the one of B1, representing a potential problem

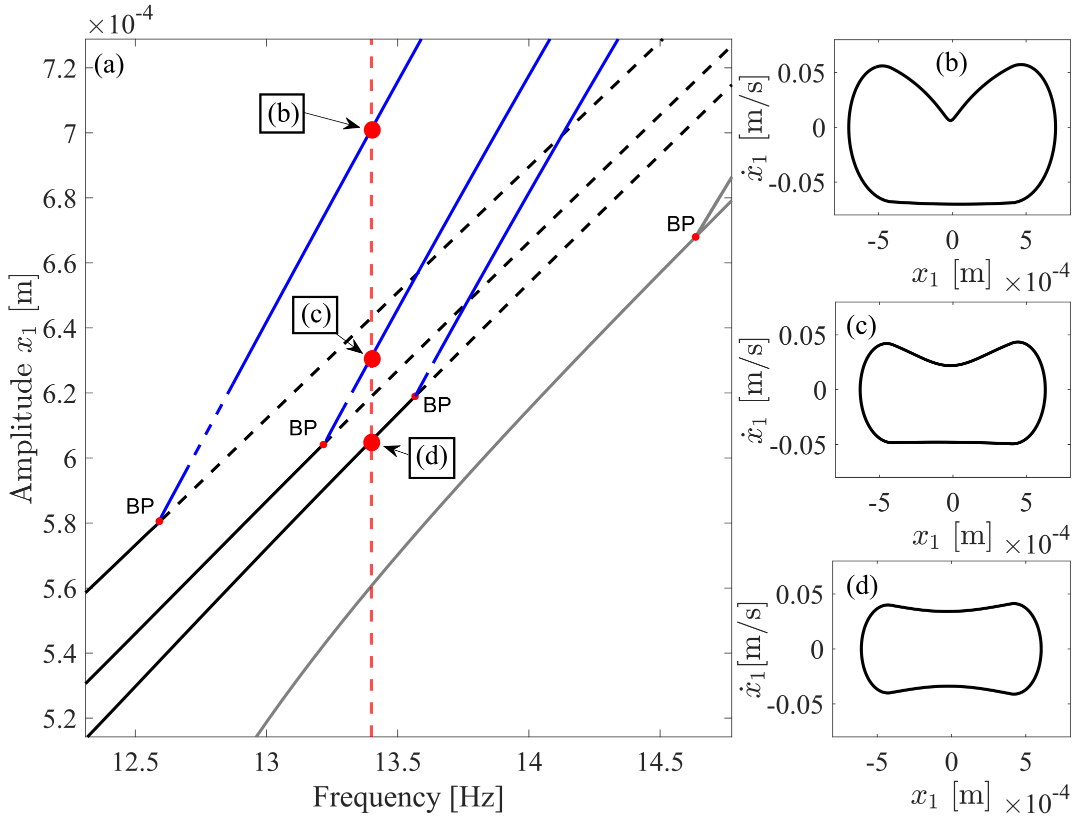

Figure 7.14: FRCs computed at different excitation amplitudes, i.e. 3.52e-4 m, 4.73e-04 m, and 7.03e-04 m. Simulations are carried out using the parameters of Tab. 6.10 and Tab. 6.11 and $\delta = 2e5$. The vertical dashed line indicates the frequency at which the degenerate orbits of panels (b-d) are found. The large dots indicated the associated amplitude.

in the design of similar mechanical structures. Finally, the presence of detached isolas is demonstrated by Fig. 7.12 (b): the figure shows that branches P2 and P3 are completely detached from the main branch B1. Interestingly these isolas have stable solutions in the region where the experimental analysis identified multi-periodic high-amplitude responses (see Fig. 5.4). The periodic orbits of the first mass associated with the stable branches and isolas are shown in Fig. 7.13: branch B1 presents the single period response which is limited in displacement amplitude by the piecewise stiffness, branch B2 shows the presence of the degenerate single period orbit, while P1, P2, and P3 show multi-periodic orbits with period 2, 3 and 5. According to the results of [1], it is expected that many other multi-periodic isolas are present in the FRC of the system;

for the sake of brevity the current numerical analysis is limited to the most important features, i.e. bifurcation of backbone curves and multi-periodic detached isolas around the first peak. From inspection of Fig. 7.12 and Fig. 7.13 it is possible to see that steady state responses with period-3 and period-5 generate detached isolas whose shape and orbits are very close to the one found experimentally in the Test Rig #1. Therefore it is possible to conclude that the experimental 'branch' of Fig. 5.4 and the associated orbits depicted in Fig. 5.4(c2,c3) belongs to an isola in the FRC. More importantly, during the experimental analysis, the system spontaneously ended in those conditions, indicating that the associated basin of attraction is potentially large. In similar systems, this phenomenon can easily lead to unwanted large-amplitude responses.

The numerical analysis also revealed the presence of the bifurcation of backbone curves in the identified ROM: in forced conditions, the bifurcation is reached with a relatively small amplitude of response, as testified by the presence of a fully developed branch B2 in the FRC. This provide further evidences that the experimental test rig possesses a bifurcation of the backbone curve and shows how easily the system develops the associated degenerate orbits (Fig. 7.13(b)). To further demonstrate the presence of the bifurcation of the backbone curve, the numerical continuation analysis is repeated in the frequency range 12-15 Hz with different excitation amplitudes: these are obtained from the experimental data associated with the degenerate orbits, i.e. the orbit shown in Fig. 5.4 (d3)). Namely the considered excitation amplitudes are: (1) the measured experimental displacement amplitude (3.52e-4 m), an equivalent displacement amplitude (4.73e-04 m) derived from the measured velocity amplitude by considering constant displacement amplitude, and twice the measured displacement amplitude (7.03e-04 m). Branches B1 and B2 are shown in Fig. 7.14 (a) with the associated orbits reported in Fig. 7.14 (b-d). The analysis demonstrates that at the same frequency of excitation at which the degenerate orbit is found experimentally, i.e. $\Omega = 13.4$ Hz, a very similar numerical orbit is found using numerical continuation, especially when the amplitude of excitation is large enough. The figure also demonstrates that the identified model captures the general dynamic response found experimentally. Finally, the analysis shows that the presence of bifurcation of the backbone curve can be demonstrated by the analysis of the forced response of the system and the associated orbits in impacting systems with multiple degrees of freedom.

7.5 Summary

In this chapter, the ROMs identified in Chapter 6 are validated and utilised to make predictions at different excitation conditions. Firstly, the ROMs representing the smooth behaviour of Test Rigs #1 and #2 are validated. Then the ROM representing the non-smooth behaviour of Test Rig #1 is validated. FRCs, time histories, and orbits are compared to demonstrate the ability of the identified nonlinear ROMs to capture the dynamics of the experimental test rigs. The identified ROMs demonstrated their accuracy in predicting not only the dynamic response utilised in the identification process, but also the dynamics of the experimental test rig associated with other excitation conditions, showing their capability to capture the global dynamic features of the system. The cross-validation, often neglected in industrial practice for time and resource constraints, is particularly important to validate the identified model and improve the degree of confidence of the associated numerical predictions. This chapter demonstrated that this practice is effective and that is relatively simple to implement with numerical continuation and integration schemes, once a ROM has been identified. A nonlinear FE model representing Test Rig #2 is updated and validated, using the NLRF method. The responses of the FE and the ROM are then compared: the analysis shows that the differences in terms of ability to capture the qualitative and quantitative dynamics of the experimental test rig are practically negligible. Thus the huge computational effort demanded to perform nonlinear dynamics FEA cannot be justified and the usage of a ROM, when possible, is highly recommended.

Finally, the identified non-smooth ROM of Test Rig #1 is used to extrapolate information about the dynamic behaviour of the system. This is possible thanks to the previous identification and validation procedure. The analysis demonstrated the presence of bifurcation of the backbone curve and detached isolas in the ROM. In addition, it is shown that it is possible to identify the presence of bifurcation of backbone curves by inspection of forced responses of the system. Specifically, this can be proved by identifying degenerate orbits. This interesting result is important as it increases the fundamental knowledge of the piecewise nonlinear system with multiple degrees of freedom and shows that it is possible to use forced responses to simplify the detection of complex phenomena like the bifurcation of the backbone curve in strongly nonlinear systems.

Chapter 8

Dynamic Behaviour of Linear and Nonlinear Structures: Two Case Studies

8.1 Introduction

The previous chapters demonstrated the importance of accounting for nonlinear dynamic phenomena and their effects on mechanical structures. This conclusive chapter discusses some engineering applications where nonlinearities, if correctly implemented, may have beneficial effects on the dynamics of the system. To this end, mechanical structures that require high performance are taken into account; specifically, Vibration Energy Harvesters (VEH) are used to develop two case studies because of their intrinsic necessity of high performance, such as high-power output and large frequency bandwidth. The chapter aims to highlight the inadequacy of linear dynamic models in describing the dynamics of high-performance nonlinear structures and conversely the capability of nonlinear systems to facilitate the achievement of exceptional performance. Specifically, the chapter discusses the following points:

- Section 8.2 proposes a short overview of how smooth and non-smooth nonlinear characteristics are used to enhance the performance of different mechanical systems such as VEHs, aeroelastic structures, Micro-Electro-Mechanical-System

(MEMS), and cutting-edge technologies such as Atomic Force Microscopy (AFM).

- Section 8.3 introduces the case study of an SDOF electromagnetic energy harvester with a bistable softening/hardening behaviour. The inadequacy of linear models in describing the system dynamics is demonstrated through numerical simulations. Employing numerical continuation and integration techniques, the analysis focuses on the nonlinear dynamic response of the system. The discussion concludes with considerations about the advantages, in terms of frequency bandwidth, resulting from the correct implementation of nonlinear characteristics into the system.

- Section 8.4 discusses dynamics and the performance of a linear planar-shaped piezoelectric energy harvester. Using finite element modelling and meta-heuristic optimisation, a scheme for the simultaneous optimisation of power output, frequency bandwidth, and efficiency is proposed. Despite the optimisation, the optimal configuration derived from a linear model reveals that the energy harvester lacks in frequency bandwidth and attains a maximum power output that is not suitable for practical applications. The discussion concludes by highlighting the potential nonlinearities that might be present in the structure and their implications on the system dynamics.

8.2 Enhancing Mechanical Systems Using Nonlinearities: overview and contextualisation

This section provides an overview of how nonlinear characteristics and nonlinear systems have been used in the literature to improve the performance of different mechanical systems and structures. Considering the breadth of the topic, the proposed overview is certainly not exhaustive and a complete description of all the possible improvements in mechanical systems falls outside of the scope of this thesis. Nonetheless, this introduction provides contextualisation for the following case studies and highlights the importance of nonlinear characteristics in high-performance mechanical structures.

8.2.1 Nonlinear Models of High-Performance Structures

Improving the performance of mechanical systems and structures is fundamental to enhance our technologies and progress in the field of engineering. Nonlinear structures have been proposed as a possible way to improve the performance of different mechanical systems. Nonetheless, depending on the application, the sought characteristics and the definition of high-performance structures may change considerably. For example, if we consider a VEH the power output and the frequency bandwidth represent important performance indicators. The literature offers many examples of vibration energy harvesters whose performance has been improved by implementing nonlinear characteristics. Cammarano et al. [6] proposed an SDOF bistable electromagnetic energy harvester. The authors proposed to exploit the bistability of the oscillator to favour the onset of high-amplitude responses at frequencies of excitation different from the natural frequency of the system. This approach aims to broaden the frequency bandwidth at which the harvester produces a sensible amount of energy. The authors demonstrated, through experiments and numerical simulations, that the nonlinear energy harvester possesses a quite large frequency bandwidth when sinusoidal excitation is applied. Zhou et al. [62] proposed to implement stoppers, i.e. non-smooth characteristics, to a cantilever piezoelectric energy harvester to improve the frequency bandwidth and the power output of the system. The idea is to exploit the hardening characteristics of the stoppers, modelled as piecewise stiffness, to increase the performance of the harvester. Wang et al. [57] proposed to use a quin-stable piezoelectric energy harvester with impact beams to harvest energy from low-frequency sources. The system works as a frequency-up conversion mechanism thanks to the presence of impacting beams that vibrate at their natural frequency when impact occurs. This frequency is much higher than the external excitation frequency, making the system highly performant and capable of harnessing energy at frequencies of excitation much lower than its natural frequency. In another example, Fasihi et al. [49] proposed to use nonlinear piezoelectric energy harvesters to suppress flutter in a two-DOF aeroelastic system. The authors investigated the effect of different parameters, such as the position, the mass, and the stiffness of the harvester, demonstrating that it is possible to improve the stability of the aeroelastic systems and at the same time extract energy from vibration.

Similarly to vibration energy harvesters, Micro/Nano-Electro-Mechanical Systems (MEMS/NEMS) can achieve higher performance by exploiting the inherited nonlinearities that are present in nano/micro-scale systems. In fact, at the nano-scale, interactions such as Van der Waals, internal material, and electrostatic forces become comparable with those experienced by the dynamic systems (e.g. inertia forces) making the overall system nonlinear. In certain cases, nonlinear properties are considered detrimental in MEMS/NEMS and compensation mechanisms are used to make the system as linear as possible [148, 149], nonetheless researchers have demonstrated that certain nonlinear dynamic phenomena, like the internal resonances, have the potential to enhance the system performance rather than limit them. Nonlinear phenomena result in useful dynamics effects that can be used to enhance the sensitivity of MEMS/NEMS sensors [150, 151], improve the resolution of AFM [152, 153], suppress noise in MEMS/NEMS signals [154], improve energy dissipation [155] and energy exchange in MEMS/NEMS [156, 157], and generate frequency locking [158] and synchronisation in MEMS [159]. Following this perspective, researchers [160] have suggested using non-smooth characteristics such as impact and contact to facilitate the generation of internal resonances in MEMS/NEMS, to further improve their capabilities.

On the other hand, some mechanical structures do not require nonlinear properties to access dynamic features that are beneficial for their performance, but rather their design induces the generation of nonlinear phenomena that can not be neglected. In these cases, dynamic models must be able to capture the nonlinear dynamics of the investigated structure. This typically happens in lightweight aeroelastic structures; these structures are often used in the aerospace industry to reduce the weight of aircraft and rotorcraft. This, in turn, allows to reduce the fuel consumption, improving the performance of the system. For example, the introduction of hinges on high-aspect-ratio wing [22] would allow the aircraft to access the currently available airports during operations like boarding/disembarking of passengers. Nonetheless, the presence of hinges in the wings may generate friction and contact, deeply affecting the dynamics of the system. In this context, nonlinear dynamic models become fundamental for investigating and designing similar systems and therefore contribute to improving the performance of mechanical aeroelastic structures.

Although not exhaustive, the proposed examples demonstrate that the nonlinearities, if correctly implemented, can improve the performance of mechanical systems and structures.

8.3 Case Study 1: A Bistable Electromagnetic Single-Degree-of-Freedom Energy Harvester

This section aims to demonstrate that, when correctly implemented, nonlinear characteristics may enhance the performance of mechanical structures, allowing the system to reach dynamic conditions that are not achievable otherwise. To this end, the dynamics of a bistable electromagnetic energy harvester are investigated via numerical simulations. Specifically, the system exploits the inherent nonlinear characteristic to enhance its energy-harvesting performance, broadening the frequency bandwidth in which high-amplitude oscillations can be achieved. To refer to a real structure, the energy harvester studied by Cammarano et al. [6] is considered in this numerical study. The harvester was fabricated, experimentally investigated, and identified by the authors and a mathematical model was validated against experimental results in different excitation conditions; this provides an excellent set of real data for the analysis of high-performance nonlinear structures.

8.3.1 Mathematical Model of an Electromagnetic Energy Harverster

The high-performance energy harvester is schematically reported in Fig. 8.1; as shown in the figure, the harvester exploits the electromagnetic coupling between the magnets and the coil to convert mechanical energy into electrical energy. The energy conversion mechanism is based on Faraday's law: the beam is excited by the base motion and vibrates. Since the magnets are positioned on the tip of the beam, the relative motion between the magnet/armature and the stator generates a variation of magnetic flux across the coils; this induces a voltage in the coils, resulting in a current when the coil

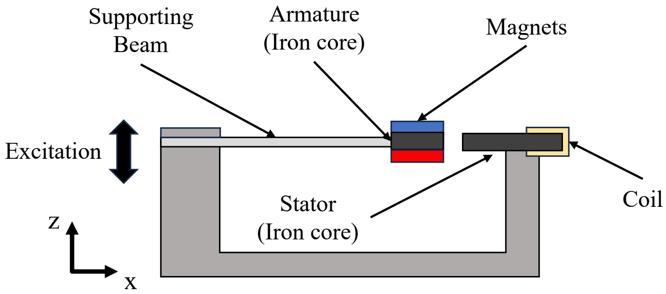

Figure 8.1: Schematic of the considered bistable energy harvester.

is a closed-circuit configuration. This current generates an opposite magnetic flux which opposes to the change of magnetic flux, resulting in an electric force which counteracts the beam movement. The electromagnetic induction phenomena can be described by the following equation [161]:

$$V = -\frac{d\Phi(t)}{dt} = -N\frac{d\phi(t)}{dt} \tag{8.1}$$

where Φ is the total magnetic flux across the coils, ϕ is the average magnetic flux across a single coil, and N is the number of coils. In general, the magnetic flux can be represented by the following equation:

$$\Phi = \sum_{i=1}^{N} \int_{A_i} BdA \tag{8.2}$$

where B is the magnetic flux density over the area A_i of a single turn. If the magnetic flux density is uniform across the coil area, it is possible to write the magnetic flux as $\Phi = NBAsin(\alpha)$ where α is the angle between the direction of magnetic flux density and the area, which leads to:

$$V = -NA\frac{dB}{dt}sin(\alpha) \tag{8.3}$$

Now, by considering that the motion between the magnets and the stator occurs in a single direction and that B does not change in time as it is generated by a permanent magnet, the voltage output equation can be approximated with the following expression [6,161,162]:

$$V = -\frac{d\Phi(t)}{dt} = -N\frac{d\phi(t)}{dz}\frac{dz}{dt} = k_t\dot{z} \tag{8.4}$$

where z is the relative displacement between the stator and the magnets and k_t is the electromagnetic coupling factor which represents the relationship between the voltage and relative velocity $\dot{z}$. Neglecting the effect of inductance in the equivalent electromagnetic circuit [163] (see Fig. 8.2) the voltage across the coils becomes $V = Ri$, where i is the current. In addition, the electromagnetic force can be represented as a damping force [161], using the following expression: $F_{elec} = c_{elec}\dot{z}$, or as an electromagnetic coupling, with the following equation: $F_{elec} = k_t i$. Considering the above-mentioned expressions, it is possible to obtain the final model representing electromagnetic force acting on the harvester:

$$c_{elec} = \frac{k_t^2}{R_{load} + R_{coil}} \tag{8.5}$$

It should be noted that, on a general basis, the electromagnetic coupling is represented by a nonlinear coefficient. Nonetheless, most of the time it reduces to a linear factor.

From a mechanical point of view, the considered electromagnetic energy harvester can be approximated with a beam, with the first mode generating the highest relative velocities between the stator and the beam tip. Under this condition, the harvester can be approximated with the mechanical SDOF model, whose general equation of motion is:

$$m\ddot{z} + c_{elec}\dot{z} + c_{mag}\dot{z} + k_{mag}z = -m\ddot{y} \tag{8.6}$$

where y is the base displacement, z is the relative displacement of the oscillator, m is mass, c_{mag} and k_{mag} are, respectively, the induced magnetic/structural damping and stiffness. The complete electro-mechanical model is schematically represented in Fig. 8.2. Using the Restoring Force Surface (RFS) method [137,138] and performing dynamic tests in open- and close-circuit, a mathematical model representing the energy harvester was obtained by Cammarano et al. [6]. The final parameters are reported in Tab. 8.1. As shown in the table, the resulting structural/magnetic stiffness is nonlinear and a 5th-order polynomial is found to approximate the relationship between the elastic

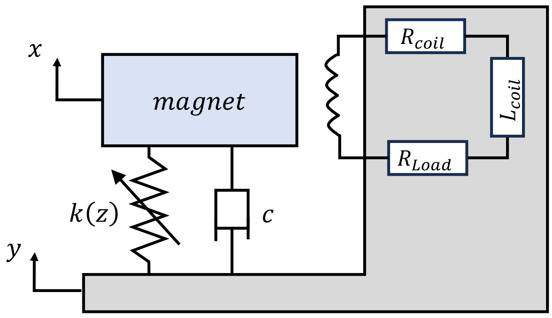

Figure 8.2: Mathematical dynamic model representing the considered base excited electromagnetic energy harverster.

Table 8.1: Energy harvester parameters identified by Cammarano et al. [6].

Parameter	Numerical Value	Units
m	0.080	Kg
c_{mag}	0.240	Ns/m
$k_{1,m}$	-9.992e2	N/m
$k_{2,m}$	-8.112e4	N/m^2
$k_{3,m}$	8.816e8	N/m^3
$k_{4,m}$	2.436e10	N/m^4
$k_{5,m}$	-5.176e13	N/m^5
k_t	10	Vs/m

restoring force and the displacement of the mass. In particular, the air gap (1.5 mm) between the stator and armature, adopted in the identified configuration, induced a softening-hardening characteristic typical of bistable systems. The identified restoring characteristic is shown Fig. 8.3. From Fig. 8.3 (a), it is clear that the identified characteristic does not behave correctly outside the experimentally validated limits (approx. $\pm$ 3 mm) as the stiffness characteristic tends to diverge to opposite sign values. On the contrary, the identified characteristic shows the expected behaviour when considered inside the experimental limits, as shown by Fig. 8.3 (b).

8.3.2 Dynamic Response of a Bistable Energy Harvester

To understand the dynamic response of the system, the bifurcation diagram is computed considering open circuit configuration and forward/backward frequency sweeps at different excitation amplitudes, namely 125 μm, 150 μm, 175 μm, and 200 μm. The results are reported in Fig. 8.4 in terms of maximum absolute accelerations: from the

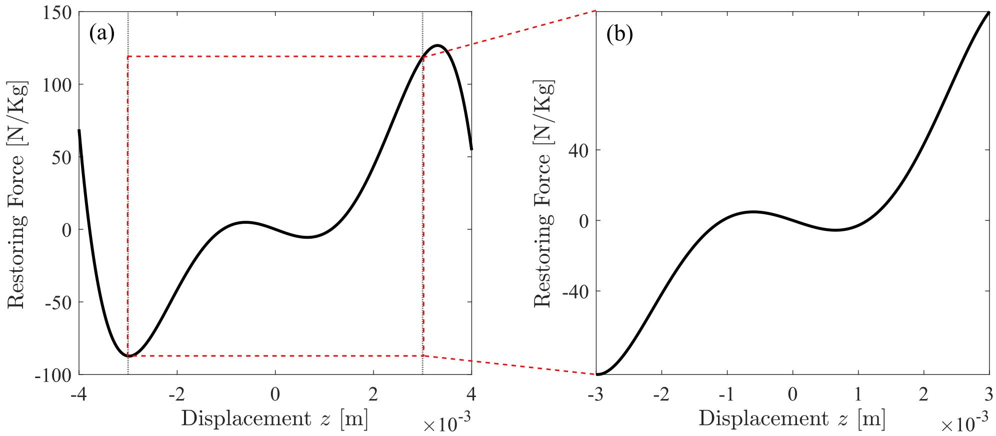

Figure 8.3: Nonlinear restoring force of the electromagnetic energy harvester. Extrapolation outside (a) and inside (b) the experimental limits.

figure, it is clear that jumps, co-existent solutions and chaotic responses appear in the dynamics of the system. The figure shows that by increasing the excitation amplitude chaos appears around the frequency bandwidths 20-25 Hz and 35-45 Hz. The bistable harvester is characterised by the presence of two potential wells and three equilibrium points in static conditions (fixed points) [6]: one equilibrium point is unstable and corresponds to a relative displacement $z = 0$ mm. The remaining two equilibrium points are stable and generate the two potential wells whose zero energy corresponds to the equilibrium conditions (one at positive displacement and one at negative displacement). These stable equilibrium points correspond to the static deflection of the beam caused by the presence of the magnetic force. In the dynamic steady state conditions ,when the energy is large enough, the harvester can escape from one well and reach the other one, generating oscillations between the wells, named interwell oscillations. Chaos occurs through the typical period-doubling cascade [75] which transforms the single-period oscillations into multi-periodic oscillations increasing their period until chaos is not reached. In particular, during chaotic oscillations, the harvester oscillates for a certain amount of time in one well and then, when enough energy is accumulated, jumps into the other well. This process is repeated over and over again, leading to aperiodic dynamic responses. The route to chaos mechanism is confirmed by Fig. 8.5 (a) where the bifurcation diagram of the harvester is reported. The diagram is computed moving

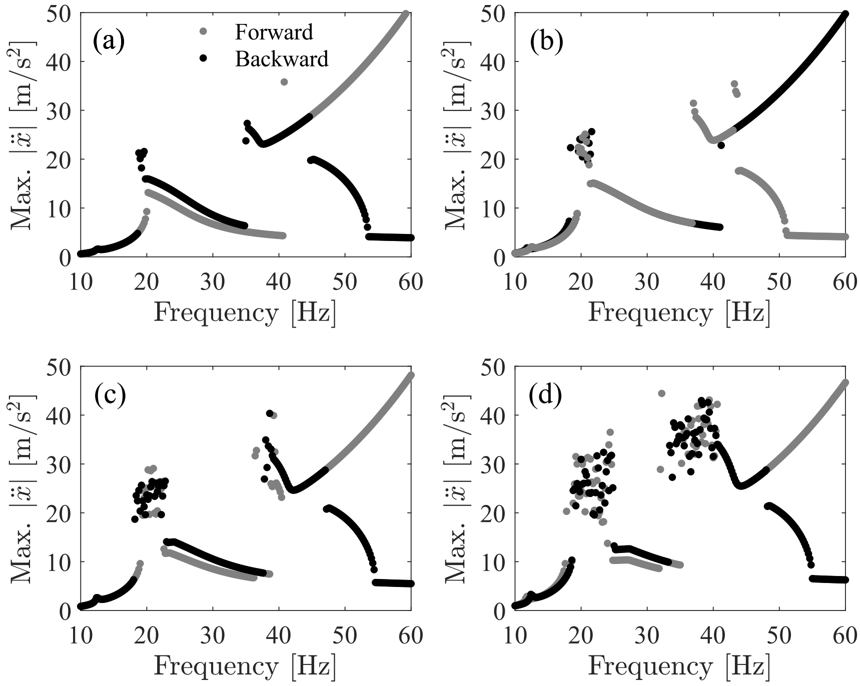

Figure 8.4: Numerical bifurcation diagram in open circuit conditions. The excitation frequency Ω represents the bifurcation parameter while the maximum absolute acceleration $|\ddot{x}|$ is the considered output. Different base amplitudes excitation are considered: 125 μm (a), 150 μm (b), 175 μm (c), and 200 μm (d)

from low to high amplitudes of excitation and Poincaré sections are used to plot the relative displacement of the harvester when the plane $\dot{x} = 0$ is intersected. The diagram shows the period-doubling phenomenon, which starts generating many branches near chaos. This is highlighted by the panels (1-3) of Fig. 8.5 (a) where the presence of multiple bifurcating branches in a very small range of excitation amplitude are shown. The figure also shows that chaos appears at an excitation amplitude of about $Y = 145$ μm. In addition, it should be noted that only the period-doubling cascade associated with the potential well at negative displacement ends in chaos. The figure shows that period-doubling bifurcations are present also in the other potential well at positive displacement. Nonetheless, the period-doubling cascade does not end in chaos but rather the dynamics of the system is attracted and remain trapped in the other potential well. This result agrees with the findings of Cammarano et al. [6] which demonstrate

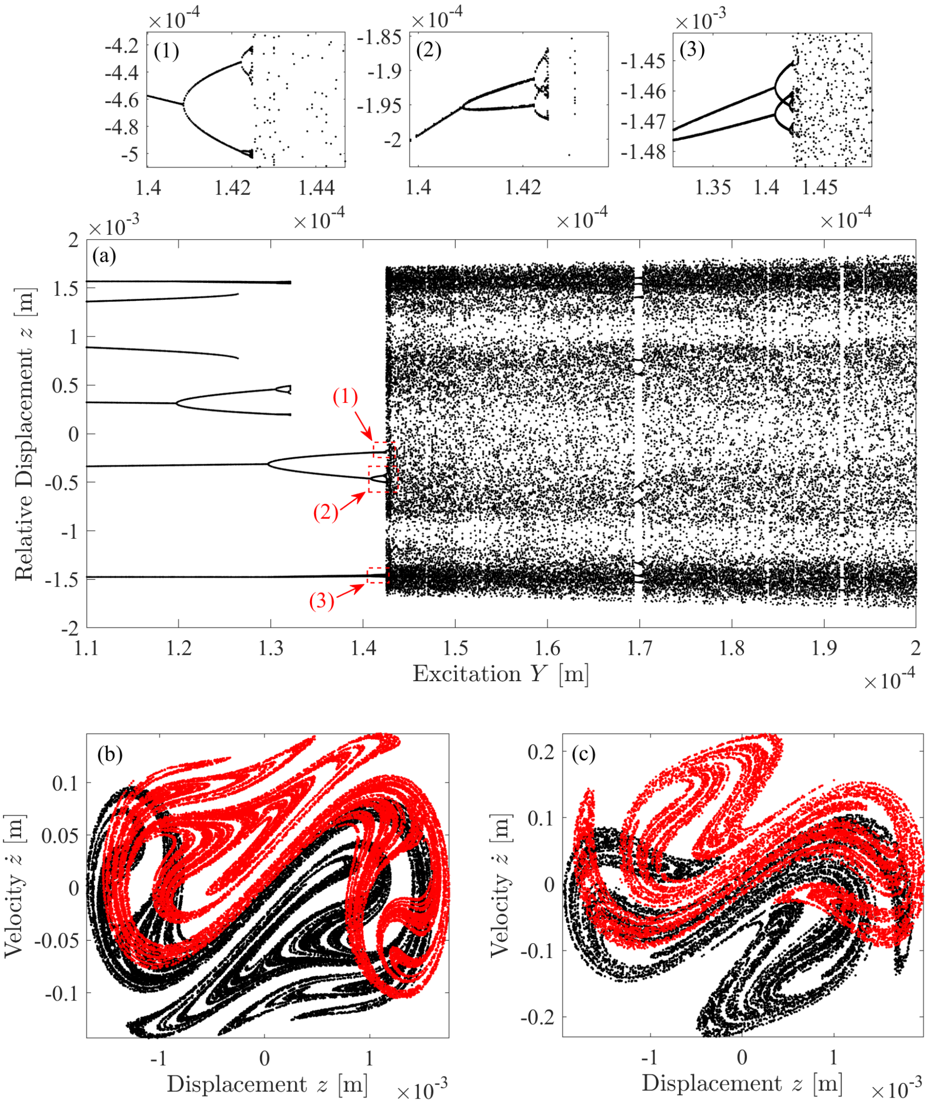

Figure 8.5: Bifurcation diagram and strange attractors of the bistable energy harvester. The bifurcation diagram (a) is computed at 20 Hz moving from low to high amplitude of excitation. Details of the period-doubling cascade are reported in panels (1-3). Poincaré maps of strange attractors are reported in panels (b,c). The red and black dots denote the Poincaré points obtained by sampling the signal every half period of excitation, using a base amplitude of 200 μm and a frequency of excitation equal to 20 Hz (a) and 38 Hz (b). Open circuit conditions are applied for all the simulations.

that the system slightly favours the potential well with a negative displacement due to its lower-energy states. To better investigate the chaotic behaviour of the harvester, the largest excitation amplitude (200 μm) is used to compute the chaotic response of the system for 30000 periods. The associated Poincaré map is then reconstructed at

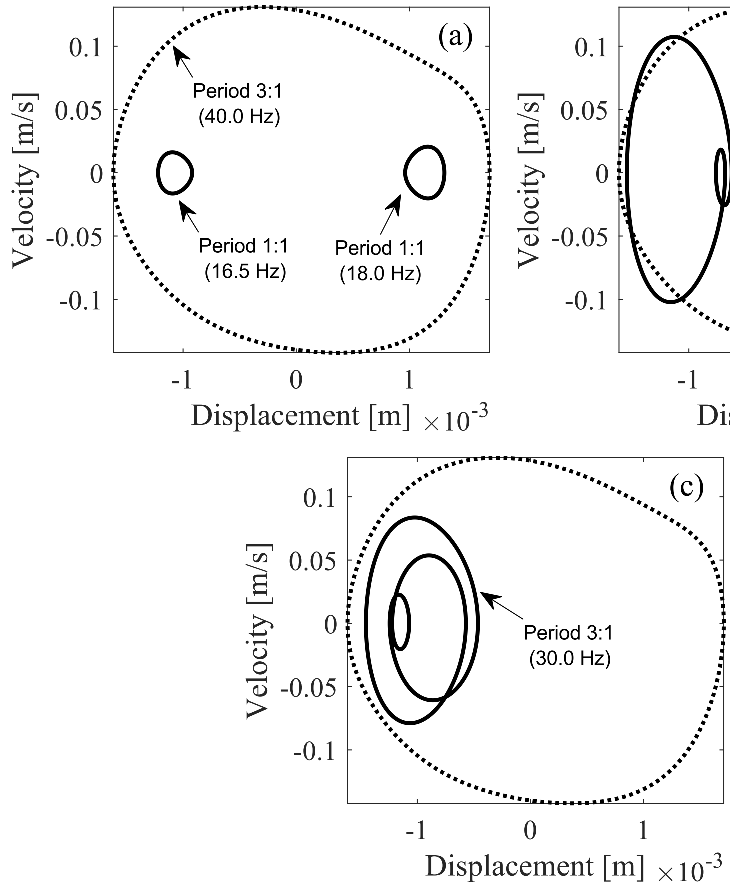

Figure 8.6: Steady-state orbits obtained at $Y = 150\mu m$. The dotted line indicates interwell oscillations while the continuous line defines single and period-doubling intrawell oscillations.

two different frequencies of excitation, 20 Hz and 38 Hz, and the results are shown in Fig. 8.5 (b,c). Two strange attractors are identified which confirm the presence of chaos.

As explained in Chapter 2 bifurcation diagram and Poincaré maps provide useful insight into the dynamics of the system; nonetheless, they are based on a numerical integration scheme which computes only stable dynamic responses. In addition, it is not easy to identify all the possible dynamics of the harvester via numerical integration as a large number of initial conditions should be considered. To better understand the intricate dynamics of the system some of the steady-state periodic solutions are continued via numerical continuation. The steady-state orbits of the considered dynamic conditions are represented in Fig. 8.6: the dotted line denotes the orbits of an interwell oscillation which is found to have a period 3:1, i.e. three times longer than the excitation period. The other orbits illustrate the single- and multi-period dynamics of the system in the two potential wells (intrawell oscillations). The figure also shows the frequency (in brackets) at which the dynamic conditions are identified using an excitation amplitude of 150 μm. The toolbox COCO [97] is used to perform the numerical calculations. The same procedure implemented in Chapter 2 for the Duffing oscillator is used here to track the orbits described by Fig. 8.6. The results of the continuation procedure are reported in Fig. 8.7 where panels (a,b) describe period 1:1 intrawell oscillators in the potential well at negative (a) and positive (b) displacement, panels (c,d) show the continuation of period 2:1 orbits in negative (c) and positive (d) displacement, and panels (e-f) illustrate the continued period 3:1 intrawell (e) and interwell (f) oscillations. Fig. 8.7 demonstrates the existence of the softening behaviour of the single-period intrawell oscillations as well as an intricate network of bifurcations with period-doubling (PD), fold (FP), and branch (BP) bifurcations. Panels (c-e) show that intrawell period 2:1 oscillations originate from stable single-period ones, while intrawell period 3:1 oscillations are generated from unstable single-period orbits. Finally, panel (f) shows the interwell period-tripling oscillations: these orbits belong to a separated branch that is not connected to the other ones, i.e. it represents an isola. The details of the isola are reported in Fig. 8.7 (g) which shows that the isola closes around 80 Hz, passing from stable to unstable dynamic behaviour.

Although simple in its design, the harvester showed quite intricate dynamic behaviour which can not certainly be described with a linear dynamic model but instead requires the definition of a more sophisticated model which incorporates nonlinear characteristics. The presence of broadband high-amplitude interwell oscillations is demonstrated through numerical simulations, using a mathematical model that was experimentally validated by Cammarano et al. [6]. The interwell oscillations generate an isola that persists at high frequencies of excitation; this feature is particularly attractive from the energy harvesting point of view. In fact, this dynamic behaviour is associated with a broadband frequency and large amplitude of response which can

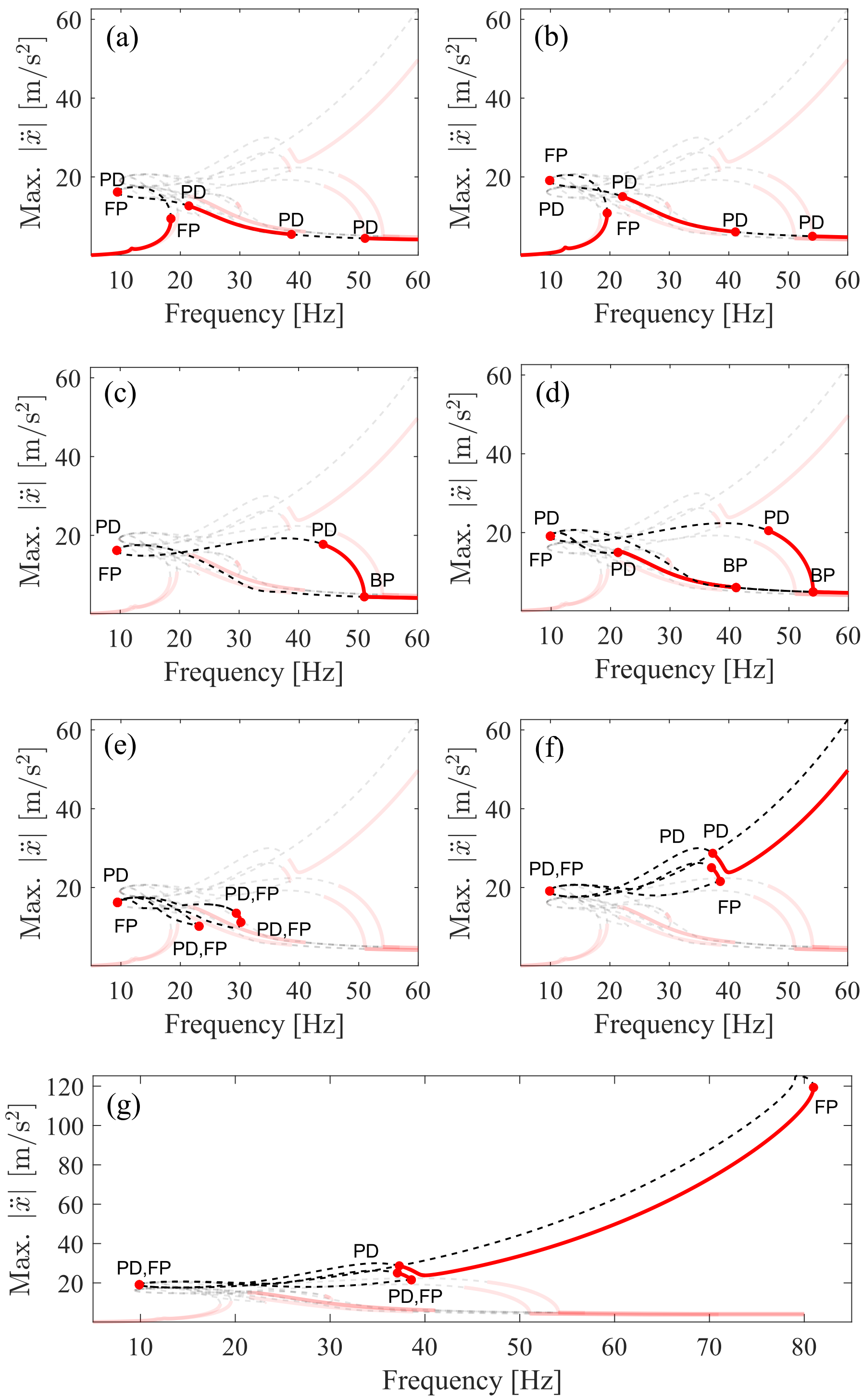

Figure 8.7: Numerical continuation of periodic orbits. Different continued solutions are highlighted in each panel: period 1:1 (a,b), period 2:1 (c,d), and period 3:1 (e,f,g).

boost the performance of the harvester in terms of frequency bandwidth and power output, solving the problem of small resonance regions in SDOF linear energy harvesters when sinusoidal excitation and steady-state conditions are considered. This example demonstrates that, if correctly implemented, nonlinearities can improve the dynamics of mechanical systems, boosting their performance.

8.4 Case Study 2: Optimisation of a Piezoelectric Planar-Shaped Energy Harvester

This section introduces a second case study: the optimisation and analysis of a planar-shaped piezoelectric energy harvester. The assumption of linear behaviour is made to simplify the dynamic analysis, enabling iterative optimization of the structure. Although optimal configurations are achieved, the performance of the energy harvester remains poor, especially from the power output point of view. In contrast with the previous analysis, the dynamics of the system do not show particularly useful features for enhancing the energy harvesting performance, highlighting the limits of SDOF/Single-mode linear energy harvesters.

8.4.1 Finite Element Model of the Piezoelectric Energy Harvester

The considered Piezoelectric Energy Harvester (PEH) is depicted in Fig 8.8 (a) and it is constituted of three elements: structural material (bronze), a piezoelectric layer in uni-morph configuration, and an electrical circuit to harvest energy from vibrations. The PEH is constrained at the bottom and it is subjected to transversal excitation. The geometry is characterised by the following design variables: width b, length h, thickness of the structural material t and piezoelectric patch t_p, angle of inclination θ, and the trapezoid base angle φ. Tab. 8.2 shows the lower/upper bounds of parameters considered in the optimisation procedure as well as their original configuration (P_0). Fig. 8.8 show additional parameters, namely f and g whose values are determined at every step of the optimisation procedure using the following expressions: $f = 1/6h\sin(\theta)$ and $g = 2/3h\sin(\theta)$.

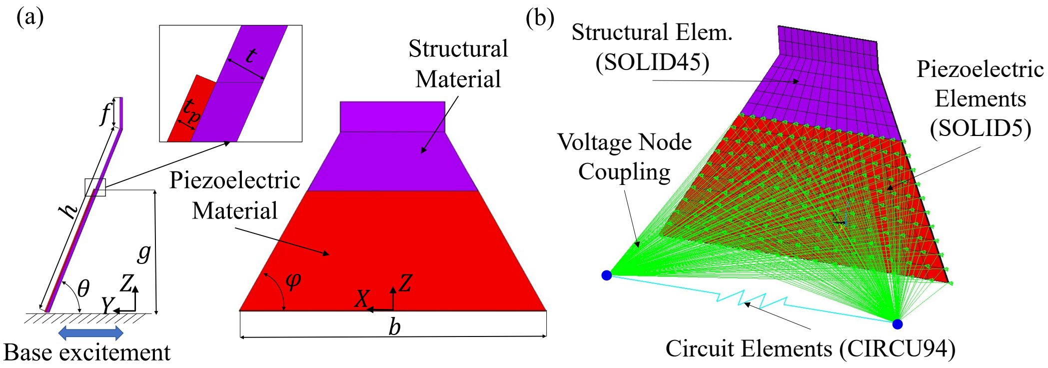

Figure 8.8: Schematic of the piezoelectric energy harvester and its main dimensions (a) and equivalent finite element model (b) [5].

Table 8.2: Lower and upper bounds, and original configuration (P_0) of the harvester parameters.

Parameter	Lower Bound	Upper Bound	P_0	Unit
h	30.0	120.0	65.3	mm
b	90.0	200.0	114.0	mm
t	0.5	2.0	0.5	mm
t_p	0.3	1.0	0.3	mm
θ	30.0	90.0	67.0	deg
φ	50.0	130.0	60.0	deg
R	1.0	10^6	1000	Ω

The PEH exploits the piezoelectric effect to harvest energy from induced vibrations, transforming mechanical energy into electrical energy. This effect refers to the capability of piezoelectric material to accumulate opposite sign charges when mechanical loads are applied and conversely to deform when electric voltages are applied to the material. To distinguish the two behaviours, the phenomenon takes the name of direct piezoelectric effect (in the first case) and inverse piezoelectric effect (in the second case). The constitutive equations of piezoelectric material describe this phenomenon, creating relationships between strain and charges of the piezoelectric material as follows:

$$\begin{Bmatrix} \mathbf{S} \\ \mathbf{D} \end{Bmatrix} = \begin{bmatrix} \mathbf{s}^{E_c} & \mathbf{d}^T \\ \mathbf{d} & \epsilon^{T_c} \end{bmatrix} \begin{Bmatrix} \mathbf{T} \\ \mathbf{E} \end{Bmatrix} \tag{8.7}$$

where $\mathbf{S}$ is the strain vector, $\mathbf{D}$ is the electric displacement vector, and $\mathbf{E}$ is the electric field vector, $\mathbf{T}$ is the stress vector. The matrices $\mathbf{s}^{E_c}$,$\mathbf{d}$, and ϵ^{T_c} are the constitutive matrices, namely, the compliant matrix, the piezoelectric strain matrix, and the dielectric matrix. The exponents E_c and T_c denote that the respective constants are evaluated at constant electric field and constant stress. The piezoelectric, dielectric, and elastic matrices of piezoelectric materials are influenced by the crystal structure or crystal class of the material [164]. Different crystal classes exhibit different symmetries, and this symmetry affects the number and arrangement of the material constants in the matrices. In the considered case-study, PZT-5H is used as piezoelectric material for the PEH and it is characterised by the following transversely isotropic behaviour [165]:

$$\left\{\begin{array}{c} S_1 \\ S_2 \\ S_3 \\ S_4 \\ S_5 \\ S_6 \\ \hline D_1 \\ D_2 \\ D_3 \end{array}\right\} = \left[\begin{array}{cccccc|ccc} s_{11}^{E_c} & s_{12}^{E_c} & s_{13}^{E_c} & 0 & 0 & 0 & 0 & 0 & d_{31} \\ s_{12}^{E_c} & s_{11}^{E_c} & s_{13}^{E_c} & 0 & 0 & 0 & 0 & 0 & d_{31} \\ s_{13}^{E_c} & s_{13}^{E_c} & s_{33}^{E_c} & 0 & 0 & 0 & 0 & 0 & d_{33} \\ 0 & 0 & 0 & s_{55}^{E_c} & 0 & 0 & 0 & d_{15} & 0 \\ 0 & 0 & 0 & 0 & s_{55}^{E_c} & 0 & d_{15} & 0 & 0 \\ 0 & 0 & 0 & 0 & 0 & 2(s_{11}^{E_c} - s_{12}^{E_c}) & 0 & 0 & 0 \\ \hline 0 & 0 & 0 & 0 & d_{15} & 0 & \epsilon_{11}^{T_c} & 0 & 0 \\ 0 & 0 & 0 & d_{15} & 0 & 0 & 0 & \epsilon_{11}^{T_c} & 0 \\ d_{31} & d_{31} & d_{33} & 0 & 0 & 0 & 0 & 0 & \epsilon_{33}^{T_c} \end{array}\right] \left\{\begin{array}{c} T_1 \\ T_2 \\ T_3 \\ T_4 \\ T_5 \\ T_6 \\ \hline E_1 \\ E_2 \\ E_3 \end{array}\right\} \tag{8.8}$$

The matrix of Eq. 8.8 comprises 5 elastic independent constants, 3 piezoelectric independent constants, and 3 dielectric independent constants which populate the matrices thanks to symmetry properties. The numerical value of these parameters is obtained from [166] and it is implemented in ANSYS to perform the FE simulations, along with the following mechanical properties: Young modulus $E = 100\ GPa$, Poisson coefficient $\nu = 0.34$, density $\rho = 8000\ kg/m^3$, and global structural damping of 2%. To guarantee the adequate quality of the mesh [167], a converge analysis is performed and revealed that 4000 elements with two layers of elements per material represents a good balance between computational effort and the quality of the results.

A FE model of the harvester is created in ANSYS: 3D structural elements (SOLID45) and 3D piezoelectric elements (SOLID5) with 8 nodes are used to model the structural part of the harvester and the piezoelectric layer. To simulate the presence of two electrodes, the voltage output of some nodes of the piezoelectric material is constrained. Specifically, all the nodes in the upper surface of the piezoelectric material are connected to a single additional node, representing an electrode, and their voltage output is forced to be same [1]. The same procedure is applied to the nodes in the lower surface, which are connected to a different node, i.e. the second electrode. The final results are shown in Fig. 8.8 (b), where the two electrodes are indicated by blue dots. An electric element (CIRCU94) is used to model an ideal resistor (the electric load) and it is connected to the two electrodes of the piezoelectric material to evaluate the produced output power under vibratory loads.

8.4.2 Optimisation of the Piezoelectric Energy Harvester

The PEH is optimised using meta-heuristic optimisation methods: unlike to gradient-based optimisation schemes, these methods can explore and exploit the search space which makes them suitable for global optimisation of non-convex problems with non-smooth constraints [169–171]. Although there is a lack of theoretical demonstration, meta-heuristic methods have been shown to be suitable for the optimisation of many engineering problems [170, 171]. Many meta-heuristic methods are available in the literature; among them, the most used are the Genetic Algorithm (GA) [131], Particle Swarm Optimisation(PSO) [132], and Differential Evolution (DE) [172].

The optimisation framework proposed in this section is based on the PSO (see Section 6.2.2 for more information about the PSO and GA): this method is chosen because it is particularly effective in solving nonlinear problems [133, 173] and allows reaching a suitable solution of the optimisation problem with relatively few iterations. In the proposed framework the method is implemented using the MATLAB function *particleswarm* which considers the modifications suggested by Mezura et al. [174] and Pedersen [175]. The proposed optimisation framework is schematically illustrated in Fig. 8.9: firstly, the particles composing the swarm are initialised randomly to cover uniformly the investigated design domain. For each particle, design variables are assigned; this includes defining the parameters presented in Tab. 8.2. Then, the constraints are

[1]SOLID5 elements have 4 DOFs, i.e. the spatial displacements in the three directions and the voltage, when the element key-option is set equal to 3 [168]

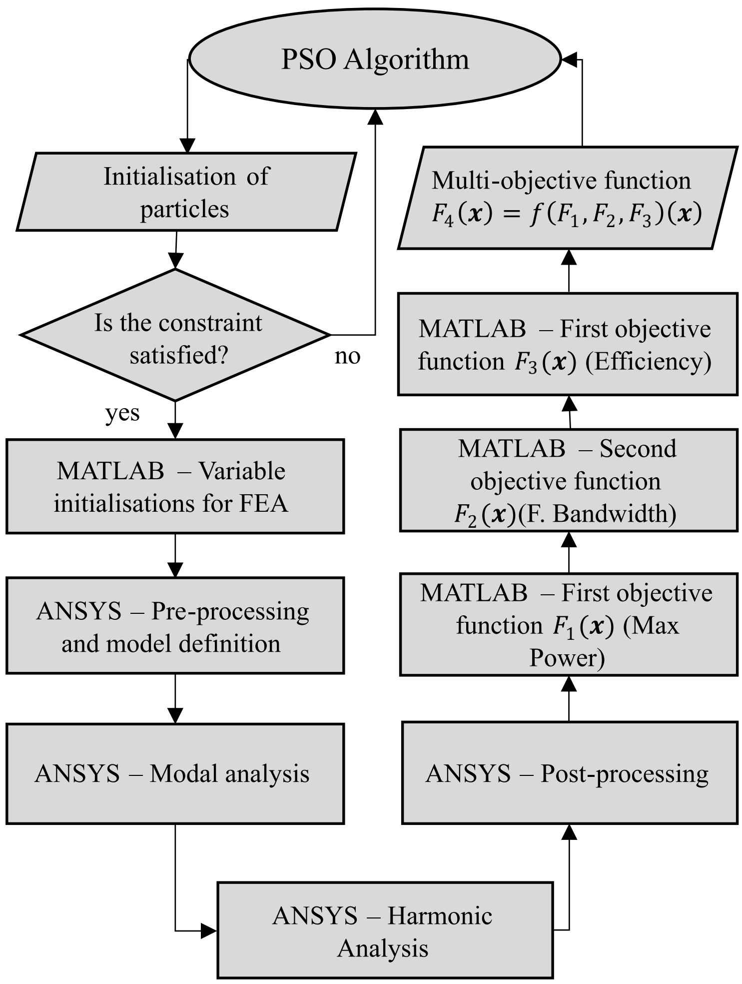

Figure 8.9: Schematic of the proposed optimisation framework [5].

checked for the selected parameters; in the specific case, a penalty function is introduced to avoid the generation of broken mesh in the FE environment. The penalty function is described by the following equation:

$$F_{val} = \begin{cases} F(\mathbf{x}) & \varphi \geq \frac{\pi}{2} \\ F(\mathbf{x}) & h \leq \frac{19}{40} b \tan(\varphi) \quad \& \quad \varphi < \frac{\pi}{2} \\ 0 & h > \frac{19}{40} b \tan(\varphi) \quad \& \quad \varphi < \frac{\pi}{2} \end{cases} \tag{8.9}$$

where $F(\mathbf{x})$ represents a generic objective function and $\mathbf{x}$ denotes the design variables vector. If the constraint is satisfied, then the selected parameters are used to initialise the variables that are necessary to perform the FE analyses. The FEA is composed of three steps: pre-processing and model definition, modal analysis, and harmonic analysis. During the first step, the model is created in ANSYS and all the necessary properties, including the material, are assigned. Once a model is built, a modal analysis is performed to evaluate the mode shapes and the natural frequencies of the system. The last step consists of performing a harmonic analysis to obtain the FRF of the system in terms of power output. For this task, a constant acceleration of the base equal to 0.2 g is considered. To reduce the computational burden, due to multiple iterations, the FRF is computed in a well-defined 'frequency window': this frequency range is selected using the first natural frequency of the system, previously obtained during the modal analysis. Once the numerical analyses are completed, the post-processing of the results starts and the four objective functions are computed: specifically, three single-objective functions ($F_1(\mathbf{x})$, $F_2(\mathbf{x})$, and $F_3(\mathbf{x})$) and one multi-objective function ($F_4(\mathbf{x})$). The first two objective functions compute the maximum power output ($F_1(\mathbf{x})$) and the frequency bandwidth at half power ($F_2(\mathbf{x})$). They can be calculated using the output of the harmonic analysis in terms of voltage FRF by applying the following expression: $P = \frac{|V|^2}{2R}$. The third single-objective function ($F_3(\mathbf{x})$) utilises a different expression to compute the efficiency of the harvester. To this end, a novel matrix formulation, based on the energy balance principle, is proposed in [5]. The proposed definition of efficiency is derived starting from the equations of motion of the electro-mechanical FE model [168]:

$$\mathbf{M}\ddot{\mathbf{u}} + \mathbf{C}\dot{\mathbf{u}} + \mathbf{K}\mathbf{u} = \mathbf{Q} \tag{8.10}$$

Considering the assumption of harmonic loading and steady-state conditions, the steady-state energy contributions per cycle can be calculated as follows:

$$\int_0^{T_p} \dot{\mathbf{u}}^T \mathbf{M} \ddot{\mathbf{u}} \, dt = -\frac{i\Omega^2 \pi}{2} [\mathbf{U}^T \mathbf{M} \bar{\mathbf{U}} - \bar{\mathbf{U}}^T \mathbf{M} \mathbf{U}] \tag{8.11a}$$

$$\int_0^{T_p} \dot{\mathbf{u}}^T \mathbf{K} \mathbf{u} \, dt = \frac{i\pi}{2} [\mathbf{U}^T \mathbf{K} \bar{\mathbf{U}} - \bar{\mathbf{U}}^T \mathbf{K} \mathbf{U}] \tag{8.11b}$$

$$\int_0^{T_p} \dot{\mathbf{u}}^T \mathbf{C} \dot{\mathbf{u}} \, dt = \frac{\Omega \pi}{2} [\mathbf{U}^T \mathbf{C} \bar{\mathbf{U}} + \bar{\mathbf{U}}^T \mathbf{C} \mathbf{U}] \tag{8.11c}$$

$$\int_0^{T_p} \dot{\mathbf{u}}^T \mathbf{Q} \, dt = \frac{i\pi}{2} [\mathbf{U}^T \bar{\mathbf{Q}} - \bar{\mathbf{U}}^T \mathbf{Q}] \tag{8.11d}$$

where $T_p = \frac{2\pi}{\Omega}$ denotes the period, $\mathbf{M}$, $\mathbf{C}$, $\mathbf{K}$, and $\mathbf{Q}$ are the generalised mass, damping, stiffness, and force matrices, $\mathbf{U}$ indicates the complex amplitude of the response $\mathbf{u}$, and $\bar{\bullet}$ defines the complex conjugated operator. Once an FE model is created in ANSYS, it is possible to export the associated global matrices $\mathbf{M}$, $\mathbf{C}$, $\mathbf{K}$, and $\mathbf{Q}$. These matrices, in turn, can be used to compute the steady-state energy contributions per cycle of the system, using the expressions reported in Eq. 8.11. It should be noted the obtained matrices are global, thus they might present contributions associated with different physical mechanisms, especially when multi-physics simulations are performed. For example in the considered case, the stiffness matrix $\mathbf{K}$ contain contributions coming from the piezoelectric and mechanical stiffness.

In the case of the considered PEH, the energy contributions from viscous and electrical damping must be separated to correctly compute the efficiency of the system: the first one denotes the energy dissipated during the harvesting process, while the second one indicates the system energy output. Dividing the structural and electrical contributions, the generalized damping matrix and load vector [168] of the harvester take the following form:

$$\mathbf{C} = \begin{bmatrix} \mathbf{C_v} & \mathbf{0} \\ \mathbf{0} & \mathbf{0} \end{bmatrix} + \begin{bmatrix} \mathbf{0} & \mathbf{0} \\ \mathbf{0} & -\mathbf{C_{vh}} \end{bmatrix} + \frac{1}{\Omega^2} \begin{bmatrix} \mathbf{0} & \mathbf{0} \\ \mathbf{0} & \mathbf{C_r} \end{bmatrix} \tag{8.12a}$$

$$\mathbf{Q} = \begin{Bmatrix} \mathbf{0} \\ \mathbf{L_a} \end{Bmatrix} + \begin{Bmatrix} \mathbf{Q_a} \\ \mathbf{0} \end{Bmatrix} \tag{8.12b}$$

where $\mathbf{C_v}$, $\mathbf{C_{vh}}$, and $\mathbf{C_r}$ are the viscous, dielectric, and electric damping matrices, $\mathbf{Q_a}$ is the structural load vector, and $\mathbf{L_a}$ represent electrical load vector. The efficiency of the harvester can be calculated by analysing the input and output energy components: the first one, denoted by the energy dissipated by the resistor, corresponds to the energy contribution of $\mathbf{C_r}$, while the second one is identified by the energy associated with external structural loads $\mathbf{Q_a}$. Using Eq. 8.11 and Eq. 8.12, it is possible to achieve the final formulation of the efficiency:

$$\eta = \frac{1}{i\Omega}\frac{[\mathbf{U}^T\mathbf{C_r^*}\bar{\mathbf{U}} + \bar{\mathbf{U}}^T\mathbf{C_r^*}\mathbf{U}]}{[\mathbf{U}^T\bar{\mathbf{Q}}_\mathbf{a}^* - \bar{\mathbf{U}}^T\mathbf{Q_a^*}]} \tag{8.13}$$

where $\mathbf{C_r^*}$ and $\mathbf{Q_a^*}$ are represented by:

$$\mathbf{C_r^*} = \begin{bmatrix} \mathbf{0} & \mathbf{0} \\ \mathbf{0} & \mathbf{C_r} \end{bmatrix} \tag{8.14a}$$

$$\mathbf{Q_a^*} = \begin{Bmatrix} \mathbf{Q_a} \\ \mathbf{0} \end{Bmatrix} \tag{8.14b}$$

The efficiency formulation of Eq. 8.13 can be applied to lumped parameters MDOF and FE models of PEHs and thus represents an extension of previous formulations of efficiency for PEHs which are valid only for SDOF models [2]. Finally, the multi-objective function $F_4(x)$ is defined by the following equation:

$$F_4(\mathbf{x}) = w_1\frac{F_1(\mathbf{x})}{P_{opt}} + w_2\frac{F_2(\mathbf{x})}{\delta_{opt}} + w_3\frac{F_3(\mathbf{x})}{\eta_{opt}} \tag{8.15}$$

where w indicates the weighting factor (imposed as $w_1 = 1/3$, $w_2 = 1/3$, and $w_3 = 1/3$, so that the sum equals 1), P_{opt} is the optimum power, δ_{opt} represents the optimum frequency bandwidth, and η_{opt} denotes the maximum possible efficiency of the harvester. The first two optimal quantities are obtained by using the proposed optimisation framework to optimise the single-objective functions $F_1(x)$ and $F_2(x)$. The maximum efficiency η_{opt}, instead, is considered to be equal to 1.

Tab. 8.3 represents the results of the optimisation process for the four objective

[2] A formal comparison with a previous definition of efficiency, introduced by Yang et al. [176] for of a lumped SDOF model of PEH, is reported in [5].

Table 8.3: Optimal design variables and function value for the objective functions $F_1(\mathbf{x})$, $F_2(\mathbf{x})$, $F_3(\mathbf{x})$, and $F_4(\mathbf{x})$.

Par./Fun	Max Power $F_1(\mathbf{x})$	Freq. Band. $F_2(\mathbf{x})$	Efficiency $F_3(\mathbf{x})$	Multi-Obj. $F_4(\mathbf{x})$
h	120.0 mm	30.0 mm	30.0 mm	30.0 mm
b	200.0 mm	90.0 mm	200.0 mm	200.0 mm
t	2.0 mm	2.0 mm	0.5 mm	2.0 mm
t_p	0.3 mm	1.0 mm	0.3 mm	1.0 mm
θ	90.0 deg	30.0 deg	30.0 deg	30.0 deg
φ	130.0 deg	50.0 deg	91.5 deg	89.0 deg
R	2323.0 Ω	2148.0 Ω	1078.2 Ω	941.0 Ω
F_{max}	51.5 Hz	2.2684×10^3 Hz	515.8 Hz	1.9892×10^3 Hz
P_{max}	18.0 mW	4.3×10^{-3} mW	1.8×10^{-2} mW	1.8×10^{-2} mW
Δ_{frq}	3.8 Hz	200.1 Hz	55.0 Hz	203.9 Hz
η	46.42 %	55.25 %	63.87 %	61.66 %

functions. The first seven rows represent the optimal values of the design variables while the last four rows denote the associated maximum power output P_{max} and frequency F_{max}, the frequency bandwidth at half power Δ_{frq}, and the efficiency η. Although the optimisation of the single- and multi-objective functions is achieved in all the considered cases, the optimised model does not show high energy harvesting performance. The maximum power output is very low and, in most cases unsuitable to power any device. When only the power output is optimised, a reasonable amount of power is achieved, i.e. 18 mW, nonetheless the associated frequency bandwidth is particularly small (only 3.8 Hz). Conversely, when the frequency bandwidth is optimised, the maximum power output decreases to particularly low values. The optimisation study suggests that the performance of the considered linear energy harvester are poor and no optimal solution can guarantee large power output for a wide range of frequency bandwidth. In contrast, the nonlinear energy harvester of previous case study was able to achieve high energy harvesting performance exploiting large-amplitude interwell oscillations. Therefore the analysis of the two case studies suggest that the absence of nonlinear characteristic might lead to poorer performance in mechanical structures.

In practical scenarios, the system might exhibit nonlinear dynamic behaviour, even under low excitation amplitudes. This could be attributed to factors such as structural and electrical nonlinearities, arising from constraints leading to friction, boundary conditions resulting in contact, or rectifiers generating electrical loading with thresholds.

The presence of similar nonlinearities, as demonstrated in the previous chapters, could change completely the dynamics of the system leading to very different dynamic behaviours and energy harvesting performance. Despite this, a detailed and complete nonlinear analysis of the dynamics of the harvester should be performed to evaluate the performance of the energy harvester when nonlinear effects are considered.

8.5 Summary

This chapter discussed some engineering applications of high-performance mechanical systems and structures. Firstly the definition of performance for different mechanical systems is discussed, showing that, when nonlinearities are correctly implemented, it is possible to obtain the enhancement of the performance. To better explain this concept, two case studies related to vibration energy harvesting are presented: in the first one, an SDOF electromagnetic energy harvester is introduced and its dynamics are analysed. In the second case study, the dynamic behaviour of planar-shaped piezoelectric energy harvester is studied and the structural and electrical parameters are optimised. The electromagnetic energy harvester is characterised by a nonlinear stiffness characteristic. Such a characteristic is induced by the presence of magnetic attracting forces which makes the system bistable. This results in multi-periodic and chaotic behaviours with the presence of co-existing solutions. The bifurcation diagram and the numerical continuation analyses show the presence of jumps and isolas with stable steady-state solutions at large amplitude of response for a wide range of frequencies of excitation. This makes the harvester a promising high-performance structure. These phenomena cannot be described or analysed with linear dynamic models, and thus, they highlight the necessity of nonlinear models for their study. On the other hand, an FE model is employed to investigate the dynamics and the performance of a planar-shaped piezoelectric energy harvester. The model is developed under the assumption of linear behaviour, and a low excitation amplitude is applied to uphold this condition. This choice is motivated by the necessity of providing a linear counterpart to the previous case study. In this way, the performance of linear and nonlinear energy harvester can be evaluated. Using the proposed optimisation framework, the system is optimised in terms of power output, frequency bandwidth, and efficiency. The results show that the harvester has poor energy harvesting performance, even when ideal conditions are met, i.e. when perfect constraints, sinusoidal excitation, and excitation near the first natural frequency, are applied. The optimised harvesters, indeed, are characterised by either a small frequency bandwidth with significant power output or insignificant power output for a large frequency bandwidth. This suggests that linear energy harvesters struggle to reach high performance and might not be suitable for improving the current energy harvesting technology, especially when only one mode is considered in the design. On the contrary, when correctly implemented, nonlinear characteristics allow the generation of dynamics conditions that are favourable for the performance of the structure, as shown in the first case study. This suggests that nonlinear systems may represent the correct way to improve the performance of mechanical structures and the capabilities of the associated technologies.

Chapter 9

Conclusions and Future Works

9.1 Conclusions and Contributions to the Fields

This thesis investigates the behaviour of strongly nonlinear systems, focusing on the dynamics of MDOF systems featuring hardening and piecewise stiffness characteristics. The thesis aims to improve the fundamental knowledge of the investigated class of systems, prove that nonlinear Reduced-Order Models (ROMs) can produce reliable predictions of the dynamics of the system outside the identification conditions, and develop tools/procedures for the analysis and identification of nonlinear systems in the current industrial practices. The key contributions of the thesis are summarised as follows:

- Demonstration that smoothing functions do not alter the overall qualitative and quantitative dynamic behaviour and bifurcations scenario of MDOF piecewise-smooth continuous systems characterised by soft contacts.

- Demonstration, via numerical and experimental analyses, of the existence of bifurcations of the backbone curve and detached isolas in the frequency response of MDOF nonlinear systems characterised by soft contacts

- Development of a novel method, named the Nonlinear Restoring Force (NLRF) method, for identification and the visualisation of the nonlinear restoring force surfaces of MDOF strongly nonlinear systems.

- Demonstration, via experimental validation, of the prediction capabilities of reduced orders models representing MDOF strongly nonlinear systems. In particular, the robustness of the identified models, in capturing the qualitative and quantitative behaviour of the investigated systems, has been demonstrated using several levels of excitation.

The first key contribution is discussed in Chapter 3, where, the dynamic behaviour of a two-DOF system with soft piecewise constraints is analysed via numerical continuation and integration procedures. The results are published in [1] and demonstrate the presence of a rich bifurcation scenario in the considered system. Many isolas are found in the FRC, and the presence of a bifurcation of the first backbone curve is proven via numerical analyses. In these conditions, high amplitudes of response might persist in the system; these phenomena are critical in the engineering context as they may lead to unforeseen large responses and unwanted vibrations/stress levels in the structure. Such dynamics are driven by nonlinear characteristics and cannot be correctly described by linear models; instead, they require the usage of dedicated techniques, e.g. the Henon method in the numerical integration or multi-segment continuation in path-following analyses, to identify the beginning/end of the contact and compute the numerical solution. These methods are computationally expensive and often difficult to implement in industrial practices, where the robustness and the simplicity of the mathematical models are fundamental requirements. To limit these problems, smoothing functions, such as sigmoids, are used to approximate piecewise characteristics and a tool for selecting the associated approximation parameter δ is proposed. It is demonstrated that the sigmoid functions do not alter significantly the dynamics of the investigated system, especially when periodic solutions are considered. The approximation allows reducing the complexity of the numerical simulations and thus it represents an attractive tool for industrial and practical implementations. The second key contribution is discussed in Chapter 4 and Chapter 5, where the existence of the intricate nonlinear dynamics discovered during the numerical analyses is proved via experimental tests. Two test rigs representing the two-DOF system (Test Rigs #1 and #2) are designed and experimentally investigated. During the design stage, a ROM is derived and utilised, along with numerical continuation analyses, to check that the desired nonlinear features are presented in the designed mechanical system. Parametric analyses are performed to understand the effect of the cubic stiffness, the piecewise stiffness, and the non-contact gap on the bifurcation of the backbone curve, demonstrating that the phenomenon occurs when the system dynamics is dominated by the piecewise stiffness restoring force. The two test rigs are experimentally analysed with forward/backward frequency sweeps at different excitation levels. The experimental results, partially published in [2–4], demonstrate the presence of the same dynamics features encountered during the numerical analysis. In particular, the same degenerate and multi-periodic orbits are found after the grazing bifurcation of the first resonance peak. This represents an evidence of the presence of isolas and bifurcation of the backbone curve in the experimental test rigs. In addition, the analysis of the Poincaré sections confirms the presence of quasi-periodic and chaotic behaviour, demonstrating that Test Rig #1 reaches chaos via period-doubling tori.

The third key contribution is introduced in Chapter 6, where reduced order models representing the two experimental test rigs are derived and equivalent parameters are identified using a novel methodology, called the NLRF method [3]. The procedure is based on the separation of the linear and nonlinear contributions of the restoring force and aims to identify the nonlinear characteristics of the system using a modified version of the RFS method. This approach can be implemented within the current industrial procedures, interfacing linear identification methods, e.g. circle fit method, with the proposed NLRF method. In this way, the identification of the nonlinear contributions is just an additional step in the identification process. The efficacy of the method is demonstrated experimentally, identifying the smooth characteristics of Test Rig #2 and the non-smooth properties of Test Rig #1. The knowledge of the NLRF surfaces is used to develop engineering considerations and reduce the mathematical complexity of the identification procedure, saving time and improving the computational effort.

The last key contribution of the thesis is discussed in Chapter 7, where it is demonstrated that the identified ROMs, with and without non-smooth characteristics, can predict the qualitative and quantitative dynamic behaviour of the experimental test rigs, not only when the excitation conditions correspond to the ones utilised in the identification process, but also when different excitation levels are considered. This confirms the robustness of ROMs in modelling strongly nonlinear systems and underscores their aptness for dynamic features extrapolation. The capabilities and the performance of the ROMs are also tested against nonlinear FEA: to this end an FE model representing Test Rig #2 is updated and validated, using the NLRF method. The responses of the FE and reduced-order models are then compared: it is shown that the steady-state dynamic responses of the FE model and the ROM are comparable and very close to the experimental data. Therefore, the high computational effort demanded to perform nonlinear dynamic FEA cannot be justified in similar systems and the usage of a ROM, when possible, is highly recommended. The identified non-smooth ROM, representing Test Rig #1, is also used to extrapolate dynamic features and obtain more insight into the dynamics of the investigated test rig. The presence of a bifurcation of the backbone curve and detached isolas is demonstrated via numerical continuation analyses of the forced responses using the identified ROM. Via numerical analyses, it is also demonstrated that the bifurcation of the backbone curve can be detected by inspection of the steady-state forced response: indeed, the considered class of system shows the presence of degenerate orbits in the stable branch of forced response when the bifurcation of the backbone curse occurs. This feature can be exploited to detect the presence of sought bifurcation without the need to directly obtain the undamped-unforced response of the system. This interesting result is an important contribution to the fundamental knowledge of the piecewise nonlinear systems with multiple degrees of freedom and represents the conclusive analysis of the designed two-DOF model.

Building on the results of the previous chapters, the project concludes by analysing two case studies of mechanical structures demanding exceptional performance. To this end, two vibration energy harvesters are numerically investigated. The two VEHs utilise a single mode for extracting energy from vibration; the first harvester is a nonlinear electromagnetic energy harvester characterised by the presence of a softening/hardening characteristic. The second one is a linear piezoelectric energy harvester with a planar shape. Numerical analyses are carried out to show that, when correctly implemented, nonlinearities can actually improve the performance of the harvester, allowing the structure to reach high amplitudes of vibration (i.e. large power output) for wider frequency bandwidth. On the other hand, the linear harvester does not show interesting dynamic features that can be utilised to improve the performance of the system. These results are partially published in [5] and, once again, suggest that nonlinearities might lead to higher performance in mechanical structures.

9.2 Future Work

The contributions of this thesis have posed the basis for a better understanding of nonlinear MDOF mechanical systems featuring strong nonlinearities and contacts. Future studies may investigate the remaining open questions that should be carefully addressed by additional research. Firstly, the nature of the bifurcation of the backbone curve in this class of systems should be studied in detail, performing parametric rigorous studies with numerical continuation techniques or deriving accurate analytical approximations, for example using the method of multiple scales. This would unveil more details about the dynamics of the systems and the interaction between modes. In particular, additional research is needed to understand how the distance in frequency between the two modes influences the bifurcation of the backbone curve and how the modal interaction of two modes affects this phenomenon. On the other side, the tools proposed in this project could be applied to larger structures. In this thesis, the proposed radius of influence was applied only to a simple mechanical system with a piecewise stiffness. Future research may test the robustness of the tool on more complicated systems, such as large structures featuring multiple contacts, specifically addressing the point of the limit threshold error that in this thesis was fixed at about 3.5% of the non-contact gap. The radius of influence was only tested on sigmoid smoothing functions but could be also extended to other smoothing approximations, comparing their performance in terms of the accuracy of the solution and computational efforts. Finally, some mathematical features identified during the development of the proposed NLRF method should be better investigated. In particular, a formal demonstration of the minimal space of coordinates which fully describes the nonlinear dynamics of mechanical systems using the NLRF surfaces should be developed. This could be linked to the Principal Component Analysis (PCA) or Machine Learning (ML) algorithms which could be exploited to identify the minimal number of degrees of freedom that fully describe the nonlinear dynamics of the system. This would allow us to directly obtain reduced-order models from experimental data, improving the current nonlinear system identification procedures. On the other hand, the NLRF method could be interfaced with ROMs [21, 93, 177, 178] obtained with different theories and methodologies. In that context, additional research is needed to understand the link between NLRF surfaces and other theories for the development of nonlinear ROMs, such as the invariant manifold theory.

9.3 Other Considerations

This thesis represents the starting point for the integration of nonlinear dynamic models in standard industrial practices for the design and certification of mechanical systems and structures. Several challenges need to be addressed before full uptake from practitioners becomes possible. Linear models have great success because of their robustness; on the contrary, nonlinear models are susceptible to slight changes in the system properties which can lead to complete changes in the dynamic response. This affects their robustness and often undermines the possibility of being used in industrial applications. This work investigated this problem demonstrating that the nonlinear ROMs are quite robust and capable of predicting the dynamics of strongly nonlinear systems at different excitation conditions. In the thesis, two experimental test rigs, representing a nonlinear two-DOF system with piecewise stiffness, have been developed/tested and the associated nonlinear ROMs have been successfully identified and validated against experimental results. Nonetheless, the investigated systems are simple and only few modes dominate their dynamic behaviour. Larger structures and their ROMs should be investigated using the approach proposed in this work, before their actual implementation in industrial procedures. Similarly, the proposed tools such as the radius of influence and the NLRF method should be investigated in more detail, testing them on large-scale systems and structures, before their usage in standard industrial practices.

Appendix A

Mathematical Definitions

A.1 Multi-Segment Continuation

The system of second order equations of motion (Eq. 3.3) can be transformed into a system of first order autonomous equations, represented by the following expressions:

$$\dot{x}_1 = y_1 \tag{A.1a}$$

$$\dot{y}_1 = -\frac{c}{m}y_1 - \frac{k}{m}x_1 - \frac{\mu}{m}x_1^3 + \frac{k_d}{m}(x_2 - x_1) + \frac{\mu_d}{m}(x_2 - x_1)^3 + \frac{c_d}{m}(y_2 - y_1) - \frac{F_p}{m} + \frac{Q_1}{m}u \tag{A.1b}$$

$$\dot{x}_2 = y_2 \tag{A.1c}$$

$$\dot{y}_2 = -\frac{c}{m}y_2 - \frac{k}{m}x_2 - \frac{\mu}{m}x_2^3 - \frac{k_d}{m}(x_2 - x_1) - \frac{\mu_d}{m}(x_2 - x_1)^3 - \frac{c_d}{m}(y_2 - y_1) + \frac{Q_2}{m}u \tag{A.1d}$$

$$\dot{u} = -\Omega v + u(1 - u^2 - v^2) \tag{A.1e}$$

$$\dot{v} = \Omega u + v(1 - u^2 - v^2) \tag{A.1f}$$

The term F_p depends on the configuration adopted: the smoothed version of the system utilises Eq. 3.2, specifically the sigmoid approximation $F_{p,3}$ with $n = 1$, while the non-approximate version adopts the definition of Eq. 3.1 to perform the numerical continuation. To remove the dependence from time, the states u and v are implemented to make the system autonomous. The vector field equations, necessary to perform the multi-segment continuation, are represented by Eq. A.1 with the following expression of F_p:

No Contact - the first mass does not experience contact:

$$F_p = 0$$

Contact up - the first mass is in contact (positive displacements) with the piecewise stiffness. The following restoring force is imposed:

$$F_p = k_p(x_1 - a)$$

Contact down - the first mass is in contact (negative displacements) with the piecewise stiffness. The following restoring force is imposed:

$$F_p = k_p(x_1 + a)$$

The event function identifies three possible conditions:

Impact up - the segment ends when the first mass is in contact with piecewise stiffness (positive displacement). In this case, the event condition r_{ev} is identified by:

$$r_{ev} = x_1 - a$$

Impact down - the segment ends when the first mass is in contact with piecewise stiffness (negative displacement). In this case, the event condition r_{ev} is identified by:

$$r_{ev} = x_1 + a$$

Velocity change - the segment ends when the first mass changes sign in its velocity. This is especially beneficial for identifying grazing bifurcation points. It can be defined by the following criteria:

$$r_{ev} = y_1$$

Lastly, the reset function establishes the criteria for restarting the next segment continuation, setting $x_{new} = x$, where x_{new} denotes the new set of initial values for the continuation of the next segment.

Eq. A.1a along with the definition of the vector field equations, and the event and reset function is used in Chapter 3 to perform the multi-segment continuation of the non-approximate system. In the same chapter, when F_p is approximate with a sigmoid function, Eq. A.1a is used to analyse the dynamic behaviour of the approximate system with path-following continuation procedures.

Appendix B

Design of an Experimental Model

B.1 Numerical Considerations

Additional analyses for the design of the experimental test rig are reported in this appendix. The results of static analyses reported in Tab. 4.2 are obtained from Ansys APDL and are described by the Fig. B.1: the analyses have been performed by constraining the system at the extremities and applying a constant gravitational field in the vertical (Z) direction. The results are graphically shown in Fig. B.1 for versions 1 and 2 of the system. Fig. B.2 instead, shows the results of the modal and static analyses of the last version of the model (Version 3).

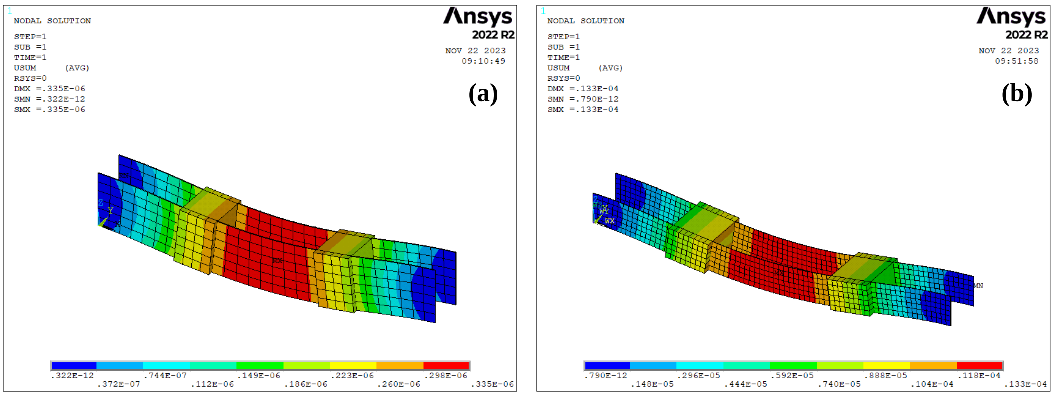

Figure B.1: Static analysis of model Version 1 (a) and Version 2 (b) of the initial stage design. Maximum displacement: 0.34 μm (a) and 13.3 μm (b)

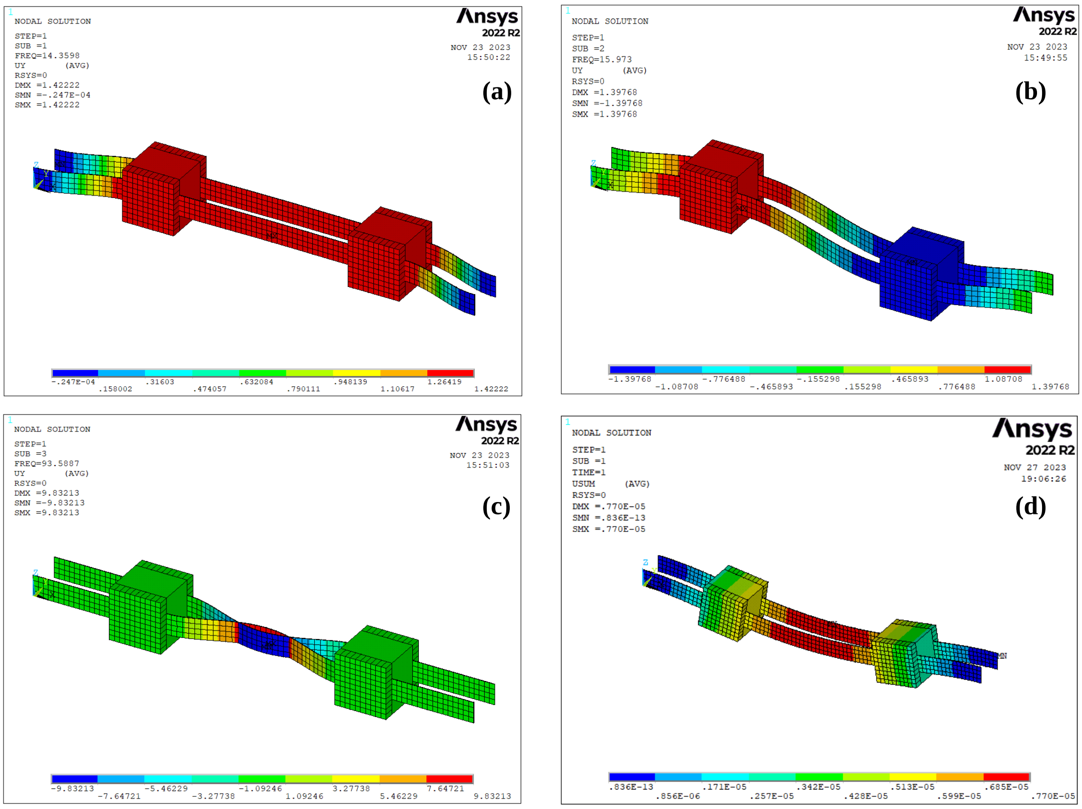

Figure B.2: First (a), second (b) and third mode (c) of model Version 3. Panel (d) shows the static deformation for the same version of the model. The modal analyses returned the following natural frequencies: 14.4 Hz (a), 16.0 Hz (b), 93.6 Hz (c) while the static analysis provided a maximum deflection of 7.7 μm

Eq. 4.3 are derived using the following modal analysis procedure: the unforced undamped version of the linear reduced order model is represented by:

$$\begin{bmatrix} m & 0 \\ 0 & m \end{bmatrix} \begin{Bmatrix} \ddot{x}_1 \\ \ddot{x}_2 \end{Bmatrix} + \begin{bmatrix} k+k_d & -k_d \\ -k_d & k+k_d \end{bmatrix} \begin{Bmatrix} x_1 \\ x_2 \end{Bmatrix} = \begin{Bmatrix} 0 \\ 0 \end{Bmatrix} \tag{B.1}$$

and in compact matrix forms:

$$\mathbf{M}\ddot{\mathbf{x}} + \mathbf{K}\mathbf{x} = \mathbf{0} \tag{B.2}$$

The modal analysis can be performed by solving the following eigenproblem:

$$(\mathbf{K} - \omega^2\mathbf{M})\boldsymbol{\Psi} = \mathbf{0} \tag{B.3}$$

where ω is natural frequency of the system and $\mathbf{\Psi}$ is the modal matrix. The natural frequencies can be obtained by solving the following equation:

$$\det(\mathbf{K} - \omega^2\mathbf{M}) = \mathbf{0} \tag{B.4}$$

which returns the following solution:

$$\omega_{n,1}^2 = \frac{k}{m} \tag{B.5a}$$
$$\omega_{n,2}^2 = \frac{k + 2k_d}{m} \tag{B.5b}$$

At this point, it is possible to utilise Eq. B.3 to obtain the mode shapes and the modal matrix which results in the following expression:

$$\mathbf{\Psi} = \begin{bmatrix} 1 & 1 \\ 1 & -1 \end{bmatrix} \tag{B.6}$$

Now, it is possible to transform the equation of motion of the system in modal coordinates (η) by modifiying Eq. 4.2 as follows:

$$\mathbf{\Psi}^T\mathbf{M}\mathbf{\Psi}\ddot{\eta} + \mathbf{\Psi}^T\mathbf{C}\mathbf{\Psi}\dot{\eta} + \mathbf{\Psi}^T\mathbf{K}\mathbf{\Psi}\eta = \mathbf{\Psi}^T\mathbf{Q} \tag{B.7}$$

which becomes:

$$\begin{bmatrix} 2m & 0 \\ 0 & 2m \end{bmatrix} \begin{Bmatrix} \ddot{\eta}_1 \\ \ddot{\eta}_2 \end{Bmatrix} + \begin{bmatrix} 2c & 0 \\ 0 & 2c + 4c_d \end{bmatrix} \begin{Bmatrix} \dot{\eta}_1 \\ \dot{\eta}_2 \end{Bmatrix} + \begin{bmatrix} 2k & 0 \\ 0 & 2k + 4k_d \end{bmatrix} \begin{Bmatrix} \eta_1 \\ \eta_2 \end{Bmatrix} = \begin{Bmatrix} Q_1 + Q_2 \\ Q_1 - Q_2 \end{Bmatrix} \tag{B.8}$$

Eq. B.8 represents the equation of motion in modal coordinates and consists of two decoupled oscillators. The equation can be further simplified by adding the modal parameters which are obtained diving Eq. B.8 by the modal mass:

$$\begin{bmatrix} 1 & 0 \\ 0 & 1 \end{bmatrix} \begin{Bmatrix} \ddot{\eta}_1 \\ \ddot{\eta}_2 \end{Bmatrix} + \begin{bmatrix} 2\omega_{n,1}\zeta_1 & 0 \\ 0 & 2\omega_{n,2}\zeta_2 \end{bmatrix} \begin{Bmatrix} \dot{\eta}_1 \\ \dot{\eta}_2 \end{Bmatrix} + \begin{bmatrix} \omega_{n,1}^2 & 0 \\ 0 & \omega_{n,2}^2 \end{bmatrix} \begin{Bmatrix} \eta_1 \\ \eta_2 \end{Bmatrix} = \begin{Bmatrix} \tilde{Q}_1 + \tilde{Q}_2 \\ \tilde{Q}_1 - \tilde{Q}_2 \end{Bmatrix} \tag{B.9}$$

where $\tilde{Q} = Q/m$.

At this stage is simple to establish a relationship between modal (ω_n and ζ) and real parameters (k and c) using Eq. B.8 and B.9 which results in the expressions described in Eq 4.3. The mass parameter, instead, is obtained by considering the volume of the masses and the density of the material ($\delta_s = 7800$ kg/m^3) and it can be calculated with the following expression:

$$m = Y_s((d_m + 2s_{m,c})h_m c_m) \tag{B.10}$$

B.2 Experimental Considerations

B.2.1 Directly Forced System

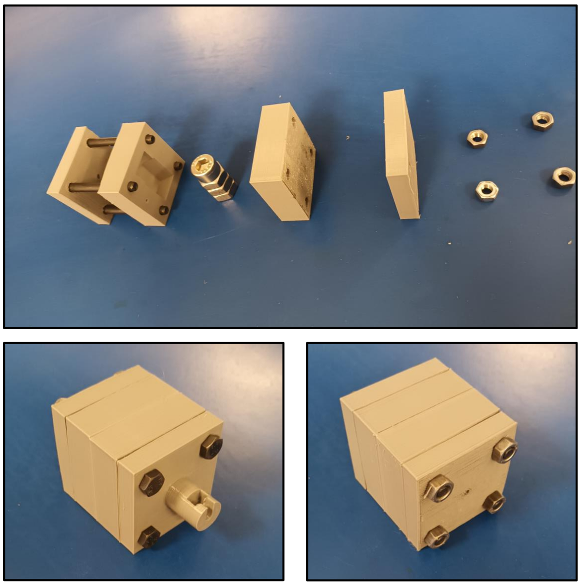

Figure B.3: Detailed views of the two mass blocks used in the directly forced version of the experimental test rig.

The two blocks are realised as illustrated in Fig. B.3. The blocks consist of PLA components containing metallic bolts, enabling the adjustment of their mass. This design feature is particularly effective in controlling the dynamics of the system and its inertia forces. The figure also depicts two variants of the blocks: one representing the excited mass (mass 2) includes an attachment for connection to the shaker, while

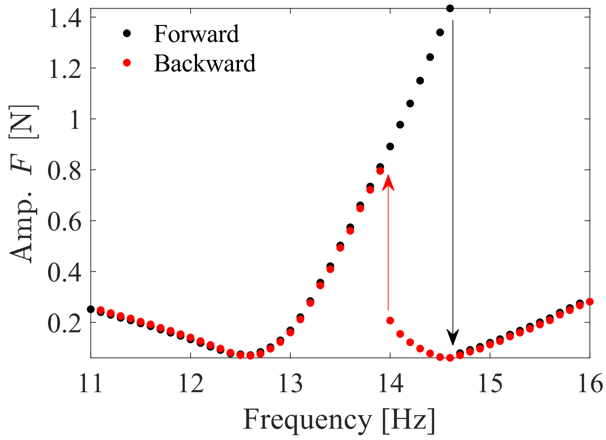

Figure B.4: Force amplitude response in forward and backward frequency sweep analysis of the experimental test rig with suspended shaker.

the other block (mass 1) is a plain squared block with flat surfaces designed for having contact with the external motion limiting constraints . The experimental analyses of test-rig represented in Fig. 4.17 show that the system does not allow large displacement of the excited mass, inhibiting some of its nonlinear effects. Nonetheless, the experimental linear TF (Fig 4.18) reveal the presence of two peaks. In the linear regime, the peaks are obtained by measuring the reduction of forces in the load cell. This occurs also in the nonlinear regime, as shown by the amplitude of force experienced by the load cell during the nonlinear analysis, reported in Fig B.4. The load cell experiences the same jumps as the FRC but also shows the presence of two 'sinks' with low values. These minimum force conditions correspond to the resonances of the system. When linear transfer functions are computed, the minimum values of force allow to obtain a second peak in the frequency representation. In the nonlinear regime, this is not possible anymore as the system behaviour depends on the excitation force and the computation of an equivalent linear TF would lead to distorted transfer function.

B.2.2 Base Excited System - Test Rig #1

During the experimental analysis of Test Rig #1, random low amplitude excitation is used to limit the effect of the nonlinearities on the dynamic response of the system. To measure the effect of the nonlinearities on the linear TF, the coherence is exploited.

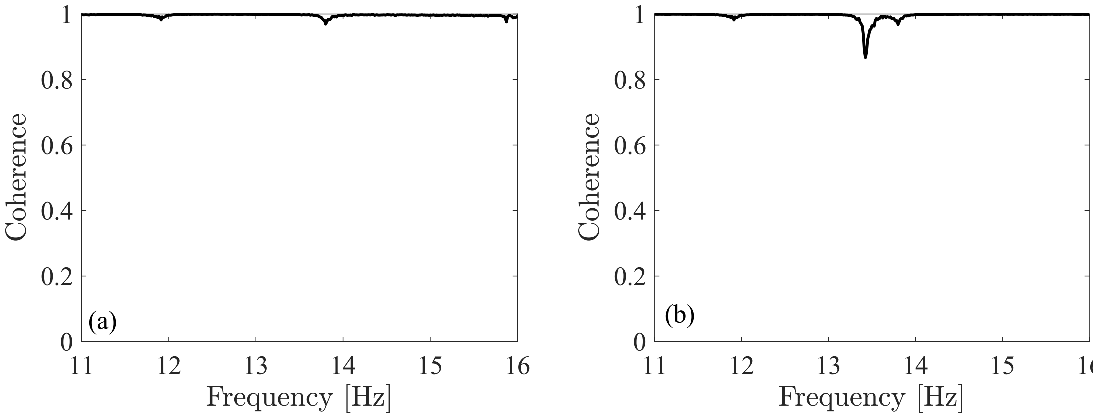

Figure B.5: Coherence of the sensors applied to mass 1 (a) and mass 2 (b).

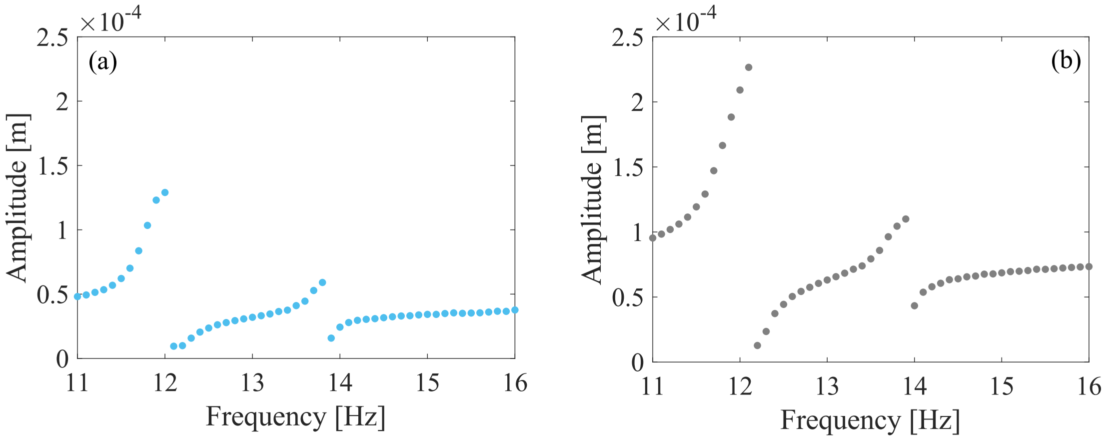

Figure B.6: Amplitude of displacement of the base for backward frequency sweep when 0.1 V (a) and 0.2 V (b) are used as excitation amplitude for the shaker.

The coherence, indeed, allows the practitioner to measure the repeatability of a signal, identifying in the random excitation, the presence of nonlinearities. If one neglects the presence of noise, a perfectly flat coherence in the frequency range of investigation indicates that the system is behaving linearly. Under this perspective, coherence is a good indicator of the quality of the measured linear TF representing the underlying linear system. Fig. B.5 shows the coherence of the two sensors applied to mass 1 and mass 2: the very low value of coherence indicates that the noise of the signal is low and that the system is behaving linearly for most of the frequency domain. Therefore the associated TFs can be considered a good approximation of the underlying linear system. The experimental analysis of the Test Rig #1 considers also forward and

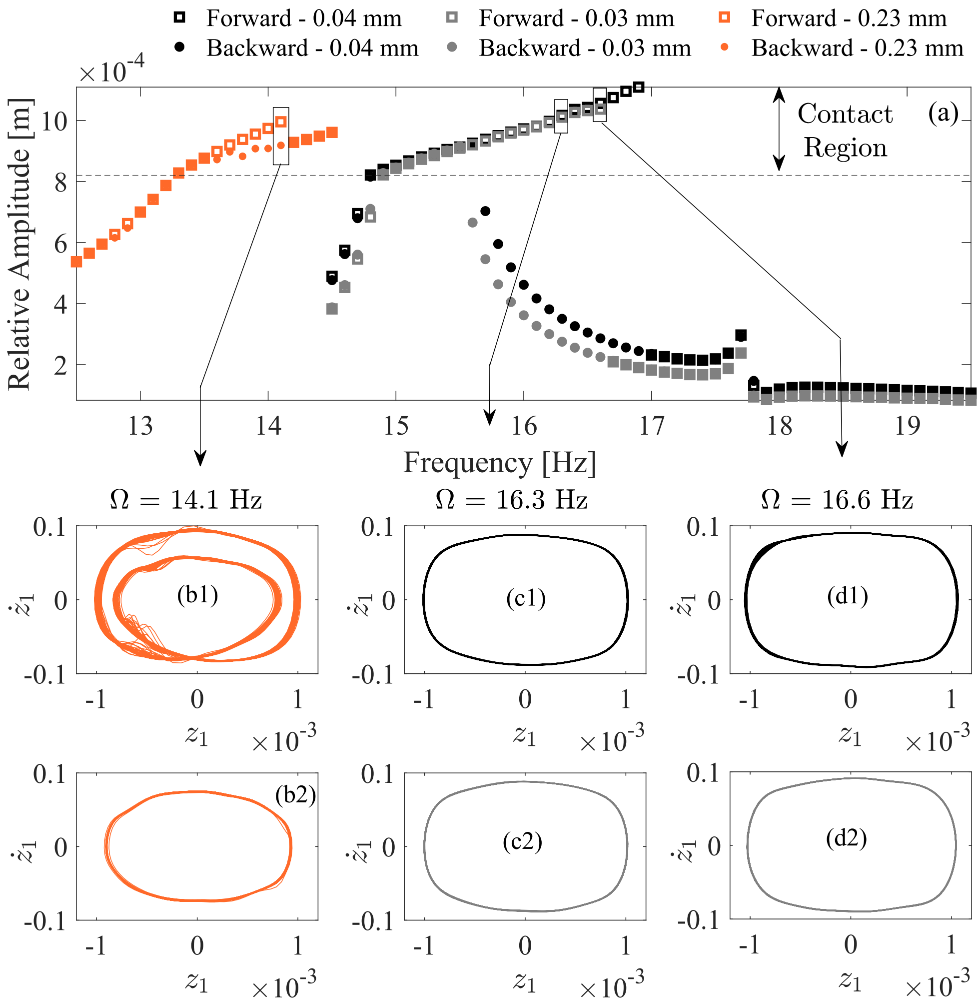

Figure B.7: Experimental frequency response curve of Test Rig #2 when contact springs with stiffness of 11.96 N/mm and a non-contact gap equal to 0.82 mm. The FRC is reported in panel (a) in terms of relative displacement of the first DOF while panel (b1-d2) show different orbits of the system in terms of relative coordinates.

backward sinusoidal frequency sweeps excitation to evaluate the nonlinear response of the system. Nonetheless, during the experimental analysis of the first test rig, only the voltage amplitude of the input signal to the shaker can be controlled. As a result, the displacement, as well as the velocity, of the base is not constant during the frequency sweep but it is affected by the shaker dynamics. Fig. B.6 shows the displacement amplitude of the base during the backward frequency sweeps with imposed voltage amplitude (0.1 V and 0.2 V). The figure shows that the amplitude of the base is not constant but instead is influenced by the dynamics of the system and the shaker. This may represent a problem during the validation process, where the dynamics of the shaker are not taken into account and the numerical simulations are carried out imposing a constant amplitude of motion to the base.

B.2.3 Base Excited System - Test Rig #2

The dynamics of Test Rig #2 are analysed with different impact spring characteristics. Fig B.7 shows the frequency response of the experimental model when a spring with nominal stiffness equal to 11.96 N/mm and a non-contact gap of 0.82 mm is used. The results are very similar to the previous analysis of the same test rig with a softer spring (Fig 5.11). After the grazing bifurcation, the FRC (Fig B.7 (a)) appears to be more inclined than the previous analysis due to the presence of a stronger piecewise stiffness, but overall the same dynamic features are found. In particular, limit cycles typically attributed to the bifurcating branch of the first resonant peak or multi-periodic isolas are present when a large amplitude of excitation is used, i.e. 0.23 mm, as shown in Fig B.7(b1).

Appendix C

Model Updating

C.1 Finite Element Model - Linear Model Updating

Table C.1: Material properties obtained with the linear model updating procedure. The non-ideal boundary stiffness ($k_{NI,1}$ $k_{NI,2}$) is set equal to 5000 N/m while the non-ideal boundary damping ($c_{NI,1}$ $c_{NI,2}$) is set equal to zero.

Stiffness	E [GPa]	ν [-]	ρ [Kg/m^3]	α [-]	β [-]
PLA	3.31	0.35	372	0.0	0.0
Beam S_1	199.6	0.28	7800	0.0	4.8e-5
Beam S_2	242.0	0.28	7800	0.0	1e-8
Beam S_3	202.6	0.28	7800	0.0	6.8e-5
Core	3.31	0.35	3000	0.0	0.0

The identification of the linear behaviour of the system is obtained with an iterative manual procedure, but it could be substituted with an automatic minimisation process. Engineering considerations are first utilised to obtain a meaningful starting point for the linear model updating process. The density of the polymeric material, mostly PLA, is estimated at 1240 kg/m^3, but considering a 30% infill due to the 3D printing process, the actual assumed density becomes 372 kg/m^3. The density of the beam is considered to be 7800 kg/m^3 as standardly used in engineering for steel while the core material density is tuned so that the actual mass of each block corresponds to the mass experimentally measured, i.e. 0.1365 kg, and results in a density of 3000 kg/m^3. At this point, the inertia properties of the FE model are considered to be correctly updated. A similar discussion is done on the Poisson coefficients which are estimated

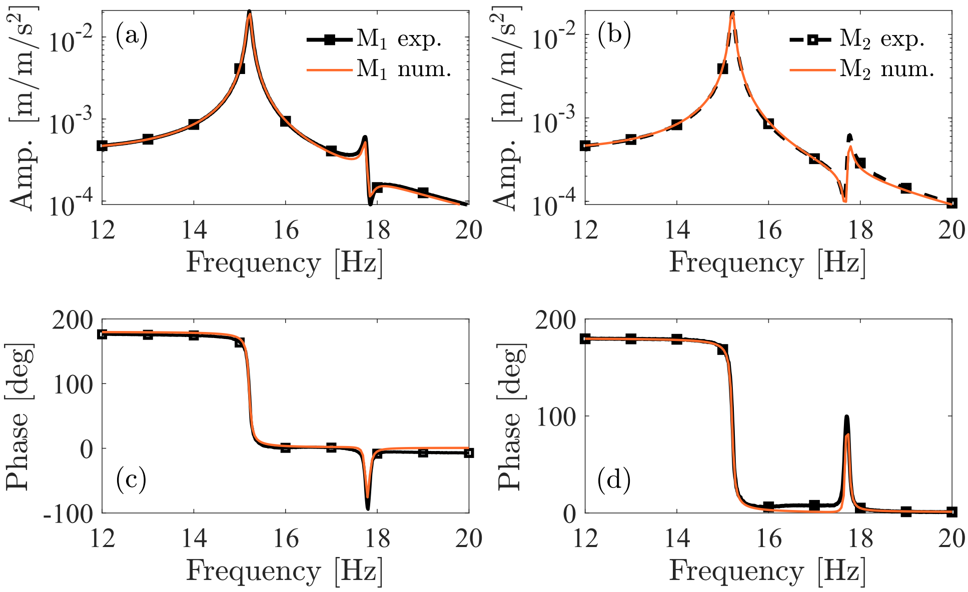

Figure C.1: Comparison between the numerical and experimental linear transfer function for the identified condition (bottom row of Tab 7.1). The transfer functions consider the acceleration of the base as input and the displacement of the masses as output. Panels (a,b) illustrate the amplitude of response while panels (c,d) show the phase.

from typical material properties and are kept fixed during the updating procedure. The elastic moduli, instead, are updated iteratively until the numerical receptances converge to the experimental ones. It is worth noticing that most of the elastic forces are produced by the beams while most of the inertial forces are generated by the two blocks; since the inertia properties are considered to be tuned, most of the updating procedure consists of tuning the elastic moduli of the beams. Finally, the definition of Rayleigh proportional damping is used to model the dissipation of energy in the beams and the parameters α and β are updated similarly to the elastic moduli. The final results, reported in Tab. C.1, are obtained by considering only a non-ideal boundary stiffness equal to $k_{NI,1} = k_{NI,2} = 5000$ N/m, and they serve as a starting point for the more complicated non-linear model updating process outlined in Section 7.3.

During the nonlinear model updating procedure, the linear properties are continuously updated. The TF of the final linear model (after the nonlinear model update) is shown in Fig. C.1 where the amplitude and phase of the FE model are compared against the experimental results. The good match between experimental and numerical data demonstrates that the linear FE model is correctly updated.

C.2 Finite Element Model - Nonlinear Model Updating

The model updating procedure is verified and validated using the amplitude and phase of the nonlinear FRC. In particular, the amplitude is computed by averaging the peaks of the steady-state response while the phase is obtained by implementing an offline phase detector, as the one proposed in [28]. The phase detector is implemented as follows: the considered signal $s(t)$ is multiplied by sine and cosine signals at the same excitation frequency but with no phase. Two different signals are obtained:

$$s_{Re}(t) = s(t) \cdot cos(\Omega t) \tag{C.1a}$$

$$s_{im}(t) = s(t) \cdot sin(\Omega t) \tag{C.1b}$$

where $\cdot$ means scalar product between vectors. These two signals are then filtered with a lowpass filter to eliminate the oscillations and the resulting steady-state values can be used to estimate the phase ϕ with the expression $\phi = atan(s_{Im}/s_{Re})$. This process is used to compute the phase between the two blocks and the base as shown in Fig. 7.9 and Fig. 7.10

Bibliography

[1] C. Martinelli, A. Coraddu, A. Cammarano, Approximating piecewise nonlinearities in dynamic systems with sigmoid functions: advantages and limitations, Nonlinear Dynamics (2023). doi:10.1007/s11071-023-08293-1.

[2] C. Martinelli, A. Coraddu, A. Cammarano, Experimental analysis of a nonlinear piecewise multi-degrees-of-freedom system, in: International Conference on Nonlinear Dynamics and Applications, Springer, 2023, pp. 665–675. doi:10.1007/978-3-031-50631-4_56.

[3] C. Martinelli, A. Coraddu, A. Cammarano, Strongly nonlinear multi-degree of freedom systems: Experimental analysis and model identification, Mechanical Systems and Signal Processing 218 (2024) 111532. doi:10.1016/j.ymssp.2024.111532.

[4] C. Martinelli, A. Coraddu, A. Cammarano, Experimental parameter identification of nonlinear mechanical systems via meta-heuristic optimisation methods, in: Society for Experimental Mechanics Annual Conference and Exposition, Springer, 2023, pp. 215–223. doi:10.1007/978-3-031-36999-5_28.

[5] C. Martinelli, A. Coraddu, A. Cammarano, Performance-aware design for piezoelectric energy harvesting optimisation via finite element analysis, International Journal of Mechanics and Materials in Design 19 (1) (2023) 121–136. doi:10.1007/s10999-022-09619-4.

[6] A. Cammarano, S. G. Burrow, D. A. Barton, Modelling and experimental characterization of an energy harvester with bi-stable compliance characteristics, Proceedings of the Institution of Mechanical Engineers. Part I: Journal of Systems and Control Engineering 225 (2011) 475–484. doi:10.1177/0959651811403093.

[7] D. J. Ewins, Modal testing: theory, practice and application, John Wiley & Sons, 2009.

[8] K. Carney, I. Yunis, K. Smith, C.-Y. Peng, Nonlinear dynamic behavior in the cassini spacecraft modal survey, in: Proceedings of the 15th InternationalModal Analysis Conference (IMAC), Orlando, Florida, 1997, pp. 811 – 817.

[9] J. R. Ahlquist, J. M. Carreño, H. Climent, R. de Diego, J. de Alba, Assessment of nonlinear structural response in a400m gvt, in: Structural Dynamics, Volume 3: Proceedings of the 28th

IMAC, A Conference on Structural Dynamics, 2010, Springer, 2011, pp. 1147–1155. doi:10.1007/978-1-4419-9834-7_101.

[10] E. Breitbach, Effects of structural non-linearities on aircraft vibration and flutter, in: 45th Structures and Matenials Panel Meeting, AGARD Reston, VA, USA, 1978.

[11] G. Kerschen, M. Peeters, J. C. Golinval, C. Stéphan, Nonlinear modal analysis of a full-scale aircraft, Journal of Aircraft 50 (2013) 1409–1419. doi:10.2514/1.C031918.

[12] J. P. Noël, L. Renson, G. Kerschen, Complex dynamics of a nonlinear aerospace structure: Experimental identification and modal interactions, Journal of Sound and Vibration 333 (2014) 2588–2607. doi:10.1016/j.jsv.2014.01.024.

[13] E. Coetzee, Application of nonlinear dynamics in civil aerospace, in: Progress in Industrial Mathematics at ECMI 2008, Springer, 2010, pp. 187–192. doi:10.1007/978-3-642-12110-4_24.

[14] P. Thota, B. Krauskopf, M. Lowenberg, Bifurcation analysis of nose-landing-gear shimmy with lateral and longitudinal bending, Journal of Aircraft 47 (2010) 87–95. doi:10.2514/1.43507.

[15] J. Rankin, E. Coetzee, B. Krauskopf, M. Lowenberg, Bifurcation and stability analysis of aircraft turning on the ground, Journal of Guidance, Control, and Dynamics 32 (2009) 499–510. doi:10.2514/1.37763.

[16] E. Coetzee, B. Krauskopf, M. Lowenberg, Nonlinear aircraft ground dynamics, in: International Conference on Nonlinear Problems in Aviation and Aerospace, 2006, pp. 1–8.

[17] M. J. Patil, D. H. Hodges, On the importance of aerodynamic and structural geometrical nonlinearities in aeroelastic behavior of high-aspect-ratio wings, Journal of Fluids and Structures 19 (2004) 905–915. doi:10.1016/j.jfluidstructs.2004.04.012.

[18] H. H. Mian, G. Wang, Z. Y. Ye, Numerical investigation of structural geometric nonlinearity effect in high-aspect-ratio wing using cfd/csd coupled approach, Journal of Fluids and Structures 49 (2014) 186–201. doi:10.1016/j.jfluidstructs.2014.04.011.

[19] L. Zhu, N. Li, P. R. Childs, Light-weighting in aerospace component and system design, Propulsion and Power Research 7 (2018) 103–119. doi:10.1016/j.jppr.2018.04.001.

[20] X. Zhu, Z. Guo, Z. Hou, Solar-powered airplanes: A historical perspective and future challenges, Progress in Aerospace Sciences 71 (2014) 36–53. doi:10.1016/j.paerosci.2014.06.003.

[21] A. Martin, F. Thouverez, Dynamic analysis and reduction of a cyclic symmetric system subjected to geometric nonlinearities, Journal of Engineering for Gas Turbines and Power 141 (4 2019). doi:10.1115/1.4041001.

[22] A. Castrichini, T. Wilson, F. Saltari, F. Mastroddi, N. Viceconti, J. E. Cooper, Aeroelastics flight dynamics coupling effects of the semi-aeroelastic hinge device, Journal of Aircraft 57 (2020) 333. doi:10.2514/1.C035602.

[23] R. Huang, X. Zhou, Parameterized fictitious mode of morphing wing with bilinear hinge stiffness, AIAA Journal 59 (2021) 2641–2656. doi:10.2514/1.J059347.

[24] R. Snoeys, P. Vanherck, M. Mertens, H. Van der Auweraer, Nonlinear dynamic behaviour of typical mechanical structures, CIRP Annals 34 (1) (1985) 309–314. doi:https://doi.org/10.1016/S0007-8506(07)61779-X.

[25] E. De Langre, G. Lebreton, An experimental and numerical analysis of chaotic motion in vibration with impact, in: American Society of Mechanical Engineers (ASME) pressure vessels and piping conference, 1996.

[26] M. Claeys, J. J. Sinou, J. P. Lambelin, B. Alcoverro, Multi-harmonic measurements and numerical simulations of nonlinear vibrations of a beam with non-ideal boundary conditions, Communications in Nonlinear Science and Numerical Simulation 19 (2014) 4196–4212. doi:10.1016/j.cnsns.2014.04.008.

[27] M. Jossic, O. Thomas, V. Denis, B. Chomette, A. Mamou-Mani, D. Roze, Effects of internal resonances in the pitch glide of chinese gongs, The Journal of the Acoustical Society of America 144 (2018) 431–442. doi:10.1121/1.5038114.

[28] V. Denis, M. Jossic, C. Giraud-Audine, B. Chomette, A. Renault, O. Thomas, Identification of nonlinear modes using phase-locked-loop experimental continuation and normal form, Mechanical Systems and Signal Processing 106 (2018) 430–452. doi:10.1016/j.ymssp.2018.01.014.

[29] A. Givois, J. J. Tan, C. Touzé, O. Thomas, Backbone curves of coupled cubic oscillators in one-to-one internal resonance: bifurcation scenario, measurements and parameter identification, Meccanica 55 (2020) 481–503. doi:10.1007/s11012-020-01132-2.

[30] J. P. Chávez, Y. Liu, E. Pavlovskaia, M. Wiercigroch, Path-following analysis of the dynamical response of a piecewise-linear capsule system, Communications in Nonlinear Science and Numerical Simulation 37 (2016) 102–114. doi:10.1016/j.cnsns.2016.01.009.

[31] J. P. Chávez, E. Pavlovskaia, M. Wiercigroch, Bifurcation analysis of a piecewise-linear impact oscillator with drift, Nonlinear Dynamics 77 (2014) 213–227. doi:10.1007/s11071-014-1285-5.

[32] H. Aftab, U. Baneen, A. Israr, Identification and severity estimation of a breathing crack in a plate via nonlinear dynamics, Nonlinear Dynamics 104 (2021) 1973–1989. doi:10.1007/s11071-021-06275-9.

[33] M. Molaie, F. S. Samani, A. Zippo, F. Pellicano, Spiral bevel gears: nonlinear dynamic model based on accurate static stiffness evaluation, Journal of Sound and Vibration 544 (2023) 117395. doi:10.1016/j.jsv.2022.117395.
URL https://linkinghub.elsevier.com/retrieve/pii/S0022460X22005788

[34] A. Mélot, Y. Benaïcha, E. Rigaud, J. Perret-Liaudet, F. Thouverez, Effect of gear topology discontinuities on the nonlinear dynamic response of a multi-degree-of-freedom gear train, Journal of Sound and Vibration 516 (1 2022). doi:10.1016/j.jsv.2021.116495.

[35] S. Shaw, P. J. Holmes, A periodically forced piecewise linear oscillator, Journal of Sound andVibration, (1983).
URL https://hal.archives-ouvertes.fr/hal-01509017

[36] U. Andreaus, M. De Angelis, Nonlinear dynamic response of a base-excited sdof oscillator with double-side unilateral constraints, Nonlinear Dynamics 84 (2016) 1447–1467. doi:10.1007/s11071-015-2581-4.

[37] B. E. Saunders, R. Vasconcellos, R. J. Kuether, A. Abdelkefi, Relationship between the contact force strength and numerical inaccuracies in piecewise-smooth systems, International Journal of Mechanical Sciences 210 (2021). doi:10.1016/j.ijmecsci.2021.106729.

[38] B. E. Saunders, R. Vasconcellos, R. J. Kuether, A. Abdelkefi, Insights on the continuous representations of piecewise-smooth nonlinear systems: limits of applicability and effectiveness, Nonlinear Dynamics 107 (2022) 1479–1494. doi:10.1007/s11071-021-06436-w.

[39] J. Ing, E. Pavlovskaia, M. Wiercigroch, Complex nonlinear response of a piecewise linear oscillator: Experiment and simulation, in: IUTAM Symposium on Dynamics Modeling and Interaction Control in Virtual and Real Environments, 2010, pp. 135–143.
URL www.springer.com/series/7695

[40] H. Dai, X. Yue, J. Yuan, D. Xie, S. N. Atluri, A comparison of classical runge-kutta and henon's methods for capturing chaos and chaotic transients in an aeroelastic system with freeplay nonlinearity, Nonlinear Dynamics 81 (2015) 169–188. doi:10.1007/s11071-015-1980-x.

[41] R. Vasconcellos, A. Abdelkefi, M. R. Hajj, F. D. Marques, Grazing bifurcation in aeroelastic systems with freeplay nonlinearity, Communications in Nonlinear Science and Numerical Simulation 19 (2014) 1611–1625. doi:10.1016/j.cnsns.2013.09.022.

[42] J. Lelkes, T. Kalmár-Nagy, Analysis of a piecewise linear aeroelastic system with and without tuned vibration absorber, Nonlinear Dynamics 103 (2021) 2997–3018. doi:10.1007/s11071-020-05725-0.

[43] P. Komodromos, P. C. Polycarpou, L. Papaloizou, M. C. Phocas, Response of seismically isolated buildings considering poundings, Earthquake Engineering and Structural Dynamics 36 (2007) 1605–1622. doi:10.1002/eqe.692.

[44] J. Shen, Z. Du, Double impact periodic orbits for an inverted pendulum, International Journal of Non-Linear Mechanics 46 (2011) 1177–1190. doi:10.1016/j.ijnonlinmec.2011.05.010.

[45] S. Yin, J. Ji, G. Wen, Complex near-grazing dynamics in impact oscillators, International Journal of Mechanical Sciences 156 (2019) 106–122. doi:10.1016/j.ijmecsci.2019.03.023.

[46] X. Lyu, Q. Gao, G. Luo, Dynamic characteristics of a mechanical impact oscillator with a clearance, International Journal of Mechanical Sciences 178 (7 2020). doi:10.1016/j.ijmecsci.2020.105605.

[47] X. F. Geng, H. Ding, X. Y. Mao, L. Q. Chen, Nonlinear energy sink with limited vibration amplitude, Mechanical Systems and Signal Processing 156 (7 2021). doi:10.1016/j.ymssp.2021.107625.

[48] X. F. Geng, H. Ding, Two-modal resonance control with an encapsulated nonlinear energy sink, Journal of Sound and Vibration 520 (3 2022). doi:10.1016/j.jsv.2021.116667.

[49] A. Fasihi, M. Shahgholi, S. Ghahremani, The effects of nonlinear energy sink and piezoelectric energy harvester on aeroelastic instability of an airfoil, Journal of Vibration and Control 28 (11-12) (2022) 1418–1432. doi:10.1177/1077546321993585.

[50] X. Wang, X. F. Geng, X. Y. Mao, H. Ding, X. J. Jing, L. Q. Chen, Theoretical and experimental analysis of vibration reduction for piecewise linear system by nonlinear energy sink, Mechanical Systems and Signal Processing 172 (6 2022). doi:10.1016/j.ymssp.2022.109001.

[51] A. F. Vakakis, Inducing passive nonlinear energy sinks in vibrating systems, Journal of Vibration and Acoustics, Transactions of the ASME 123 (2001) 324–332. doi:10.1115/1.1368883.

[52] H. Ding, L. Q. Chen, Designs, analysis, and applications of nonlinear energy sinks, Nonlinear Dynamics 100 (2020) 3061–3107. doi:10.1007/s11071-020-05724-1.

[53] A. F. Vakakis, O. V. Gendelman, L. A. Bergman, D. M. McFarland, G. Kerschen, Y. S. Lee, Nonlinear targeted energy transfer in mechanical and structural systems, Vol. 156, Springer Science & Business Media, 2008. doi:10.1007/978-1-4020-9130-8.

[54] H. Li, B. Deng, H. Ren, S. Sun, Investigation on the nonlinear effects of the vertical motions and vertical bending moment for a wave-piercing tumblehome vessel based on a hydro-elastic segmented model test, Marine Structures 72 (7 2020). doi:10.1016/j.marstruc.2020.102757.

[55] X. Hu, J. Du, Robust nonlinear control design for dynamic positioning of marine vessels with thruster system dynamics, Nonlinear Dynamics 94 (2018) 365–376. doi:10.1007/s11071-018-4364-1.

[56] D. Wang, Z. Hao, E. Pavlovskaia, M. Wiercigroch, Bifurcation analysis of vortex-induced vibration of low-dimensional models of marine risers, Nonlinear Dynamics 106 (2021) 147–167. doi:10.1007/s11071-021-06808-2.

[57] C. Wang, Q. Zhang, W. Wang, Low-frequency wideband vibration energy harvesting by using frequency up-conversion and quin-stable nonlinearity, Journal of Sound and Vibration 399 (2017) 169–181. doi:https://doi.org/10.1016/j.jsv.2017.02.048.
URL https://www.sciencedirect.com/science/article/pii/S0022460X17301645

[58] N. Tran, M. H. Ghayesh, M. Arjomandi, Ambient vibration energy harvesters: A review on nonlinear techniques for performance enhancement, International Journal of Engineering Science 127 (2018) 162–185. doi:https://doi.org/10.1016/j.ijengsci.2018.02.003.

[59] C. Wei, X. Jing, A comprehensive review on vibration energy harvesting: Modelling and realization, Renewable and Sustainable Energy Reviews 74 (2017) 1–18. doi:https://doi.org/10.1016/j.rser.2017.01.073.

[60] K. Vijayan, M. I. Friswell, H. Haddad Khodaparast, S. Adhikari, Non-linear energy harvesting from coupled impacting beams, International Journal of Mechanical Sciences 96-97 (2015) 101–109. doi:https://doi.org/10.1016/j.ijmecsci.2015.03.001.

[61] A. Erturk, D. Inman, Broadband piezoelectric power generation on high-energy orbits of the bistable duffing oscillator with electromechanical coupling, Journal of Sound and Vibration 330 (2011) 2339–2353. doi:https://doi.org/10.1016/j.jsv.2010.11.018.

[62] K. Zhou, H. L. Dai, A. Abdelkefi, Q. Ni, Theoretical modeling and nonlinear analysis of piezoelectric energy harvesters with different stoppers, International Journal of Mechanical Sciences 166 (105233) (2020). doi:https://doi.org/10.1016/j.ijmecsci.2019.105233.

[63] H. Li, W. Qin, J. Zu, Z. Yang, Modeling and experimental validation of a buckled compressive-mode piezoelectric energy harvester, Nonlinear Dynamics 92 (2018) 1761–1780. doi:https://doi.org/10.1007/s11071-018-4160-y.

[64] H. L. Dai, Z. Yan, L. Wang, Nonlinear analysis of flexoelectric energy harvesters under force excitations, International Journal of Mechanics and Materials in Design 16 (2020) 19–33. doi:10.1007/s10999-019-09446-0.

[65] D. A. Czaplewski, S. Strachan, O. Shoshani, S. W. Shaw, D. López, Bifurcation diagram and dynamic response of a mems resonator with a 1:3 internal resonance, Applied Physics Letters 114 (6 2019). doi:10.1063/1.5099459.

[66] D. Upadrashta, Y. Yang, Finite element modeling of nonlinear piezoelectric energy harvesters with magnetic interaction, Smart Materials and Structures 24 (4) (2015) 1–13. doi:10.1088/0964-1726/24/4/045042.

[67] D. Upadrashta, Y. Yang, L. Tang, Material strength consideration in the design optimization of nonlinear energy harvester, Journal of Intelligent Material Systems and Structures 26 (15) (2015) 1980–1994. doi:https://doi.org/10.1177/1045389X14546651.

[68] R. N. Yancey, Challenges, Opportunities, and Perspectives on Lightweight Composite Structures: Aerospace Versus Automotive, Elsevier Inc., 2016. doi:10.1016/B978-1-78242-325-6.00002-5.

[69] D. F. Braga, S. M. Tavares, L. F. D. Silva, P. M. Moreira, P. M. D. Castro, Advanced design for lightweight structures: Review and prospects, Progress in Aerospace Sciences 69 (2014) 29–39. doi:10.1016/j.paerosci.2014.03.003.

[70] G. Kerschen, K. Worden, A. Vakakis, J. Golinval, Past, present and future of nonlinear system identification in structural dynamics, Mechanical System and Signal Processing 20 (2006) 505–592. doi:https://doi.org/10.1016/j.ymssp.2005.04.008.

[71] J. P. Noël, G. Kerschen, Nonlinear system identification in structural dynamics: 10 more years of progress, Mechanical Systems and Signal Processing 83 (2017) 2–35. doi:10.1016/j.ymssp.2016.07.020.

[72] M. R. Jeffrey, Modeling with Nonsmooth Dynamics, Springer Nature, Cham,Switzerland, 2020. URL http://www.springer.com/series/13763

[73] D. Wagg, S. Neild, Nonlinear vibration with control: for flexible and adaptive structures, Springer, 2015.

[74] K. Worden, G. R. Tomlinson, K. Yagasaki, Nonlinearity in structural dynamics: detection, identification and modeling, Appl. Mech. Rev. 55 (2) (2002) B26–B27.

[75] S. H. Strogatz, Nonlinear dynamics and chaos with student solutions manual: With applications to physics, biology, chemistry, and engineering, CRC press, 2018.

[76] N. Perkins, Nonlinear systems, overview, in: S. Braun (Ed.), Encyclopedia of Vibration, Elsevier, Oxford, 2001, pp. 944–951. doi:https://doi.org/10.1006/rwvb.2001.0036.
URL https://www.sciencedirect.com/science/article/pii/B0122270851000369

[77] J. C. Butcher, Numerical methods for ordinary differential equations, John Wiley & Sons, 2016.

[78] D. F. Griffiths, D. J. Higham, Numerical methods for ordinary differential equations: initial value problems, Vol. 5, Springer, 2010. doi:10.1007/978-0-85729-148-6.

[79] L. Pei, A. S. Chong, E. Pavlovskaia, M. Wiercigroch, Computation of periodic orbits for piecewise linear oscillator by harmonic balance methods, Communications in Nonlinear Science and Numerical Simulation 108 (5 2022). doi:10.1016/j.cnsns.2021.106220.

[80] Z. Zhang, J. P. Chávez, J. Sieber, Y. Liu, Controlling grazing-induced multistability in a piecewise-smooth impacting system via the time-delayed feedback control, Nonlinear Dynamics 107 (2022) 1595–1610. doi:10.1007/s11071-021-06511-2.

[81] A. S. Chong, Y. Yue, E. Pavlovskaia, M. Wiercigroch, Global dynamics of a harmonically excited oscillator with a play: Numerical studies, International Journal of Non-Linear Mechanics 94 (2017) 98–108. doi:10.1016/j.ijnonlinmec.2017.03.015.

[82] M. Wiercigroch, Modelling of dynamical systems with motion dependent discontinuities, Chaos, Solitons and Fractals 11 (2000) 2429–2442. doi:https://doi.org/10.1016/S0960-0779(00)00032-1.

[83] R. Vasconcellos, A. Abdelkefi, F. D. Marques, M. R. Hajj, Representation and analysis of control surface freeplay nonlinearity, Journal of Fluids and Structures 31 (2012) 79–91. doi:10.1016/j.jfluidstructs.2012.02.003.

[84] Y. A. Kuznetsov, I. A. Kuznetsov, Y. Kuznetsov, Elements of applied bifurcation theory, Vol. 112, Springer, 1998. doi:10.1007/978-1-4757-3978-7.

[85] M. Krack, J. Gross, Harmonic balance for nonlinear vibration problems, Vol. 1, Springer, 2019. doi:10.1007/978-3-030-14023-6.

[86] T. C. Yuan, J. Yang, L. Q. Chen, A harmonic balance approach with alternating frequency/time domain progress for piezoelectric mechanical systems, Mechanical Systems and Signal Processing 120 (2019) 274–289. doi:10.1016/j.ymssp.2018.10.022.

[87] H. Ranjbarzadeh, F. Kakavand, Determination of nonlinear vibration of 2dof system with an asymmetric piecewise-linear compression spring using incremental harmonic balance method, European Journal of Mechanics, A/Solids 73 (2019) 161–168. doi:10.1016/j.euromechsol.2018.07.005.

[88] L. Peletan, S. Baguet, M. Torkhani, G. Jacquet-Richardet, A comparison of stability computational methods for periodic solution of nonlinear problems with application to rotordynamics, Nonlinear dynamics 72 (2013) 671–682. doi:10.1007/s11071-012-0744-0.

[89] H. Wolf, J. Kodvanj, S. Bjelovučić-Kopilović, Effect of smoothing piecewise-linear oscillators on their stability predictions, Journal of Sound and Vibration 270 (2004) 917–932. doi:10.1016/S0022-460X(03)00639-4.

[90] H. Wolf, D. Banić, A. Sušić, Influence of small harmonic terms on eigenvalues of monodromy matrix of piecewise-linear oscillators, Meccanica 43 (2008) 485–494. doi:10.1007/s11012-008-9112-z.

[91] T. Detroux, L. Renson, L. Masset, G. Kerschen, The harmonic balance method for bifurcation analysis of large-scale nonlinear mechanical systems, Computer Methods in Applied Mechanics and Engineering 296 (2015) 18–38. doi:10.1016/j.cma.2015.07.017.

[92] D. Jordan, P. Smith, Nonlinear ordinary differential equations: an introduction for scientists and engineers, OUP Oxford, 2007.

[93] A. Vizzaccaro, Y. Shen, L. Salles, J. Blahoš, C. Touzé, Direct computation of nonlinear mapping via normal form for reduced-order models of finite element nonlinear structures, Computer Methods in Applied Mechanics and Engineering 384 (10 2021). doi:10.1016/j.cma.2021.113957.

[94] B. Krauskopf, H. M. Osinga, J. Galán-Vioque, Numerical continuation methods for dynamical systems, Vol. 2, Springer, 2007. doi:10.1007/978-1-4020-6356-5.

[95] E. L. Allgower, K. Georg, Numerical continuation methods: an introduction, Vol. 13, Springer Science & Business Media, 2012. doi:10.1007/978-3-642-61257-2.

[96] A. Dhooge, W. Govaerts, Y. A. Kuznetsov, H. G. Meijer, B. Sautois, New features of the software matcont for bifurcation analysis of dynamical systems, Mathematical and Computer Modelling of Dynamical Systems 14 (2008) 147–175. doi:10.1080/13873950701742754.

[97] H. Dankowicz, F. Schilder, Recipes for continuation, SIAM (2013).
URL https://epubs.siam.org/doi/book/10.1137/1.9781611972573

[98] E. J. Doedel, A. R. Champneys, F. Dercole, T. F. Fairgrieve, Y. A. Kuznetsov, B. Oldeman, R. Paffenroth, B. Sandstede, X. Wang, C. Zhang, Auto-07p: Continuation and bifurcation software for ordinary differential equations, FTP from pub/doedel/auto (2007).

[99] A. Cammarano, T. L. Hill, S. A. Neild, D. J. Wagg, Bifurcations of backbone curves for systems of coupled nonlinear two mass oscillator, Nonlinear Dynamics 77 (2014) 311–320. doi:10.1007/s11071-014-1295-3.

[100] M. di Bernardo, C. Budd, A. Champneys, P. Kowalczyk, Piecewise-smooth Dynamical Systems: Theory and Applications, first edition Edition, Springer, London, 2009. doi:/10.1007/978-1-84628-708-4.

[101] K. H. Johansson, M. Egerstedt, J. Lygeros, S. Sastry, On the regularization of zeno hybrid automata, Systems & Control Letters 38 (1999) 141–150.
URL www.elsevier.com/locate/sysconle

[102] M. R. Jeffrey, The ghosts of departed quantities in switches and transitions, SIAM Review 60 (2018) 116–136. doi:10.1137/15M1035756.

[103] W. Chin, E. Ott, H. E. Nusse, C. Grebogi, Grazing bifurcations in impact oscillators, Physical Review E (1994) 4427–4444doi:10.1103/Phys.
URL https://hal.archives-ouvertes.fr/hal-01386141

[104] M. R. Jeffrey, T. I. Seidman, M. A. Teixeira, V. I. Utkin, Into higher dimensions for nonsmooth dynamical systems, Physica D: Nonlinear Phenomena 434 (6 2022). doi:10.1016/j.physd.2022.133222.

[105] M. R. Jeffrey, Hidden Dynamics, Springer Nature, Cham, Switzerland, 2018. doi:10.1007/978-3-030-02107-8.

[106] M. Silveira, P. Wahi, J. C. Fernandes, Exact and approximate analytical solutions of oscillator with piecewise linear asymmetrical damping, International Journal of Non-Linear Mechanics 110 (2019) 115–122. doi:10.1016/j.ijnonlinmec.2018.12.007.

[107] J. Fei, B. Lin, S. Yan, X. Zhang, Approximate solution of a piecewise linear–nonlinear oscillator using the homotopy analysis method, JVC/Journal of Vibration and Control 24 (2018) 4551–4562. doi:10.1177/1077546317729972.

[108] A. B. Nordmark, Universal limit mapping in grazing bifurcations, Physica Review E 55 (1997). doi:10.1103/PhysRevE.55.266.

[109] J. Molenaar, J. G. de Weger, W. van de Water, Mappings of grazing-impact oscillators, Nonlinearity 14 (2) (2001) 301. doi:10.1088/0951-7715/14/2/307.

[110] H. Tao, J. Gibert, Periodic orbits of a conservative 2-dof vibro-impact system by piecewise continuation: bifurcations and fractals, Nonlinear Dynamics 95 (2019) 2963–2993. doi:10.1007/s11071-018-04734-4.

[111] S. Dallas, K. MacHairas, E. Papadopoulos, A comparison of ordinary differential equation solvers for dynamical systems with impacts, Journal of Computational and Nonlinear Dynamics 12 (11 2017). doi:10.1115/1.4037074.

[112] M. Hénon, On the numerical computation of poincaré maps, Physica D: Nonlinear Phenomena 5 (2-3) (1982) 412–414. doi:https://doi.org/10.1016/0167-2789(82)90034-3.

[113] L. F. Shampine, S. Thompson, Event location for ordinary differential equations, Computers and Mathematics with Applications 39 (2000) 43–54.
URL www.elsevier.nl/locate/camwa

[114] P. Brzeski, A. Chong, M. Wiercigroch, P. Perlikowski, Impact adding bifurcation in an autonomous hybrid dynamical model of church bell, Mechanical Systems and Signal Processing 104 (2018) 716–724. doi:10.1016/j.ymssp.2017.11.025.

[115] H. Jiang, A. S. Chong, Y. Ueda, M. Wiercigroch, Grazing-induced bifurcations in impact oscillators with elastic and rigid constraints, International Journal of Mechanical Sciences 127 (2017) 204–214. doi:10.1016/j.ijmecsci.2017.02.001.

[116] M. Liao, Y. Liu, J. P. Chávez, A. S. Chong, M. Wiercigroch, Dynamics of vibro-impact drilling with linear and nonlinear rock models, International Journal of Mechanical Sciences 146-147 (2018) 200–210. doi:10.1016/j.ijmecsci.2018.07.039.

[117] Y. Liu, J. Paez Chavez, E. Pavlovskaia, M. Wiercigroch, Analysis and control of the dynamical response of a higher order drifting oscillator, Proceedings of the Royal Society A: Mathematical, Physical and Engineering Sciences 474 (2 2018). doi:10.1098/rspa.2017.0500.

[118] P. Thota, H. Dankowicz, Tc-hat (t$\hat{\text{C}}$): A novel toolbox for the continuation of periodic trajectories in hybrid dynamical systems, SIAM Journal on Applied Dynamical Systems 7 (2008) 1283–1322. doi:10.1137/070703028.

[119] R. Alcorta, S. Baguet, B. Prabel, P. Piteau, G. Jacquet-Richardet, Period doubling bifurcation analysis and isolated sub-harmonic resonances in an oscillator with asymmetric clearances, Nonlinear Dynamics 98 (2019) 2939–2960. doi:10.1007/s11071-019-05245-6.

[120] L. P. Miguel, R. de Oliveira Teloli, S. da Silva, Some practical regards on the application of the harmonic balance method for hysteresis models, Mechanical Systems and Signal Processing 143 (9 2020). doi:10.1016/j.ymssp.2020.106842.

[121] M.-F. Danca, Continuous approximations of a class of piecewise continuous systems, International Journal of Bifurcation and Chaos 11 (2 2014). doi:https://doi.org/10.1142/S0218127415501461.

[122] M. F. Danca, Synchronization of piecewise continuous systems of fractional order, Nonlinear Dynamics 78 (2014) 2065–2084. doi:10.1007/s11071-014-1577-9.

[123] M. F. Danca, Lyapunov exponents of a class of piecewise continuous systems of fractional order, Nonlinear Dynamics 81 (2015) 227–237. doi:10.1007/s11071-015-1984-6.

[124] D. J. Simpson, V. Avrutin, S. Banerjee, Nordmark map and the problem of large-amplitude chaos in impact oscillators, Physical Review E 102 (8 2020). doi:10.1103/PhysRevE.102.022211.

[125] E. J. Doedel, R. C. Paffenroth, H. B. Keller, D. J. Dichmann, J. Galán-Vioque, A. Vanderbauwhede, Continuation of periodic solutions in conservative systems with application to the 3-body problem, International Journal of Bifurcation and Chaos 13 (2003) 1353–1381.
URL https://www.researchgate.net/publication/284686576

[126] J. P. Wright, J.-S. Pei, Solving dynamical systems involving piecewise restoring force using state eventlocation, Journal of Engineering Mechanics 138 (2012) 997–1020. doi:10.1061/(asce)em.1943-7889.0000404.

[127] S. Natsiavas, Dynamics of multiple-degree-of-freedom oscillators with colliding components, Journal of Sound and Vibration 165 (1993) 439–453. doi:10.1006/jsvi.1993.1269.
URL https://hal.science/hal-01510834

[128] A. Cammarano, S. G. Burrow, D. A. Barton, A. Carrella, L. R. Clare, Tuning a resonant energy harvester using a generalized electrical load, Smart Materials and Structures 19 (2010). doi:10.1088/0964-1726/19/5/055003.

[129] J. Brownjohn, A. Pavic, Experimental methods for estimating modal mass in footbridges using human-induced dynamic excitation, Engineering Structures 29 (11) (2007) 2833–2843. doi:https://doi.org/10.1016/j.engstruct.2007.01.025.

[130] G. Quaranta, W. Lacarbonara, S. F. Masri, A review on computational intelligence for identification of nonlinear dynamical systems, Nonlinear Dynamics 99 (2020) 1709–1761. doi:10.1007/s11071-019-05430-7.

[131] J. H. Holland, Adaptation in natural and artificial systems: an introductory analysis with applications to biology, control, and artificial intelligence, MIT press, 1992.

[132] J. Kennedy, R. Eberhart, Particle swarm optimization, in: Proceedings - International Conference on Neural Networks, Vol. 4, IEEE, 1995, pp. 1942–1948. doi:10.1109/ICNN.1995.488968.

[133] Y. Shi, R. Eberhart, A modified particle swarm optimizer, in: 1998 IEEE international conference on evolutionary computation proceedings. IEEE world congress on computational intelligence (Cat. No. 98TH8360), IEEE, 1998, pp. 69–73.

[134] A. E. Charalampakis, C. K. Dimou, Comparison of evolutionary algorithms for the identification of bouc-wen hysteretic systems, Journal of Computing in Civil Engineering 29 (5 2015). doi:10.1061/(asce)cp.1943-5487.0000348.

[135] G. Quaranta, G. C. Marano, R. Greco, G. Monti, Parametric identification of seismic isolators using differential evolution and particle swarm optimization, Applied Soft Computing 22 (2014)

458–464. doi:https://doi.org/10.1016/j.asoc.2014.04.039.
URL https://www.sciencedirect.com/science/article/pii/S1568494614002154

[136] H. Modares, A. Alfi, M.-M. Fateh, Parameter identification of chaotic dynamic systems through an improved particle swarm optimization, Expert Systems with Applications 37 (5) (2010) 3714–3720. doi:https://doi.org/10.1016/j.eswa.2009.11.054.

[137] L. N. Virgin, Introduction to experimental nonlinear dynamics: a case study in mechanical vibration, Cambridge University Press, 2000.

[138] S. Masri, T. Caughey, A nonparametric identification technique for nonlinear dynamic problems, Journal of Applied Mechanics 46 (1979) 433–447.

[139] S. F. Masri, F. Tasbihgoo, J. P. Caffrey, A. W. Smyth, A. G. Chassiakos, Data-based model-free representation of complex hysteretic mdof systems, Structural Control and Health Monitoring 13 (2006) 365–387. doi:10.1002/stc.147.

[140] E. Bonisoli, A. Vigliani, Identification techniques applied to a passive elasto-magnetic suspension, Mechanical Systems and Signal Processing 21 (2007) 1479–1488. doi:10.1016/j.ymssp.2006.05.009.

[141] D. Rizos, G. Feltrin, M. Motavalli, Structural identification of a prototype pre-stressable leaf-spring based adaptive tuned mass damper: Nonlinear characterization and classification, Mechanical Systems and Signal Processing 25 (2011) 205–221. doi:10.1016/j.ymssp.2010.07.001.

[142] D. Anastasio, A. Fasana, L. Garibaldi, S. Marchesiello, Nonlinear dynamics of a duffing-like negative stiffness oscillator: Modeling and experimental characterization, Shock and Vibration 2020 (2020). doi:10.1155/2020/3593018.

[143] S. Masri, H. Sassi, T. Caughey, Nonparametric identification of nearly arbitrary nonlinear systems, Journal of Applied Mathematics 49 (1982) 619–628. doi:https://doi.org/10.1115/1.3162537.

[144] C. M. Richard, R. Singh, Identification of multi-degree-of-freedom non-linear systems under random excitations by the "reverse path" spectral method, Journal of Sound and Vibration 213 (1998) 673–708. doi:https://doi.org/10.1006/jsvi.1998.1522.

[145] D. Adams, R. Allemang, A frequency domain method for estimating the parameters of a non-linear structural dynamic model through feedback, Mechanical Systems and Signal Processing 14 (4) (2000) 637–656. doi:https://doi.org/10.1006/mssp.2000.1292.
URL https://www.sciencedirect.com/science/article/pii/S0888327000912925

[146] S. Marchesiello, L. Garibaldi, A time domain approach for identifying nonlinear vibrating structures by subspace methods, Mechanical Systems and Signal Processing 22 (2008) 81–101. doi:10.1016/j.ymssp.2007.04.002.

[147] K. Worden, Data processing and experiment design for the restoring force surface method, part i: Integration and differentiation of measured time data, Mechanical Systems and Signal Processing 4 (1990) 295–319. doi:https://doi.org/10.1016/0888-3270(90)90010-I.

[148] Z. Hu, B. J. Gallacher, Effects of nonlinearity on the angular drift error of an electrostatic mems rate integrating gyroscope, IEEE Sensors Journal 19 (2019) 10271–10280. doi:10.1109/JSEN.2019.2929352.

[149] J. Jia, X. Ding, Z. Qin, Z. Ruan, W. Li, X. Liu, H. Li, Overview and analysis of mems coriolis vibratory ring gyroscope, Measurement: Journal of the International Measurement Confederation 182 (9 2021). doi:10.1016/j.measurement.2021.109704.

[150] A. Sarrafan, S. Azimi, F. Golnaraghi, B. Bahreyni, A nonlinear rate microsensor utilising internal resonance, Scientific Reports 9 (12 2019). doi:10.1038/s41598-019-44669-3.

[151] C. Xia, D. F. Wang, T. Ono, T. Itoh, R. Maeda, A mass multi-warning scheme based on one-to-three internal resonance, Mechanical Systems and Signal Processing 142 (8 2020). doi:10.1016/j.ymssp.2020.106784.

[152] B. Jeong, C. Pettit, S. Dharmasena, H. Keum, J. Lee, J. Kim, S. Kim, D. M. McFarland, L. A. Bergman, A. F. Vakakis, H. Cho, Corrigendum: Utilizing intentional internal resonance to achieve multi-harmonic atomic force microscopy (2016 nanotechnology 27 125501), Nanotechnology 27 (2016). doi:10.1088/0957-4484/27/19/199501.

[153] R. Potekin, S. Dharmasena, H. Keum, X. Jiang, J. Lee, S. Kim, L. A. Bergman, A. F. Vakakis, H. Cho, Multi-frequency atomic force microscopy based on enhanced internal resonance of an inner-paddled cantilever, Sensors and Actuators, A: Physical 273 (2018) 206–220. doi:10.1016/j.sna.2018.01.063.

[154] D. H. Zanette, Effects of noise on the internal resonance of a nonlinear oscillator, Scientific Reports 8 (12 2018). doi:10.1038/s41598-018-24383-2.

[155] A. Keşkekler, O. Shoshani, M. Lee, H. S. van der Zant, P. G. Steeneken, F. Alijani, Tuning nonlinear damping in graphene nanoresonators by parametric–direct internal resonance, Nature Communications 12 (12 2021). doi:10.1038/s41467-021-21334-w.

[156] O. Shoshani, S. W. Shaw, M. I. Dykman, Anomalous decay of nanomechanical modes going through nonlinear resonance, Scientific Reports 7 (12 2017). doi:10.1038/s41598-017-17184-6.

[157] J. Güttinger, A. Noury, P. Weber, A. M. Eriksson, C. Lagoin, J. Moser, C. Eichler, A. Wallraff, A. Isacsson, A. Bachtold, Energy-dependent path of dissipation in nanomechanical resonators, Nature Nanotechnology 12 (2017) 631–636. doi:10.1038/nnano.2017.86.

[158] X. Wang, R. Huan, W. Zhu, D. Pu, X. Wei, Frequency locking in the internal resonance of two electrostatically coupled micro-resonators with frequency ratio 1:3, Mechanical Systems and Signal Processing 146 (1 2021). doi:10.1016/j.ymssp.2020.106981.

[159] P. Taheri-Tehrani, A. Guerrieri, M. Defoort, A. Frangi, D. A. Horsley, Mutual 3:1 subharmonic synchronization in a micromachined silicon disk resonator, Applied Physics Letters 111 (10 2017). doi:10.1063/1.4997195.

[160] L. Ruzziconi, N. Jaber, L. Kosuru, M. I. Younis, Activating internal resonance in a microelectromechanical system by inducing impacts, Nonlinear Dynamics 110 (2022) 1109–1127. doi:10.1007/s11071-022-07706-x.

[161] S. Priya, D. J. Inman, Energy harvesting technologies, Springer US, 2009. doi:10.1007/978-0-387-76464-1.

[162] M. L. Monaco, C. Russo, A. Somà, Investigation of gravitational energy harvesters for iot power supply in freight train monitoring, in: 2023 25th European Conference on Power Electronics and Applications (EPE'23 ECCE Europe), 2023, pp. P.1–P.8. doi:10.23919/EPE23ECCEEurope58414.2023.10264497.

[163] X. Wang, Frequency analysis of vibration energy harvesting systems, Academic Press, 2016.

[164] A. N. S. Institute, An American National Standard: IEEE Standard on Piezoelectricity Standard, IEEE, 1988.

[165] A. Erturk, D. J. Inman, Piezoelectric energy harvesting, John Wiley & Sons, 2011.

[166] J. Yang, Analysis of Piezoelectric Devices, World Scientific, Singapore, 2006.

[167] J. Whiteley, Finite Element Methods: A Practical Guide, Springer, 2017. doi:10.1007/978-3-319-49971-0.

[168] Ansys, Academic Research - Help System, Release 2020 R1, ANSYS Inc (2020).

[169] A. Kaveh, S. Talatahari, A novel heuristic optimization method: Charged system search, Acta Mechanica 213 (2010) 267–289. doi:10.1007/s00707-009-0270-4.

[170] A. Kaveh, K. B. Hamedani, Advanced metaheuristic algorithms and their applications in structural optimization, Vol. 1059, Springer Nature, 2022. doi:/10.1007/978-3-031-13429-6.

[171] A. Kaveh, M. I. Ghazaan, Meta-heuristic algorithms for optimal design of real-size structures, Springer, 2018. doi:10.1007/978-3-319-78780-0.

[172] R. Storn, K. Price, Differential evolution - a simple and efficient heuristic for global optimization over continuous spaces, Journal of global optimization 11 (1997) 341–359. doi:10.1023/A:1008202821328.

[173] G. Lindfield, J. Penny, Chapter 3 - particle swarm optimization algorithms, in: G. Lindfield, J. Penny (Eds.), Introduction to Nature-Inspired Optimization, Academic Press, Boston, 2017, pp. 49–68.

[174] E. Mezura-Montes, C. A. Coello Coello, Constraint-handling in nature-inspired numerical optimization: Past, present and future, Swarm and Evolutionary Computation 1 (2011) 173–194. doi:https://doi.org/10.1016/j.swevo.2011.10.001.

[175] M. Pedersen, Good parameters for particle swarm optimization, Tech. rep., Hvass Laboratories (2010).

[176] Z. Yang, A. Erturk, J. Zu, On the efficiency of piezoelectric energy harvesters, Extreme Mechanics Letters 15 (May) (2017) 26–37. doi:https://doi.org/10.1016/j.eml.2017.05.002.

[177] Y. Shen, N. Béreux, A. Frangi, C. Touzé, Reduced order models for geometrically nonlinear structures: Assessment of implicit condensation in comparison with invariant manifold approach, European Journal of Mechanics, A/Solids 86 (3 2021). doi:10.1016/j.euromechsol.2020.104165.

[178] C. Touzé, A. Vizzaccaro, O. Thomas, Model order reduction methods for geometrically nonlinear structures: a review of nonlinear techniques, Nonlinear Dynamics 105 (2021) 1141–1190. doi:10.1007/s11071-021-06693-9.